
Development and Operation of Miniaturised Ion Traps for Scalable Quantum Computation

Dissertation

zur Erlangung des Doktorgrades an der
Fakultät für Mathematik, Informatik und Physik
der Leopold-Franzens-Universität Innsbruck

vorgelegt von

Felicity Erin Splatt

durchgeführt am Institut für Experimentalphysik

unter der Leitung von

Univ. Prof. Dr. R. Blatt

Innsbruck

August 2009

Abstract

The advent of quantum information processing promises the merging of two of the deepest and most successful scientific and technological developments of the last century: quantum physics and computer science. Ions stored as strings in linear Paul traps are among the most promising systems for the experimental realisation of a quantum device harnessing the computing power inherent in the laws of quantum physics.

Scaling ion trap quantum computers to large numbers of qubits requires a new approach. One proposal is the “quantum charge coupled device”, which describes an architecture for a large number of interconnected traps, with the possibility of sorting ions and transporting ions between traps. Implementation of a large number of interconnected traps can be achieved by a segmented(-electrode) ion trap, where the segmentation of the dc electrodes of a linear Paul trap enables a sophisticated control of the axial trapping potential. The promise held by this approach has led to vigorous research in this direction by a number of groups worldwide.

The goal of this thesis is the design and construction of a microtrap, and subsequently to gather first experiences in shuttling and sorting mechanisms as required in future quantum computation devices. Work towards this goal has been completed on two fronts: using a rapid-prototype macroscopic printed circuit board trap, and in the design and development of a miniaturised microfabricated segmented ion trap.

First experiments were carried out with a segmented surface PCB ion trap. This easy-to-fabricate, rapidly prototyped trap was used to gain a deep understanding of the tailored potentials possible with segmented control electrodes. This knowledge is used in two different ways; in the realisation of long strings of ions, and in the deterministic reordering of ions in a crystal.

The macroscopic surface trap has eleven dc electrodes, and the understanding of the effects of these individual electrodes allowed us to realise long (up to 43 ion) strings with almost equal ion spacing. This very long string may be applied to a recent theoretical proposal for quantum computation with ions in an anharmonic trap.

In the same trap, ions in a crystal were deterministically reordered – this operation being one of the crucial primitives required of quantum computation in a segmented ion trap. The reordering of ions can be achieved through the use of time-dependent voltages which rotate the principal axes of the trap. These rotations have been implemented in two different ways. In one configuration, a two ion crystal is moved through a path similar to that traversed in a “three-point turn”, the ions finally returning to their origin with positions reversed. This process is deterministic and has a success rate of 93%. A different path was also realised, a rotation of the weak principal axis around a point, in analogy to a “pirouette”. Here two-, three- and four-ion crystals had their positions reversed, with a success rate of 97%. This path requires less deviation of the ions from the radiofrequency null and therefore is expected to entail less motional heating.

Work was also carried out in the design of a microfabricated segmented electrode ion trap. This two-layer, gold-on-alumina trap has the desirable features of a large number of control electrodes, small dimensions allowing tight confinement and therefore fast gate operations, suppression of axial pseudopotential components, and a design minimising exposed dielectrics. The optimisation of trap dimensions is thoroughly explained, the trap parameters simulated and the fabrication and assembly process is described.

Zusammenfassung

Quanteninformationsverarbeitung verspricht die Zusammenführung von zwei der erfolgreichsten Disziplinen von Wissenschaft und Technik, nämlich Quantenphysik und Computerwissenschaften. In linearen Paul-Fallen gespeicherte Ionenketten stellen eine vielversprechende experimentelle Realisierung dar, um die Rechengesetze der Quantenmechanik nutzbar zu machen.

Bei der Entwicklung eines nützlichen Quantencomputers spielt die Frage der Skalierbarkeit von auf Ionenfallen basierenden Quantencomputern eine zentrale Rolle. Eine mögliche Umsetzung dieses Problems ist eine Fallenarchitektur mit segmentierten Elektroden, welche zahlreiche einzelne Ionenfallen zu einer Gesamtstruktur verbindet und die Möglichkeit zu hochkomplexer Kontrolle des Fallenpotentials bietet.

Das Ziel dieser Arbeit ist das Design und die Konstruktion einer Mikrofalle, mit deren Hilfe in Hinblick auf die Entwicklung eines zukünftigen Quantenrechners erste Erfahrungen zu Ionen-transport und -sortierung gesammelt werden können. Die Arbeit behandelt vor allem zwei Aspekte: makroskopische Fallen basierend auf konventioneller Leiterbahn-Technologie zur raschen Erstellung von Prototypen und die Entwicklung von miniaturisierten Mikrofallen.

Erste Experimente wurden mit Hilfe einer Oberflächenfalle ausgeführt, welche leicht und vor allem schnell zu realisieren ist. Sie wurde benutzt, um tieferes Verständnis der durch die segmentierten Elektroden erzeugten, massgeschneiderten Potentiale zu erlangen. Damit konnten lange Ionenketten realisiert, sowie gezielte Umstellung der Anordnung von Ionen im Ionenkristall gezeigt werden.

Diese makroskopische Falle besitzt elf Gleichspannungs-Elektroden, mit deren Hilfe eine Ionenkette bestehend aus bis zu 43 Ionen mit gleichförmigen Abstand zu den Nachbar-Ionen erzeugt werden konnte. Das könnte eine Anwendung bei der kürzlich (theoretisch) vorgeschlagenen Realisierung von Quanteninformationsverarbeitung in einer anharmonischen Falle finden. In der gleichen Falle konnte die Anordnung eines Ionenkristalls gezielt verändert werden - ein Grundbaustein zur Quanteninformationsverarbeitung in einer segmentierten Ionenfalle. Die reproduzierbare Anordnung kann durch eine zeitabhängige Variation der Fallenpotentiale erreicht werden. Zuerst wurde ein Kristall aus zwei Ionen über einen Pfad mit drei Eckpunkten in die Ausgangsposition verschoben, wobei die Positionen der Ionen vertauscht wurden. Ein ähnliches Resultat wurde erzeugt indem das Fallenpotential so verändert wurde, dass sich die Ionen um den gemeinsamen Schwerpunkt drehen. Hier erwartet man weniger Aufheizen der Ionen, da sich die Ionen näher am Radiofrequenz-Minimum befinden. Die Erfolgsrate für den ersten Prozess beträgt 93%, für den zweiten 97%.

Ein weiterer Teil der Arbeit beschäftigt sich mit der Entwicklung einer mikrostrukturierten segmentierten Ionenfalle. Die Zweischicht-Falle besteht aus einer grossen Zahl von Kontrollelektroden mit kleiner Ausdehnung und erlaubt starken Einschluss der Teilchen und deswegen schnelle Gatteroperationen. Die Optimierung und Simulation der Fallenparameter, sowie die Fertigung und Zusammenbau der Falle werden beschrieben.

Contents

1	Introduction	1
2	Theory	7
2.1	Radiofrequency Ion Traps	7
2.1.1	Radial Confinement	8
2.1.2	Axial Confinement: the Linear Paul Trap	10
2.1.3	The Quantum Charge-Coupled Device: Segmented-Electrode Ion Traps	11
2.1.4	Linear Paul Trap Geometries with Microfabricated Structures	12
2.1.5	Ion Strings in a Linear Paul Trap	12
2.2	Electronic energy Levels of $^{40}\text{Ca}^+$ and ^{40}Ca	13
2.3	Laser-Ion Interaction	15
2.3.1	Detection and Measurement	15
2.3.2	Doppler Cooling	16
2.3.3	Coherent Manipulations	17
3	Trap Design and Simulation	19
3.1	Trap Design	19
3.1.1	Trap Geometry	20
3.1.1.1	Radial Confinement	20
3.1.1.2	Axial Confinement	23
3.1.2	Materials and Fabrication	28
3.1.2.1	Electrode Material	29
3.1.2.2	Substrate Material	30
3.1.2.3	Electrical Breakdown	31
3.1.3	Practical Considerations	32
3.1.3.1	Excess Micromotion Compensation	32
3.1.3.2	Orientation of Trap Axes	32
3.1.3.3	Ion Loading	35
3.1.3.4	Trap Packaging and Electrical Connections	35
3.2	Trap Simulation	36
3.2.1	Electric Potential <i>Basis Functions</i>	36
3.2.2	Numerical Simulation Methods	37
3.2.2.1	The Finite Element Method	37
3.2.2.2	The Boundary Element Method	37
3.2.2.3	Comparison between the Boundary Element Method and the Finite Element Method.	38
3.2.2.4	Other Notable Solving Methods	39
3.2.3	Numerical Field Simulation and Analysis	42
3.2.3.1	Numerical Field Simulation	42
3.2.3.2	Electric Potential Analysis	43

4	Trap Layout and Fabrication	47
4.1	Trap Layout and Simulation of Trap Parameters	47
4.1.1	Surface trap <i>Bastille</i>	47
4.1.1.1	Surface Trap <i>Bastille</i> Layout	48
4.1.1.2	Surface Trap <i>Bastille</i> Numerical Field Simulation and Analysis	49
4.1.2	Two-Layer Gold-on-Alumina Trap	61
4.1.2.1	Two-Layer Gold-on-Alumina Trap Geometry	61
4.1.2.2	Two-Layer Gold-on-Alumina Trap Numerical Field Simulation and Analysis	63
4.2	Trap Fabrication	69
4.2.1	Surface Trap <i>Bastille</i>	69
4.2.2	Two-Layer Gold-on-Alumina Trap	69
4.2.2.1	Laser Machining of Alumina Wafers	70
4.2.2.2	Gold Evaporation	70
4.2.2.3	Electroplating	71
4.2.2.4	Electrical Insulation	72
4.2.2.5	Chip Dicing	72
4.2.2.6	Etching	73
4.2.2.7	Assembly	73
5	Experimental Setup	75
5.1	Trap Mounting Hardware and Accessories	75
5.2	Vacuum Chamber and Vacuum Pumps	79
5.3	Laser Systems	81
5.4	Optical Access and Detection	84
5.5	Experimental Control	87
6	Experimental Results	89
6.1	A Long, Almost-Evenly Spaced String of Ions	89
6.2	Long Ion Strings as Electrical Field Probes	90
6.3	Deterministic Reordering of Ions	94
6.3.1	The <i>Three-Point Turn</i>	94
6.3.2	The <i>Pirouette</i>	97
6.3.3	Generalisation of Method to Two-Layer Trap Geometries	101
7	Summary and Outlook	105
	Bibliography	109

Chapter 1

Introduction

The idea of confinement of charged particles was first introduced by K.H. Kingdon in 1923, in experiments where a metal filament surrounded by a metal cylinder, with a static voltage applied between the cylinder and filament, is able to “imprison” [Kin23] a cloud of charged particles for an indefinite period of time. In 1936, Frans Penning pioneered the idea of a charged particle trap based on static electric and magnetic fields [Pen36], which was first built by Hans Georg Dehmelt in 1959 [Deh67]. In a Penning trap, radial confinement of charged particles is achieved by a strong homogeneous axial magnetic field, with axial confinement provided by a electric quadrupole field. In the same decade, Wolfgang Paul developed an ion trap based on the combination of static and radiofrequency electric fields [PS53, POF58]. In 1980, a single atomic ion was trapped and observed by Neuhauser et al. for the first time [NHTD80].

Initially the ability to trap ions allowed the investigation of the charge, mass and spin of trapped particles. Such experiments continue to provide precise measurements of mass [DNBP94, GPQ⁺95] and fundamental physical constants [OHDG06]. Interrogation of trapped ions entered a new era with the advent of laser cooling [WDW78, NHTD78] and laser spectroscopy [WI81, BSW82]. Experiments were able to make precision measurements of atomic internal structure [MBG⁺06], precise spectroscopic studies [WIBH87, RYB⁺00], fundamental tests of quantum mechanics [BHI⁺89, SNBT86] and cosmology [RHS⁺08]. The exquisite isolation of the ion from its surroundings, and the possible storage time of months, led to the rapid adoption of ion traps for use in atomic clocks [BPIW85].

In recent years, ion traps have found application in the exciting new field of quantum computation.

In the last few decades, improvements in semiconductor processing have allowed an exponential increase in classical computer speeds, a trend known as Moore’s law. However, the inexorable advance towards smaller devices and denser chips (and thus faster computers), is expected to reach a fundamental limitation when the component size approaches the point where quantum effects, anathema to their deterministic nature, will dominate the behavior of electrons in transistors.

While classical computing seeks to eliminate these “undesirable” quantum effects, quantum computing seeks instead to utilise the advantages offered by quantum properties. Using the unique properties of quantum mechanics in a computational device was first conceived by Paul Benioff [Ben80, Ben82] and Richard Feynman [Fey82, Fey85] in the early 1980s. Their idea of using information stored in quantum states for computation was initially envisioned as a means of simulating quantum systems. As quantum systems become exponentially larger and more complex with a linear increase in size, classical computers are impractical for simulating all but the simplest quantum problems, while quantum computers, provided appropriate preparation and manipulation capabilities of its quantum states, could naturally store and process that information. For about a decade,

this idea remained more of a curious oddity.

However, the field of theoretical quantum computing gained fresh motivation in 1994 when Peter Shor discovered an algorithm capable of factoring large numbers [Sho94, Sho96]. Using this algorithm, processing time scales as $\mathcal{O}(\log(N))^3$ with the size of N (the number being factored), while the number field sieve, the best classical known algorithm, scales exponentially worse ($\mathcal{O} \exp(\sqrt{\log N \log \log N})$). Experimental realisation of this factoring algorithm for large composite numbers is of significant importance, as certain cryptography methods are based on the computational difficulty of factoring large numbers. For example, it would render frequently used public key encryption systems (such as the RSA key) obsolete, allowing eavesdropping which could find obvious application by intelligence agencies. Quantum mechanics, however, also provides a solution in the form of a secure communication which uses quantum key distribution schemes. This quantum cryptography has been theoretically shown to be unconditionally secure. The usefulness of a universal quantum computer is also demonstrated in the search algorithm for unsorted databases discovered by Lov K. Grover in 1996, which exhibits a quadratic increase in speed over its classical search equivalent. The discovery of quantum error correction codes [Ste96, Sho95] allows the implementation of these algorithms by correcting for the inevitable environmental influence on a quantum system. Error correcting codes set a threshold level for fault tolerance and ensure that when the error is below this level, a quantum algorithm can be reliably implemented.

However, the importance of the quantum computing motivation driven by the doomsday scenario envisioned by Moore's law should not be overemphasised. Firstly, classical computers might be made faster by any number of other strategies developed by the semiconductor industry and computer scientists. Secondly, only a few quantum algorithms have been discovered which exhibit a speedup over their classical counterparts, and the goal of solving broader problems remains an open question [Aar05]. Finally, building a useful quantum computer is technologically difficult, and manipulating large entangled systems is so far an unexplored regime.

While quantum computers might not surpass classical computers any time soon in these classical computation algorithms, one application in which they might first exceed the capabilities of classical computers is the simulation of a quantum system. Here, the number of qubits required and the complexity of operations is more lenient than that required for quantum computation schemes. Current computing technology is unable to simulate certain quantum systems consisting of n ($n \gtrsim 50$) qubits, while a quantum computer requires only n qubits to perform the same task. Such a realisation may not be far away.

The fundamental operations required for quantum computation have been demonstrated, however the assembly of these building blocks to a large-scale quantum computer is difficult. Useful algorithms require thousands, or possibly even larger quantities, of qubits, depending on the use of error correction codes. The requirements for the implementation of a quantum information processor are stated by the criteria of DiVincenzo [Div00]: a scalable physical system with well-characterised qubits, the ability to initialise the state of the qubits to a simple fiducial state, relevant decoherence times, much longer than the gate operation time, a universal set of quantum gates and a qubit specific measurement capability. An additional two criteria: the ability to interconvert stationary and "flying" qubits, and the ability to faithfully transmit "flying qubits" between specified locations, extend the requirements to that of the faithful transport of quantum information, that is, the ability to interconnect separate quantum systems to create quantum networks.

Prototypes of quantum information processors have been realised in a variety of experimental systems: optical photons [KLM01], optical cavity quantum electrodynamics [DRBH95], nuclear magnetic resonance (NMR) systems [Jon00, VC05], Josephson junctions [YTN02, MSS01, MOL⁺99], quantum dots [LD98, HKP⁺07], silicon-based nuclear spins [Kan98], neutral trapped atoms [PGCZ95, BCJ⁺00, DBJ00], and ion traps [CZ95, Ste97]. This list and the references therein

Chapter 1. Introduction

are by no means exhaustive. The most complex quantum algorithms involving the highest number of qubits were so far implemented in NMR technology [VC05]. Since it is not currently clear how to scale this system, it cannot yet be considered as a long-term viable implementation.

In 1995 Ignacio Cirac and Peter Zoller devised a scheme for quantum information processing with trapped ions [CZ95]. In this proposal, laser-cooled Coulomb crystals of many ions are held in an ion trap, with interaction between qubits achieved through the collective motion of the ions in the trap. This publication has initiated lively research and several other proposals for the implementation of gate operations in ion traps have followed [SM99, JPK00]. Before this proposal was experimentally implemented, ion traps had already demonstrated three of the five DiVincenzo criteria: initialisation [WBID80], readout [NSD86, SNBT86, BHIW86] and long coherence times [BHI⁺91]. Additionally, laser-cooled Coulomb crystals of many ions held in ion traps could serve as a quantum register [DPC⁺87, WBI⁺87, RBG⁺92, RGB⁺92].

In the fourteen years since its proposal ion trap based quantum computers have cemented their place as a leading contender of an experimental realisation of a quantum computer. The final four DiVincenzo criteria have been well demonstrated: qubit-specific measurement capability using the quantum jump technique [NSD86, SNBT86, BHIW86], qubits encoded in ions held in a trap have been initialised to the ground state [WBID80], coherence times exceeding ten minutes have been achieved [BHI⁺91], universal sets of quantum gates have been performed [SKK⁺00, DBL⁺02, SHR⁺03, SHG⁺03, LDM⁺03, HBD⁺05, HML⁺06], even operating with fidelities above 99% [BKRB08]. Some of the achievements of ion trap based quantum systems include two-qubit gate operations [LDM⁺03, SHR⁺03], entangled states of two [TWK⁺98] and four [SKK⁺00] ions, a variety of universal gate operations [SKK⁺00, DBL⁺02, SHR⁺03, LDM⁺03, HBD⁺05, HML⁺06], the first demonstration of a quantum algorithm outside NMR; the Deutsch-Jozsa algorithm with a single ion [GRL⁺03], quantum teleportation [BCS⁺04, RHR⁺04], error correction [CLS⁺04], the creation of multi-particle entangled states of up to eight ions [HHR⁺05, RRH⁺04, LKS⁺05], decoherence-free subspaces [KMR⁺01], implementation of Grover's search algorithm [LBD⁺05], entanglement purification [RLK⁺06], simulation of a nonlinear beam-splitter [LDM⁺02], partial readout of an entangled quantum register [RLR⁺04], quantum gate and quantum process tomography [RKS⁺06], entanglement of ions held in separate traps, using ion-photon interaction [DHL⁺04, MMO⁺07], entanglement swapping [RMK⁺08], and the realisation of the quantum Toffoli gate [MKH⁺09]. While ion trap based quantum computers have achieved considerable success, interestingly it is the first of the DiVincenzo criteria that is not easily met in ion traps: that of scalability. While the Cirac-Zoller approach is in principle scalable because the required resources (storage and processing) scale as the polynomial rather than an exponential with the number of qubits, as the number of ions in a linear ion trap increases, the inter-ion spacing decreases (for a fixed trap frequency). Individual addressing of ions with laser beams becomes technologically prohibitive. Maintaining a reasonable inter-ion spacing by decreasing the trap frequencies would have the undesired effect of reducing gate speeds. More critically, mode addressing is usually accomplished by spectrally isolating the frequency of one mode of interest. As the number of trapped ions increases, the spectral density of motional modes renders spectral isolation impractical. Despite the significant success achieved in linear ion traps to date, current linear ion traps with a simple axial harmonic potential do not appear to be scalable beyond approximately ten qubits, therefore limiting the complexity of quantum algorithms which can be performed. A linear Paul trap with harmonic axial potential therefore seems unsuitable as a long-term vision for quantum computer in regards to the first DiVincenzo criteria. This situation is not unique to ion trap realisations of quantum information processors: one of the main obstacles on the quantum information science and technology roadmap [htt04] remains the "climbing (of) Mount Scalable" [BCD02] for all physical realisations.

The ion trap approach to quantum information processing and quantum computing attempts to

realise DiVincenzo’s criteria of a “scalable physical system” is the idea of the division of quantum hardware into chunks, with the architecture resembling the charge-coupled device [KMW02]: a quantum chip that can propel strings of individual ions through a grid of linear traps. This architecture for a large-scale ion-trap quantum computer resembles the charge-coupled device in that it imagines a quantum chip that consists of a large number of interconnected ion traps. Ions can be confined in individual traps or moved between traps by changing the operating voltages of the traps. Manipulation of ions in any particular trap is achieved with methods already demonstrated, and connections between traps allow communication between sets of ions. Ions may be stored in memory regions, and moved into interaction regions to perform logic gates by applying appropriate voltages to the electrode segments. The required trapping and transport potentials are realised using a combination of radiofrequency and quasistatic electric fields.

The quantum-charge coupled device proposal hints at the possibility of scaling up the already considerably successful linear ion trap quantum computation. “Segmented(-electrode) ion traps” are geometries which attempt to realise the proposal’s target of large number of interconnected ion traps by segmenting the dc control electrodes of a linear Paul trap. Due to their promise in extending linear ion trap quantum computing to the use of large numbers of ions and the realisation of more complex quantum computations, they have become an active area of research. Using this approach, it appears straightforward (although technically demanding) to scale up the trapped ion approach to much larger numbers of qubits.

Fabrication of microtraps has utilised a variety of materials and fabrication techniques. In first iterations, microtraps sought to retain the good optical access and high trap depths of two-layer designs by assembling multiple wafers to form a traditional Paul trap type design. True scalability of this geometry requires a monolithic approach, and this has been attempted in several traps [SHO⁺06, BWG⁺06]. Several three-layer traps have also been fabricated [HOS⁺06]. Simplification in fabrication can be achieved by considering planar traps, at the expense of 1/6 to 1/3 of the motional frequencies and 1/30 to 1/200 trap depths of more conventional quadrupole geometries at comparable radiofrequency potentials and ion-electrode distances [CBB⁺05a].

The original proposal featured a three-layer trap (a dc middle layer sandwiched by radiofrequency layers), as this geometry allows stable transport of ions around “T” and “X” junctions, allowing complex, multiply connected structures to be built. A three-layer trap composed of gold electrodes on alumina, including a T-shaped junction shuttled ions in two dimensions [HOS⁺06]. Geometry proposals optimised for the fast separation of trapped ions included a number of three-layer designs [HS06].

Two-layer geometries are also used to realise segmented ion traps. Two-layer traps have deep and stiff potentials, and offer a good shielding from stray fields on other surfaces. The microfabricated equivalent to the prototypical four-rod Paul trap uses two insulating substrates patterned with electrodes that are then clamped or bonded together with an insulating spacer, assembling multiple wafers to form a traditional Paul trap type design. One of the first realisations of this trap design featured gold electrodes patterned on an alumina substrate [RBD⁺02]. Other versions of this geometry of trap were implemented with smaller dimensions and more segments [SPZS08] or using different materials, for example boron-doped silicon on silicon dioxide [WLB⁺05].

While two-layer traps have excellent trap depths and tight confinement, most two-layer trap designs require manual alignment, which is not resilient to errors. They are also generally difficult to fabricate and connect. These issues can be greatly ameliorated by deforming the geometry into an asymmetric planar structure with ions residing above a planar array of electrodes [CBB⁺05b]. This approach is promising and has made significant inroads since the first demonstration with the trapping of charged polystyrene balls on a trap manufactured using standard printed circuit board fabrication techniques [PLB⁺06]. Printed circuit board traps composed of copper electrodes on an

Chapter 1. Introduction

ultra-high vacuum compatible, low radiofrequency-loss substrate have been miniaturised and used in several experiments [BCL⁺07]. The simple geometry of planar (surface) traps, with electrodes lying on the plane of one substrate, lends itself to rapid production of microfabricated traps. The first surface electrode trap for atomic ions was a fused quartz substrate with electroplated gold electrodes [SCR⁺06]. Traps have also been microfabricated with silver electrodes on a quartz substrate [LGA⁺08, LGL⁺08], boron-doped silicon wafers anodically bonded to a glass substrate [BLB⁺06] and boron-doped silicon-on-insulator wafers. Their ease and speed of fabrication render them ideal for testing a variety of trap geometries and materials. However, complex geometries may be difficult to realise in surface electrode traps, and require the incorporation of multiple conducting layers into the design, with only the field from the top layer affecting the ion [ASW⁺07, KPM⁺05].

Future miniaturised segmented ion traps designs clearly require the ability to be miniaturised and scaled, while minimising assembly and wiring overheads. A reliable monolithic design would greatly enhance the research field and enable considerable progress. While complex and small features are routinely produced even in closely related fields such as neutral atom traps, the radiofrequency fields and high voltages required for ion traps render many materials commonly used completely undesirable. A monolithic segmented ion trap has been built using GaAs on AlGaAs [SHO⁺06], while monolithic gold-coated silicon dioxide on silicon [BWG⁺06] and MEMS trap using gold or tungsten on silicon nitride or silicon dioxide [PPL⁺06, BRC⁺04] have been proposed. While an extremely important first step, the monolithic GaAs trap suffered from very low trap depths and high heating rates, while other proposals are hindered by the difficulty in finding external partners which have the capability to fabricate to specification.

Nevertheless, new miniaturised segmented ion traps are being designed and built, either by ion trapping research groups developing in-house fabrication facilities or by the continued collaboration with external partners. A “trap foundry” initiated by DTO (now IARPA) generated microfabricated traps produced by Sandia National Laboratory (Matthew Blaine) and Lucent Technologies (Richard Slusher, now at Georgia Tech Research Institute). Several groups have seen trapping in the Lucent trap, a 17-zone surface electrode trap, and the Sandia trap (a five-zone planar trap, where the ions reside in-plane with the electrodes) has been used to trap ions in two laboratories. Several university research group have now established in-house capabilities for ion-trap microfabrication. Continued advanced microfabricated ion trap development is underway.

The basic operations required of a segmented ion trap are the transport of ions between segments, the splitting and recombination of an ion string, and the ability to move ions in two dimensions, through junctions. Segmented ion traps have demonstrated transport of ions between segments [RBD⁺02, BCS⁺04, SHO⁺06, HOS⁺06, HDS⁺07], separation of ion strings for further processing without loss of qubit coherence [RBD⁺02, BCS⁺04] and with minimal energy gain. Splitting and recombination of ion strings has also been demonstrated [BAB⁺08].

Multi-dimensional arrays incorporating junctions would allow arbitrary ions, selected from various locations, to be reliably grouped together for multi-qubit gates. Transport through a two-dimensional “T” junction [HOS⁺06] has been achieved with cadmium ions, however, in that experiment, the success probability for round-trip transit was 0.98, and ions experience considerable energy gain, estimated to be 1 eV. In 2009, transport through a cross junction was reported, with a success probability of greater than 0.9999 and less than 10^{-7} eV energy gain [BOV⁺09]. Junctions allowing the reordering of ions in a string remain an important trap geometry pursued by many groups investigating segmented ion traps. The reordering of ions in a linear string may be achieved without the use of junction structures. One idea is to use a four-ion, two-species crystal. Tightening and the subsequent relaxation of the axial potential allows reordering the heavier ions to the central part of the crystal [Win]. However, this process is not yet deterministic and does not allow an arbitrary reordering, and necessarily induces heating of the ions.

This thesis reports on the first experiments with two segmented ion traps. One trap is a two-layer gold-on-alumina trap which has a large number of dc electrodes and a tight confinement. The design and fabrication of this trap is described. The second trap is a larger printed circuit board surface ion trap. This trap was used to gain a deep understanding of electric potentials in a planar ion trap. Armed with this knowledge, very long, almost-evenly spaced strings of ions were realised, a method of electric field measurement using long strings of ions as probes was developed, and ions in a string were deterministically reordered. Chapter 2 covers the theoretical background of ion trapping and cooling. Chapter 3 describes ion trap design and simulation, and the concepts and simulations are applied to the two traps used in this thesis work in Chapter 4. Chapter 5 describes the entire experimental setup; the vacuum apparatus, laser systems and computer control. In Chapter 6, the main experimental results are explained. Chapter 7 offers a conclusion and gives an outlook for the future of segmented ion trap experiments.

Chapter 2

Theory

The original architecture for ion trap based quantum computing consisted of a string of ions in a linear quadrupole ion trap. In each ion, a qubit is encoded in two long-lived electronic levels. Gate manipulations are achieved by individually addressing the ion-qubits with focussed laser beams. Qubits are coupled via the phonon modes of collective oscillations of the ion string, and readout of the state of the ion-qubit is performed using electron shelving.

This Chapter reviews the relevant theory of the basic components required for linear ion trap quantum computing: the radiofrequency ion traps (Section 2.1) used to contain the ions, the atomic species of choice: calcium, and the electronic transitions in ionic calcium (Section 2.2), and the light-ion interactions (Section 2.3) used for laser cooling, encoding the quantum information in the ions' internal electronic states, and readout of the ions' state.

2.1 Radiofrequency Ion Traps

Göttingen physicist and philosopher Georg Christoph Lichtenberg wrote over two hundred years ago in one of his notebooks (quoted in [Pau90]):

*“I think it is a sad situation in all our chemistry
that we are unable to suspend the constituents of matter free”.*

Likewise, one of the founding fathers of quantum mechanics, the Austrian physicist, Erwin Schrödinger, said [Sch52]

*” ... of course, we never experiment with just one electron or atom or (small)
molecule ... we are not experimenting with single particles
any more than we can raise Ichthyosauria in the zoo”*

imagining such a scenario (experiments with a single isolated atom) as an unrealisable utopia.

The work of Hans G. Dehmelt and Wolfgang Paul in the 1950s on ion traps allowed exactly what Schrödinger and Lichtenberg could not have dared hope for; the trapping of isolated free particles in space. Their work overcame the textbook problem of the impossibility of confining a charged particle in a static electric field. Instead, the Paul traps (developed by Wolfgang Paul and coworkers) use oscillating electric fields to create a dynamic equilibrium and the Penning traps (developed by Hans Dehmelt and coworkers) rely on an additional magnetic field to stabilise the motion of an ion. This work was honored by the award of the 1989 Nobel Prize in Physics.

Earnshaw's theorem states that a charged particle(s) cannot be confined in a stable stationary equilibrium configuration solely by electrostatic fields. This stems from Gauss's law, which states that the divergence of any electrical force field is zero in free space:

2.1. Radiofrequency Ion Traps

$$\Delta\Phi = 0, \quad (2.1)$$

i.e. there are no local minima or maxima of the field potential in free space, only saddle points.

This is particularly evident for a field that harmonically confines the particle along at least one direction. In particular, most often confronted is a static field originating from a quadratic potential of the form:

$$\Phi = \alpha_x x^2 + \alpha_y y^2 + \alpha_z z^2.$$

Applying the Laplace equation to this potential yields $\alpha_x + \alpha_y + \alpha_z = 0$: therefore, at least one of the three coefficients must be negative. This corresponds to a repulsive potential along the respective axis.

Linear Paul traps achieve three-dimensional confinement of ions by the combination of a radial confinement produced by a time-dependent radiofrequency field, and axial confinement produced by static fields. The radial confinement and axial confinement are discussed in the next two Subsections.

2.1.1 Radial Confinement

A two-dimensional quadrupole field, i.e. one with no axial confinement, can be experimentally realised by hyperbolic-shaped electrodes, as shown in Fig. 2.1. Here, the axial direction is denoted as the x -axis, and the y - and z -axes are the radial directions.

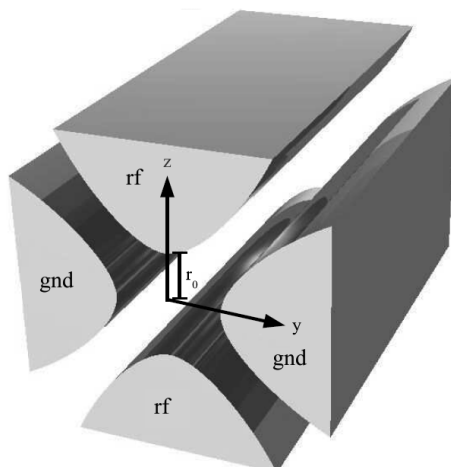


Figure 2.1: Hyperbolic-shaped electrodes: two of the four electrodes are connected to a radiofrequency field (rf), while the other two are grounded (gnd).

In this case, the Laplace equation gives $\alpha_y = -\alpha_z$, which results in a quadratic potential of the form

$$\Phi(r, t) = \frac{y^2 - z^2}{2r_0^2} V(t),$$

where $r = (y, z)$ and r_0 is the minimum distance from the centre to an electrode surface.

When a static potential $V(t) = V_0$ is applied to the electrodes, the potential is saddle-shaped around the origin and does not confine charged particles. However, if the potential is modulated at some angular frequency Ω :

Chapter 2. Theory

$$V(t) = V_{\text{RF}} \cos(\Omega t) , \quad (2.2)$$

charged particles can be confined radially. Ω is typically in the radiofrequency range of several MHz. Typically, one pair of diagonal electrodes is oscillating with $V(t)$, while the other diagonal pair is held at radiofrequency ground (cf. Fig. 2.1). The potential at the origin is equal to zero, $\Phi(0, t) = 0$, and is called the “radiofrequency null”. A charged particle in this effective potential (cf. Fig. 2.2) will have its motion centered around this point.

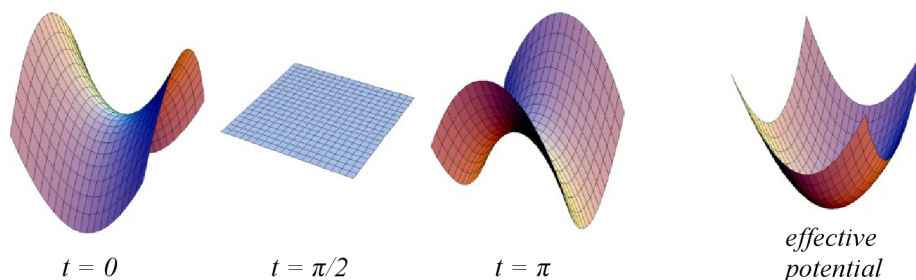


Figure 2.2: The potential due to the radiofrequency electrodes is an oscillating saddle-point potential: a). at $t = 0$, b). at $t = \pi/2$, c). at $t = \pi$. The ion feels an effective potential as depicted in d).

The hyperbolic electrode configuration was the starting point of all radiofrequency traps, and was invented by Wolfgang Paul in 1953 as a mass filter [PS53].

The classical equations of motion for an ion of mass m and electric charge e in the potential $\Phi(r, t)$ are given by the Lorentz force, $\mathbf{F} = -Q \nabla \Phi = m \ddot{\mathbf{r}}$ which, for a linear Paul mass filter with hyperbolic shaped electrodes, leads to a set of *Mathieu equations*:

$$\begin{aligned} \frac{d^2 y}{dt^2} + 2q \frac{\Omega^2}{4} \cos(\Omega t) y &= 0 \\ \frac{d^2 z}{dt^2} + 2q \frac{\Omega^2}{4} \cos(\Omega t) z &= 0 . \end{aligned}$$

The stability parameter q is given by [Pau90]:

$$q = \frac{2QV_{\text{RF}}}{mr_0^2\Omega^2} , \quad (2.3)$$

for which stable solutions exist when $0 < q < 0.908$ [Gho95]. If the potential is not perfectly harmonic close to the radiofrequency null then the ion can be driven by higher-order harmonic terms and areas of instability can occur within an otherwise stable region of parameter space [AHM⁺95]. These multipole contributions can lead to nonlinear resonances [MT95] which can cause trapping instabilities for $0.5 \lesssim q < 0.908$. These resonances become more densely spaced towards larger q -values near 0.908. Traps are typically operated in the region $q \simeq 0.6$, e.g. [SWG01, RBD⁺02, SHO⁺06] .

In the limit that $q \ll 1$ the motion of the ion in the trap can be approximated as

$$r_i(t) \approx r_i^0 \left[1 + \frac{q}{2} \cos(\Omega t) \right] \cos(\omega_i t + \phi_i) , \quad (2.4)$$

where r_i^0 is the amplitude of the motion in the radial direction. The motion can be understood as a harmonic motion with ω_{rad} called the *secular motion*, which corresponds to an oscillation of

2.1. Radiofrequency Ion Traps

motion around the trap centre, and an amplitude-modulated fast driven motion with frequency Ω called *micromotion*. The amplitude of the micromotion is proportional to the distance of the ion from the radiofrequency null.

From Eq. 2.4 and Eq. 2.3, for a given fixed q , an ions' radial motional frequency ω_{rad} , is proportional to the drive frequency Ω . For $q^2 \ll 2$, this can be approximated by [WMI⁺97, BWHG03]:

$$\omega_{\text{rad}} \simeq \frac{q}{2\sqrt{2}}\Omega. \quad (2.5)$$

Analysis of the time-varying potential generated by the radiofrequency voltages can be simplified using a *pseudopotential* or *secular* approximation. The pseudopotential (in eV) is given by [Deh67]

$$\psi(x, y, z) = \frac{Q}{4m\Omega^2} |\nabla V_{\text{RF}}(x, y, z)|^2, \quad (2.6)$$

and the radial secular frequency is given by [WMI⁺98]:

$$\omega_{\text{rad}}^2 = \frac{Q}{m} \frac{\partial^2 \psi}{\partial r^2}. \quad (2.7)$$

The applied radiofrequency potential provides radial confinement of a charged particle, but motion axially remains unbounded.

2.1.2 Axial Confinement: the Linear Paul Trap

Radially confining electrode geometries (cf. Fig. 2.1) can be made axially confining by the addition of a pair of electrodes (called *endcaps*) to which a static voltage is applied; three example geometries are depicted in Fig. 2.3. The static voltages applied to the endcaps add an axially confining potential to the radially confining potential arising from the radiofrequency electrodes: motion along the x -axis become bounded, and the charged particle is now confined in three dimensions. This axially confining potential implies a repulsive force along the radial directions - this is overcompensated by the radiofrequency pseudopotential.

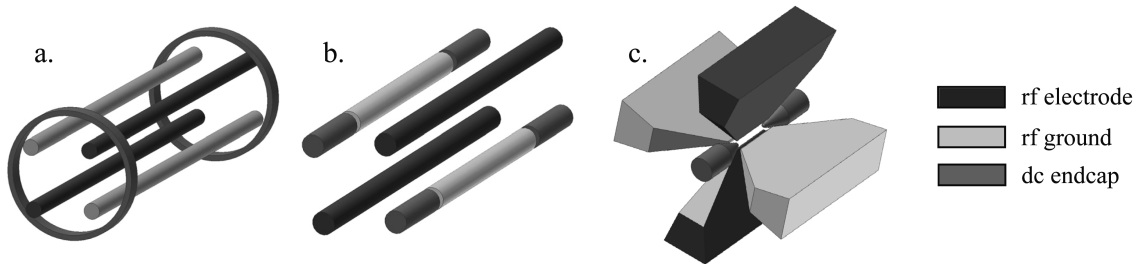


Figure 2.3: Electrode structure of traditional radiofrequency ion traps. a). radiofrequency electrodes are rod-like, and dc endcaps are rings. b). rod-like electrodes: the radiofrequency ground electrodes are segmented - the endcaps are the outer segments of the ground electrode. c). partial geometry of the linear ion trap currently in use in an number of experiments in Innsbruck. The radiofrequency electrodes are blade like and have rounded edges which approximate rods or hyperbolic surfaces. Endcaps are conical tips (with rounded points).

The axial potential ϕ_{ax} is a simple harmonic potential, with

$$\phi_{\text{ax}} = \frac{m\omega_{\text{ax}}^2}{2Q} x^2, \quad (2.8)$$

and an axial secular frequency ω_{ax} of

Chapter 2. Theory

$$\omega_{\text{ax}} = \sqrt{\frac{Q}{m} \kappa_x}, \quad (2.9)$$

where κ_x is the axial electric potential curvature.

Fig. 2.3 depicts three ion traps which have three-dimensional confinement. The idealised hyperbolic shaped electrodes of Fig. 2.1 have been deformed into rods (Fig. 2.3a.-b.) and blades (Fig. 2.3c.). Departure from a hyperbolic electrode still retains a harmonic potential near the trap centre [JMBW95, DOS⁺06, YND91, BDK92, SPSW93]. Typical ion traps with macroscopically fabricated electrodes: rods or blades for radiofrequency confinement and endcaps or segmented dc electrodes for axial confinement; are depicted in Fig. 2.3. As the dimensions of ion traps decrease, rods become more difficult to machine precisely, and blade-like constructions can instead be used, as depicted in Fig. 2.3c. Axial confinement is provided by conical shaped endcaps supplied with a static voltage. This geometry is very similar to that used in several ion trap experiments in Innsbruck.

2.1.3 The Quantum Charge-Coupled Device: Segmented-Electrode Ion Traps

A recent proposal suggests a geometry linking a number of small ion-trap quantum systems in an array-based approach [KMW02]. This “quantum charge-coupled device” (QCCD) architecture consists of a large number of interconnected ion traps. Ions are confined in each trap or shuttled between traps by changing the operating voltages of the trap. Within each trap, ions can be manipulated using methods already demonstrated, while connections between traps allows communication between sets of ions. Fig. 2.4 shows a diagram of the proposed device; the large number of interconnected ion traps (between which ions can be shuttled) are achieved by subdividing the dc electrodes of the trap, and such traps are colloquially called “segmented(-electrode) ion traps”. Trapped ions storing quantum information are held in storage regions. To perform quantum computation, the relevant ions are moved to processing regions by applying appropriate voltages to the electrode segments. Here, the ions are held close together, enabling the coupling necessary for computation. Lasers are focussed through the interaction region to drive gates, and ions can be moved again to prepare for the next operation. In addition, such a multiplexed architecture would allow for massively parallel gate execution, as each zone can support independent motional modes.

Each trapping zone requires both radiofrequency and dc electrodes to create appropriate confining potentials. Control of the axial position of the ions is achieved by “segmenting” the dc

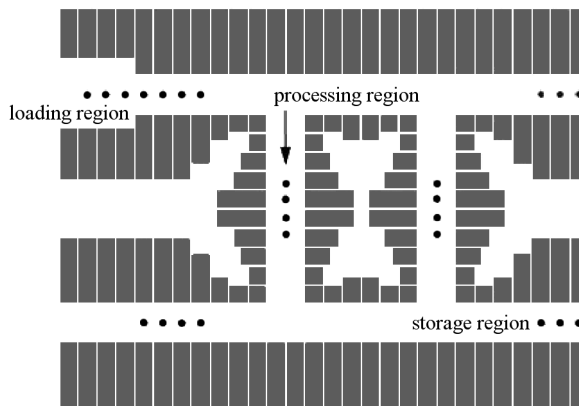


Figure 2.4: Diagram of the quantum charge-coupled device (QCCD) [KMW02]. Ions are stored in the storage region and moved to the interaction region for logic operation. There may be an additional region for loading of ions. The junctions in the architecture allow reordering of ions.

2.1. Radiofrequency Ion Traps

electrodes, with the radial confinement provided by radiofrequency electrode continuous along their length. The segmented dc electrodes can have different voltages applied to each segment, allowing a complex tailoring of the axial trap potential. In this way, ions can be shuttled between regions, held in independent harmonic potentials, and a string of ions can be split or two separate ion strings merged.

2.1.4 Linear Paul Trap Geometries with Microfabricated Structures

A variety of electrode geometries have been used to create the required radiofrequency and static fields and several macroscopic traps were depicted in Fig. 2.3. As ion traps become more miniaturised and the dc control electrodes are segmented, it becomes favorable to create the electrodes from planar structures. Microfabricated traps fabricated from planar structures are depicted in Fig. 2.5. Fig. 2.5a depicts a three-layer trap, where an radiofrequency electrode is sandwiched between two segmented dc electrodes. Fig. 2.5b shows a conventional four-rod Paul trap deformed into planar structures, with segmented dc electrodes. The most significant departure from the idealised hyperbolic geometry is the surface trap (as the ions are trapped above the surface) shown in Fig. 2.5c. In this case, the four radiofrequency electrodes are placed in a common plane, with alternating radiofrequency and dc electrodes. Fig. 2.5c shows one version of this geometry, a “five-wire” surface trap.

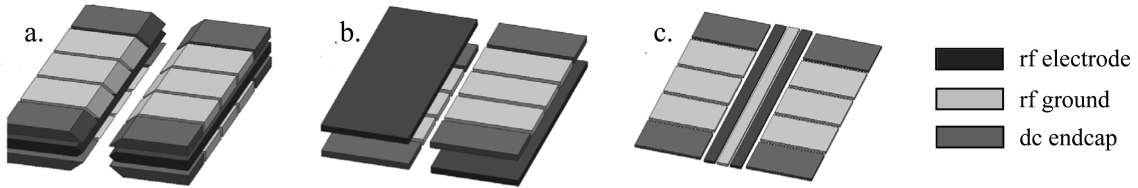


Figure 2.5: Linear Paul Trap geometries with planar electrode surfaces. a). Three-layer trap with segmented dc electrodes. b). Two-layer trap with segmented dc electrodes. c). Surface trap with segmented dc electrodes

2.1.5 Ion Strings in a Linear Paul Trap

The linear Paul traps described in the previous sections provide three-dimensional confinement of a chain of ions. In these geometries, the radiofrequency null is a line. Choosing a radial frequency much higher than the axial frequency causes ions placed in the trap to be arranged in a string along the radiofrequency null.

For a chain of N ions in a trap, which are assumed to be strongly bound in the radial direction, and weakly bound in a harmonic potential along the x -axis, the motion of each ion will be influenced by an overall harmonic potential due to the trap electrodes and by the Coulomb force exerted by all the other ions.

The minimum inter-ion spacing Δx_{\min} for N ions in a harmonic potential is given by [Jam98]

$$\Delta x_{\min} \approx \frac{2.018}{N^{0.599}} \left(\frac{Q^2}{4\pi\epsilon_0 m \nu_{\text{ax}}^2} \right)^{1/3}, \quad (2.10)$$

where Q is the electronic charge, ϵ_0 is the permittivity constant, m is the mass of the ion, and ν_{ax} is the axial trap frequency.

For a fixed axial trap frequency, the distance between neighbouring ions decreases as the ion number increases. This distance needs to be kept above the diffraction limit of the addressing laser beam, which results in relatively low motional frequencies for large ion strings. Low motional

Chapter 2. Theory

frequencies are not compatible with ground state cooling, and limit the gate speeds for computation. Additionally, multi-qubit operations spectrally isolate single modes of the ions motion. For N ions, there are $3N$ modes of motion, and for large N , the mode spectrum becomes so dense that gate speeds must be decreased to avoid off-resonant coupling to other modes.

For a harmonic trapping potential, the number of ions that can reside on the trap axis is limited: past a certain threshold of axial to radial trap frequencies, the ions bulge out in a two-dimensional zig-zag pattern. A transition from a strictly linear ion string to a two-dimensional zig-zag structure occurs at a critical transition ratio of the radial and axial secular frequencies. The ions in the centre of the chain, where the interparticle distance is smallest, are alternately transversely displaced from their original position, forming a zig-zag pattern. To maintain a linear ion string, the motional frequencies must obey the inequality [CRSP98]

$$\left(\frac{\omega_{\text{rad}}}{\omega_{\text{ax}}}\right)^2 > 3.23N^{-1.83}. \quad (2.11)$$

With the currently used laser optics, a linear string of 10 ions with a $\omega_{\text{rad}}/2\pi = 4$ MHz requires a minimum inter-ion spacing of $\sim 3.2 \mu\text{m}$, which is achieved for $\omega_{\text{ax}}/2\pi = 700$ kHz.

While much longer strings of ions cannot be usefully held in ion traps with harmonic axial potentials before they form a zig-zag, or their inter-ion spacing becomes too small for individual addressing, a single linear crystal with a large number of ions can instead be stably confined using an anharmonic axial potential. In a generalised quartic potential

$$\Phi(x) = D_2x^2 + D_4x^4, \quad (2.12)$$

the ions are nearly equally spaced when [LZI⁺09]:

$$D_4 \approx -\frac{D_2}{12.2} \left| \frac{D_2}{e^2} \right|^{2/3}.$$

Using such an anharmonic potential, 120 ions should be able to be trapped, with the inner 100 ions spaced by $\sim 10 \mu\text{m}$, with a variation in the inter-ion spacing of $\sim 0.26 \mu\text{m}$.

2.2 Electronic energy Levels of $^{40}\text{Ca}^+$ and ^{40}Ca

The ion chosen as a qubit of an ion trap computer must satisfy several requirements. The ion must have at least two sufficiently long-lived levels to store and manipulate the quantum information. The ion must have a suitable dipole-allowed transition for Doppler cooling, readout and for Raman transitions. Finally, from a practical standpoint, these transitions must be at wavelengths compatible with practical laser technology.

Various ions used in atomic frequency standards experiments satisfy these requirements. For example, ions employed as qubits in an ion trap systems include (not exhaustive) $^9\text{Be}^+$ (National Institute for Standards and Technology Boulder, Imperial College), $^{24}\text{Mg}^+$ (Imperial College London), $^{25}\text{Mg}^+$ (Max-Planck-Institut für Quantenoptik Garching, Imperial College), $^{40}\text{Ca}^+$ (Universität Innsbruck, University of Oxford, Universität Ulm, Georgia Institute of Technology, Imperial College, Max-Planck Institute Garching, McMaster University), $^{43}\text{Ca}^+$ (Universität Innsbruck, Oxford University, Aarhus), $^{88}\text{Sr}^+$ (National Physical Laboratory, Los Alamos National Laboratory, Massachusetts Institute of Technology), $^{111}\text{Cd}^+$ (University of Maryland, University of Sussex), $^{137}\text{Ba}^+$ (IBM Almaden, University of Washington), $^{171}\text{Yb}^+$ (Universität Siegen, University of Maryland, Griffith University, University of Cambridge).

$^{40}\text{Ca}^+$ is chosen as a qubit for several reasons. It has no nuclear spin, which results in a simple level structure; its P levels have a strong transition to the ground state, which can be used for

2.2. Electronic energy Levels of $^{40}\text{Ca}^+$ and ^{40}Ca

efficient cooling and detection; the metastable D state, with a lifetime of ~ 1 s enables encoding of the qubit and sideband cooling; and the atomic transitions can be accessed with titanium-sapphire or diode lasers.

Calcium is the fifth most abundant element in the Earth's crust, and is an earth-alkaline element with two valence electrons. Ionisation of neutral calcium from the ground state requires 6.11 eV. The level scheme of ^{40}Ca is shown in Fig. 2.6.

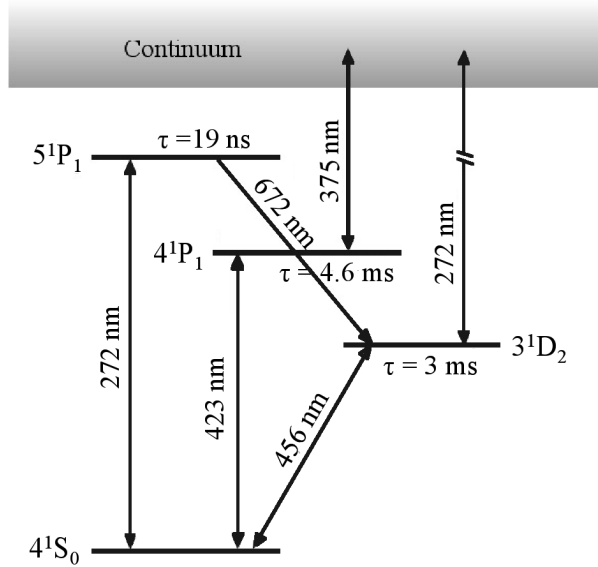


Figure 2.6: Level scheme of ^{40}Ca . Photoionisation of neutral atoms is achieved with two lasers, at wavelengths 423 nm and 375 nm [Ebl06].

To produce singly-ionised calcium, a two-photon process is used. In the first step, light at 423 nm (a photon energy of 2.93 eV) excites the atom from the 4^1S_0 to the 4^1P_1 level. The lifetime of the excited state is 4.6 ms, with a linewidth of 34.7 MHz. The second step corresponds to an excitation from the 4^1P_1 state into the ionisation continuum. This is achieved using a laser with wavelength 375 nm, corresponding to a photon energy of 3.32 eV.

Singly ionised calcium has a single valence electron and therefore an energy level structure similar to neutral alkali atoms. $^{40}\text{Ca}^+$, the most abundant calcium isotope, comprises 97% of the natural occurrence. As for most of the other stable calcium isotopes, $^{40}\text{Ca}^+$ has zero nuclear spin ($I = 0$). An important exception is $^{43}\text{Ca}^+$, whose nuclear spin of $I = 7/2$ gives rise to a rich hyperfine structure, including transitions that are independent of the first-order Zeeman shift.

The relevant lowest lying levels of $^{40}\text{Ca}^+$ are depicted in Fig. 2.7 and the parameters listed in Table 2.1.

$S_{1/2} \leftrightarrow P_{1/2}$ -Transition

The $S_{1/2} \leftrightarrow P_{1/2}$ transition has a wavelength of $\lambda = 397.389$ nm and a linewidth of 20.96 MHz. It is used for Doppler cooling, and for state preparation and detection. The lifetime of the $P_{1/2}$ level is 7.4 ns (cf. Tab. 2.1).

$D_{3/2} \leftrightarrow P_{1/2}$ -Transition

The $P_{1/2}$ state can decay with a probability of 7% (branching ratio 15:1) into the metastable $D_{3/2}$ state. To prevent optical pumping into this state, a laser at 866.214 nm is employed to excite the $P_{1/2} \leftrightarrow D_{3/2}$ transition and empty the metastable level.

Chapter 2. Theory

transition	λ_{air} (nm) [htt06]	Γ_{nat} (Hz) [JC93, GKZ ⁺ 08, htt06]	τ_{nat} (s) [Jam98, KBL ⁺ 05]	I_{sat} (W/m ²)
$4^2S_{1/2} \leftrightarrow 4^2P_{3/2}$	393.478	$2\pi \cdot (21.49 \pm 5, 8) \cdot 10^6$	$7.4(3) \cdot 10^{-9}$	502.6
$4^2S_{1/2} \leftrightarrow 4^2P_{1/2}$	397.389	$2\pi \cdot (20.96 \pm 5, 6) \cdot 10^6$	$7.7(2) \cdot 10^{-9}$	466.3
$4^2S_{1/2} \leftrightarrow 4^2D_{3/2}$	732.389	$2\pi \cdot 0.2$	1.176(11)	
$4^2S_{1/2} \leftrightarrow 3^2D_{5/2}$	729.147	$2\pi \cdot 0.2$	1.168(9)	
$3^2D_{3/2} \leftrightarrow 4^2P_{3/2}$	849.802	$2\pi \cdot (0.15 \pm 44) \cdot 10^6$	$901 \cdot 10^{-9}$	0.38
$3^2D_{5/2} \leftrightarrow 4^2P_{3/2}$	854.209	$2\pi \cdot (1.35 \pm 0.39) \cdot 10^6$	$101 \cdot 10^{-9}$	3.31
$3D_{3/2} \leftrightarrow 4^2P_{1/2}$	866.214	$2\pi \cdot (1.47 \pm 0.42) \cdot 10^6$	$94.3 \cdot 10^{-9}$	3.40

Table 2.1: Wavelengths, natural linewidths and lifetimes, and saturation intensities of the transitions between the five lowest energy levels of $^{40}\text{Ca}^+$.

$S_{1/2} \leftrightarrow D_{5/2}$ -Transition

The optical transition between the $S_{1/2}$ and $D_{5/2}$ levels is an electric quadrupole transition with a wavelength of 729.157 nm and a narrow natural linewidth of $\Gamma/2\pi = 0.2$ Hz. As this transition is dipole-forbidden, the $D_{5/2}$ level is metastable with a lifetime of $\tau = 1.168(9)$ s. The qubit is encoded in the $S_{1/2} \leftrightarrow D_{5/2}$ transition (i.e. the levels $S_{1/2}$ and $D_{5/2}$ are associated with the logic states of the qubit), and the long lifetime of the $D_{5/2}$ level ensures coherence of the qubit over this timescale. Because the effective natural linewidth of this transition is much smaller than the trap frequency, motional sidebands can be resolved. When the $D_{5/2}$ is quenched through the $D_{5/2} \leftrightarrow P_{3/2}$ transition, it can be used for sideband cooling.

$D_{5/2} \leftrightarrow P_{3/2}$ -Transition

The $S_{1/2} \leftrightarrow D_{5/2}$ -transition can also be used for sideband cooling, however, the long lifetime of the $D_{5/2}$ state limits the cooling rate that can be attained. To increase this cooling rate, the $D_{5/2}$ level needs to be emptied. The lifetime of this level is *quenched* using the $D_{5/2} \leftrightarrow P_{3/2}$ transition at 854.209 nm which transfers population from the $D_{5/2}$ level to the $P_{3/2}$, from which it can quickly decay back to the ground ($S_{1/2}$) state. This transition is also used to “reset” the qubit in quantum computation.

2.3 Laser-Ion Interaction

The following section briefly outlines how lasers interact with trapped ions to manipulate their external state (temperature) and internal states (electronic).

2.3.1 Detection and Measurement

Discrimination between the two qubit states can be achieved for a situation where the ion scatters light only if it is in the ground state, and not if it is in the excited state. When the ion is in the $D_{5/2}$ state, the optically active electron of the ion is *shelved* [Deh75, SNBT86, NSD86, BHIW86]. Determination of the state of the ion is achieved by employing the dipole transition at 397 nm. This connects to only the $S_{1/2}$ level and not the $D_{5/2}$ level: if the ion is in the $S_{1/2}$ level, light is scattered on the $S_{1/2} \leftrightarrow P_{1/2}$ transition, conversely, if the ion is in the $D_{5/2}$ state, no fluorescence is detected. Fluorescence is therefore state sensitive. Because of the long lifetime of the $D_{5/2}$ state, collection of fluorescence light can be carried out over a sufficiently long period that the state can be discriminated with a high level of accuracy.

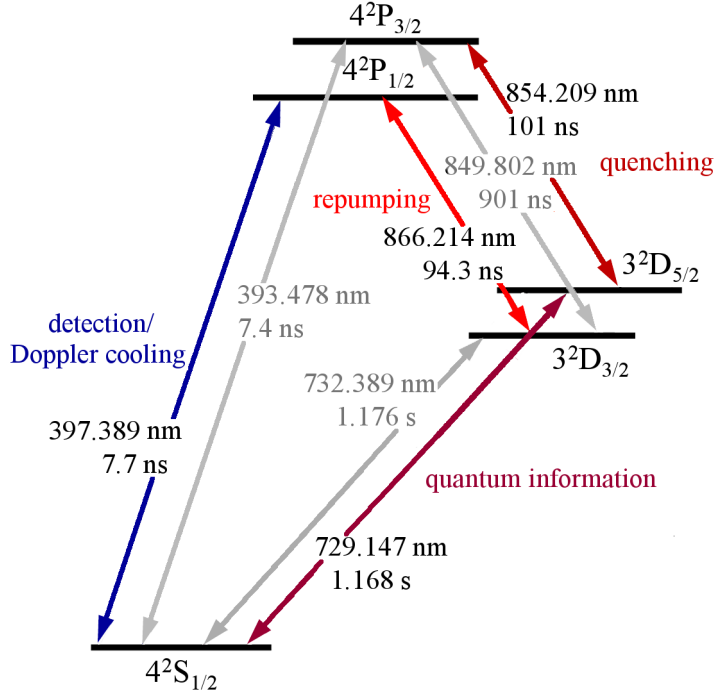


Figure 2.7: Lowest lying energy levels of $^{40}\text{Ca}^+$, with the wavelengths of the dipole- and quadrupole-allowed transitions.

2.3.2 Doppler Cooling

Laser cooling has been independently proposed by Hänsch and Schawlow for the cooling of free atoms [HS75] and by Wineland and Dehmelt for the cooling of trapped ions [WD75] and it exploits the Doppler effect and momentum conservation in the absorption of photons to cool a sample of atoms or ions. This technique is commonly used for cooling trapped ions, and there exist numerous reviews on the topic [DHB89, WDW78, WI79, IW82, BLP⁺88].

Doppler cooling works as follows. An ion is excited by absorbing a photon, and the associated momentum, which is incident upon it from a particular direction. The ion will spontaneously decay to its ground state, emitting a phonon in a random direction and receiving a randomised momentum kick. Averaged over many absorption-emission cycles, the ion experiences a net reduction in its velocity towards the incident light source. When the laser wavelength is detuned below the transition resonance the motion of the ion Doppler shifts the light into resonance when it moves towards the source, and out of resonance when moving away from it.

Cooling a free particle in three dimensions would require six pairwise counter-propagating laser beams, and this laser beam geometry is used for neutral trapped atoms: in contrast, in an ion trap, counter propagating laser beams are not necessary as the radiation pressure exerted by the laser beam is counteracted by the trapping potential. Cooling of the ions' harmonic motion in all three oscillator directions is accomplished by a laser beam incident at an angle oblique to all three principal axes of the ion's motion. The laser only Doppler cools in one direction, but as long as the laser beam is not perpendicular to a particular principal trap axis, the motion in the other directions will be coupled, and a single laser can cool all three dimensions. This also requires the trap frequencies are not degenerate, otherwise one principal axis could be chosen normal to the laser beam's \mathbf{k} -vector, and no cooling would occur along this direction.

At an optimal detuning of $\Delta = -\Gamma/2$ from resonance the ion reaches the Doppler temperature [WI79]:

Chapter 2. Theory

$$T_D \equiv \frac{\hbar\Gamma}{2k_B}. \quad (2.13)$$

This is the lowest motional state that can be achieved by Doppler cooling and is reached when the heating effect arising from the randomised momentum kicks balances the cooling, such that no further net cooling results.

The calcium ions are cooled with light at 397 nm on the $4s^2S_{1/2} \leftrightarrow 4p^2P_{1/2}$ transition. Since this transition is not closed (as the $4p^2P_{1/2}$ level may decay to the $^2D_{3/2}$ level), addition of laser light at 866 nm prevents ions from permanently escaping to the $^2D_{3/2}$ level. While the Doppler limit has been derived for a simple two-level atom, and is therefore not strictly applicable to cooling on this transition, it is a valid approximation when the $2D_{3/2} \leftrightarrow 2P_{1/2}$ transition is saturated, and is close to the theoretical limit of $T_D = 0.5$ mK.

The mean vibrational quantum number [BLP⁺88] at the Doppler temperature is

$$\bar{n}_{\min} = \frac{1}{2} \left(\frac{\Gamma}{\omega} - 1 \right). \quad (2.14)$$

For example, with a transition linewidth $\Gamma_{(S_{1/2}-P_{1/2})}/2\pi = 20.96$ MHz, and a trap frequency of $\omega_{\text{rad}}/2\pi = 1.2$ MHz, a calcium ion can be cooled to a motional quantum number $\bar{n} \approx 9$.

2.3.3 Coherent Manipulations

For quantum information processing experiments, the quantum information may be encoded in any of the long-lived states of $^{40}\text{Ca}^+$. In typical experiments, the $S_{1/2}$ ($m = -1/2$) and $D_{5/2}$ ($m = -1/2$) levels are used to encode the qubit, as the long lifetime of the $D_{5/2}$ level ensures a long qubit coherence time, and is the least susceptible to magnetic field fluctuations. Rotations of this internal qubit can be accomplished by resonant excitations on this transition, implemented by a laser pulse. While coherent manipulations of a qubit were not carried out in this thesis work, the principle is important, and will be briefly explained.

Ion trap quantum computing couples ions in a trap by using the vibrational modes of the trap as an additional, vibrational, qubit. Fig. 2.8 depicts the coupling of a single trapped ion and the vibrational modes of a harmonic potential. The centre-of-mass (COM) vibrational mode is common to all ions trapped in the potential, and can be used to couple ions in the trap. Transitions which are resonant to the qubit transition do not change the number of motional quanta in the system and are called carrier transitions. When laser light of the qubit transition is detuned to the red (blue) sideband, the motional quanta in the system are decreased (increased) by one if a photon is absorbed (emitted).

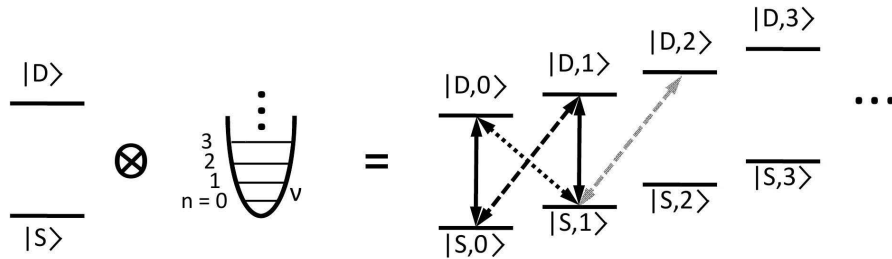


Figure 2.8: The internal (electronic) degree of freedom of a single ion combined with the vibrational mode (of a harmonic oscillator of frequency ν) form the computational basis states of the combined system shown on the right hand side of the equation. The black arrows denote carrier transitions, where the number of motional quanta in the system does not change, while dotted (dashed) arrows indicate sideband transitions which decrease (increase) the motional quanta by one.

Chapter 3

Trap Design and Simulation

The driving force of this work has been the construction of an ion trap that paves the way for a truly scalable ion-based quantum computer. The structure of such a trap is far more complex than a single “macroscopic” ion trap, and therefore it may only be achieved by bringing the electrodes close to the ions and structuring them on the characteristic length scale of the envisioned trapping potential. This structure size is in the range between a few tens of microns to several hundreds of microns, right at the transition where small macroscopic fabrication ends and where microfabrication begins. Depending on the needs (and costs and fabrication time) either technique may be chosen. The conception of a new microtrap is therefore an interplay of many different aspects, covering ideal trapping fields, material and fabrication methods, optical access for qubit manipulation and detection and numerical field simulations.

This Chapter discusses these different aspects in the design and simulation of microfabricated ion traps. Section 3.1 discusses the issues involved in trap design: the optimisation of trap geometry (Subsection 3.1.1) and choice of suitable materials (Subsection 3.1.2). Practical considerations such as exposed dielectrics, micromotion compensation are discussed in Subsection 3.1.3. Useful segmented dc electrode ion trap designs involve complicated geometries: the electric potential arising from these geometries cannot be calculated analytically and is instead numerically simulated, as described in Section 3.2. Subsection 3.2.2 describes methods of simulation and Subsection 3.2.3 describes numerical simulation of the electric field of a trap geometry and analysis of the trap potential.

3.1 Trap Design

Miniaturised ion traps can be designed in a number of different geometries. Two- or three-layer geometries are inspired by the classical four-rod geometry of a hyperbolic ion trap, can realise tight confinements and have good optical access. However, the design and microfabrication of these structures is usually complex and is often hindered by fabrication difficulties and delays. In contrast, surface ion traps are much simpler to fabricate, but have smaller trap depths than two- or three-layer traps of comparable dimensions and usually confine optical access to a single plane.

The classical hyperbolic shaped (or “four-rod”) electrode geometry of a linear Paul trap has been implemented macroscopically in a number of ways: as macroscopic rods in quadrupole formation; as a quadrupole formed by the inside edges of slots cut into pairs of alumina wafers; and various other designs. Most of these designs involve macroscopic machining of some sort, which does not offer a path towards the smaller, more complicated devices that will be necessary for large scale quantum information processing. While semiconductor microfabrication techniques offer a great lateral flexibility of lithography, creating a monolithic trap with the required vertical structure through etching or machining is extremely difficult. Materials typically used (Si, GaAs) have a

3.1. Trap Design

significant radiofrequency loss (which heats the material and subsequently the ions), while thick layers of low-loss materials (sapphire, alumina and quartz) are difficult to deposit and etch. A monolithic microfabricated segmented electrode ion trap with high aspect ratio has been fabricated [SHO⁺06], but suffers from low trap depths. Two-layer traps with aspect ratios closer to unity are generally difficult to fabricate monolithically due to an incompatibility in desired materials and available fabrication techniques. Instead, two-layer traps can be assembled from two structured and patterned conducting layers separated by an insulating spacer.

The inherent problems of microfabrication of multi-layer structures can be ameliorated through simplifying the fabrication by locating trap electrodes in one plane [CBB⁺05b], where ions are trapped above the electrode plane. Such surface traps are easy to fabricate, amenable to modern fabrications (e.g. very-large-scale integration: VLSI), able to be fabricated on a large scale and easy to scale to many zone traps. Additionally, planar trap designs may seek to incorporate on-board electronics, and integrate CMOS (Complementary Metal Oxide Semiconductor) logic into the chip for controlling dc voltages for ion shuttling. However, surface ion traps suffer from several considerable disadvantages. They have a small trap depth (intrinsic to a 2d geometry) which is $\sim 0.5\text{--}3\%$ of comparably sized 3d traps [CBB⁺05b]. While this is not a problem once ions are loaded and cooled, it makes loading from a thermal ion source at room temperature or above difficult, and makes ions more susceptible to loss through collisions with background gas particles. Reducing the ion-electrode distance can increase the trap depth, but this decreased ion-electrode distance dramatically increases motional heating, with heating proportional to $1/d^4$, where d is the ion-electrode distance [DOS⁺06]. Optical access for laser beams requires special consideration for surface traps: as electrodes are located in a plane with a substrate underneath, optical access for beams is blocked along the axis orthogonal to the trap substrate. Surface traps can be designed with cut-outs allowing laser access perpendicular to the trap surface. On scales relevant to miniaturised ion traps, this slot may require tight focusing of the laser beam. Incident laser beams are generally confined to a plane parallel to the trap substrate.

3.1.1 Trap Geometry

The following section examines the optimal aspect ratios and dimensions for a segmented ion trap structure for the desired electrical potential properties. The geometry can be analysed and optimised in terms of the radial and axial geometries. Radial confinement is provided by the radiofrequency electrodes. High radial and axial secular frequencies are desired, such that there is tight dynamical confinement of the ions within the Lamb-Dicke regime [Dic53, MECZ99]. Anharmonicities of the radial trapping potential need to be minimised, as, especially for large q -values with relatively high trap drive power, non-linear resonances have been observed (cf. Sect. 2.1.1). Axial confinement is provided by the segmented dc electrodes. The axial trap frequencies have to be lower than the radial frequency, $\omega_{ax} < \omega_{rad}$, in order to maintain a linear ion crystal (as described in Sect. 2.1.5), have a tight axial confinement and enable optimised transport of an ion between segments and the splitting and recombination of of an ion string.

3.1.1.1 Radial Confinement

The major contribution to the radial confinement is produced by the radiofrequency field that is typically applied through dedicated “radiofrequency electrodes”. An additional small contribution arises from the static field that is used to confine the ions along the axis, but first the radiofrequency contribution is investigated.

A traps potential $V(r, \theta)$ near the trap axis can be decomposed into a series of circular harmonics [MHS⁺04]:

Chapter 3. Trap Design and Simulation

$$V(r, \theta) = V_0 \left[\sum_{n=0}^{\infty} c_n \left(\frac{r}{r_{\text{fit}}} \right)^n \cos(n\theta) + \sum_{m=1}^{\infty} s_m \left(\frac{r}{r_{\text{fit}}} \right)^m \sin(m\theta) \right]. \quad (3.1)$$

where c_m and s_n are expansion coefficients and θ is taken as the angle from the x axis, and r_{fit} is the radius over which the fit is made. For a radial geometry, odd-numbered terms c_1, c_3, \dots are negligible, and the potential offset c_0 is irrelevant. The c_2 coefficient describes the quadrupole potential strength in the radial direction, and is a good measure of the trap stiffness or strength. Note that this definition of the c_n coefficients is different from that defined in [SPSS06]. When electrode shapes deviate strongly from the ideal hyperbolic form, higher-order expansion coefficients (c_4, c_6, \dots) can become significant.

The geometry of the radiofrequency electrodes in a two-layer trap (based on a four-rod geometry, such as that depicted in Fig. 2.5b), can be parameterised by the wafer gap a , the wafer separation d and the thickness of the electrodes t , as depicted in Fig. 3.1. These variables can be defined in terms of the aspect ratio:

$$\alpha \equiv \frac{a}{d}, \quad (3.2)$$

and the ratio of layer separation to layer thickness:

$$\delta \equiv \frac{d}{t}. \quad (3.3)$$

An optimum radial confinement has maximum radial trap stiffness, as characterised by the c_2 expansion coefficient, and minimum higher-order terms. The radial confinement is now investigated as a function of aspect ratio and of layer separation to layer thickness ratio.

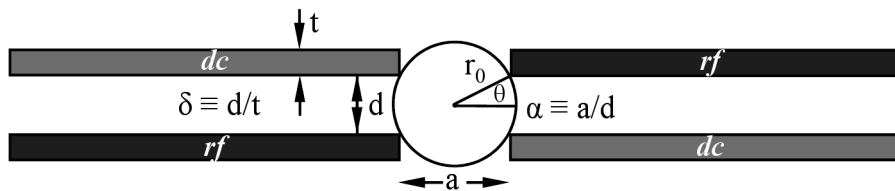


Figure 3.1: Cross-section of a two-layer radiofrequency trap. This geometry is used as a two-dimensional model for optimising radial confinement, in terms of the geometric parameters α ($\equiv a/d$) and δ ($\equiv d/w$). The ion-electrode distance is r_0 .

Aspect Ratio, α Two-layer traps generally seek to retain the unit ratio ($\alpha = 1$) of a conventional hyperbolic electrode shape quadrupole trap in order to obtain the best trap depth and highest secular frequencies, however, deviations from a unit aspect ratio may be favoured for ease of fabrication, ion loading, or optical access.

Using a two-dimensional geometry as depicted in Fig. 3.1, numerical electric potential simulations are carried out which vary the aspect ratio α , keeping the layer thickness fixed at $\delta = 1$ (which is a common and reasonable assumption for currently fabricated two-layer linear microtraps, cf. Sect. 4.1.2.1). In the electric potential simulations, the radiofrequency electrodes are held at $V_{\text{RF}} = U_0 \text{ V}$, and the dc electrodes at $V_{\text{DC}} = 0 \text{ V}$, with $U_0 = 1 \text{ V}$. The resultant electric potential is then decomposed into the radial components of the expansion Eq. 3.1. To obtain easily comparable dimensionless parameters, the c_n are normalised with respect to the ion-electrode distance r_0^n , and the results are shown in Fig. 3.2. The normalisation allows a true comparison of the coefficients, without effects from a variable ion-electrode distance. The applied voltage of $U_0 = 1 \text{ V}$ gives normalised coefficient dimensions of V^{-1} .

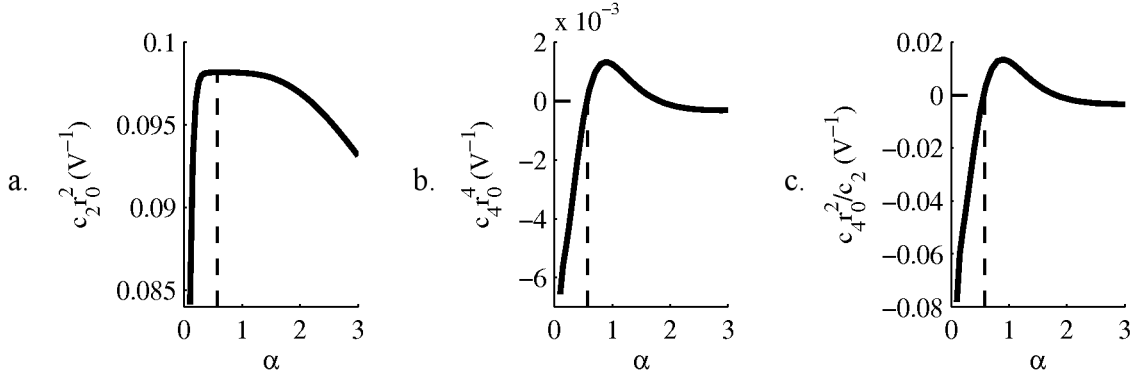


Figure 3.2: a). Normalised trap stiffness, $c_2 r_0^2$, in the radial direction, as a function of aspect ratio, α . b). The normalised octupole coefficient, $c_4 r_0^4$, as a function of aspect ratio, α . c). The octupole coefficient normalised by the normalised quadrupole coefficient $c_4 r_0^2 / c_2$. The dashed lines indicate the maximization of the normalised trap stiffness, $c_2 r_0^2$ and the minimization of the normalised octupole coefficient $c_4 r_0^4$, and octupole coefficient normalised by the normalised quadrupole coefficient $c_4 r_0^2 / c_2$, all at $\alpha = 0.58$.

The normalised quadrupole coefficient $c_2 r_0^2$ is maximised, the normalised octupole coefficient, $c_4 r_0^4$, is zero, and the normalised octupole to quadrupole coefficient $c_4 r_0^2 / c_2$ is zero, all for $\alpha = 0.58$ (indicated by the dashed lines). From these plots, to maximize $c_2 r_0^2$ and minimize $c_4 r_0^2 / c_2$ microtraps are best designed with $0.3 \lesssim \alpha \lesssim 2$.

Layer Separation to Layer Thickness, δ Rather than directly using the polynomial expansion coefficient c_2 the geometric efficiency factor, η better allows comparison of geometries of different δ . The geometric efficiency factor η is defined as the ratio of the quadrupole part of the potential $V^{(2)}$ and that of a hyperbolic trap with $V_{\text{hyp}}^{(2)}$, i.e.

$$\eta = \frac{V^{(2)}}{V_{\text{hyp}}^{(2)}}. \quad (3.4)$$

There are two analytically solvable cases for η ; that of hyperbolic shaped electrodes (which by definition has $\eta = 1$), and that of a trap in the limit of high aspect ratio (i.e. $\alpha \rightarrow \infty$) where $\eta \rightarrow 1/\pi$ [MHS⁺04].

Fig. 3.3 shows the geometric efficiency factor, η , as a function of both α and δ . The geometric efficiency is greatest for unit aspect ratios with thickness near unity and greater efficiency factor is also achieved for thicker electrode layers. Note that the strength of the microtrap decreases as the layer thickness decreases with respect to the layer separation. Fig. 3.3 indicates that thick electrode layers results in tighter radial confinement, thick electrode layers may limit optical access. This may be alleviated by increasing α , but this decreases the geometric efficiency factor η . As a purely practical concern, thick trap electrode layers are also usually difficult to fabricate, requiring the covering of all wafer surfaces with a conducting layer or the electroplating or growing of thick layers of electrode material which can be time-consuming, expensive, or technically demanding. For these reasons, geometries with $\delta < 1$ are not considered here.

In summary, the strongest radial confinement, characterised by the polynomial expansion coefficient c_2 or the geometric efficiency factor η is obtained for aspect ratios close to unity, and for electrodes whose thickness is comparable to the layer separation. Anharmonic polynomial expansion coefficients are minimised for aspect ratios close to unity.

Chapter 3. Trap Design and Simulation

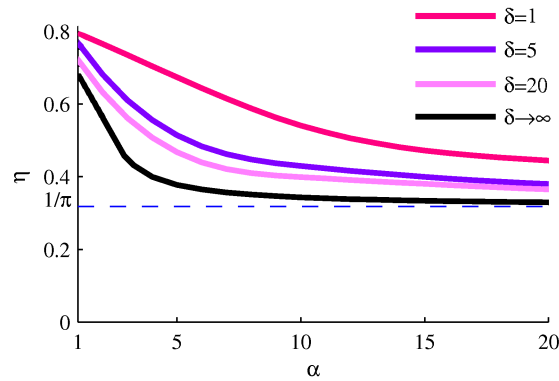


Figure 3.3: Geometric efficiency parameter η is maximised for a $\alpha = 1$, and approaches $1/\pi$ for high aspect ratios.

3.1.1.2 Axial Confinement

For confinement of the ions along the radiofrequency null axis, static, or slowly varying (compared to radiofrequency) voltages are used. While the pseudopotential from the radiofrequency field is typically not changed during trap operation, the “static” potential can be varied, in order to adjust trap parameters to sort and shuttle ions.

The electrode geometry, especially the axial width of the individual electrode segments, determines how the static potential can be influenced. There are four main tasks for the axial potential:

- a tight axial confinement, reaching the Lamb-Dicke regime [Dic53, MECZ99],
- capability to transport ions between different regions on the radiofrequency axis,
- capability to bring together or separate, rapidly, pairs or strings of ions,
- breaking the symmetry of the radial potential in order to enhance Doppler cooling.

This section proceeds as follows: first, a polynomial expansion of the axial potential is applied to a model which varies segment width. The coefficients of the expansion are investigated in terms of the optimal axial confinement. The requirements of the axial potential for transporting an ion between axial segments is discussed, and finally the general requirements of an axial potential capable of bringing together or separate rapidly a pair of ions is discussed. The effect of gap spacing between axial segments is then examined.

The axial static trap potential along the trap x can be expanded into polynomial components as:

$$\phi_x(x, t) \propto \sum_n d_n x^n. \quad (3.5)$$

The expansion coefficients d_n will now be used to investigate optimal axial confinement and transport of ions between segments.

Tight Axial Confinement There are several requirements that influence the choice of the axial potential strength. An upper bound for the stiffness is given by the fact that an ion chain remains in a linear configuration only for certain ratios of ω_{ax} and ω_{rad} (cf. Subsect. 2.1.5). Additionally, quantum computation schemes requiring individual laser addressing of ions require that ions have an inter-ion spacing compatible with attainable laser beam waist diameters. Besides this, it is desirable

3.1. Trap Design

to choose an axial confinement that is as tight as possible in order to increase the speed of gate operations [Ste97, SRS⁺00] and to achieve faster adiabatic transport of ions [SPSS06]. Miniaturised segmented-electrode ion traps used for quantum information processing schemes should have axial frequencies exceeding a few MHz. In this range, cooling techniques are simpler [EMSB03]. The desired deep axial potential needs to be obtained using moderate or reasonable dc voltages (ideally those obtainable directly from DAC cards, i.e. ± 10 V). The axial trap frequency ω_{ax} as a function of normalised segment width \hat{w}_x should be maximised.

The following simulation and results follows the method described in [SPSS06]. The numerical three-dimensional electric potential simulation model is depicted in Fig. 3.4a. In this model, the electrode geometries are two-dimensional rectangular geometries embedded in a three-dimensional space. The width of the segment (the central dc electrode) is varied. The axial extent of the entire structure is large compared to the axial extent of the relevant segment ($50w_x$), and the length of the electrodes is also large ($5w_x$). The gap between the central and adjacent segments is small ($g/r_0 = 0.02$). These dimensions are chosen so that the central segment width is the only parameter expected to affect the calculated electric potential. Following the expansion in Eq. 3.5, the quadrupole coefficient d_2 is calculated for different segment widths, and the results are shown in Fig. 3.4b.

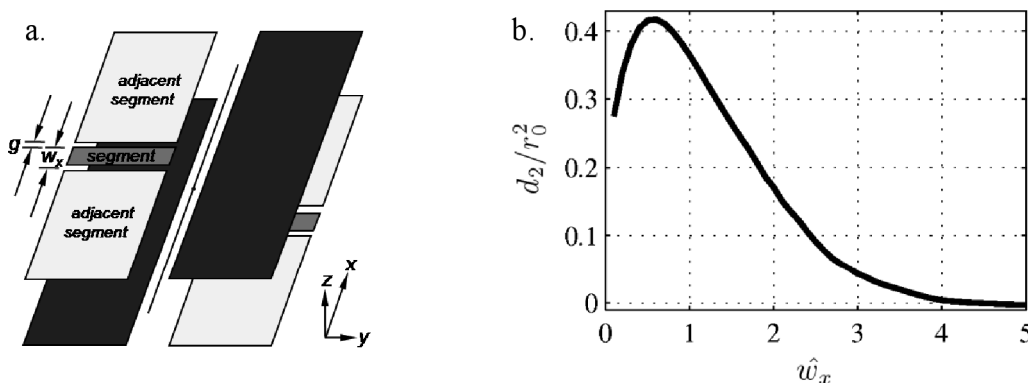


Figure 3.4: Electrode configuration of a two-layer trap, with a single pair of dc electrodes set to 1 V. a). The segment is set to 1 V, and the adjacent segments, and the other electrode in the same plane (the radiofrequency electrode) are set to ground. b). Numerical computation results of the normalised axial trap stiffness $\hat{d}_2 \equiv d_2/r_0^2$ as a function of the normalised (to the electrode-ion distance) segment width \hat{w}_x . The gap between segment and adjacent segments is 1/50 th of the trap axis-electrode distance ($g/r_0 = 0.02$). The adjacent electrodes and radiofrequency electrodes extend to $\pm\infty$ in the x -direction. The electrodes extend back in the y -direction by ~ 10 times the layer separation. The electrodes are infinitely thin.

The results show the intuitively expected results: for large segment widths, the electric potential is shallow, and for very short segment widths the electric potential falls rapidly off from the electrode tips such that a weak confinement is found. The optimum segment width for maximum axial confinement occurs for a normalised segment width of $\hat{w}_x \sim 0.65$.

Ion Transport Between Segments The original proposal [KMW02] for quantum computation using segmented ion traps seeks to avoid the limitations of ion traps with a simple harmonic axial potential by using quantum communication between a number of small ion-trap quantum registers, specifically, shuttling ions from trap to trap. A complete gate operation between qubits initially at different locations would involve five steps; splitting and recombination, transport, cooling and operation [SPSS06]:

Chapter 3. Trap Design and Simulation

$$\begin{aligned}\tau_{\text{gate}} &= \tau_{\text{split/recomb}} + \tau_{\text{transp}} + \tau_{\text{cool}} + \tau_{\text{op}} \\ &= \frac{2}{\nu_{\text{COM}}} + \frac{10}{\nu_{\text{rad}}} + \tau_{\text{cool}} + \tau_{\text{op}},\end{aligned}$$

where the first term describes the time required for splitting and recombination processes, described in terms of the centre-of-mass (COM) frequency of a pair of ions at the moment during the split/recombination when the potential barrier just appears/disappears, the second term describes the total ion transport time in terms of the radial confinement frequency, τ_{cool} the time required to recool the ions, and τ_{op} is the gate operation time. Typical operating conditions indicate that the first two terms could occupy up to 95% of the operation time in realistic algorithms [HDS⁺07]. As qubits have a limited coherence time, maximisation of the clock speed of a segmented ion trap requires minimisation of shuttling times.

An ideal axial potential for ion transport would closely approximate

$$\phi(x, t) = \phi_{\text{local}}(x - x_0(t)),$$

where $x_0(t)$ is the transport function describing the temporal shift of the harmonic well, and

$$\phi_{\text{local}}(x) = \frac{m\omega_{\text{ax}}^2}{2Q}x^2,$$

is purely quadratic with constant curvature in a sufficiently large range around the minimum, with an axial frequency of ω_{ax} .

The important properties of the axial potential during an ideal shuttling sequence are:

- the axial frequency is kept constant, as a change of frequency can cause parametric heating
- the potential local to the minimum is harmonic

A tight axial confinement can be achieved by judicious selection of segment width as described in the previous section, and can be maintained at all points in the transport.

The second property, of a harmonic potential over a sufficiently large range, entails two components. The first is to ensure that the potential is harmonic, i.e. that anharmonicities arising from higher order coefficients (cf. Eq. 3.5) are suppressed.

As the ion is displaced during the transport process, it is expected that the anharmonic terms d_4, d_5, \dots of the potential will cause heating [SPSS06]. Optimal effective segment width for ion transport therefore minimises the d_4 (and higher-order) terms. The model used to investigate the d_2 parameter as a function of w_x also yields results of the dependence of the fourth-order coefficient d_4 on normalised segment width, and the results are depicted in Fig. 3.5. This anharmonic coefficient is zero at a normalised segment width of $\hat{w}_x = 1.25$. The net dc potential, however, arises from the potentials on all segmented electrodes, and the d_4 coefficient of a single segmented electrode is not a good method of characterising this net dc potential; the section (to follow) on splitting/recombination of an ion string explains this further.

The final requirement is that the axial potential is maintained as harmonic over a sufficient range. The finest control of the axial potential would be achieved with small segments which give rise to a large number of dc basis potentials at closely spaced axial intervals. These basis potentials would exhibit a large potential overlap and allow detailed control over the axial potential shape for the entire range. However, the small segment width would result in a smaller absolute voltage on the radiofrequency null, would not produce optimal axial confinement, would require more gaps between segments, would increase design complexity and number of control channels required, and

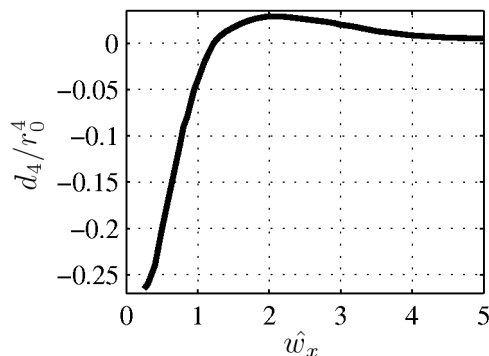


Figure 3.5: The normalised anharmonic $\hat{d}_4 \equiv d_4/r_0^4$ as a function of the normalised segment width \hat{w}_x . The \hat{d}_4 coefficient is equal to zero for $\hat{w}_x = 1.25$.

would have larger anharmonic components. Additionally, this level of control is not required for the entire axial potential. The axial potential needs to be harmonic only over a “sufficiently large range” about the ion, where this range is of the order of one or a few segments. This can be achieved by creating a net dc potential which is a property of a larger set of segments [HS06], rather than relying on only local segments.

In summary, optimised transport of an ion between segments requires electrodes which have a sufficiently large potential overlap along the trap axis for fine control of the time-dependent axial shuttling potential. Minimisation of the anharmonic component d_4 occurs when for a normalised segment width of 1.25. However, this parameter is not a good characterisation of the anharmonic components of the net dc potential, and this will be discussed in the following section.

Splitting and Recombination of an Ion String One of the crucial primitives for transport of ions in a segmented trap is separating or bringing together pairs of trapped ions. Ideally this is achieved while keeping the frequencies of the normal modes of oscillation of the ions constant and as high as possible, without excessive heating of the ions. Separation and recombination of ions in a string is more difficult than ion transport, and has been usefully experimentally demonstrated in [RBD⁺02, BCS⁺04].

In a simple picture, a central electrode introduces a potential hill which pushes the ions apart. The ion separation can be small compared to ion-electrode distance, or the segment width. This is true even when the potential well is about to divide into two local minima. If the splitting/recombination procedure were influenced predominantly by the central electrode, an ion separation on the order of the ion-electrode distance or segment width would be expected. Instead, the much smaller distance indicates that the potential shape in the region between the ions is a joint property of the whole set of electrodes. The properties of the net potential required for splitting and recombination of an ion string are now investigated.

The analysis presented here follows the discussion in [HS06]. First, consideration of the general properties of the electric potential for two Paul traps located at $(x, y, z) = (\pm s, 0, 0)$ will allow determination of which parameters are important for optimisation of a splitting/recombination operation. The x -direction is the axial direction, and the vibrational frequencies ω_x , ω_y and ω_z are assumed to be the same for the two traps. The precise relative sizes of the secular frequencies are not important, but is most useful if the axial frequency $\omega_x \ll \omega_y, \omega_z$.

The distance from the trap axis to the nearest electrode surface is r_0 . For the desired tight traps and distant electrodes, s is assumed $\ll r_0$. The electric potential V near the origin is analysed

Chapter 3. Trap Design and Simulation

with a multipole expansion, and assumed to have a degree of symmetry which causes odd-order terms in the expansion to be negligible. The potential, V , along the trap axis, is given by:

$$V(x, 0, 0) \simeq V_0 + D_2 x^2 + D_4 x^4. \quad (3.6)$$

Note that the D coefficients are a property of the net dc potential, while the d coefficients (cf. Eq. 3.5) are the polynomial expansion coefficients of the axial potential arising from a single segmented dc electrode.

Creation of a double well potential requires $D_2 < 0$ and $D_4 > 0$, for example, as shown in Fig. 3.6.

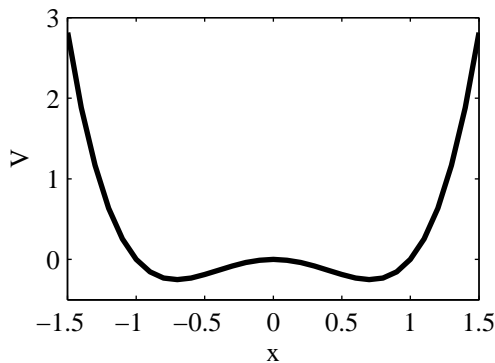


Figure 3.6: A double well potential, $V(x)$ (Eq. 3.6) for $V_0 = 0$, $E_0 = 0$, $D_2 = -1$, $D_4 = 1$.

Solving $dV/dx = 0$ for $D_2 < 0$, the potential wells are centered at

$$s = \sqrt{\frac{-D_2}{2D_4}}. \quad (3.7)$$

At either well centre, $\partial^2 V / \partial x^2 = 4D_4$. For a radiofrequency null along the x -axis, the axial trap frequency is

$$\omega_{\text{ax}} = \sqrt{\frac{-4eD_2}{m}}, \quad (3.8)$$

where m and e is the mass and electronic charge of the ion. For example, at an axial frequency of $\omega_{\text{ax}}/2\pi = 1$ MHz, $|D_2| \simeq 4$ MV/m² for a ⁴⁰Ca⁺ ion. In summary, the quadratic term D_2 in the Taylor expansion sets the trap tightness (ω_{ax} , cf. Eq. 3.8), and the ratio of the quadratic to quartic terms D_2/D_4 sets the trap separation (cf. Eq. 3.7).

If the geometry has segmented dc electrodes of width w_x , then

$$|D_2| \simeq \frac{V_0}{w_x^2}, \quad |D_4| \simeq \frac{V_0}{w_x^4}.$$

Without special geometry design, the separation of the potential wells, s is of the same order as the segment width w_x . To obtain a double well spacing much smaller than the segment width, $s \ll w_x$, $D_2/D_4 \ll w_x^2$ is required. Ideally, ω_{ax} is maintained, and obtaining the required $s \ll w_x$ must then be achieved by an electrode geometry which minimises D_2 with respect to D_4 , with the voltages on all electrodes then being raised together.

3.1. Trap Design

The electrode structure which achieves this is one which creates an electric hexapole or octupole configuration. The octupole is more desirable as it contains symmetry which avoids a linearly varying electric potential at the origin, and the following analysis will concentrate on an octupole configuration. To optimise this potential for splitting/recombination operations, the D_4/D_2 ratio must be maximised.

The challenge in creating a geometry optimised for splitting and recombination is in obtaining a large dc octupole moment. A miniaturised segmented ion trap of current fabrication dimensions optimised for splitting and recombining a string of ions would specifically design a geometry which maximises the D_4 coefficient, through variation of electrode positions and relative sizes.

A range of electrode geometries were investigated in [HS06], comparing three- and two-layer, and surface designs of varying aspect ratio α and segment width w_x . Three-layer traps provide the largest octupole coefficient D_4 for higher aspect ratios ($\alpha \geq 1$), while two-layer traps are better at low aspect ratios ($\alpha < 0.5$). A two-layer trap was found to have maximum D_4 for a segment width of approximately half the ion-electrode distance, i.e. $w_x \sim r_0/2$ (for the case where the spacing between segments was equal to $w_x/2$). This finding is in reasonable agreement with the optimised width for tight axial confinement and optimal overlap. In comparison to three-layer designs, surface traps have a reduction of a factor of ~ 150 in the geometry efficiency factor of the octupole D_4 . For a surface design to obtain the same motional frequency as a three-layer trap, it would need to be ~ 5 times smaller. However, as heating scales as $\sim r_0^{-4}$, this would increase the heating rate by ~ 800 . Instead, comparing structures with the same heating rate, the surface trap would have a motional frequency ~ 7 times lower. The ease of fabrication of surface traps may render acceptable the seven-fold reduction in motional frequencies. However, for quantum computation schemes which require the transport and splitting/recombination of ion strings, these operations could consume a large amount of the overall logic speed, requiring higher motional frequencies and decreasing the suitability of surface traps.

In summary, the publication [HS06] investigated a wide range of geometries and the optimisation of the geometrical parameters for the splitting and recombination of ion strings. They suggest that for any specific design there are useful improvements in the octupole and ac quadrupole confinements to be gained through detailed adjustment of the widths and placements of electrodes. This implies that a careful optimisation of any specific design is worthwhile.

Gap Spacing An additional parameter that affects the axial potential is the gap spacing between segments, g . Large gaps serve to decrease a segments field contribution while a lower limit on gap spacing is usually set by fabrication limitations. Gap spacing is chosen after consideration of the anticipated electrical breakdown voltages (for the materials used) and fabrication parameters.

In summary, larger segment widths offer insufficient coverage of curvatures of individual potential along the transport axis, for the necessary amount of control, and smaller electrodes do not appreciably improve transport performance, while increasing fabrication and connectivity overhead. For maximum curvature in axial confinement and optimised ion transport between segments, a normalised segment width of $\hat{w}_x = 0.5 - 1$ is indicated.

3.1.2 Materials and Fabrication

While ion traps have existed for about fifty years, the simplicity of the trapping potentials used so far required have necessitated only relatively large structures which could be machined (using conventional techniques), from large pieces of metal and then assembled. The application of trapped ions to quantum computation, and the desire for segmented ion traps, has led to the miniaturisation of these traps, and the natural move to chip-based ion traps. Traps that are entirely metallic are no

Chapter 3. Trap Design and Simulation

longer feasible, instead, the traps consist of conducting electrodes on an insulating substrate. The materials used for both the substrate and the electrodes are constrained by the physical properties required, and the fabrication methods to be used to produce the desired trap geometry.

The sophisticated community researching and manufacturing both silicon and gallium arsenide based technologies regularly produce complicated devices with very small and detailed features. These structures even find application in the closely-related field of atom chip research (for example [CCF⁺00, CHH⁺00, GKW⁺04, SCK⁺05, ATLM06, TSC⁺06, MSSM08, WGFS09]). The currently desired feature sizes of miniaturised ion traps are within the reach of a range of microfabrication methods.

In direct contrast to atom chips, ion traps require radiofrequency voltages in order to produce trapping fields. Radiofrequency fields are able to dissipate heat into materials with large radiofrequency loss tangents [WLB⁺05, CBL⁺05], which in turn may lead to heating of the trapped ions [Bro07] or instability/destruction of the setup.

3.1.2.1 Electrode Material

The electrodes carry the voltages (radiofrequency and dc) which produce the trapping potential. Desirable properties in an electrode material include a high electrical conductivity, resistance to corrosion and oxidation, the ability to produce a very smooth surface, absence of magnetism (to avoid the production of uncontrolled magnetic fields near the trapping region) and compatibility with fabrication techniques.

Most miniaturised ion trap designs feature electrodes formed from transition metals: beryllium [TKK⁺00, DK02], molybdenum [DHL⁺04, TKK⁺00, DBIW89, RZR⁺99], NbN [Ła08], aluminium [Slu06b], tantalum [LWB⁺07], tungsten [DOS⁺06], gold [DHL⁺04, WLB⁺05], silver [ŁGA⁺08] and copper [BCL⁺07].

Printed circuit board (PCB) manufacturing techniques using an appropriately low radiofrequency-loss substrate allow for the rapid fabrication and prototyping of macroscopic and mesoscopic segmented ion traps. PCB manufacturers commonly use copper as the trace (conductive path) material in the fabrication of printed circuit boards - these traces may be shaped to form trap electrodes. Copper, when fresh, has a pinkish or peachy colour, and is the second most electrically conductive metal (after silver). This conductivity, and its high degree of malleability and ductility, make it ideal for construction of PCB traps. However, copper quickly oxidises in air and the oxide layer may hold stray charges that perturb the trap.

When considering microfabricated traps, a wider choice of metallic electrodes is possible. Gold is highly electrically conductive and is resistant to corrosion and oxidation. It also produces very clean surfaces and does not passivate (form a hard non-reactive surface film) in air. A comparison between similar traps fabricated from gold or silver revealed that traps fabricated from gold produced data which was more repeatable, indicating a more stable process or a lower susceptibility to contamination and chemical reactions, and the gold traps yielded much lower measured heating rates [Ła08]. Gold is also straightforward to evaporate, electroplate and etch, and these properties render it an ideal material for electrodes. Notably, gold and silver are not allowable in VLSI cleanrooms, but may be added in an additional step [LŁC⁺09].

Electrode Surface Finish While the surface of a metal is ideally an electrical equipotential, in reality it exhibits significant potential variations of up to hundreds of millivolts over micron distances. These patch potential variations generate local electric fields with an intrinsic component thought to originate from differences in the work function between crystal facets, further modified

by adsorbates. The thermally fluctuating occupation of patch potentials create time-varying electric fields that generate heating. While the process is not well understood, the surface quality is believed to be an important parameter affecting patch potential fluctuations. To minimise this, fabrication should seek to produce electrode surfaces with as low surface roughness as possible.

3.1.2.2 Substrate Material

Chip-based ion traps require a substrate material on which to lay the electrodes. The substrate requires certain physical and mechanical characteristics. The substrate needs to be rigid, so that the geometry of the trap structure is structurally stable and well-defined, however, if the trap requires assembly, a fragile or brittle substrate is undesirable. The substrate often has considerable structure, for example, slits or holes. These features are made by either mechanical or laser machining, or through chemical procedures such as etching or epitaxial growth. Substrates to be mechanically or laser machined need to be amenable to those procedures and robust against breakage.

To minimise substrate heating, a material with a low radiofrequency loss tangent needs to be chosen. Those materials favoured by the manufacturing community (Si, GaAs) have undesirably high radiofrequency loss tangents, rendering them unsuitable for use as supporting structure in a miniaturised ion trap. The employment of insulating, low-loss SiO_2 between electrodes and substrate may mitigate these problems, and efforts are being made in this direction. If capacitive coupling between electrodes and substrate can be minimised, there exists exciting possibilities using these materials and their respective fabrication technologies in miniaturised ion trap manufacturing. Alternately, a thick insulation layer of a low-loss material could be placed between electrodes and substrate.

Some specific printed circuit board (PCB) materials (such as 4350-B (Rogers Corporation), FR-4, P97 (Isola) or GML-1000) have suitably low radiofrequency loss tangents, and are also compatible with ultra-high vacuum environments. Standard PCB fabrication technologies however, have minimum feature and drill sizes on the order of hundreds of microns and thus enable the production of only relatively large ion traps. Nevertheless, these macroscopic and mesoscopic traps provide a rapid and accurate test-bed for traps of different geometries and electrode layouts, and experience and understanding gained in this arena can ease the transition to truly miniaturised ion traps.

Substrate materials somewhat amenable to microfabrication techniques and with a suitably low radiofrequency loss tangent include sapphire and quartz. While these materials are difficult to etch or machine, they often find application in surface trap designs which do not require this capability. AlN and Al_2O_3 are readily machined and are often used as substrates for miniaturised ion traps.

Exposed Dielectric Surfaces Insulating parts close to the trapping region need to be minimised, as stray charges may accumulate on those surfaces and lead to uncontrollable potentials felt by the ions. Depending on the resistivity of the dielectric, these charges can remain on the surfaces for minutes or even much longer. These time-dependent stray electric fields can seriously affect the trapping potential, resulting in either manageable or unmanageable trap drifts, or even a non-confining trapping potential. Previously designed ion traps with dielectric exposed or near the ion-trapping region experienced severe or even fatal trapping potential modification. Exposed dielectric surfaces pose a serious threat to the stability of an ion trap, and need to be avoided: current trap designs therefore seek to avoid, as much as possible, exposed dielectrics.

Surface traps usually consist of metallic electrode structures supported by an insulating substrate. Spaces between the electrodes expose the substrate, which is in close proximity to the ion. There are several ways to mitigate this: increasing the thickness of the electrodes, coating additional exposed edges, or removal of the substrate between the electrodes. Increasing the thickness of

Chapter 3. Trap Design and Simulation

the electrodes (cf. Fig. 3.7c) effectively increases the distance between the trapping region and any exposed dielectric. Increased electrode thickness may also geometrically shield dielectric surfaces from the trapping region (cf. Fig. 3.7d). Substrate removal may be achieved either mechanically or chemically. For example, the macroscopic ion trap *Bastille* (detailed in Chapter 4) is a PCB trap with the sections between radiofrequency and ground, and ground and segmented electrodes removed mechanically. While this is an effective method, as trap dimensions decrease, mechanical removal becomes increasingly difficult. Fig. 3.7b shows dielectric material between electrodes in a surface trap removed, and Fig. 3.7g. shows removal of substrate material in a two-layer wafer trap. In two-layer traps, coating of additional wafer surfaces also shields the trapped ions from the substrate (cf. Fig. 3.7f.): this concept is applied to the two-layer microfabricated gold-on-alumina detailed in Chapter 4.

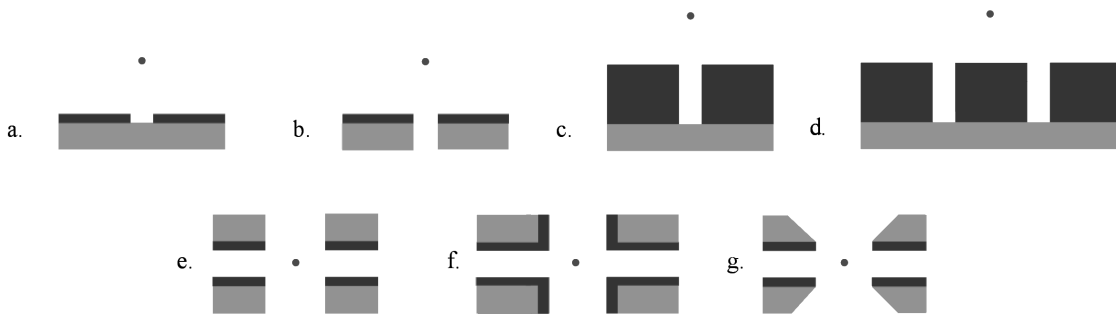


Figure 3.7: Some methods of shielding ions from dielectric substrates. a). surface trap: ions unshielded from underlying dielectric substrate. b). removal of dielectric substrate between electrodes in surface traps shields ions from exposed dielectrics. c). increasing the thickness of surface trap electrodes distances the ions from the dielectric substrate. d). in some cases, thickened electrodes can geometrically shield trapped ions from the dielectric substrate. e). two-layer wafer trap with electrodes patterned on one surface. Ions are exposed to (dielectric) wafer edges. f). coating additional edges of the wafer shields the ions from the dielectric substrate. g). removal of dielectric substrate close to ions.

3.1.2.3 Electrical Breakdown

The endeavour to avoid all exposed dielectric naturally leads to the desire to place electrodes as closely as possible to each other. However, this leads to the possibility of electrical breakdown. The field strength at which electrical breakdown occurs is influenced by the frequency of the applied voltage (e.g. radiofrequency or dc), the geometry (shape and size) of the electrodes and substrate, their surface finishes and adsorbed gasses, and by history of previous arcing. For dc voltages, breakdown through vacuum or substrate occurs approximately in the range of $30 \text{ V}/\mu\text{m}$ [GKB⁺89, BHAW04]. In some materials, electrical breakdown can occur across the substrate-vacuum interface at even lower values [Mil89].

Electrical breakdown occurs at lower field values when the applied voltage is in the radiofrequency domain (compared to dc voltages). Segmented traps typically have large radiofrequency voltages applied, therefore gaps between radiofrequency and neighbouring electrodes are larger. Typical operating voltages at radiofrequency are on the order of 100 V, and using a limiting field strength of $30 \text{ V}/\mu\text{m}$ (which is a value comparable to that necessary to cause field emission and dielectric breakdown of a range of substrate materials), requires that electrode gaps of several tens of microns be used. Typical dc voltages for miniaturised segmented-electrode ion traps are smaller, on the order of tens of volts, so gaps of few to tens of microns are required.

In terms of materials and geometries, substrates with high electric breakdown voltages should be used to minimise the risk of electrical breakdown. Electrode geometries should avoid sharp or

rough features, as these concentrate electric field lines and facilitate breakdown.

3.1.3 Practical Considerations

3.1.3.1 Excess Micromotion Compensation

In Sect. 2.1.1 the ion motion was revealed to have two components, the secular motion and the micromotion. At the centre of the trap there is a radiofrequency null at the nodal position of the radiofrequency field, and the pseudopotential approximation (cf. Sect. 2.1.1) is valid. When stray dc fields displace an ion from the radiofrequency null, a driven motion called excess micromotion results; micromotion of the ion can only be avoided when the ion is trapped at a point of zero radiofrequency field. Hence there are two important requirements for the design of an ion trap: there must be a radiofrequency null (line) where an ion (or ion string) can be trapped, and sufficient dc electrodes need to be provided to precisely position the ions at the desired location.

Excess micromotion can be caused by: a radiofrequency phase difference ϕ_{RF} between two radiofrequency electrodes; or by a uniform static electric field E_{DC} . Radiofrequency phase shifts ϕ_{RF} can be caused by: asymmetries in the electrical impedances of the electrodes, for example, if the leads to the trap electrodes have different inductances due to different lengths or geometrical arrangements; or a different capacitive coupling to ground of these leads.

A uniform static electric field E_{DC} may arise from: deviations of the trap geometry from the idealised geometry. Specifically, this could result from a manual alignment inaccuracy or as a result of tolerances in fabrication. E_{DC} can also be caused by stray charges on surfaces. Trap electrodes may become covered in contaminants from the atomic oven, resulting in contact potentials of a fraction of a volt, trap electrodes or other dielectric or oxide layers may become unevenly charged when the atomic coating described above becomes charged by emitted electrons. Additionally, patch effects on electrodes due to different crystal planes at the surface can produce surface potential variations of ~ 100 mV.

Therefore, in addition to a careful design to minimise excess micromotion, a method of compensation for residual excess micromotion still needs to be incorporated into any trap design. The ability to manipulate the position of the ion in two dimensions is necessary in order to shift the position of the ion back to the radiofrequency null.

3.1.3.2 Orientation of Trap Axes

To cool an ion in all directions, the \mathbf{k} -vector of the Doppler cooling beam must have a component along all three principal axes of the trap [IW82]. In particular, this requires that the trap frequencies not be degenerate, otherwise the trap axes in the plane containing those modes are not well defined, and the motion in a direction perpendicular to the Doppler laser beam \mathbf{k} -vector will not be cooled, and will be heated due to photon recoil. Radiofrequency confinement is cylindrically symmetric about the trap axis and the radial trap frequencies are degenerate. This symmetry must be broken by the addition of dc fields, which set the trap principal axes.

The first consideration is to ensure that no trap frequencies are degenerate. Axial confinement is supplied by static voltages, and can be chosen independently of the radial confinement in order to avoid degeneracy of trap frequencies (axial and radial). Correct choice of axial trapping potential also breaks the radial trap frequency degeneracy as the axial trapping potential, which must have (by Laplace's equation) a radial component to the electric field. If this radial component is not cylindrically symmetric, the degeneracy of the radial frequencies will be lifted.

The second consideration is to ensure that optical access along a direction with components along all three principal axes is possible. Non-surface electrode traps are usually relatively open,

Chapter 3. Trap Design and Simulation

which allows the necessary access. Surface electrode traps, as introduced in Sect. 2.1.4, however, usually have laser beams constrained to be parallel to the chip surface, or, when shining through a slit in the substrate, with components only perpendicular to the surface and along the radiofrequency axis. If a radial principal axis is perpendicular to the trap surface, the Doppler cooling beam will have no component along that axis, and cooling will not occur along this axis. The Doppler laser beam cannot be directed at an angle to the surface, because this might cause the beam to hit the surface of the trap, which can result in scattered light (negatively affecting ion detection) and potentially charging exposed dielectrics through photoemission. Likewise, one may envision beams passing through a slit in the surface trap. While a design utilising this idea may be possible, miniaturisation of ion traps would place increasingly challenging demands on beam diameter, focus and alignment required for experimental realisation.

Surface Trap Geometries The typical surface electrode geometry can be thought of as a deformation of the classical four rod layout. The obvious planar deformation is to move one control electrode and one radiofrequency electrode into the plane of the remaining two electrodes (cf. Fig. 3.8).

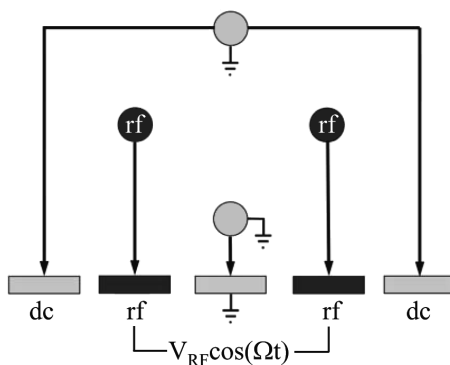


Figure 3.8: Four-rod trap unfolded to surface trap.

The trap axis remains in approximately the same position. Due to symmetry, there is a mirrored trap axis, but this usually resides within the substrate. Axial confinement and additional control of the dc potential is required, and this needs to be achieved by segmentation of the electrodes.

Segmentation of both dc electrodes in a four-wire geometry poses the difficulty of making electrical connections to the inner dc control electrodes - this requires the use of multi-layer processing or vias¹ (cf. Fig. 3.9a). Instead of segmenting both control electrodes, the outer electrodes could be segmented: i.e. the outer radiofrequency and control electrodes (cf. Fig. 3.9b). Another option is segmentation of only the outer dc control electrode (cf. Fig. 3.9c), but the lateral field resulting from this asymmetric arrangement requires adjustment from the other non-segmented control electrode. A further serious limitation of the four-wire design, due to its lack of symmetry transverse to the trap axis, is that structures such as junctions seem too difficult to construct.

The four-wire quadrupole can instead be transformed into a five-wire design that alleviates these problems: the central and outer electrodes are dc electrodes, and the other two electrodes are radiofrequency, and the outer control electrodes can be segmented (cf. Fig. 3.9d). Connections to these segmented electrodes are easily made, and the non-segmented radiofrequency and dc electrodes can be connected from the (axial) side. The trap axis for this design resides above (and below) the centre electrode. This design is transversely symmetric, and junctions are therefore more straightforward. For useful segmented surface traps, a five-wire geometry is desirable from a fabrication and connectivity standpoint.

¹electrical through-hole paths through an insulating material, connecting two conductive layers

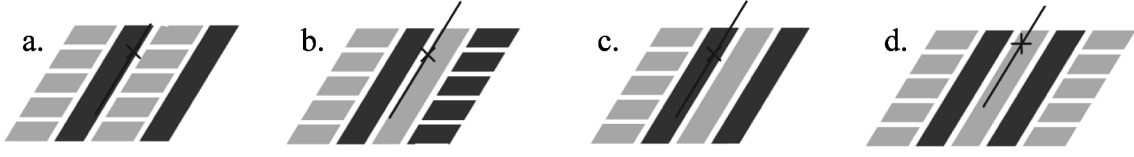


Figure 3.9: Four- and five-wire surface trap geometries. a. Four wire geometry with segmented dc control electrodes. Electrical connection to inner control segments requires the use of multi-layer processing or vias. b. Segmentation of the outer electrodes - radiofrequency and dc. c. Segmentation of outer dc control electrode. d. Five wire geometry with segmented outer dc control electrodes.

While the four-wire design has an orientation of the trap radiofrequency principal axes of $\pm 45^\circ$ from horizontal (parallel to the substrate) for a large range of electrode potentials, the five wire design, by symmetry, has trap axes perpendicular and parallel to the substrate. Because surface traps require laser beams parallel to the trap surface, a principal axis perpendicular to the trap surface, and the laser beam, will not allow cooling along this direction.

Rotation of the trap axes in a five wire design may be achieved in a number of ways. The radiofrequency electrodes defined the radiofrequency null and the radiofrequency potential is radially degenerate: rotation of the trap axes is achieved purely by the dc potential. It is therefore the dc potential that determines the amount of symmetry breaking and the orientation of the radial principal axes.

Three conceptually different methods have been suggested to choose a suitable orientation of the radial trap axes (cf. Fig. 3.10)

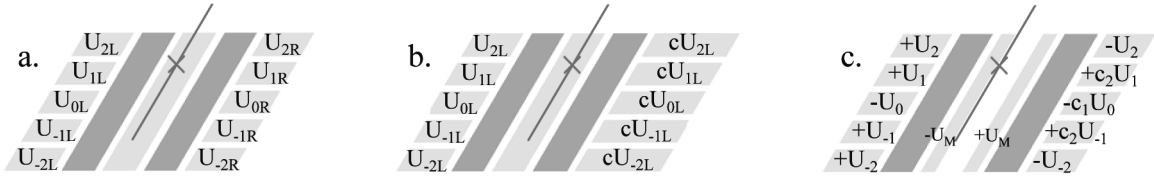


Figure 3.10: Three five-wire geometries and the voltages on the control electrodes to choose the orientation of the radial trap axes. a). the segmented electrodes have asymmetric dc voltages applied to each side. b). the segmented dc electrodes have different widths. The dc segments have a constant ratio, c , of voltages applied to each side. c). A five-wire geometry with equal width segmented dc electrodes and a split central dc electrode. The split central rails have equal voltages of opposite sign applied ($\pm U_M$).

1. dc segments with symmetrically equal widths (cf. Fig. 3.10a). To these, appropriate non-symmetric voltages are applied, the angle of rotation depending on the voltages, and typically in the range of $-\pi/2 \lesssim \theta \lesssim +\pi/2$.
2. dc segments of asymmetric widths (cf. Fig. 3.10b). To these, a fixed voltage ratio between the dc sides is applied, this resulting in a fixed angle of principal axis rotation.
3. dc electrodes with symmetric widths and a split dc centre electrode (cf. Fig. 3.10c). To these, antisymmetric voltages are applied, resulting in a rotation of the principal axes of up to $\theta = \pi/2$.

The third method is particularly appealing as the rotation of trap axes and radial secular frequency splitting can be chosen once the trap is operating, and doesn't need to be designed in at the fabrication stage. The rotation is more easily obtained and the rotation is decoupled from the endcap electrodes [All08]. For this type of design, the extra degree of symmetry reduces the

Chapter 3. Trap Design and Simulation

number of free variables and provides more decoupling between operating parameters (rendering voltage selection and optimisation easier): the process for rotating a surface trap’s principal axes is outlined in Sect. 3.2.3.2. A symmetric design is also likely to be preferable for junction structures.

3.1.3.3 Ion Loading

Ions are loaded into traps by the ionisation of atoms as they pass through the trapping region. Atoms are supplied by either a heated oven, background vapour in the vacuum or laser ablation of a sample. They are then ionised by electron-impact ionisation or photoionisation. The use of an electron gun in electron-impact ionisation can charge trap surfaces. Photoionisation has a higher efficiency than electron-impact ionisation which means that the atomic beam density can be decreased, avoiding the sputtering of unwanted material onto the trap electrodes. Photoionisation is also isotope selective, which allows production of high purity ion crystals [KHT⁺00].

Neutral atom flux needs to reach the trapping region, but not deposit in large quantities on insulating spacers (which may cause shorting between adjacent trap electrodes) or on electrodes, modifying their electric properties.

In practice, atomic deposition is avoided by using minimum but sufficient oven currents, geometrically optimal direction of atomic flux specifically to the trapping region through the use of a collimated atomic beam and shielding the trap surfaces from atomic flux. In particular, for surface traps, this shielding may also be achieved by loading the ions through a hole from the back side. The QCCD architecture lends itself to designs which optimize different trapping regions for different purposes. Traps may also be designed with specified “loading zones”: areas in which ions are loaded, and whose electrodes may be susceptible to atomic deposition. The loading regions are separated from “processing” zones that are used for quantum information; processing zones therefore hopefully have minimised atomic deposition on the electrodes.

3.1.3.4 Trap Packaging and Electrical Connections

Segmented ion traps being designed and fabricated at the current time consist of up to an order of one hundred control electrodes. Such a large number of control electrodes necessitates a clever approach to trap packaging and physical wiring.

Surface trap geometries as depicted in Fig. 3.9d. can be designed with physical access to electrode bond pads transversely (segmented dc electrodes) and axially (radiofrequency and central “axial” electrodes). If the axial dc electrode is segmented [Win], electrical connection of the segments requires use of multi-layer technology which will join traces with bond pads away from the central trapping region. Incorporation of junctions into surface trap designs also increases connectivity complexity, and requires careful consideration.

Two layer “sandwich” type traps usually have connections to the electrodes of the upper sandwich layer inside the sandwich, hidden from easy access. Making them accessible for electrical connection requires that they come through the substrate (using multi-layer technology) or wrap around the edges of the substrate, both of which increase the design complexity. If electrode leads in a two-wafer design both travel radially towards bond pads on the same edge of a wafer, these may also need to be “interleaved”. That is, successive bond pads may be alternately assigned to electrodes on upper and lower wafers, requiring further care in electrical connectivity design.

Ideally a trap is designed with good physical access for electrical connectivity to all electrodes. Junctions and multiple electrode layers complicate the design. As the number of electrodes and trap geometry complexity increases the ability to quickly and cleverly electrically connect electrodes requires consideration.

3.2. Trap Simulation

Static control voltages additionally require low-pass filtering to reduce pickup voltages from the radiofrequency electrodes. Filters should be placed as close as possible to the trap electrodes. They can be placed outside the vacuum chamber, if this distance is not too large. alternately, some previous packaging solutions placed surface mount device (SMD) components inside vacuum, however this quickly becomes space-prohibitive and extremely manually demanding. Instead, hybrid filter boards inside vacuum are used (cf. Sect. 5.1, Figs. 5.2 and 5.4), or the filters are placed immediately outside the vacuum chamber (cf Sect. 5.1 and Fig. 5.5).

3.2 Trap Simulation

The complex geometry of segmented ion traps prohibits analytic calculations of the electric potentials, and they are typically obtained using numerical methods. These methods are outlined in the following section.

3.2.1 Electric Potential *Basis Functions*

The electric potential in any complex multi-zone ion trap can be simulated by developing electric potential *basis functions* for a given trap geometry. The electric potential for any arbitrary voltage configuration of the trap electrodes can then be built up as a linear combination of the electric potential basis functions.

Radiofrequency Pseudopotential

The radiofrequency pseudopotential represents the solution of the Laplace equation (cf. Eq. 2.1) when unit voltage is applied to the radiofrequency electrodes. As the secular ion motion is dependent only on the gradient of $V_{\text{RF}}(x, y, z)$ (cf. Eq. 2.6) the ponderomotive potential can be calculated using an electrostatic analysis.

The radiofrequency potential basis function $\hat{\phi}_{\text{RF}}$ represents the solution of the Laplace equation when unit voltage is applied to the radiofrequency electrodes, and setting all other electrodes to ground. The radiofrequency pseudopotential ψ (in eV) is then

$$\psi(x, y, z) = \frac{Q}{4m\Omega^2} V_{\text{RF}}^2 \left| \nabla \hat{\phi}_{\text{RF}}(x, y, z) \right|, \quad (3.9)$$

where V_{RF} is the voltage on the radiofrequency electrodes.

DC Potential

The electric potential basis functions $\hat{\phi}_i$, $i = 1 : n$ arising from the n dc electrodes are obtained by setting $U_i = 1$ V, with $U_{j \neq i} = 0$, and calculating the electric potential. The net dc potential V_{DC} is then given by:

$$V_{\text{DC}} = \sum_{i=1}^n U_i \hat{\phi}_i, \quad (3.10)$$

where U_i is the voltage applied to the electrode i .

Net Potential

The net trap potential is the sum of the radiofrequency pseudopotential ψ and the net dc potential:

$$\Psi = \psi + V_{\text{DC}}. \quad (3.11)$$

Chapter 3. Trap Design and Simulation

The basis functions are obtained using numerical simulation methods, which are described in the next section.

3.2.2 Numerical Simulation Methods

There exist several numerical methods for solving the electromagnetic field equations required to calculate the basis potentials for a segmented ion trap. These include the Finite Element Method (FEM), the Boundary Element Method (BEM), the Finite Difference Method (FDM) and the Finite Integration Method (FIM). Commercial software packages are available which implement these methods to solve electromagnetic problems: COMSOL 3.4 (FEM), CPO (BEM), IESs Coulomb 3D (BEM and FEM), Toscas Vector Fields (FEM), Ansofts Maxwell 3D (FEM), CSTs MAFIA 4 (FIM).

Simulation results presented in this thesis were carried out predominantly with CPO, and in isolated and specific cases with Comsol 3.2-3.4.

3.2.2.1 The Finite Element Method

The Finite Element Method (FEM) is a general computational method to find approximate solutions to partial differential equations (PDEs). The solution is based on either eliminating the differential equation, or turning the PDE into an ordinary differential equation (ODE), which is then solved using standard techniques, such as finite differences. The program used was COMSOL 3.4².

For this method, a bounded region needs to be defined, in which the solution is sought. This “bounding box” needs to be chosen sufficiently large so that its shape does not influence the solution. The boundary regions are set to electric ground, to reflect the experimental conditions at infinity (i.e. the vacuum chamber).

The entire bounded problem domain is then discretised into a mesh consisting of nodes and elements. The nodes are related to each other by simple functions, and the solver uses an iterative approach such as “energy minimisation” to obtain the potential at each node so that the boundary conditions are satisfied. The interpolating functions for each element relating nodal solutions are then used to find the solution throughout the entire solution domain.

One disadvantage of the Finite Element Method is the requirement of a bounded problem domain or “bounding box”. The area or volume of this bounding box needs to be meshed, and solutions found at all node points. In two-dimensions, this presents only moderate restrictions, but when three-dimensional solutions are required (as for ion traps), the accuracy required for the solution can mean that the problem becomes unwieldy to solve, and even fast computers may reach their practical limits.

3.2.2.2 The Boundary Element Method

The Boundary Element Method (BEM) is a numerical computational method of solving linear PDEs which have been formulated as integral equations, and does not necessitate a bounded region. The program used is CPO (Charged Particle Optics)³.

In a system of conducting electrodes, real charges appear on the surfaces of the electrodes to which electric potentials are applied. These surface charges are then the sources of all the potentials and fields in the system. In the BEM, the electrodes are effectively replaced by these charges. If the surface charges are known then all the potentials and fields are also known.

²formerly known as *Femlab*

³www.electronoptics.com

3.2. Trap Simulation

A numerical simulation begins with subdivision of the electrode geometry. The subdivisions are chosen to be sufficiently small, such that the surface charge density on each subdivision can be assumed as uniformly distributed over its surface. A potential U_j is then applied to the N subdivisions. The charges Q_i that would give rise to this potential must then be determined. The charges are related to the potential through the equation

$$Q_i = \sum_{j=1}^N C_{ij} U_j, \quad (3.12)$$

where C_{ij} is the capacitance matrix and $i, j = 1$ to N indicate the segments. There are N equations for N unknowns, and the charges Q_i are obtained by inverting the capacitance matrix C_{ij} . The numerical inversion can be carried out once and then be used for the charge computation for all electrode basis functions. From the capacitance matrix, potentials or fields at any location in space can be calculated.

3.2.2.3 Comparison between the Boundary Element Method and the Finite Element Method.

There are several important differences between BEM and FEM:

- The BEM solves the unknowns only on the geometry boundaries, while the FEM solves over a given region of space. Hence BEM requires a mesh only over boundary surfaces, and not over the entire domain, and allows a reduction of the problem size by one dimension. A three-dimensional domain mesh generation for complex geometries with fine details is demanding in computation and storage.
- The FEM creates a mesh over an entire space, and requires a bound to this space on which boundary conditions are set. This “bounding-box” and the conditions on it should not perturb the solution in the region of interest, which generally requires that it be located far from that region, thus greatly increasing the region over which the FEM must mesh.
- FEM calculates the solution over the entire domain, whilst BEM calculates first the solution on the boundary, and then, if required, the solution at domain points are found in an additional step. When, for example, the area of interest lies on the boundary, or is localised in a particular part of the domain, calculation of an entire domain solution is not required.
- The BEM approximates the boundary conditions and solves the differential equations exactly, while the FEM approximates the differential equations. This ensures that solutions obtained with the BEM are locally smooth, while those obtained with the FEM can exhibit potential discontinuities.
- In general, the BEM generates a dense, non-symmetric matrix, while the FEM generates a sparse symmetric matrix. The difference in size of these matrices arises from the differences in size between a domain mesh and a surface mesh. Sparse symmetric matrices can be solved very efficiently, while dense, non-symmetric matrices are more demanding in computation time and storage requirements.
- The use of iterative solvers (in contrast to direct solvers) can ease computation requirements. For the FEM there exist a wide range of well-established iterative solvers, while effective iterative solvers for the BEM are still sought.
- The FEM can routinely solve systems with millions of degrees of freedom, while the BEM is limited to systems with orders of magnitude less degrees of freedom.

Chapter 3. Trap Design and Simulation

A comparison in accuracy and speed between three programs based on the FEM, the BEM and the Finite Difference Method (FDM) was carried out using a set of benchmark tests [CLRZ99]. In the FDM and FEM programs the level of error and the computing time are determined by the choice of the number and spacing of mesh points and the inaccuracy parameter for the iterative solution of the mesh potential equation. In the BEM these levels depend on the number and distribution of the boundary segments, as well as on the inaccuracy parameters for the evaluation of the potentials and fields.

A full simulation of segmented traps needs to be three-dimensional, and the comparison study involves only BEM 2D, BEM 3D and FEM2D (FDM 3D, FDM 2D), therefore, no direct comparison between BEM and FEM is available for the 3D case. However, for the benchmark tests, BEM 2D shows an order of magnitude decrease in percentage error over FEM 2D for computed values of angular aberration, energy dispersion, potential and field for a given computation time.

The BEM allows a reduction of the problem size by only meshing over surfaces instead of over volumes, does not require a bounding surface, and calculates the surface charge directly, obtaining much smoother results. In terms of the specific software used, the BEM-based CPO obtained much more accurate results than FEM-based COMSOL 3.4 and was used for almost all trap simulations. COMSOL 3.4 is highly sophisticated in terms of geometry definition and meshing of surfaces. Geometries can be imported in a variety of formats, or defined within COMSOL using a wide range of versatile tools. These geometry objects can then be meshed with a high degree of control. Therefore, a geometry was occasionally defined, and then meshed using COMSOL 3.4, and the resultant geometry and mesh exported for use in CPO; this process combines some of the strengths of both programs.

3.2.2.4 Other Notable Solving Methods

As previously mentioned, there exist many more solving methods to compute the electric potential arising from a complicated electrode structure. Two notable examples, the Fast Multipole Method and the Biot-Savart-like law for electrostatics in the gapless plane approximation, are now briefly outlined.

Fast Multipole Method While the Boundary Element Method produces results with excellent accuracy, when the number of unknowns to solve for becomes large, the computational and storage requirements become prohibitive even for modern computers. If the number of unknowns is N , the computation cost is $\mathcal{O}(N^3)$ and the storage cost is $\mathcal{O}(N^2)$. These costs can be reduced by using an iterative (instead of direct) solver, which reduces the computation cost to $\mathcal{O}(N_{\text{iter}}N^2)$, where N_{iter} is the number of iterations, and the storage cost to $\mathcal{O}(N^2)$. Employment of a clever iteration strategy reduces the number of iterations N_{iter} , but there are still $\mathcal{O}(N^2)$ computations per iteration.

The $\mathcal{O}(N^2)$ computation cost per iteration results from the dense and non-symmetric capacitance matrix (cf. Eq. 3.12). A dense and non-symmetric matrix is computationally expensive. As a first step in reducing computation time the capacitance matrix C is broken into sparse and dense components C_{sparse} and C_{dense} .

The two components arise from distinct physical interactions. The C_{sparse} component represents contributions from diagonal elements and neighbouring element influences. The sparse matrix can be efficiently solved using the standard BEM with iterative solvers. The C_{dense} component contains mostly pairwise interactions from remotely located elements. The C_{dense} component is computationally and memory-wise more expensive, but can be reduced in processing and storage requirements by utilisation of a method called the Fast Multipole Method (FMM).

3.2. Trap Simulation

The Fast Multipole Method [GR87, Gre94], acclaimed as one of the top ten algorithms of the 20th century [DS00], achieves significant computational speedups for certain type of problems. The FMM has been applied to a wide range of computational problems, for example, gravitational and electrostatic problems, and solving of Helmholtz and Maxwell equations, but has not found widespread application mainly for historical reasons. First, it is an analysis based algorithm, which required analytical work to develop the FMM and care in translating this analysis to software. The software requires a proper implementation of FMM data structures and needs to be adaptive to attain maximum efficiency; these requirements can be difficult. For these reasons, FMM is not widely known, or is perceived of as a “difficult to implement” algorithm. The FMM has been implemented in a number of software packages (FastBEM⁴, Fantalgo⁵, PUMA-EM⁶) but is nevertheless relatively unknown in the field of solving electromagnetic problems.

The FMM takes C_{dense} and exploits factorised local and far-field (multipole) expansions of the systems Greens function via the addition theorem. It effectively groups sources that lie together and treats them as a single source. The function is then expressed in an appropriate functional space with a given basis. This analytical manipulation of the series is used to achieve a faster summation. A nearby (much easier to solve) problem that gives almost the same answer as the exact problem is solved. Finally, an analytic expression is used to bound the error.

In whole, the computation requirements are reduced from $\mathcal{O}(N^3)$ to $\mathcal{O}(N_{\text{iter}}N \log N)$ and the storage requirements from $\mathcal{O}(N^2)$ to $\mathcal{O}(N \log N)$.

Biot-Savart-like Law for Electrostatics in the Gapless Plane Approximation The Biot-Savart law is a well-known and powerful theoretical tool which has found application in a range of physical problems. In classical electrodynamics, the Biot-Savart law provides a useful technique to calculate the magnetic field generated by a current carrying wire, and has had successful use in the field of neutral atom traps (e.g. [Hae00, FAS04, HHS⁺05]). The success of the Biot-Savart law in performing magnetic field calculations, combined with its general nature, led to the formulation of a Biot-Savart-like law for electrostatics [OM01].

This formulation allows the calculation of an electric field due to an arbitrary shaped surface region maintained at a fixed scalar potential V , with the rest of the plane held at zero potential. This calculation is analogous to the evaluation of the magnetic field due to a flat current carrying wire of the same shape. Instead of a brute-force calculation of the electric field due to an arbitrarily shaped region held at a fixed potential using boundary-value techniques, the electrostatic Biot-Savart law allows an analytical solution.

This technique was further applied to the analytical calculation of the field resulting from an arbitrary configuration of surface electrodes in the “gapless plane” approximation [Wes08a]; a geometry that approaches that of surface electrode ion traps. The formulation completely avoids the computation of charges and does not require computation of values through a whole bounding box. Instead, it yields an analytic solution.

The application to surface electrode traps first assumes a plane gaplessly covered with electrodes; the gaps between individual electrodes are assumed to be infinitely small and the electrodes are assumed to fully cover an infinite plane with no other conductors above the plane. This approximation is valid when the gaps between electrodes are smaller than the ion-electrode distance; the extent of the trap is much larger than the ion electrode distance; and the distance from the ion to other conducting surfaces is much larger than than the ion-electrode distance. Unfortunately, the

⁴ <http://www.fastbem.com/>

⁵ <http://www.fantalgo.com/FMM.html>

⁶ <http://sourceforge.net/projects/puma-em/>

Chapter 3. Trap Design and Simulation

gapless-plane approximation excludes geometries with slits or cut-outs, and those with considerable three-dimensional structure.

While surface electrode traps have finite gaps between electrodes, these gaps are often very small in order to shield the ion from dielectric surface susceptible to stray charges. Furthermore, the electrodes are often thick, which increases the distance to the exposed dielectric surface dielectric. Under these assumptions, the approximation is reasonably well satisfied.

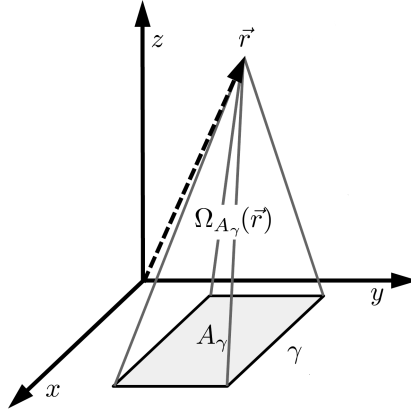


Figure 3.11: A patch electrode γ covering a region A_γ of the electrode plane (located in the xy -plane at $z = 0$) spans a solid angle of solid angle $\Omega_{A_\gamma}(\vec{r})$ as seen from \vec{r} .

In the gapless plane approximation, the electrostatic model for a patch electrode γ covering a region A_γ of the electrode plane (cf. Fig. 3.11) reduces to identifying the unique potential $\bar{V}_\gamma(\vec{r})$ so that $\nabla^2 \bar{V}_\gamma(\vec{r}) = 0$ and

$$\bar{V}_\gamma(x, y, 0) = \begin{cases} V_\gamma & \text{for } (x, y) \in A_\gamma \\ 0 & \text{otherwise} \end{cases}, \quad (3.13)$$

with the substrate located in the plane $z = 0$.

The electric potential $\bar{V}_\gamma(\vec{r})$ satisfying the boundary condition of Eq. 3.13 can be elegantly expressed [OM01] in terms of the solid angle $\Omega_{A_\gamma}(\vec{r})$ spanned by A_γ as seen from \vec{r} ,

$$\bar{V}_\gamma(\vec{r}) = V_\gamma \frac{\Omega_{A_\gamma}(\vec{r})}{2\pi}.$$

With the electrodes in the $z = 0$ plane, and assuming $z > 0$,

$$\Omega_A(\vec{r}) = \int_A \frac{(\vec{r} - \vec{r}') \cdot \hat{z}}{|\vec{r} - \vec{r}'|^3} dx' dy'.$$

The corresponding electric field is

$$E_\gamma(\vec{r}) = \frac{V_\gamma}{2\pi} \oint_{\partial A_\gamma} \frac{d\vec{r}' \times (\vec{r} - \vec{r}')}{|\vec{r} - \vec{r}'|^3}, \quad (3.14)$$

where the integral is anticlockwise (as seen from above) along the edge ∂A_γ of A_γ . This integral is a Biot-Savart integral, so E_γ is proportional to the magnetic field that would be observed if a current was run along a wire following the edge of A_γ . The electric field is then obtained from analytic (simple wire geometries) or numerical (more complicated wire geometries) integration of Eq. 3.14.

3.2.3 Numerical Field Simulation and Analysis

The method of developing a set of electric potential basis functions was described in Subsect. 3.2.1, and numerical field simulation methods in Subsect. 3.2.2. This subsection describes the processes in the numerical field simulation of a given trap geometry, and the analysis of the resulting trapping potential.

3.2.3.1 Numerical Field Simulation

Simulation Geometry Defining a geometry for numerical simulations requires choice of the necessary level of detail. Small geometry features introduce only very small perturbations to the trapping potential, and the inclusion of those features in a simulation would increase computational complexity, in both geometrical definitions and in the number of segments. In order to alleviate the computational requirements it is helpful to omit details that are not expected to alter the potential in the region of interest. The simulated geometry should therefore contain an optimal amount of detail; crucial geometry detail needs to be included, and appropriate simplifications made. This typically refers to removing geometries sufficiently far away from the trapping region (whose effect is believed to be negligible) and approximating thin three-dimensional structures as two-dimensional, as well as other appropriate simplifications.

An example of a simplification, Fig. 3.12 shows the geometry of surface trap *Bastille* as entered into CPO. This geometry is simplified compared to the actual *Bastille* geometry (depicted in Fig. 4.1). The actual trap is composed of copper electrodes on a PCB substrate (this will be further detailed in Sect. 4.1.1.1). In order to shield dielectric material from the trapping region the copper electrodes fold into slots machined into the substrate. This detail, along with the vias, have been omitted from the simulation.

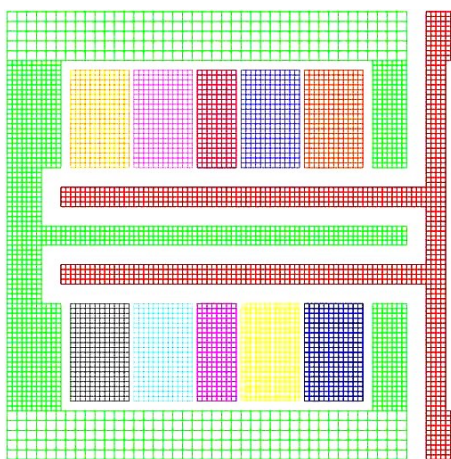


Figure 3.12: Geometry of surface trap *Bastille* as used for electric field simulation in CPO.

Discretisation - Subdivision or Meshing Following simulation geometry definition, the surfaces or solution space is discretised. Depending on the method (boundary or finite element) used, this results in subdivision of either a surface (BEM) or a volume (FEM). In the boundary element method, lines (2d) or surfaces (3d) are subdivided into smaller sections. Fig. 3.12 depicts the geometry used for numerical field simulation in CPO of the surface trap *Bastille*. Here each electrode surface is axially and transversely subdivided. Fig. 3.12 shows a simple subdivision with uniform electrode subdivision throughout almost the entire geometry (with only the extremely transverse electrode sections having a slightly coarser subdivision). A more sophisticated subdivision might have finer division in regions thought to be more critical to the final solution. This geometry shows

Chapter 3. Trap Design and Simulation

rectangular subdivisions, which is appropriate for this geometry, but triangular and other shaped subdivisions exist (which are suitable for other geometries). Greater accuracy is achieved when subdivision elements have unit aspect ratio. Numerical simulation of this geometry using a finite element method implementation would require meshing over a three-dimensional volume, greatly increasing both computation and storage requirements.

3.2.3.2 Electric Potential Analysis

Following geometry definition and discretisation, the electric potential basis functions are generated. The net potential can then be analysed for various choices of electrode voltages. The most important trap parameters are depth, secular frequencies, the orientation of principal axes and anharmonicities.

Anharmonicities The radiofrequency pseudopotential can be analysed for anharmonicities. A two-dimensional radiofrequency potential can be decomposed according to the polynomial expansion given in Eq. 3.1. The c_2 coefficient characterises the harmonicity of the trap, while portions of the confinement in higher order coefficients characterise the anharmonicity and lead to ion heating. These coefficients are determined by fitting polynomial functions to the radiofrequency pseudopotential.

Trap Depth An important trap parameter is the trap depth. The trap depth determines the maximum energy of an ion which can be trapped, and how energetic a collision with the background gas can be before an ion is lost from the trap. Trap depth is determined by the saddle point which occurs in the net potential (cf. Fig. 3.13); the trap depth is given by the difference between the potential at the saddle point and that at the potential minimum.

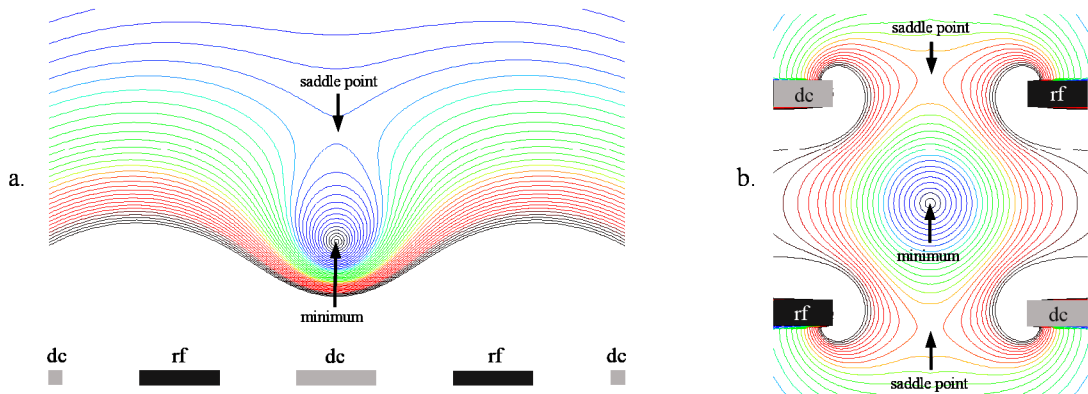


Figure 3.13: The depth of the trap is determined by the lowest point of the net potential radial from the trap minimum; the potential saddle point. Location of trap minimum and saddle points in a). a surface trap and b). in a two-layer trap.

Principal Axes and Secular Frequencies Cooling all three motional degrees of freedom requires a cooling laser with components of its \mathbf{k} -vector oblique to all three principal axes of the ions motion. For a given trap, it is therefore important to determine these principal axes. Near the trap axis, the radiofrequency pseudopotential is radially symmetric. Symmetry is broken by the addition of dc potentials: the saddle shape of the static potential adding to the pseudopotential in one direction, and subtracting from it in another.

The Hessian matrix H is the square matrix of second order partial derivatives of a function, and describes the local curvature of a function of many variables. The net potential $\Psi(x, y, z)$

3.2. Trap Simulation

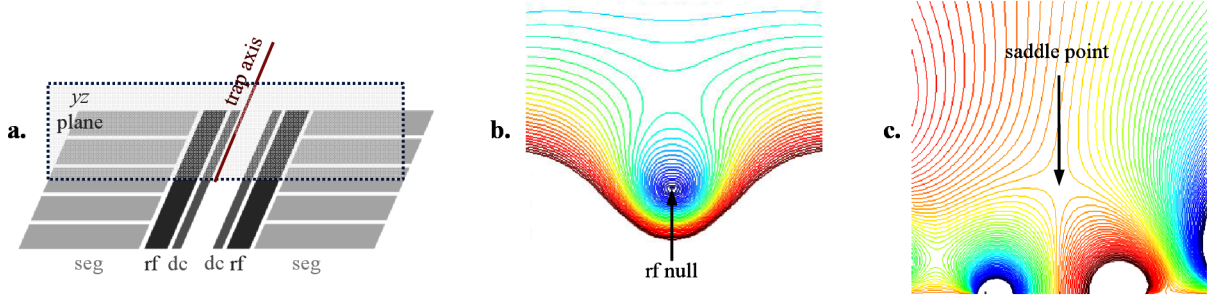


Figure 3.14: a). Surface trap geometry for the creation of radial trap axes tilted $\sim 45^\circ$ with respect to the trap surface: darkest grey electrodes are the radiofrequency electrodes. The size and position of these electrodes, relative to the static electrodes, sets the position of the radiofrequency null (indicated by the line, which is above the plane of the electrodes). Electrodes “inside” the radiofrequency electrodes are dc electrodes and those “outside” are the segmented electrodes. The inner static electrodes would merge into one electrode in a conventional five-rod surface electrode design (cf. Fig.3.9d). Here, this electrode is split, and a significant gap introduced: the split central electrode aids in axis tilting, and the gap would extend through the substrate material, to facilitate loading and optical access. The figure also depicts the yz -plane, in which radiofrequency and dc potential contours will be shown (in subsequent subplots). b). Two-dimensional radiofrequency pseudopotential contour plot and the location of the radiofrequency null. c). Two-dimensional dc contour plot with dc saddle on radiofrequency null.

resulting from the radiofrequency pseudopotential and the dc potentials, is real-valued and has second partial derivatives which exist. The Hessian is given by:

$$H(\Psi_{i,j}) = \partial_i \partial_j \Psi, \quad i, j = x, y, z. \quad (3.15)$$

The Hessian is calculated at the trap potential minimum. From this, the eigenvalues and eigenvectors are determined. Since $H(\Psi_{i,j})$ is symmetric, the eigenvectors of H can be chosen orthogonal and give the **principal axes** of the trap, x' , y' and z' .

The eigenvalues of H are the **principal curvatures** $\kappa_{x'}$, $\kappa_{y'}$ and $\kappa_{z'}$ and can be used to calculate the trap frequencies ω_i along the principal axes:

$$\omega_i = \sqrt{\frac{Q}{m} \kappa_i}, \quad i = x', y', z'. \quad (3.16)$$

Calculation of the Hessian (and principal axes and curvatures) is conveniently carried out using the gradient function in Matlab.

Orientation Of Trap Axes The radiofrequency potential is radially symmetric. Degeneracy of the radial modes is lifted by the static electrodes and the geometry and voltages on these electrodes determine the principal axes of the ion trap. The steps required to determine appropriate static voltages which will tilt the trap axes while keeping the net potential saddle point on the radiofrequency null are now briefly outlined.

For a given geometry, the basis potentials for each electrode are determined, and from these, the electric field components. The static potential requires a saddle point located on the radiofrequency null, i.e. that the scaled sum of field components at the position of the radiofrequency null needs to be zero, or:

$$\sum_{i=1}^n V_i \cdot \nabla \hat{\phi}_i (y = 0, z = z_0) = 0,$$

Chapter 3. Trap Design and Simulation

where n is the number of dc electrodes, V_i is the voltage on electrode i , $\nabla\hat{\phi}_i$ is the normalised electric field from the electrode i and (y_0, z_0) is the (transverse, vertical) position of the radiofrequency null. In addition to this requirement, the dc potential also needs to be optimised for both axis orientation and trap depth. There may be more free parameters (voltages to be applied to electrodes) than constraints. In such a case, additional conditions may be imposed, such as the choice of minimum values or symmetries that seem appropriate to the situation. The use of a suitable algorithm can determine an optimal voltage set to be applied to the electrodes. One particularly clear method for determining a set of voltages (in terms of rotation of trap axes and trap depth) is outlined in [Sti07].

Chapter 4

Trap Layout and Fabrication

General geometric design considerations, material, fabrication and practical concerns in segmented ion trap design, and the numerical simulation of trapping fields produced by a given trap geometry have been discussed in the previous Chapter. In this Chapter, these general concepts are applied to the two specific segmented ion traps used during the course of this thesis.

The first trap is a printed circuit board (PCB) based trap, called *Bastille*¹, provided by Prof. Isaac Chuang at the Massachusetts Institute of Technology. The second ion trap was produced as part of the EU STREP project MICROTRAP² and is a two-layer, gold-on-alumina trap.

First the trap design for both traps is considered, outlining the choices in geometry, material, and other aspects. Numerical simulation results for both traps are presented and interpreted, and finally, the fabrication steps in the manufacturing process of both traps is detailed.

4.1 Trap Layout and Simulation of Trap Parameters

In this section, the fabrication and design choices for the two traps used and designed during the course of this work are explained in light of the design principals detailed in the previous Chapter. The electric potential arising from these trap geometries are then simulated and analysed.

4.1.1 Surface trap *Bastille*

Progress in miniaturised ion trap development has been complicated by long turnaround times and high fabrication costs. Significant fabrication complexity reduction is achieved by moving all electrodes into a plane, in the geometry of a surface trap. Yet another reduction in fabrication complexity, time and cost can be gained by using standard printed circuit board (PCB) manufacturing techniques to produce an ion trap.

Ion traps fabricated using UHV-compatible printed circuit board technology allow the production of sub-millimeter sized segments using common etching procedures. While the size scale of a PCB ion trap is not suitable for large-scale quantum computation, PCB traps can be constructed at a size scale similar to ion traps currently used in quantum information processing experiments and allow few-qubit ion traps to be readily realised. The fast and reliable fabrication (and consequent quick turnaround time), combined with low fabrication costs, enables progress and a greater understanding of segmented traps.

¹after the medieval fortress-prison Bastille Saint-Antoine in Paris, with the French word bastille meaning castle, stronghold or bastion

²IST-2006-517675: Development of a pan-European Microtrap Technology capability for Trapped Ion Quantum Information Science, www.microtrap.eu

4.1. Trap Layout and Simulation of Trap Parameters

4.1.1.1 Surface Trap *Bastille* Layout

The surface trap *Bastille* [LCL⁺07], designed in the group of Prof. Isaac Chuang (Massachusetts Institute of Technology), follows the geometry of a five-rod surface Paul trap (cf. Figs. 3.8, 3.9d.) and has a minimum electrode size of $508\ \mu\text{m}$. The trap consists of two radiofrequency electrodes and eleven dc electrodes. One dc electrode is a central or axial electrode, which is located between the radiofrequency electrodes. The other ten dc electrodes are located (five on each side) to either side of the radiofrequency electrodes. The trap geometry is depicted in Fig. 4.1.

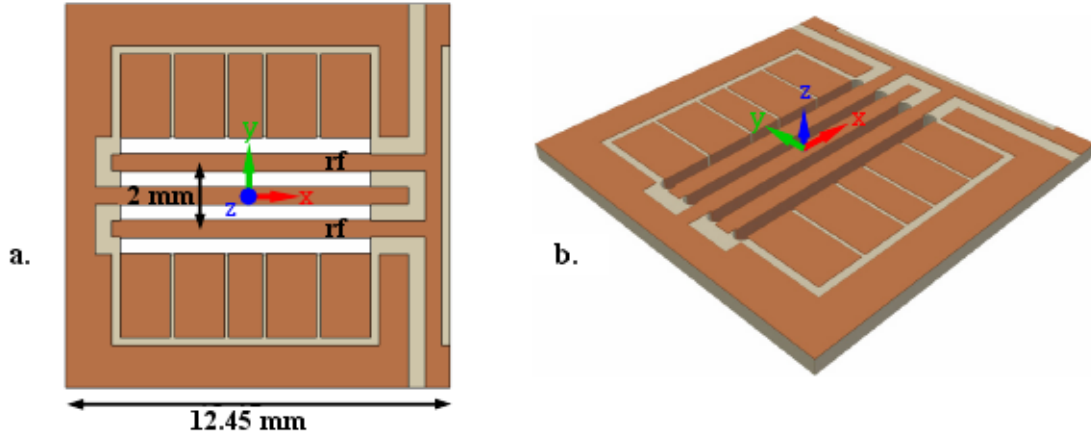


Figure 4.1: Electrode layout of *Bastille* trap. The radiofrequency electrodes of width $508\ \mu\text{m}$ are spaced by $\sim 2\text{ mm}$, which leads to an ion height above the trap of $830\ \mu\text{m}$ (at the geometric centre). The long central (*axial*) electrode is held at radiofrequency ground and the segmented electrodes carry dc potentials. Spaces between radiofrequency and central, and radiofrequency and segmented dc electrodes, have been mechanically removed, and the copper electrodes wrap into these slots, shielding the dielectric substrate from the trapped ions. The coordinate reference defines the trap origin at the geometric trap centre (i.e., in x , in the middle of the central segmented electrode, and in y , in the centre of the axial electrode) and on the surface of the trap. b). Perspective view of the trap, revealing how the electrodes wrap around the edges of the slits, reducing the trapped ions exposure to dielectric surfaces.

Between the radiofrequency and central, and radiofrequency and segmented electrodes, slots are milled to prevent exposure to dielectric and shorting due to atomic vapour buildup. Additionally, the inner surfaces of these slots are covered with copper to minimise potential trap distortion due to the accumulation of stray surface charges. These features are visible in Fig. 4.1b. While standard PCB fabrication techniques can produce traces (electrodes) on the order of $100\ \mu\text{m}$, the minimum slot size commonly available is $\sim 508\ \mu\text{m}$. For surface traps, failure to remove substrate between radiofrequency and central, and radiofrequency and segmented electrodes may be fatal to trapping ability, and so the slot size therefore sets a lower limit on the trap miniaturisation which may be achieved using conventional PCB fabrication techniques. The dimensions of ion trap *Bastille* are listed in Tab. 4.1.

The radiofrequency electrodes and the axial electrode are placed on $508\ \mu\text{m}$ wide bars, separated by $508\ \mu\text{m}$ wide gaps. The thickness of the copper electrodes ($20\ \mu\text{m}$), and the desirable feature of the electrode structure wrapping into the edges of these slits, increases (decreases) the widths of the electrodes (gaps). The dimensions of all electrodes are thus increased by $20\ \mu\text{m}$ on each side facing a gap. Consequently, the gaps are reduced in size by $40\ \mu\text{m}$, compared to the geometry of the underlying substrate.

Chapter 4. Trap Layout and Fabrication

geometry feature (axis)	size (μm)
width (y) of radiofrequency electrodes	508 + 40
width (y) of axial electrode	508 + 40
width (x) of middle electrode	1016
width (x) of steering electrodes	1524
width (x) of endcap electrodes	1524
length (y) of segmented electrodes	2540 + 20
gap (y) between radiofrequency and axial electrode	508 - 40
gap (y) between radiofrequency and segmented electrodes	508 - 40
gap (x) between segmented electrodes	127
thickness of copper electrodes (z)	20
substrate thickness (z)	635

Table 4.1: Geometric dimensions of the surface trap *Bastille*.

4.1.1.2 Surface Trap *Bastille* Numerical Field Simulation and Analysis

Simulation Geometry *Bastilles* simulation geometry was depicted in Fig. 3.12. The transverse symmetry of the trap geometry (cf. Fig. 4.1) allows reduction of the number of simulations. For each basis function, the solution was exported over a three-dimensional grid of points. From here the pseudopotential and net potential were calculated, according to Eq. 3.2.3.1.

Radiofrequency Confinement The pseudopotential from the voltage on the radiofrequency electrodes will define the height of the trap axis above the electrode surfaces, the trap depth (to first order) and the radial curvature.

Height Above Trap Surface Two-layer traps possess a symmetry which defines the position of the radiofrequency null. The situation is different for surface traps - the radiofrequency null resides above the surface of the trap, and the position of this null is determined by the geometry of the trap electrodes: their widths and relative positions.

In the ideal case of infinitely long parallel radiofrequency electrodes, the radiofrequency pseudopotential isosurfaces would be cylindrical with an axis parallel to the electrodes. The finite extent of *Bastilles* radiofrequency electrodes (cf. Fig. 4.1) makes the pseudopotential deviate significantly from the ideal case. Fig. 4.2 shows a low-energy isosurface of the radiofrequency pseudopotential. Note that the scale of the axial and radial axes is not equal. At each axial position, the isosurface is approximately circular, as expected for a radiofrequency pseudopotential in 2d. However, the isosurface is closed at $-x$ due to the finite extent of the radiofrequency electrodes. This means that the radial confinement slowly increases as the axial displacement in the $-x$ -direction increases, and it entails a net force pushing the ions along the x -axis. Additionally, the axis of the pseudopotential is not parallel to the surface of the trap; it is higher at $+x$ due to a connecting bar joining the two radiofrequency electrode “rails” (cf. Fig. 4.1).

The inclination of the radiofrequency null axis visible Fig. 4.2 is more clearly depicted in Fig. 4.3 (over two length scales). Over the length of the trap, the difference in height above the surface of the radiofrequency null varies by almost $200 \mu\text{m}$. In the typically used areas from -1 to $+1$ mm, that imaged by the CCD camera (see Sect. 5.4), the height of the radiofrequency null above the surface varies by $\sim 40 \mu\text{m}$.

4.1. Trap Layout and Simulation of Trap Parameters

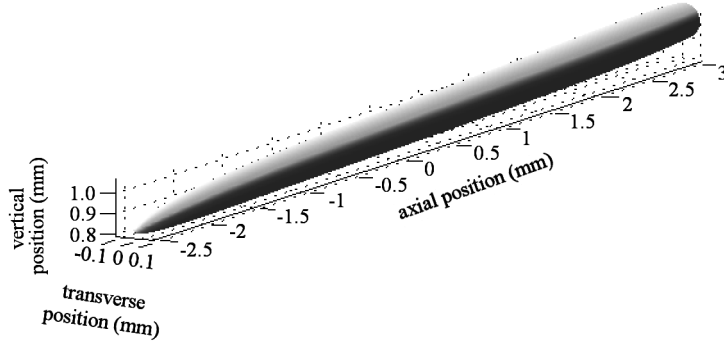


Figure 4.2: A low-energy isosurface of the radiofrequency pseudopotential. Due to the axial asymmetry of the radiofrequency electrodes, the isosurface is not cylindrical and the radiofrequency null is not parallel to the trap surface.

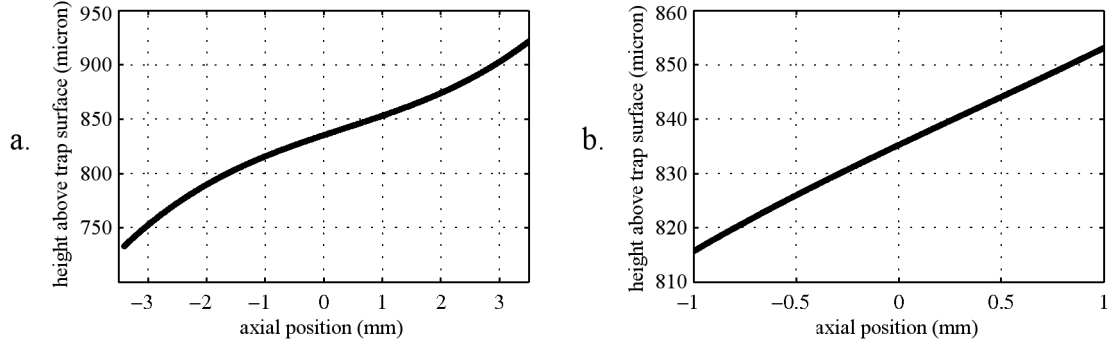


Figure 4.3: Height of the radiofrequency null above the trap surface. The axial asymmetry (cf. Fig. 4.1) of the geometry of the radiofrequency electrode results in a axially dependent height above the trap surface of the radiofrequency null. Note that the horizontal and vertical axes in this plot are not equal. a). The height of the radiofrequency null over the entire axial extent of the trap. b). Detail of the central 2 mm axial range. In this range, the radiofrequency null height above the surface varies approximately linearly between $\sim 815 \mu\text{m}$ and $855 \mu\text{m}$.

Trap Depth The trap depth is given by the potential difference between the trap minimum and the lowest trap maximum located close to the minimum. For *Bastille*, this maximum is directly above the radiofrequency null. For the operating parameters $\Omega/2\pi = 10.26 \text{ MHz}$, $V_{\text{RF}}(0 - \text{peak}) = 300 \text{ V}$, numerical field simulations give a trap depth of $d_0 = 750 \text{ meV}$: a contour plot in the yz -plane at $x = 0$ (the geometric trap centre), and plot of pseudopotential as a function of height above trap surface, is shown in Fig. 4.4. However, this trap depth is modified significantly by the addition of a static dc potential (and this is detailed later in this section).

Radial Secular Frequency In the absence of dc fields, *Bastille* has degenerate radial frequency of $\omega_{\text{rad}}/2\pi = 429 \text{ kHz}$ for an applied radiofrequency voltage of 320 V . Fig. 4.5 shows the axial, transverse and vertical trap frequencies as a function of the applied radiofrequency voltage, when all other electrodes are set to ground. The transverse and vertical trap frequencies are very nearly degenerate, and the axial trap frequency is very close to, but not zero. The lifting of degeneracy of the radial frequencies is due to the finite and asymmetric geometry of the radiofrequency electrodes, this also contributing to the slight axial confinement arising from the radiofrequency electrodes. For a fixed trap drive frequency, the trap frequency is linearly dependent on applied radiofrequency voltage, according to Eq. 2.7.

Chapter 4. Trap Layout and Fabrication

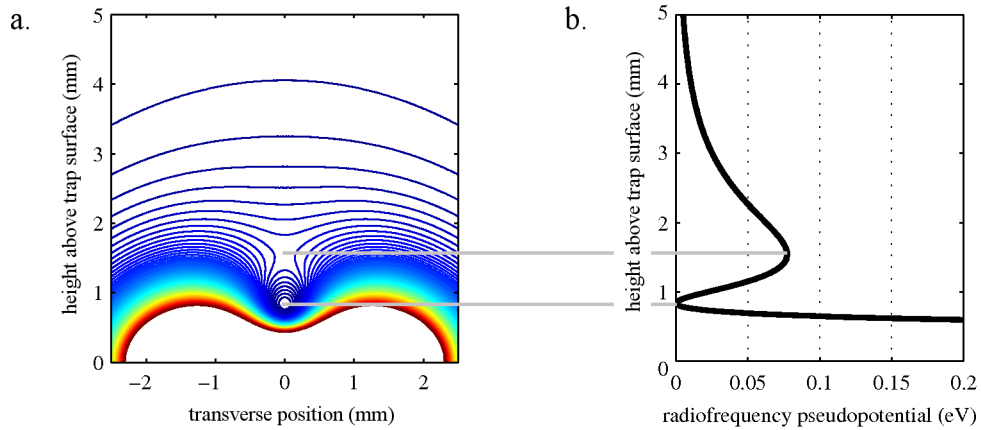


Figure 4.4: a). Contour plot of the radiofrequency pseudopotential: this slice is at the geometric axial centre ($x = 0$). The radiofrequency null is located $830 \mu\text{m}$ above the surface. For the operating parameters $\Omega/2\pi = 10.26 \text{ MHz}$, $V_{\text{RF}}(0 - \text{peak}) = 300 \text{ V}$. b). Radiofrequency pseudopotential in the vertical direction, passing through the trap minimum (radiofrequency null) and local maximum. Numerical field simulations give a trap depth of $d_0 = 750 \text{ meV}$.

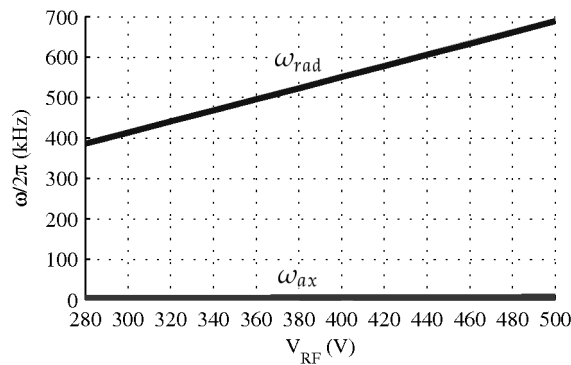


Figure 4.5: Pure radiofrequency pseudopotential (all other electrodes at 0 V). There is a small axial confinement (cf. Fig. 4.2) due to the asymmetry of the radiofrequency electrodes. The radial trap frequencies are degenerate and increase linearly with increasing radiofrequency voltage (cf. Eq. 2.7).

Static Confinement Addition of a dc potential lifts the radial secular frequency degeneracy, modifies the trap depth, and allows axial and transverse displacement of the trap minimum.

Nomenclature and Grouping of DC Electrodes Operation of *Bastille* can be understood by dividing the dc electrodes into four groups: the *axial* electrode, the *endcap* electrodes, the *middle* electrode, and the *steering* electrodes. This nomenclature is explained in Fig. 4.6.

The axial electrode was initially envisaged as a ground electrode, however, it can be operated with an applied dc voltage. It runs parallel to the x -axis at $y = 0$, and is axially asymmetric, having the lead to the left side of the trap.

Of the segmented electrodes, the four outermost electrodes are used as *endcap* electrodes. These electrodes have a high voltage ($\sim 50 \text{ V}$) applied, which provides the axial confinement of the ion string. The middle electrodes are the two segmented electrodes normally closest to the trapped ion string. In our current implementation they are both supplied with the same voltage. The steering electrodes are used to steer, or finely control the movement of the ion string, particularly the orientation of the principal axes. Experimental control of the steering electrodes groups them to

4.1. Trap Layout and Simulation of Trap Parameters

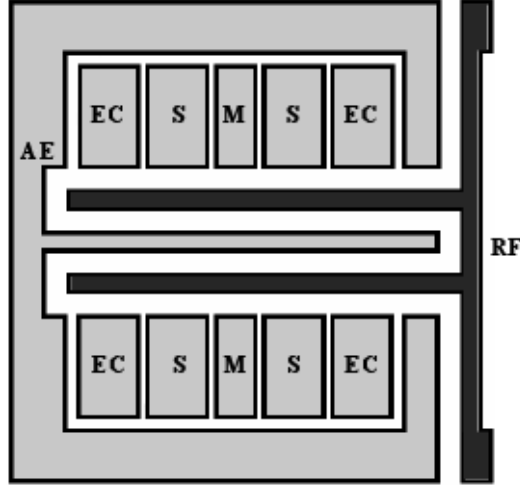


Figure 4.6: *Bastille* geometry and electrode nomenclature. Between the radiofrequency electrode lies the so-called *axial* electrode (AE), whose length runs axially, or parallel to the trap radiofrequency null. The segmented electrodes consist of the outer *endcaps* (EC), the four *steering* (SE) electrodes and the *middle* electrodes (ME).

achieve particular movements, as depicted in Fig. 4.7. An *offset* applies a uniform voltage to all four steering electrodes. *Transverse balance* (TB) control applies a differential voltage between “upper” (+ y) and “lower” ($-y$) steering electrodes creating a rather homogeneous field in the transverse direction (y). In this way, an entire ion string can be moved transversely. Likewise, *lateral balance* (LB) control applies a differential voltage control to left ($-x$) and right ($+x$) steering electrodes, this moving an ion string laterally (in x). *Diagonal* control applies the differential voltage control across diagonally opposed steering electrodes, which does not create an electric field in the very centre but adds a diagonally oriented 2d quadrupole field.

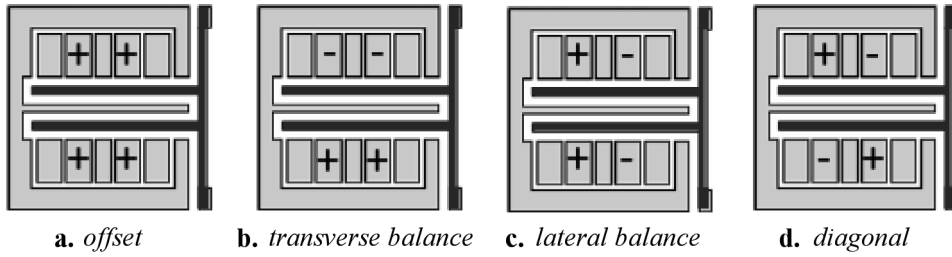


Figure 4.7: Grouping of the steering electrodes to achieve particular movements: a). an *offset*, b). *lateral balance* (LB) allows transverse movement of the ion string, c). *transverse balance* (TB) control allows axial movement of the ion string, and d). *diagonal* control allows rotation of the principal axes ($x \rightarrow x'$, $y \rightarrow y'$).

Contributions From Individual DC Electrodes or Groups of Electrodes Fig. 4.8a depicts the electric potential from the segments along the radiofrequency null. Fig. 4.8b shows a 2d contour plot, in the transverse (yz -) plane of one of the middle electrodes, and Fig. 4.8c shows the electric potential from the axial electrode along the radiofrequency null.

As shown in Sect. 4.1.1.2, due to the geometry of *Bastille*, the radiofrequency null is not located at a constant height above the surface. The contributions from the (symmetric) dc electrodes on this null will therefore not be symmetric. While the radiofrequency null is located higher on at $+x$ than at $-x$, the strength of the segments is also higher at $+x$. Interestingly, on their

Chapter 4. Trap Layout and Fabrication

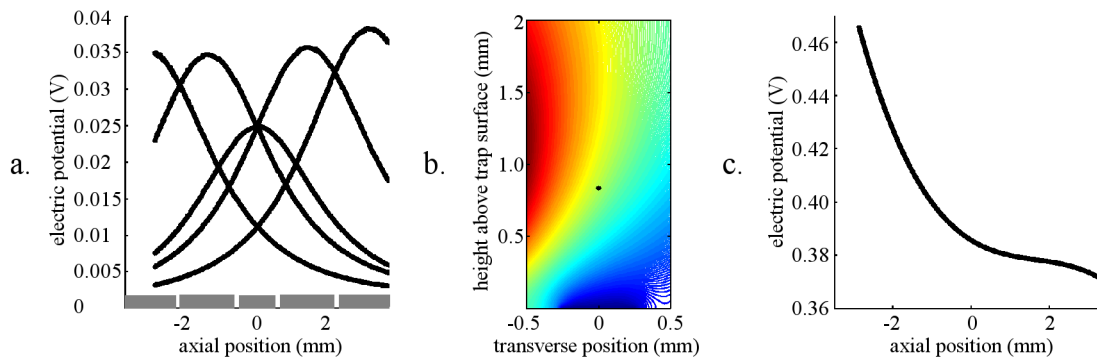


Figure 4.8: a). Contributions from the segmented electrodes on the radiofrequency null, with the electrodes size and position depicted along the x -axis. The contribution becomes stronger towards $+x$, as the radiofrequency null is located at a higher height above the surface, where the influence of the segmented electrodes is larger: this is depicted in b). a contour plot of the electric potential from one middle electrode, in the yz -plane at $x = 0$. c). The electric potential from the axial electrode on the radiofrequency null.

electrode(s)	applied voltage (V)
radiofrequency	280 — 320 (0-peak)
endcaps (EC)	+40 — +60
middle electrodes (ME)	+10 — +30
steering electrodes (SE)	-10 — +10
axial electrode (AE)	+5 — +10

Table 4.2: Typical electrode voltages applied to *Bastille*.

respective sides those dc electrodes have a weaker influence for which the radiofrequency null is closer to the surface. This is due to the shielding effect from the lower rails, outweighing the marginal increase in proximity. The dc electrodes, in addition to the radiofrequency electrode, are transversely symmetric, so the influence of the upper right endcap is the same as the lower right endcap. Also shown is the influence of the axial electrode on the radiofrequency null. This electrode has a stronger influence than the segmented electrodes, as it is much closer (directly beneath) to the radiofrequency null than the segmented electrodes (located to the sides).

Net Potential

Typical Operating Voltages Typical operating voltages applied to the electrodes are shown in Tab. 4.2.

Trap Depth Using the pure radiofrequency pseudopotential above, with an applied radiofrequency voltage of 300 V (0-peak) and a drive frequency of $\Omega/2\pi = 10.25$ MHz, a trap depth of $d_0 = 0.75$ eV was calculated. However, the dc potentials significantly modify the trap depth. This effect is now considered in detail.

Since the critical point of loss in surface traps is above the radiofrequency null, the trap depth is significantly increased if an additional pushing force towards the surface is added to the forces from the radiofrequency pseudopotential. This modified trap depth, d_1 , has been shown in results obtained from the simulation model in [PLB⁺06], in which a plane at positive dc voltage placed at a height h above the trap surface trap (which had trap height (radiofrequency null) at r_0) increased the trap depth by up to a factor of 40 for a large range of h/r_0 . This pushing force towards the

4.1. Trap Layout and Simulation of Trap Parameters

surface can be provided by the plane at a height above the trap surface [PLB⁺06], and interestingly, a similar effect can be caused by the segmented electrodes. This increase of trap depth caused by the segmented electrodes in *Bastille* is now described.

Fig. 4.9 shows electric potential contours in the transverse plane, for voltages applied to different electrode sets. The segmented electrodes are located transverse (y) to the radiofrequency null (axis), and the electric field from those electrodes is directed down ($-z$), from above the radiofrequency null, therefore acting as an effective positively biased plane at h ($> r_0$), and increasing the trap depth. Fig. 4.9a shows the electric potential contours arising when the endcap electrodes are held at 40 V, with all others at 0 V. Here, endcap electrodes held at positive voltage give rise to an electric field whose field lines point towards the trap surface. All other segmented electrodes, held at positive voltage, give rise to electric field lines which point in the same direction. The effect of the segmented electrodes being held at positive voltage is to *increase* the trap depth. Conversely, the axial electrode, being located directly below the radiofrequency null, has an electric field directed away from the trap surface, as shown Fig. 4.9b; this acts to *decrease* trap depth. Fig. 4.9c shows a net dc potential contour plot (for typical operating voltages) with effective positive voltage at height $h > r_0$, and field lines directed towards the trap surface. The radiofrequency pseudopotential is shown in the Fig. 4.9d, with the small trap depth evident with reference to the colour scale. The net potential in Fig. 4.9e, is the sum of the radiofrequency pseudopotential (Fig. 4.9d) and the net potential (Fig. 4.9c), shows a clearly increased trap depth (see colour scale) over that of the bare radiofrequency pseudopotential in Fig. 4.9d.

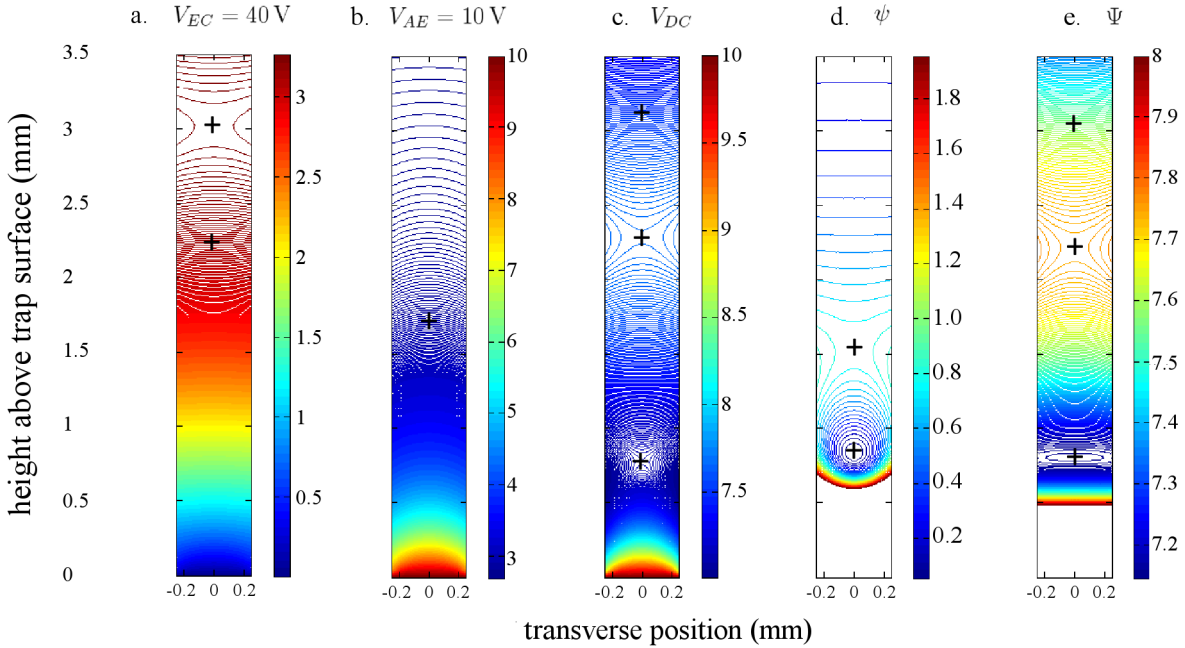


Figure 4.9: Electric potential contours yz -plane (at $x = 0$) for different electrode sets. Note that the colour scales differ between plots. a). Endcap voltages at $V_{EC} = 40$ V. b). $V_{AE} = 10$ V. c). net dc voltage $V_{DC} = V_{EC} = 40$ V + $V_{ME} = 20$ V + $V_{offset} = 5$ V + $V_{AE} = 10$ V. d). bare radiofrequency pseudopotential ψ e). net potential $\Psi = \psi + V_{DC}$. The addition of the dc potential (c.) to the radiofrequency pseudopotential (d.) results in a net potential (e.) whose trap depth is significantly greater than that of the bare radiofrequency pseudopotential. This is a result of the fact that a positive voltage applied to the segmented electrodes (but not the axial electrode) give rise to an electric field whose field lines point towards the trap surface.

Fig. 4.10 demonstrates the effects of modifying the dc voltages on trap potential. For a pure radiofrequency potential (left-most curve of Fig. 4.10a. the trap depth is low (750 meV, cf. Sect. 4.1.1.2).

Chapter 4. Trap Layout and Fabrication

When endcap voltages of $V_{EC} = 10, 20, 30, 40$ or 50 V are added (the larger values corresponding to experimentally used values), the trap depth increases with increasing endcap voltages (curves from left to right with increasing endcap voltage). In Fig. 4.10b., using a net potential with applied radiofrequency voltage of 300 V and endcaps at 50 V, the effect of increasing middle electrode voltage (curves from left to right) from 0 to 30 V (experimentally reasonable values) shows that the trap depth increases slightly. These results are in agreement with the idea introduced above, of an effective positively biased plane at $h > r_0$. Finally, in Fig. 4.10c. a potential with an applied radiofrequency voltage of 300 V, endcaps at 50 V and a middle electrode voltage of 20 V is supplied with increasing axial electrode voltages which results in a decreasing trap depth, as expected.

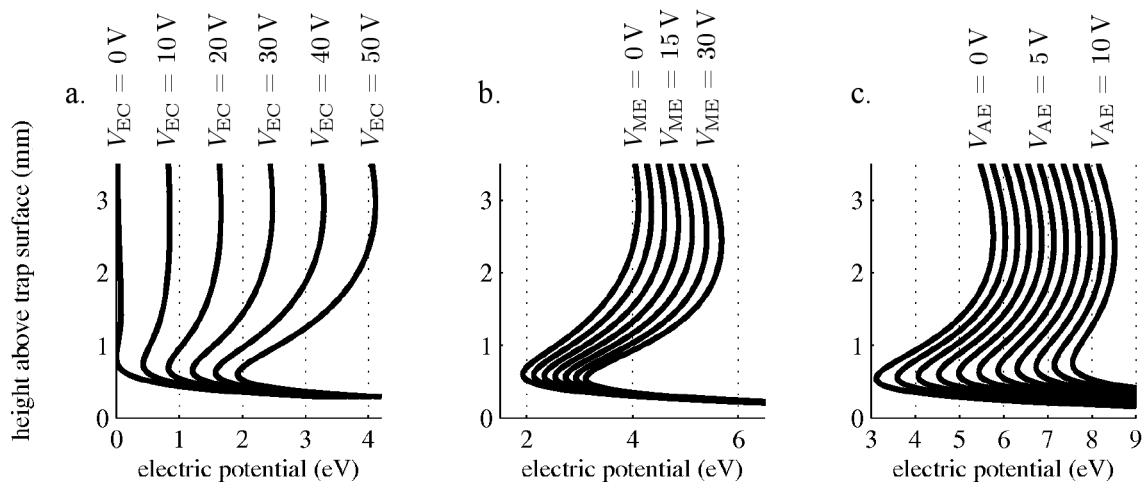


Figure 4.10: Net potential and trap depth for various dc electrode settings (V_{EC} , V_{ME} , V_{AE}) and applied radiofrequency voltage of 300 V at trap drive $\Omega/2\pi = 10.26$ MHz. a). as endcap voltage increases $V_{EC} = \{0, 10, 20, 30, 40, 50\}$ V, trap depth increases b). increasing the middle electrode voltage, $V_{ME} = \{0, 5, 10, 15, 20, 25, 30\}$ V, slightly increases the trap depth. c). increasing $V_{AE} = \{0, 1, 2, 3, 4, 5, 6, 7, 8, 9, 10\}$ V decreases trap depth.

The typical offset voltage applied to the steering electrodes is ~ 5 V. This applied voltage would result in an electric field which also increases the trap depth slightly. The values used in the examples in Fig. 4.10 are all typical experimental voltages, and indicate the trap depth for *Bastille* as operated in the experiment is in the range of ~ 1 eV.

Trap Secular Frequencies For the parameters typically used, *Bastille* exhibits a strong degree of trap frequency anisotropy - the potential is strongly confining in the vertical direction. The ions are essentially confined to the plane parallel to the trap surface. For typical operating voltages (cf. Tab. 4.2), trap frequencies are $\omega_{ax}/2\pi = 120$ – 200 kHz, $\omega_{trans}/2\pi = 200$ – 400 kHz, and $\omega_{vert}/2\pi = 800$ kHz– 1.1 MHz.

Electrodes Influence on Net Potential The effect of the individual electrode or group of electrodes on the net potential is investigated by varying the voltage on that electrode (or group of electrodes) while holding other electrode voltages constant.

Increasing the endcap voltages increases axial, transverse and radial trap frequencies (cf. Fig. 4.11a) and pushes the height of the trap down, away from the radiofrequency null (cf. Fig. 4.11b).

As the middle electrode voltage is increased, trap secular frequencies increase (cf. Fig. 4.12a) and the height of the ion above the trap decreases (cf. Fig. 4.12c). The axial position of the ion moves from the left to the right (cf. Fig. 4.12b).

4.1. Trap Layout and Simulation of Trap Parameters

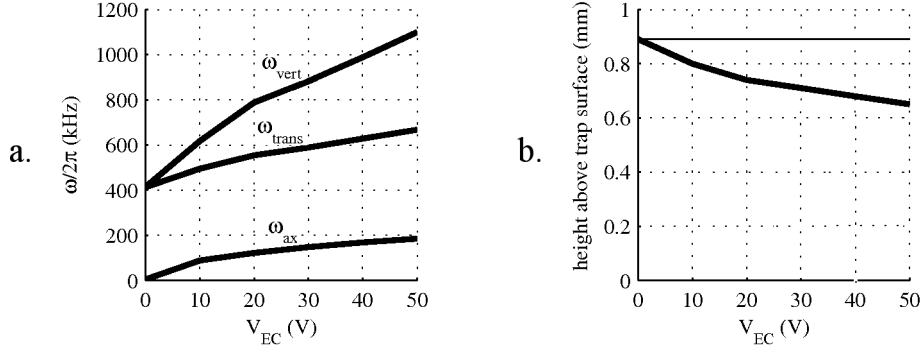


Figure 4.11: Trap parameters: a). secular frequencies and b). vertical location of the trap minimum, for varying endcap electrode voltages, $V_{EC} \in [0, 50]$ V, with an applied radiofrequency voltage of $V_{RF} = 300$ V. As endcap voltage is increased, all trap secular frequencies increase. The vertical trap frequency increases more rapidly than the axial and transverse trap frequencies. Increasing the endcap voltages pushes the trap minimum away from the radiofrequency null towards the surface of the trap. The axial and transverse position of the trap minimum is not affected.

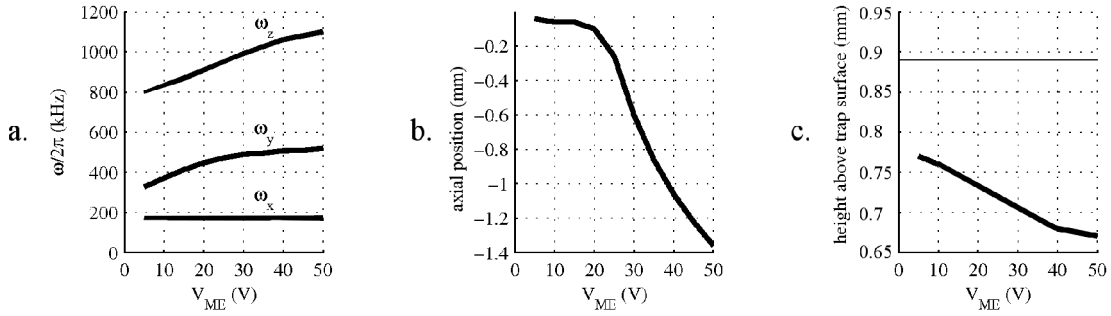


Figure 4.12: Trap parameters: a). secular frequencies, b). axial and c). vertical positions of the trap minimum, for varying middle electrode voltages, $V_{ME} \in [0, 50]$ V, with $V_{RF} = 300$ V, $V_{EC} = 45$ V. Increasing V_{ME} increases the trap frequencies, shifts the trap minimum laterally towards $+x$, and decreases the height of the trap minimum above the surface.

Increasing the axial electrode voltage lowers the transverse and vertical trap frequencies (cf. Fig. 4.13a), and increases the height of the ion above the trap (cf. Fig. 4.13c). As the axial electrode voltage is increased, the trap minimum moves from right to left (cf. Fig. 4.13b).

The finest control of the trap potential minimum, frequencies, and orientation of the trap principal axes is achieved through modification of the steering electrode voltages (cf. Subsect. 4.1.1.2). The steering electrodes are further grouped according to the movements they can produce, and this control is described in the following paragraphs.

Applying a common voltage, or offset to all steering electrodes causes the trap height to decrease (away from the radiofrequency null) and the transverse and vertical trap frequencies to increase, as shown in Fig. 4.14. Electrodes are held at voltages typically used in experiments, specifically, $V_{RF} = 320$ V, $V_{EC} = 50$ V, $V_{ME} = 30$ V, $V_{AE} = 8$ V, and with the offset voltage varying between $V_{offset} \in [-5, 9]$ V.

Pairing steering electrodes residing at the same transverse location, called the transverse balance control, V_{TB} (cf. Fig. 4.7), allows transverse displacement of the location of the trap minimum. With trap operating voltages of $V_{RF} = 320$ V, $V_{EC} = 50$ V, $V_{ME} = 30$ V, $V_{AE} = 8$ V, and $V_{TB} = [-5, 5]$ V, the trap minimum is transversely displaced by $\sim 320 \mu\text{m}$ (axial and vertical position are unaffected),

Chapter 4. Trap Layout and Fabrication

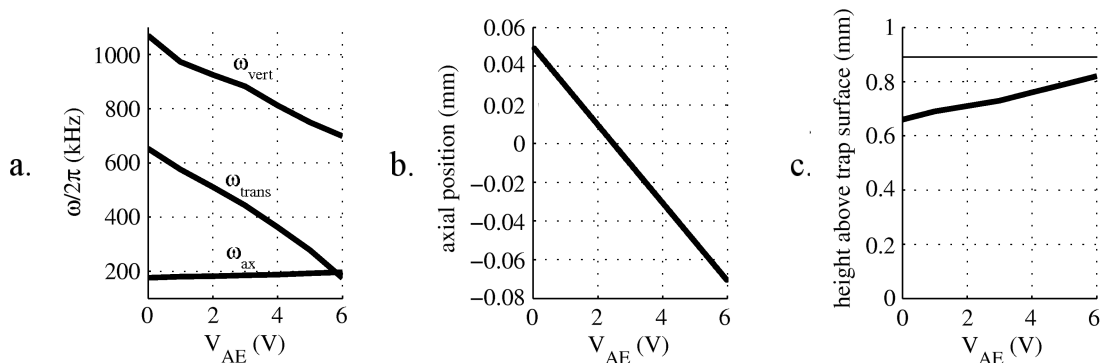


Figure 4.13: Trap parameters: a). secular frequencies, b). axial and c). vertical positions of the trap minimum, for varying axial electrode voltages, $V_{AE} = [0, 6]$ V. $V_{RF} = 300$ V, $V_{EC} = 45$ V, $V_{ME} = 0$ V, which is consistent with typically used experimental voltages (cf. Tab. 4.2). The behaviour of the axial electrode is opposite that of the other dc electrodes, due to its location directly beneath the radiofrequency null. a). Increasing the voltage on the axial electrode decreases trap frequencies. The transverse trap frequency can be decreased below that of the axial trap frequency, that is, the weakest trap frequency is then the transverse trap frequency and an ion string will be aligned perpendicular to the radiofrequency null. b). Changing the axial electrode voltage moves the electrodes from the right ($+x$) to the left ($-x$). c). Again in contrast to the other dc electrodes, the axial electrode moves the trap minimum upwards, towards the radiofrequency null.

as shown in Fig. 4.15a. For this range of V_{TB} , the trap frequencies are relatively unaffected, as shown in Fig. 4.15b.

Pairing steering electrodes residing at the same lateral location, called the lateral balance control (cf. Fig. 4.7), allows axial displacement of the location of the trap minimum. With trap operating voltages of $V_{RF} = 320$ V, $V_{EC} = 50$ V, $V_{ME} = 30$ V, $V_{AE} = 8$ V, the voltage applied to the middle electrode creates a slight potential hill in the axial centre of the trap. Varying the lateral balance voltage control demonstrates this double well potential, as shown in Fig. 4.16a. This plot shows, in the xy -plane, the trap minimum and contour lines at $\Psi_{net, min} + 1$ meV above the trap minimum, lateral balance voltages of $V_{LB} = [-10, 14]$ V. The double well potential is apparent by the absence of potential minima in the central axial region - for close to zero lateral balance voltage, the trap minimum will not be located centrally along x , but will fall either side of the potential hill into one of the two axial potential wells. The plots are not symmetric about zero axial displacement, due to the axial asymmetry of the trap geometry (the radiofrequency and axial electrodes).

The contour lines ($\Psi_{net, min} + 1$ meV) also indicate the directions and relative strengths of the trap axes. The trap potential, and the axis lengths of the contour ellipses are proportional to ω^2 . The colour scale of the contours varies over ~ 1 meV.

The most significant feature of Fig. 4.16a. occurs for large magnitudes of V_{LB} . First, ω_{ax} decreases as ω_{trans} increases, until the weak trap axis is aligned perpendicular to the radiofrequency null. Eventually, for further increase in V_{LB} , the trap minimum splits transversely into a double well potential. Further increase in V_{LB} pushes these double well potential minima further transversely and axially. It seems as though the double well potential minimum location for increasing V_{LB} follows a curved “wall”: this wall arises from the strong influence of the endcaps.

Fig. 4.16b. details the variation in $\omega_{ax, trans}$ with V_{LB} . At $V_{LB} = 1$ V, $\omega_{trans}/\omega_{ax} \sim 3$. Increasing V_{LB} decreases ω_{ax} and increases ω_{trans} until eventually ω_{trans} becomes the weak trap axis. The orientation (with respect to the x -axis) of the weak principal trap axis is plotted in Fig. 4.16c. At $V_{LB} = -3$ V and $V_{LB} = 7$ the transverse trap confinement becomes weaker than the axial trap confinement, and the orientation of the weak axis transitions from 0 to $\pm\pi/2$. Increasing V_{LB}

4.1. Trap Layout and Simulation of Trap Parameters

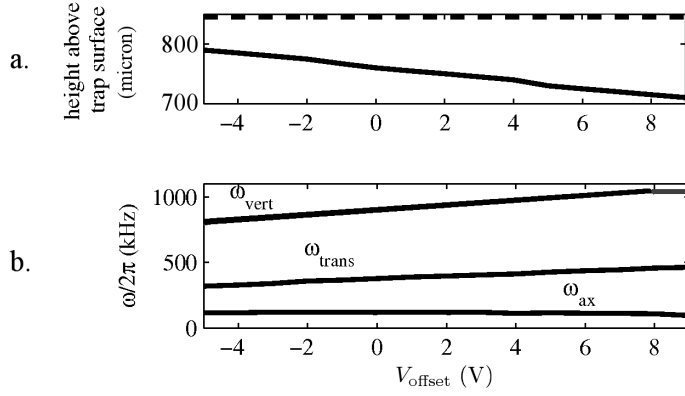


Figure 4.14: Vertical trap position and secular trap frequencies for the voltage V_{offset} applied to the steering electrodes in the range $V_{\text{offset}} = [-5, 9]$ V a). the trap minimum moves towards the trap surface (away from the radiofrequency null) for increasing V_{offset} and b). ω_{trans} and ω_{vert} increases.

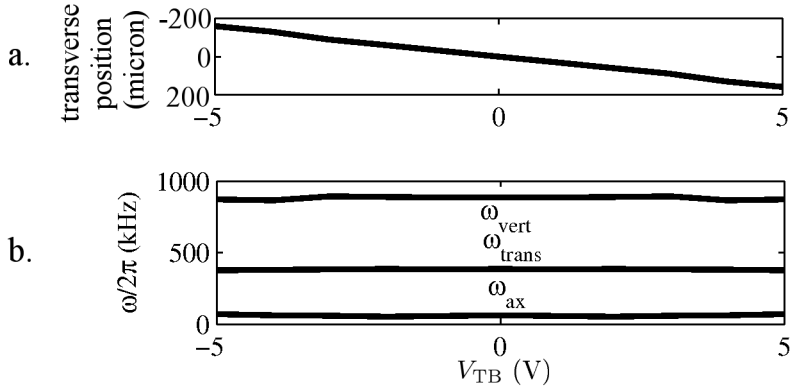


Figure 4.15: Varying V_{TB} a). moves the trap minimum laterally, b). with trap frequencies unaffected.

further pushes the trap potential minimums around the endcap wall, which modifies the orientation to $\pm\pi/2 \mp \varepsilon$, where $\varepsilon \lesssim \pi/6$.

The results shown in the previous section, varying the lateral balance control, were carried out at a transverse balance of zero (i.e. $V_{\text{VB}} = 0$); the potential was balanced in the transverse (y) direction. The case is considered now where the starting position is transversely displaced from the radiofrequency null, that is, the vertical balance control voltage is not zero. In this case, rather than having the weak axis abruptly transition from x to y to y' , the weak axis is smoothly varied from x towards y . The rotation of the weak principal trap axis is smooth with increasing lateral balance control voltage, varying from being aligned along x ($\theta = 0$) towards being aligned along $\pm y$ ($\theta = \pm\pi/2$).

Moving the trap minimum away from the radiofrequency null causes heating of the trapped ions. Rotation of the trap axes while keeping the trap minimum on the radiofrequency null is achieved using the diagonal control of the steering electrodes.

The demonstrative results shown below are for operating voltages of: $V_{\text{RF}} = 320$ V, $V_{\text{EC}} = 50$ V, $V_{\text{ME}} = 10$ V, $V_{\text{AE}} = 7$ V, $V_{\text{LB}} = 0.8$ V, $V_{\text{TB}} = 0$ V and $V_{\text{diagonal}} = [-10, 10]$ V. For these voltages (which are in the range of typical operating voltages), the position of the trap minimum remains always in the same location. When the diagonal voltage control is zero, the weak trap axis is oriented parallel to the radiofrequency null. An increase in magnitude of the diagonal voltage control smoothly rotates the weak trap axis, maintaining the same position of the trap minimum. For the

Chapter 4. Trap Layout and Fabrication

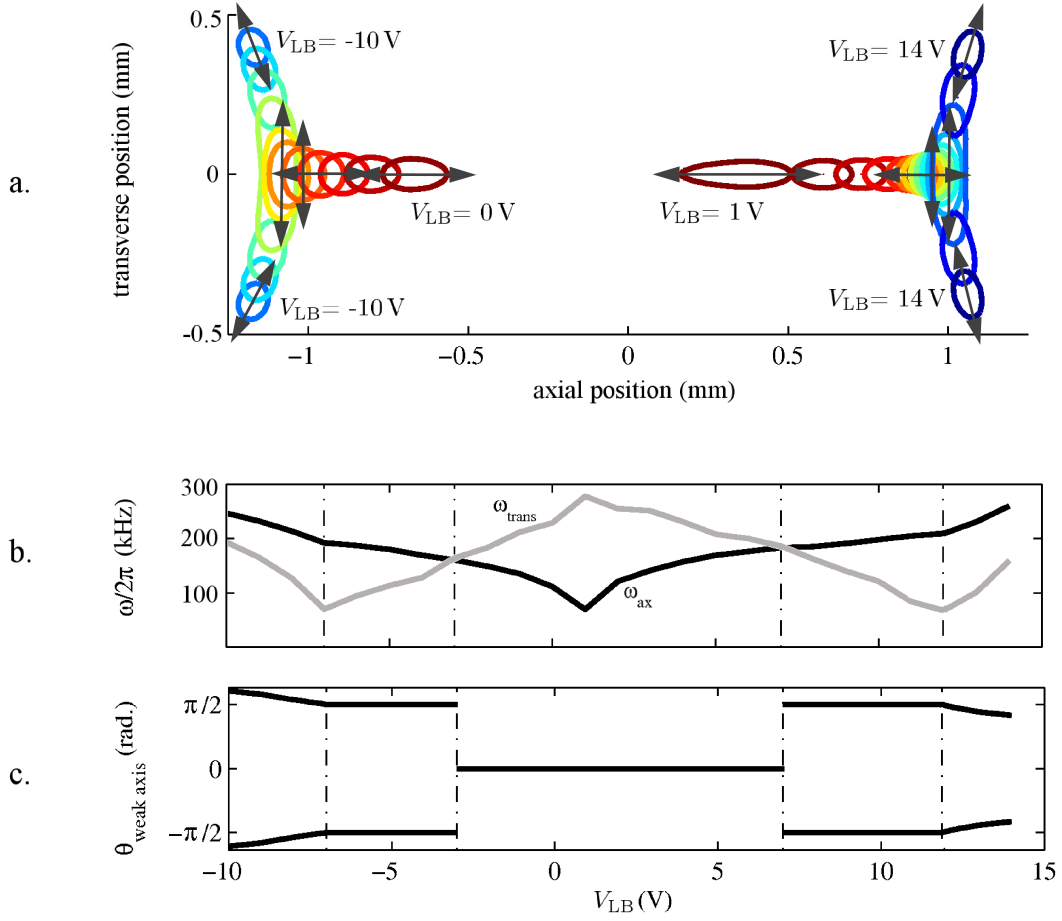


Figure 4.16: For $V_{RF} = 320$ V, $V_{EC} = 45$ V, $V_{ME} = 30$ V, $V_{AE} = 8.5$ V, $V_{offset} = 5$ V, $V_{LB} = [-10, 14]$ V, consistent with typical trap operating voltages (cf. Tab. 4.2) these plots show a). the position (in the xy -plane) of the trap minimum (dots) and contour lines of the net potential (at 1 meV above the trap minimum) in the xy -plane (at z of the trap minimum) for different values of the lateral balance voltage V_{LB} . The shape of the contour lines indicate the relative strengths of the trap frequencies, and the orientation of the trap axes, which are given in b). the axial and transverse trap frequencies, and c). the orientation of the weak trap axis with respect to the x -axis.

parameters demonstrated here, the axial and transverse trap frequencies vary with varying diagonal voltage control of the steering electrodes (the vertical trap frequency, not shown, is unaffected), and the rotation of the axis varies between $\sim \pi/8$ and $\pi/8$ (cf. Fig. 4.18). Rotation through a full 2π is achieved by simultaneous variation of additional control voltages. Additionally, these can be optimised to maintain constant trap frequencies.

4.1. Trap Layout and Simulation of Trap Parameters

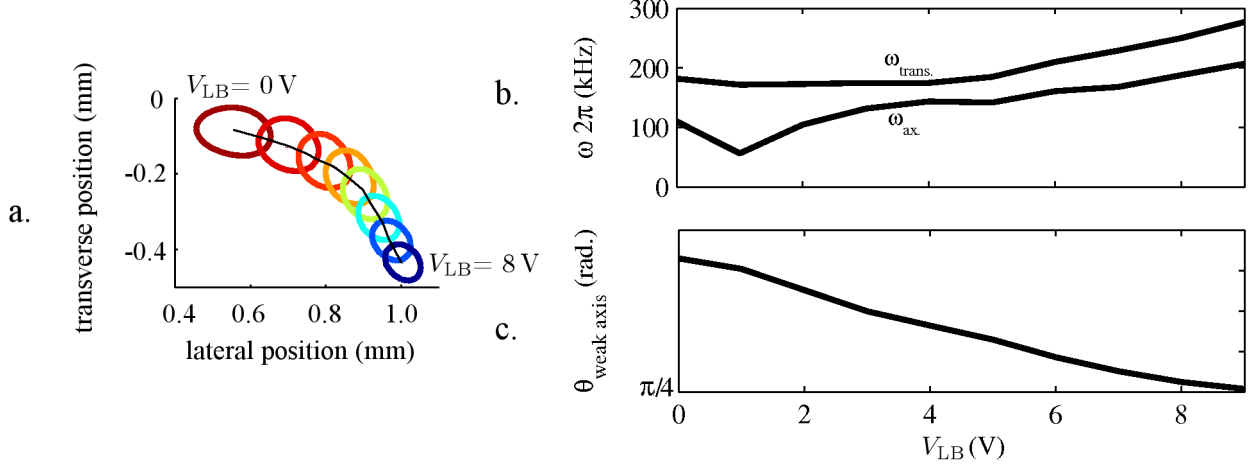


Figure 4.17: Variation of $V_{LB} = [0, 8]$ V for a non-zero transverse balance voltage $V_{TB} = 0.8$ V. a). path of the trap minimum. Similar paths are possible on the other side of the radiofrequency null (mirrored about y), or at the other (axial) end of the trap (mirrored about x , mirrored about x and y). b). secular frequencies and c). orientation of the weak trap axis. Other trap operating parameters are $V_{RF} = 320$ V at trap drive frequency of $\Omega/2\pi = 10.25$ MHz, and dc voltages of $V_{EC} = 45$ V, $V_{ME} = 30$ V, $V_{AE} = 8.5$ V, $V_{offset} = 5$ V.

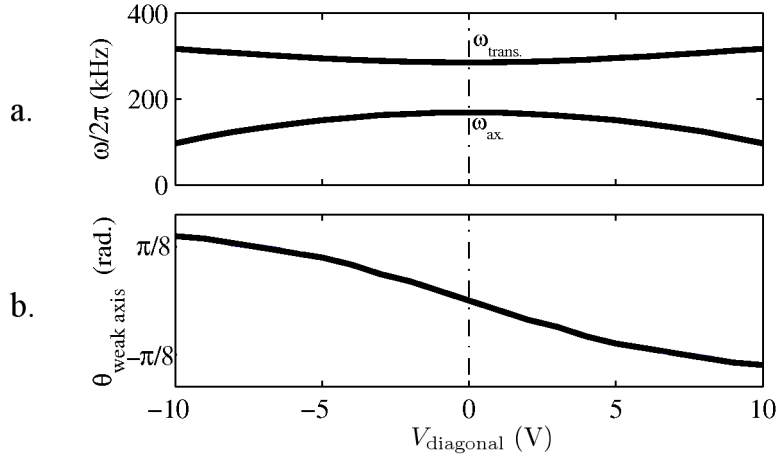


Figure 4.18: Effect of variation of $V_{diagonal} = [-10, 10]$ V control of the steering electrodes on a). secular frequencies and b). orientation of weak trap axis, for trap operating parameters of $V_{RF} = 320$ V at a trap drive frequency of $\Omega/2\pi = 10.25$ MHz, with dc voltages of $V_{EC} = 50$ V, $V_{ME} = 10$ V, $V_{AE} = 7$ V, $V_{LB} = 0.8$ V, $V_{TB} = 0$ V.

Chapter 4. Trap Layout and Fabrication

4.1.2 Two-Layer Gold-on-Alumina Trap

The two-layer microfabricated wafer trap is a logical continuation of conventional linear Paul trap designs. For the trap, an alumina substrate, which can be accurately laser machined is used. The electrode material is gold, chosen for its favorable material properties (high conductivity, smooth surfaces, absence of native oxides) and fabrication possibilities (cf. Sect. 3.1.2.1). The design of this trap was carried out as a collaborative effort as a part of the EU STREP project MICROTRAP.

4.1.2.1 Two-Layer Gold-on-Alumina Trap Geometry

The two-layer trap is composed of two electrode layers separated by an insulating spacer, as depicted schematically in Fig. 4.19. The spacer has a thickness of $125\ \mu\text{m}$. The electrode layers have two different slit sizes which define two regions: a storage zone with a slit width of $a = 500\ \mu\text{m}$ ($\alpha = 4$), and a processing zone with a slit width of $250\ \mu\text{m}$ ($\alpha = 2$).

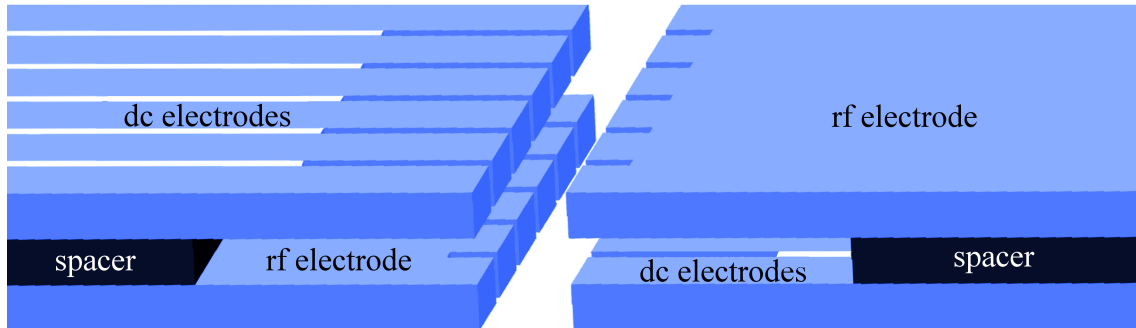


Figure 4.19: The trap is formed from two wafers “sandwiched” with a spacer in between. The radiofrequency electrodes are “notched”, with these notches located directly opposite the gaps separating the segmented dc electrode fingers.

The electrodes themselves have an effective thickness equal to the wafer thickness ($\delta = 1$), as the entire wafer is covered in gold to form the electrodes. The electrodes are defined in the fabrication steps depicted schematically in Fig. 4.20. First, a wafer (with a slot already machined) has electrode “fingers” defined by femtosecond pulsed laser micromachining (Fig. 4.20a). The entire wafer is then coated with gold (Fig. 4.20b). Electrical insulation between electrodes on the large faces of the wafers is achieved through laser machining through the gold to the alumina substrate (Fig. 4.20c). The electrodes are still electrically connected through the small channels running between the fingers. This path (and some substrate material) is removed by drilling holes along the channels (Fig. 4.20d).

These fabrication steps achieve a high electrode thickness, δ (increasing η , cf. Sect. 3.1.1.1), and a minimum of exposed insulating surfaces close to the trapping area (cf. Sect. 3.1.2.2). The trap has aspect ratios of 2 (4) and a thickness of 1 (1) in the processing (storage) zone. Aspect ratios closer to unity would provide a stronger confinement, however, due to the scale and the thickness of the wafer, this would render optical access unnecessarily difficult.

The electrodes finger geometry described above is also mimicked in the radiofrequency electrodes geometry. To ensure well-balanced electric potentials on the trap axis, the electrode layers should be as symmetric as possible, so that micromotion can be minimised. Increased symmetry is realised by cutting “notches” into the radiofrequency electrodes, which are located precisely opposite the separate cuts in the dc electrodes (cf. Fig. 4.19). These notches suppress axial bumps in the radiofrequency field and improve the axial electric field symmetry.

4.1. Trap Layout and Simulation of Trap Parameters

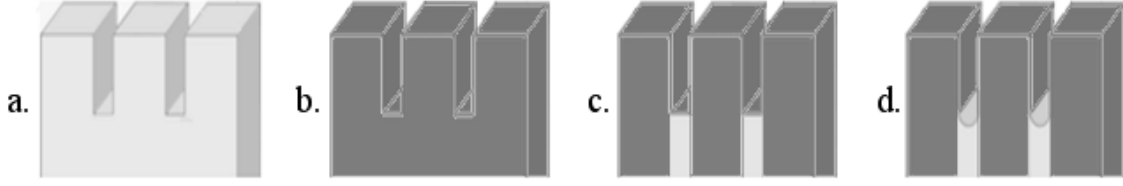


Figure 4.20: Fabrication process of the single electrode layers. a). Laser machining of the geometric structures (e.g. “fingers”) of the alumina substrate wafer. The cuts extend back $200\ \mu\text{m}$ into the wafer b). The entire wafer is coated in gold. c). Laser ablation of the gold layer defines electrical isolation between electrodes on the wafer surfaces (front and back). Note that all “fingers” are still electrically connected d). The electrical connection between the fingers is removed by further laser-machining of the substrate. Radiofrequency electrodes are also “notched” to mirror the geometry of the electrode fingers. For the rf electrodes, steps a.) and b). are carried out, with the laser machining of the “notching” extending just $60\ \mu\text{m}$ back into the wafer. The radiofrequency electrode is continuous, and so fabrication steps c). and d). are not required.

Two different linear designs were fabricated as part of the MICROTRAP project. As ion heating is dependent on the distance from the ion to the electrodes, it is advantageous to design a trap with zones which have different ion-electrode separations (to investigate this effect). The regime where ion-electrode distance is $140 = \sqrt{62.5^2 + 125^2}$ ($258 = \sqrt{62.5^2 + 250^2}$) μm in the processing (storage) region is chosen as it is small enough to be an interesting step in the direction of ion-trap miniaturisation yet is large enough to remain technologically feasible in terms of alignment accuracy and optical access. Both the linear trap designs include a wider (non-unit-aspect ratio) zone which can be used to load ions; this zone has a larger trap volume and a higher loading efficiency. An additional advantage of a dedicated loading zone is that contamination of electrodes due to the incident atomic beam can be confined to this area. Computation can be carried out in other, uncontaminated zones, and therefore possible problems arising from shorted or impure electrode surfaces can be avoided for sensitive measurements.

The first linear design (see Fig. 4.21) consists of a storage and a processing zone joined by a transition zone. In the storage region the central slit width is $500\ \mu\text{m}$, while the transfer region narrows the slit to $250\ \mu\text{m}$, which is the slit width of the processing zone. The storage zone is divided into nine segments (and an additional wide electrode at the far end) of $250\ \mu\text{m}$ width. A transition zone between the two regions has three electrodes of $250\ \mu\text{m}$ width. The processing zone has nineteen (and an additional wide electrode at the far end) electrodes of $100\ \mu\text{m}$ width with $30\ \mu\text{m}$ spacing. The radiofrequency notches match the opposing dc electrodes and are cut back by a length of $60\ \mu\text{m}$.

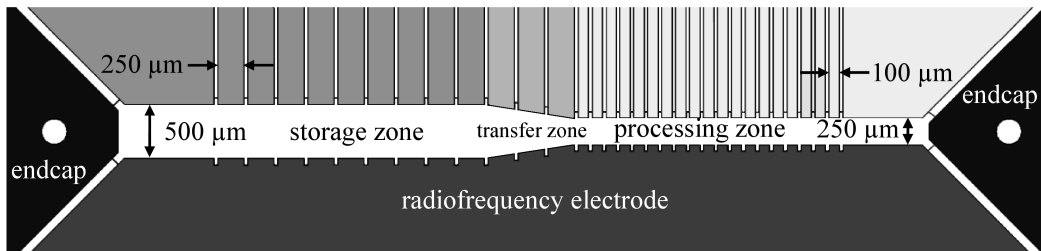


Figure 4.21: Schematic of the linear two-layer trap. There are three zones, a storage zone with ten electrodes each of width $250\ \mu\text{m}$ and a gap of $500\ \mu\text{m}$, a transfer zone with three electrodes of width $250\ \mu\text{m}$ each and a slit width varying linearly between 500 and $250\ \mu\text{m}$, and a processing zone, with 19 electrodes of $100\ \mu\text{m}$ width and a gap width of $250\ \mu\text{m}$.

The layout of the both upper and lower wafers can be seen in Fig. 4.22. Holes with a diameter

Chapter 4. Trap Layout and Fabrication

of $240\ \mu\text{m}$ in the outer region of the wafers allow alignment of the two wafers.

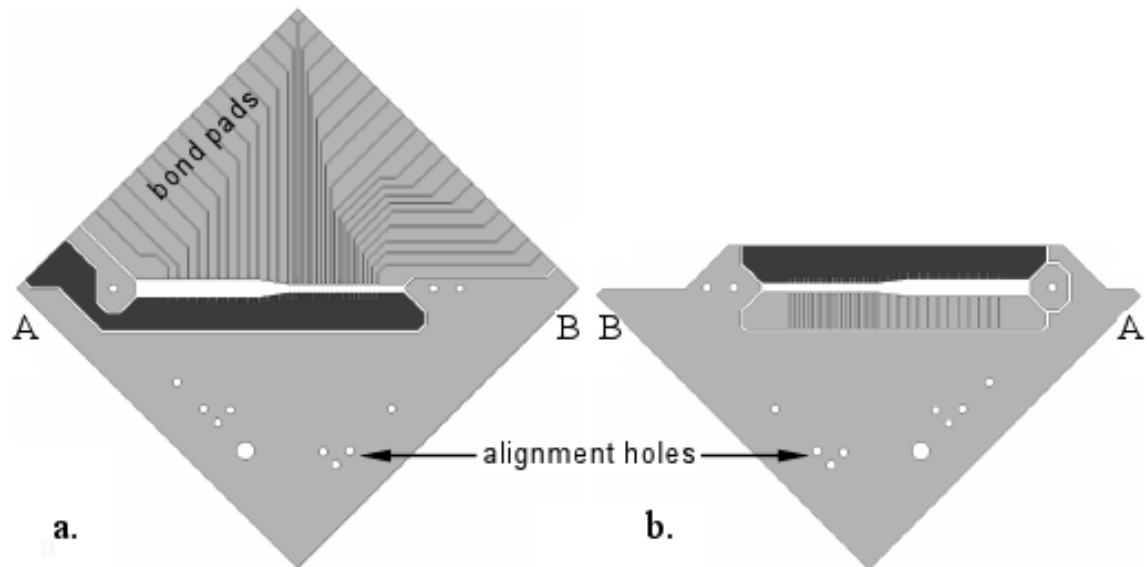


Figure 4.22: Inner faces of the linear gold-on-alumina two-layer trap: a). lower wafer b). upper wafer, flipped about the right corner to reveal the inner side. Segmented (dc) electrodes are shown in light grey, and radiofrequency electrodes are dark grey. The two layers are placed together in a “sandwich”, with a $125\ \mu\text{m}$ spacer separating them (the circular holes in the two wafers align). Each wafer has electrical connections to two edges of its wafer. The top wafer is designed such that the bond pads of the lower substrate remain accessible after assembly.

A second linear design (not described in this thesis) contains two computation zones (and one storage zone) of different slot widths (and therefore ion-electrode distances). This is useful for measuring the dependence on heating of different ion-electrode distances, whilst keeping all other relevant trap material properties as constant as possible. Additionally, a smaller ion-electrode distance can achieve higher trap frequencies and could be used to increase the speed of computation.

4.1.2.2 Two-Layer Gold-on-Alumina Trap Numerical Field Simulation and Analysis

Simulation Geometry To numerically simulate the electric fields of the trap each finger is modelled as an independent geometrical object. The simulation electrodes extend away from the trapping region for $400\ \mu\text{m}$. The simulation geometry is depicted in Fig. 4.23.

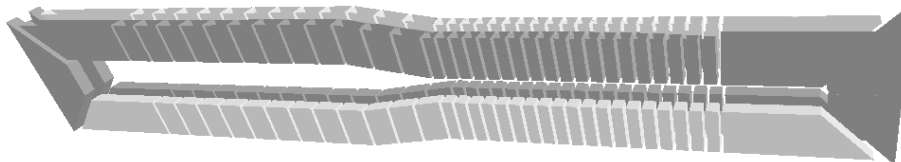


Figure 4.23: The geometry of the two-layer trap, as entered in numerical field simulation program CPO. Notice that the radiofrequency electrode (lighter coloured shapes) is modelled as discrete elements. This is a close approximation to the designed and fabricated geometry. This image is very similar to what can be seen on the CPO screen.

Radiofrequency Confinement

4.1. Trap Layout and Simulation of Trap Parameters

Trap Depth The smallest local maximum near the trap minimum defines the trap depth, and is located vertically above and below the trap minimum, visible in the contour plots and cross-sections of the radiofrequency pseudopotential in Fig. 4.24.

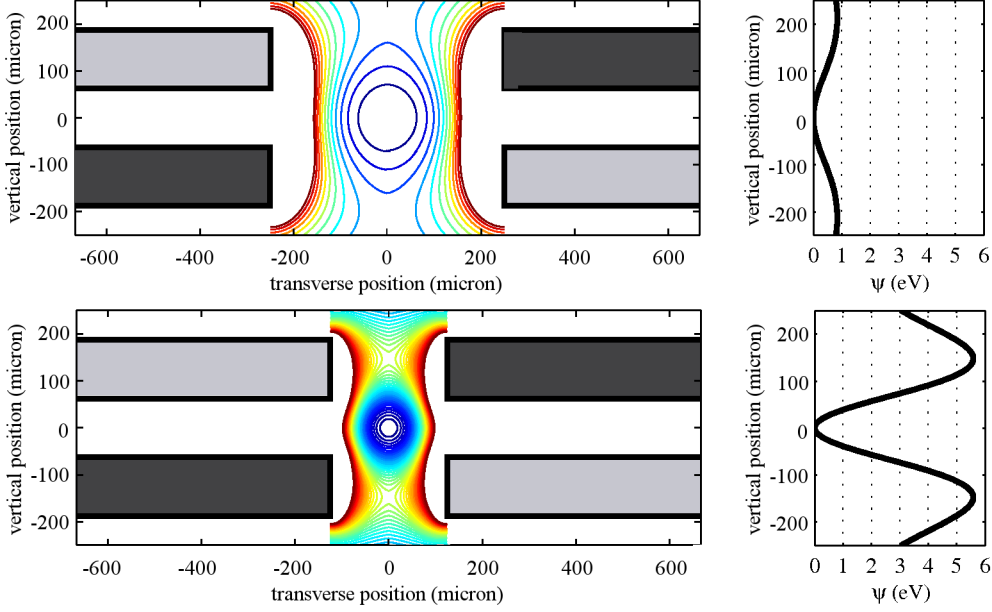


Figure 4.24: Radiofrequency pseudopotential in the storage region (upper plots) and processing region (lower plots), for an applied radiofrequency voltage of 140 V(0-peak) at a drive frequency of $\Omega/2\pi = 24.8$ MHz. The contour lines mark intervals of 0.25 eV for both geometries. The electric potential along the z -axis (vertical) is shown on the right hand side of the figure: this is the direction of the nearest local maximum near the trap minimum, and is the direction along which an ion would escape. The trap depth due to the purely radiofrequency pseudopotential is ~ 75 meV in the storage region, and 5.5 eV in the processing region.

For an applied radiofrequency voltage of $V_{\text{RF}} = 140$ V (0-peak), and a trap drive frequency of $\Omega/2\pi = 24.8$ MHz, the trap depth is ~ 75 meV in the storage region, and 5.5 eV in the processing region, which is adequate for both loading from a thermal beam and resilient to ion loss.

Curvature In the absence of dc fields, the trap has a quadrupole component of the electric potential (for an applied voltage of $V_{\text{RF}} = 1$ V), in the storage region of $c_2 = 0.522 (\pm 0.001) \cdot 10^7 \text{ V}^{-1} \text{ m}^{-2}$, and in the processing region, the stronger confinement of $c_2 = 1.876 (\pm 0.015) 10^7 \text{ V}^{-1} \text{ m}^{-2}$. The weaker curvature in the storage region is expected, due to the larger aspect ratio. The axial variation of the radiofrequency curvature is shown in Fig. 4.25. The vertical dotted lines in the graph indicate the extent of the electrodes and gaps. It is noticeable that the radiofrequency confinement is slightly increased between the wider electrodes at each side of the trap. The transfer region, consisting of three segments, provides a relatively smooth transition between the weaker and stronger confinement regions.

The most significant feature of the radiofrequency curvature plot is the periodic variation in both storage and processing regions due to the discrete nature of the electrodes. The periodicity, in each region, is exactly spaced by the inter-electrode distance. Fig. 4.25 shows detail of the variation in c_2 in the processing region: there are 19 segments in this region, and this is evident in the number of periods of the variation.

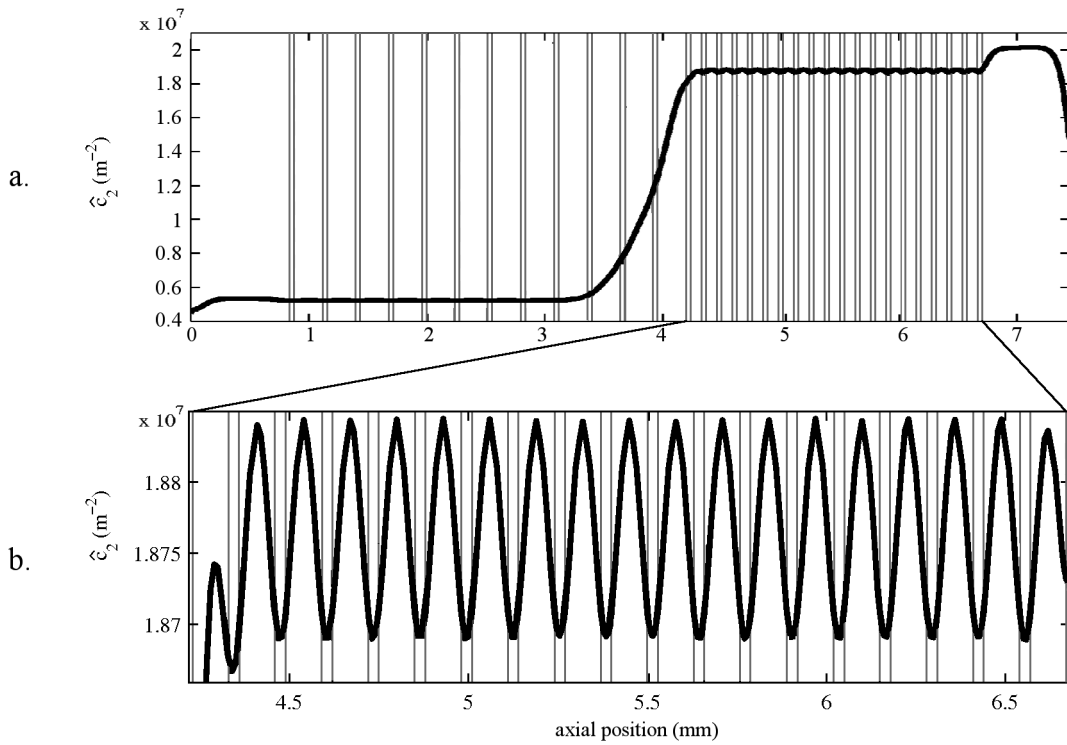


Figure 4.25: Axial variation of the radiofrequency confinement, characterised by the quadrupole component of the potential c_2 . Vertical grey lines indicate the electrodes and gaps. a). The storage region has a curvature $c_2 = 0.522 (\pm 0.0011) \cdot 10^7 \text{ V}^{-1} \text{ m}^{-2}$. As the slit width narrows in the transition region (middle of the plot) the curvature increases, to its value in the processing section of $c_2 = 1.876 (\pm 0.015) \cdot 10^7 \text{ V}^{-1} \text{ m}^{-2}$. Within each region, the curvature has a periodic modulation, indicated by the values in brackets. This periodic variation is a result of the discrete nature of the electrode fingers. b). Detail of the c_2 modulation in the processing zone. The processing zone has nineteen segments of width $100 \mu\text{m}$ with gaps between of $30 \mu\text{m}$. This number of segments and spacing is clearly evident in the c_2 variation.

Axial Contributions to Radiofrequency Field Ideally, the radiofrequency confinement in a linear Paul trap is purely radial, so the axial component to the electric field arising from the radiofrequency electrode, E_x , should be zero. The motivation for “notching” the radiofrequency electrodes (as previously described) is to suppress axial contributions to the radiofrequency field. Fig. 4.26 shows detail of $E_x(y = 0, z = 0)$ in the centre of the storage zone and the centre of the processing zone for both “notched” and continuous radiofrequency electrode geometries. E_x is small but not zero, and shows periodic variation on a period consistent with the electrode spacing (as depicted by the dashed lines).

Along the trap axis, the axial contribution to the radiofrequency field is suppressed by notching the radiofrequency electrode to mimic the geometry of the segmented dc electrodes. The amplitude of the periodic variations is $\approx 2.2 \text{ V/m}$ (2.7 V/m) in the storage (processing) zone, for a continuous radiofrequency electrode geometry. This is reduced to an amplitude of 0.15 V/m (0.07 V/m) in the storage (processing) zone, for a notched radiofrequency electrode geometry. Therefore, notches in the radiofrequency electrode suppress the axial contribution of the radiofrequency field by 98% (93%) in the processing (storage) zone.

4.1. Trap Layout and Simulation of Trap Parameters

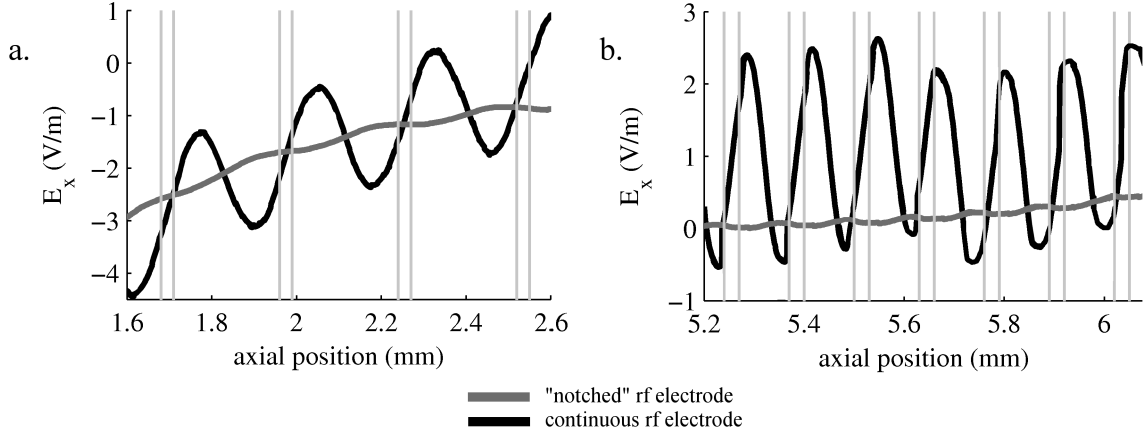


Figure 4.26: Detail of the axial component E_x of the radiofrequency field in the a). storage and b). processing zones, for the notched and continuous radiofrequency electrode geometries. Grey vertical lines indicate the extent of the segmented electrodes (and corresponding radiofrequency notches). The notched radiofrequency electrode shows a clear suppression of the axial component in comparison to the continuous radiofrequency electrode, and is a result of the increased trap symmetry.

Static Confinement

DC Segmented Electrode Contributions For axial confinement, opposing dc electrodes are set to the same voltage U_i , $i = 1, \dots, 30$. The electric potential basis functions $\phi_i(x)$ obtained when only U_i is set to 1 V and all other voltages are set to zero are shown in Fig. 4.27.

The left end cap has a very strong electric potential on axis, due to both its size (large) and position (centered on axis). The wide storage zone electrode is next, with a relatively strong potential on axis. The nine storage zone electrodes electric potential contributions are, as expected, uniform. They exhibit a good spatial overlap, indicating that the segment width in relation to aspect ratio has been appropriately chosen. The electric potentials on axis from the transition zone electrodes are immediately obvious - while their width remains constant, the slit width decreases linearly over this zone, therefore the strength on axis increases. Next is the contribution from the nineteen processing zone electrodes, characterised by their small width and large spatial overlap (greater than that obtained in the storage zone). This zone is designed for computation, which would include shuttling. The large spatial overlap of these potential contributions maximises shuttling efficiency. Finally, the large final processing zone electrode, and the right end cap.

Axial Secular Frequencies Fig. 4.28 shows the electric potential basis functions, $\hat{\phi}_{\text{stor}}$ and $\hat{\phi}_{\text{proc}}$ for a single electrode in the middle of the storage and processing zones. The normalised polynomial expansion coefficients (for an applied voltage of -1 V on one pair of electrode, all other electrodes grounded) are $d_{2, \text{stor}} = -1.0573 \cdot 10^6 \text{ V}^{-1} \text{ m}^{-2}$ and $\hat{d}_{2, \text{proc}} = -4.2764 \cdot 10^6 \text{ V}^{-1} \text{ m}^{-2}$. These enable high axial trap frequencies of $\omega_{\text{ax}, \text{stor}}/2\pi$ ($\omega_{\text{ax}, \text{proc}}/2\pi$) ~ 1.5 (2.5) MHz when moderate (i.e. with amplitude less than 10 V) negative voltages are applied to one pair of segmented electrodes, with all other electrodes held at ground. The axial frequencies together with the radial trap frequencies, in both zones are presented together in the next section.

Net Potential

Trap Secular Frequencies Axial confinement can be provided by holding one pair of segmented electrodes at negative voltages, with all others held at ground. Fig. 4.29 shows the radial and axial

Chapter 4. Trap Layout and Fabrication

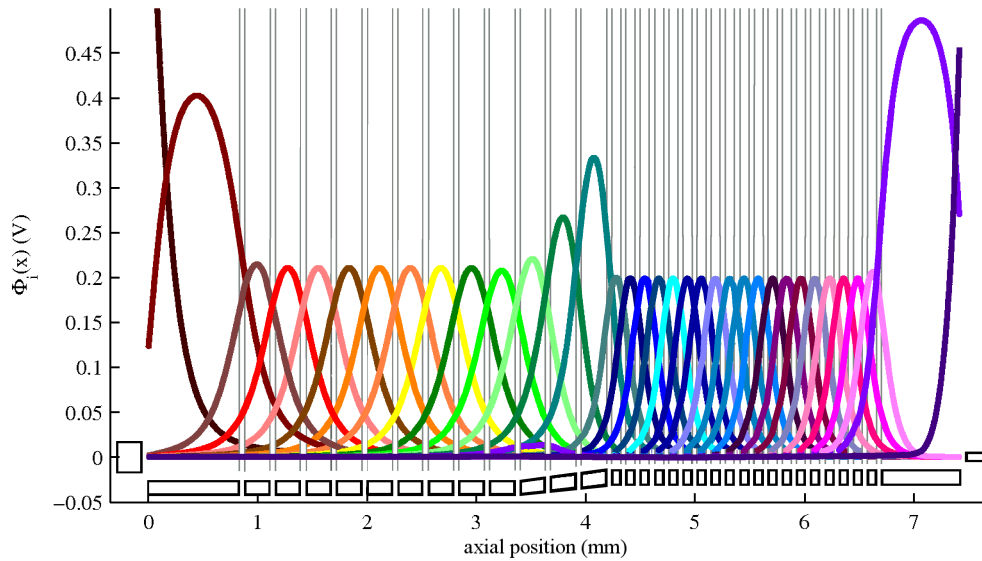


Figure 4.27: Individual electrode potentials $\phi_i(x)$ on the trap axis. Vertical grey lines, and the rectangles along the x -axis indicate the electrodes and gaps. Narrow electrodes show a lower maximum potential due the smaller amount of surface charges. An arbitrary axial potential is formed by superposing individual contributions.

trap frequencies obtained in the storage and processing zones for this dc voltage configuration. Here, $V_{\text{RF}} = 140 \text{ V}$ at a trap drive frequency of $\Omega/2\pi = 24.8 \text{ MHz}$, and with the central pair of segmented electrodes (“segment 7” - the segments centrally located in the storage zone, and “segment 24” - the segments centrally located in the processing zone) held at $V_{\text{seg.7}} = [-10, -3] \text{ V}$ and $V_{\text{seg.24}} = [-10, -1] \text{ V}$ (with all other segmented electrodes held at 0 V).

4.1. Trap Layout and Simulation of Trap Parameters

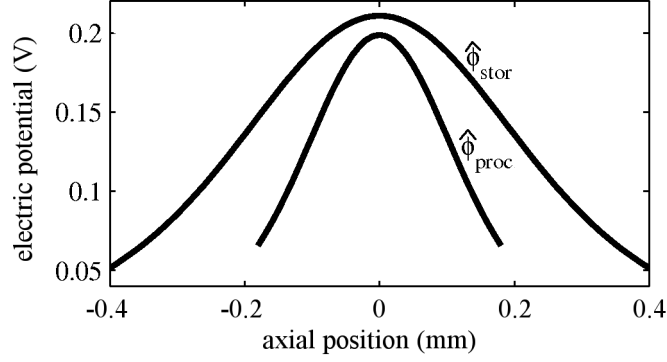


Figure 4.28: The electric potential basis functions, $\hat{\phi}_{stor}$ and $\hat{\phi}_{proc}$ for a single electrode in the middle of the storage and processing zones.

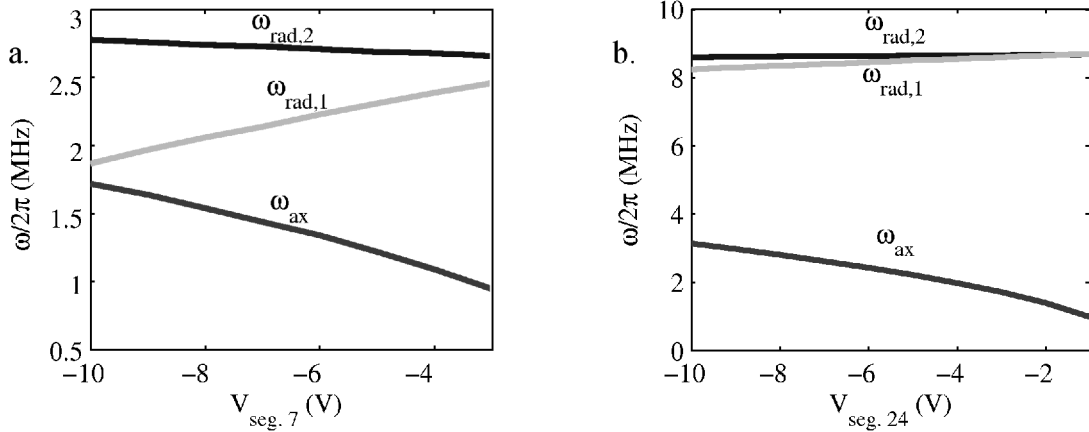


Figure 4.29: The radial and axial trap frequencies in the a). storage zone, and b). processing zone, for $V_{RF} = 140$ V (at a trap drive frequency of 24.8 MHz), and dc voltages of $[-3, -10]$ V and $[-1, -10]$ V on one pair of segmented electrodes, with all other electrodes held at ground.

Chapter 4. Trap Layout and Fabrication

4.2 Trap Fabrication

The following section describes the fabrication of the macroscopic PCB trap *Bastille*, and the microfabricated two-layer gold-on-alumina trap.

4.2.1 Surface Trap *Bastille*

The PCB surface ion trap as described in Sect. 4.1.1.1 was fabricated by a prototype PCB manufacturing company (*Hughes Circuits*, San Marcos, California, USA), and is shown in Fig. 4.30.

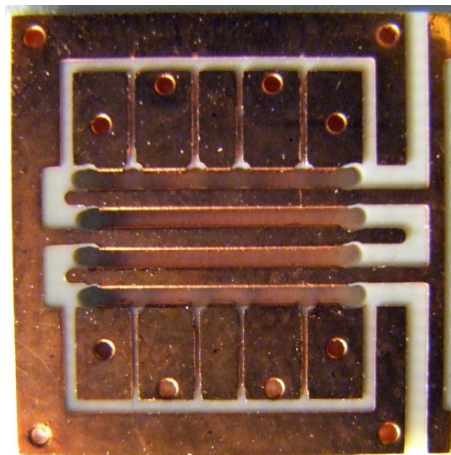


Figure 4.30: Photo of the PCB surface ion trap *Bastille*. The two radiofrequency electrodes extend from a common rail at the right, and the remaining electrodes are at variable dc potential. The holes visible are vias which pass through the substrate to the back side, where they connect pairwise transverse electrodes. These connections were removed so that individual control of the segmented electrodes was possible.

Before mounting, the trap had pairwise connections between transversely opposite electrode segments (through vias) removed to allow for individual control of electrodes. The trap was cleaned in acetone in an ultrasonic bath. Copper oxidation was removed with a gentle electropolishing treatment.

4.2.2 Two-Layer Gold-on-Alumina Trap

The fabrication of the two-layer, gold-on-alumina trap (whose layout was described in Sect. 4.1.2.1), was carried out by a series of external partners. Etching and assembly were carried out in our research group.

Fabrication of the two layer trap consists of six fabrication steps: geometrical definition of trap structure with laser cutting, gold evaporation, gold electroplating, electrical definition of electrodes through laser ablation, completion of electrical insulation by mechanical drilling of holes, wafer dicing. The individual steps are described in more detail in the following sections, while an overview of these steps is depicted in Fig. 4.31.

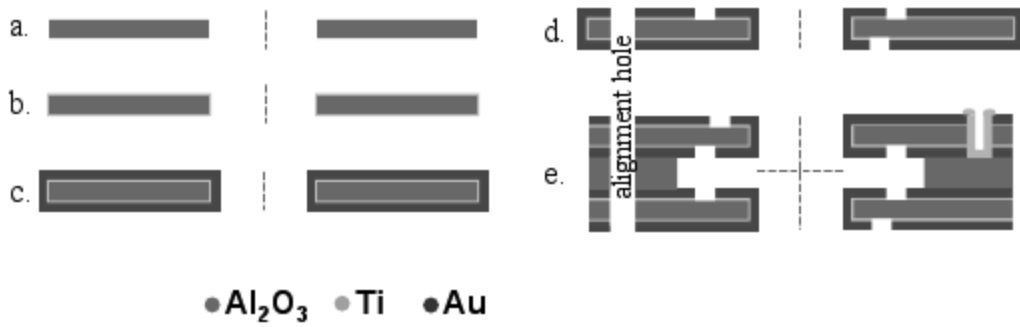


Figure 4.31: Fabrication process of the two-layer gold-on-alumina trap: The Al_2O_3 wafer is a). machined, b). and c). cleaned and coated, and finally, d). laser machined to electrically define electrodes. In e). two wafers are sandwiched with a spacer in between, and held in place with a UHV-compatible epoxy. The microfabricated trap is then ready for packaging.

4.2.2.1 Laser Machining of Alumina Wafers

The wafers for the trap are made from $125\ \mu\text{m}$ thick Al_2O_3 (alumina). Alumina was chosen for its rigidity and ease of machining with lasers.

In the first processing step, blank 2-inch squared wafers (from *Reinhardt Microtech AG*, Wangs, Switzerland) are micromachined using a femtosecond pulsed laser source (*Micreon GmbH*, Hannover, Germany).

Machining defines several structures:

- the central slot: this slot separates the dc (segmented) and radiofrequency sides of each wafer, and allows optical access into the trapping region
- the dc segments: here, cuts are made $200\ \mu\text{m}$ into the wafer (perpendicular to the slot described above). In this way, individual dc fingers are produced
- the notches in the radiofrequency electrode are defined ($60\ \mu\text{m}$ deep): these notches increase the symmetry of the radiofrequency pseudopotential and reduce its modulation along the trap axis

The design avoids blank Al_2O_3 areas. Previous wafer traps have been fabricated with electrodes defined solely by patterning gold on a wafer with a simple slit cut in the substrate, so that the patterned electrodes resided on just one side of the wafer. Gaps between electrodes were therefore composed of a dielectric material. None of these traps were successful in trapping ions, and it is believed that the failure of these traps is due to the uncertainty of the electric potential in these regions.

Unavoidable isolation lines between the electrode segments are shifted more than $100\ \mu\text{m}$ away from the ions position by the extended electrode finger design.

4.2.2.2 Gold Evaporation

The laser cut wafers are first prepared in an ultrasonic cleaning procedure (acetone ($\text{C}_3\text{H}_6\text{O}$), isopropyl ($\text{C}_2\text{H}_6\text{O}$) and Caro's acid (H_2SO_5)) and then with an oxygen plasma cleaning. The blank, laser cut Al_2O_3 wafer is then coated in an electron beam evaporator during a continuous rotation with a declination angle of 45° , so that all exposed surfaces are uniformly covered. This ensures that gold uniformly coats all surfaces of the machined wafers: both sides of the wafer, and the edges of all segments and radiofrequency notches. Following the first metallisation there

Chapter 4. Trap Layout and Fabrication

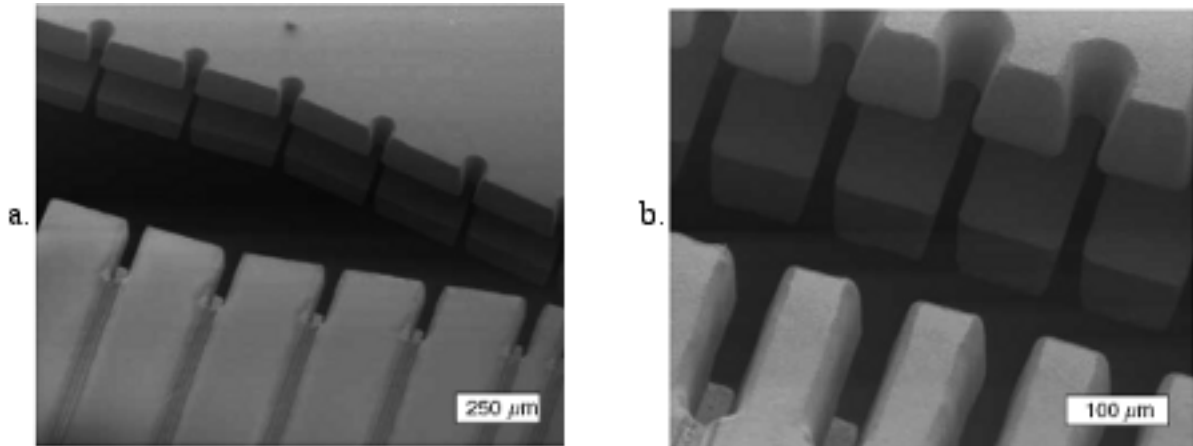


Figure 4.32: Electron microscope images of the bare laser-machined alumina wafers in the a). storage and transition regions and b). processing zones. The laser cutting procedure introduces a slight tapering to the shapes of the fingers, with the narrower side on the outer (compared to the inner) face of the wafers.

is a 50 nm titanium adhesion layer and 500 nm gold layer (*Laser Zentrum Hannover*, Hannover, Germany). Atomic force microscopy then verified a surface roughness of less than 10 nm. The thin gold layer is then used as a seed layer for electroplating.

4.2.2.3 Electroplating

The gold evaporated wafers were then sent to an external company (*MicroGaN GmbH*, Ulm, Germany) for gold electroplating, from which a uniform thickness of 3-5 μm over all wafer surfaces was requested. Following the electroplating procedure, electron microscope analysis revealed a gold surface thickness of 10-15 μm .

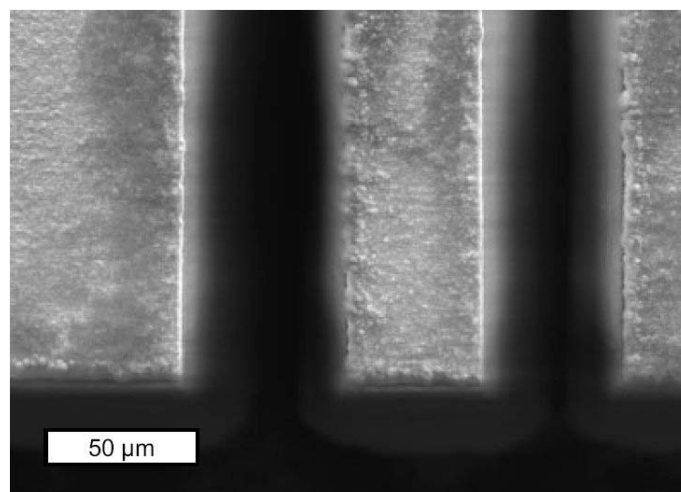


Figure 4.33: Electron microscope of several electrode fingers after electroplating. The gold coating is smooth, with a slight excess of material seen along the electrode edges. Electrode edges and protrusions support a higher current density and allow a faster deposition rate, therefore plating metal is preferentially attracted to these areas.

4.2.2.4 Electrical Insulation

The uniformly covered gold wafer now requires definition of discrete electrodes by removal of some of the gold.

Track Cutting This next crucial step electrically defines the electrodes by laser machining insulating tracks between electrodes. The machining of these tracks is carried out on both sides of the wafer. In this way, all dc segments, ground planes and radiofrequency electrodes are defined. The laser cuts are made with a pulsed femtosecond laser (*Micreon GmbH*, Hannover, Germany), which can cut through 3-5 μm thick gold down to the alumina substrate: the wafer with a considerably thicker layer (10-15 μm , see above) proved considerably more difficult to laser machine. The width of the insulating tracks is 30 μm (when separating dc electrodes), or 50 μm (when separating radiofrequency electrodes from dc electrodes). Two passes are made along each insulating track.

Hole Drilling After laser cutting of gold tracks separates electrodes on the two sides of the wafer, the electrodes are still electrically connected through the edge of the wafer, this being due to the fact that the wafer was coated with gold on all exposed surfaces. This means that the electrodes are electrically shorted as the coated surfaces wrap around the wafer from one side to the other, necessarily (and desirably) passing over all the cut surfaces on the edges of the wafer. In order to complete the insulation of the electrodes, the substrate, together with the gold layer, has holes drilled at the extremity of the laser cuts which geometrically defines different electrodes. In this way, the insulating tracks on either side of the wafer are joined by a mechanically drilled hole (cf. Figs. 4.20d, 4.34). The dc finger segments are gold plated completely from all sides, this being verified by electron microscopy analysis.

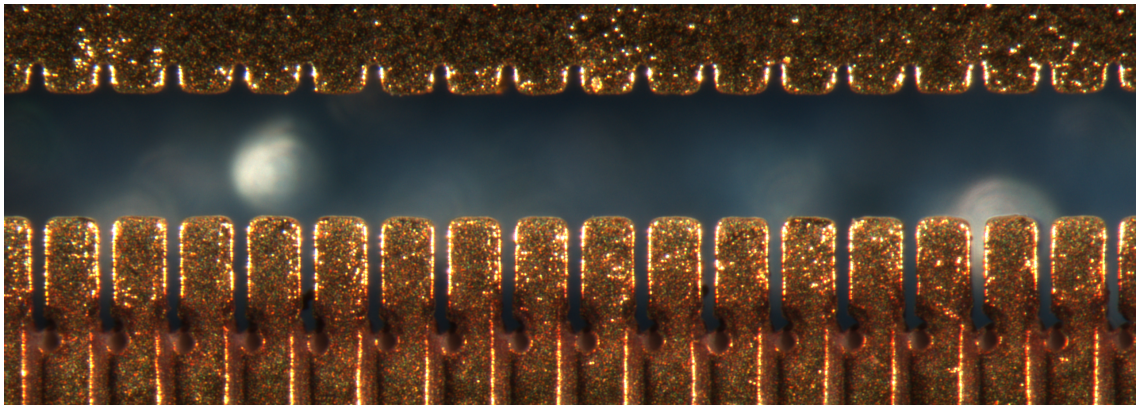


Figure 4.34: Detail of the electrodes after electroplating and electrical insulation through track cutting and hole drilling. The tracks between the electrode fingers in the lower section of the image show a slight sheen of reflective gold material, indicating that not all gold has been removed to leave bare alumina. The holes drilled as a final step in the electrical isolation procedure can also be seen – several holes were drilled at each site.

4.2.2.5 Chip Dicing

To this stage, all traps have been part of one large alumina wafer, for ease of handling during fabrication. Now that all processing steps are complete, the wafer can be diced into component chips.

Chapter 4. Trap Layout and Fabrication

4.2.2.6 Etching

Unfortunately, machining through the gold layer to form insulating tracks was not entirely successful. After cutting with the femtosecond laser, there should be a track of bare alumina, which will separate electrodes on the wafer sides. However, visual inspection of the wafers revealed a light gold cover in some tracks (cf. Fig. 4.34), and electrical testing revealed shorts between a number of electrodes. The failure of the laser machining to completely cut through the gold layer is likely due to the considerably increased thickness of the gold layer. Microscope images indicated that the gold material in the insulating tracks was minimal. This material was removed from the wafers with a gentle gold etch..

Gold can be etched using *aqua regia*. Aqua regia (Latin: royal water) is a (fresh) mixture of nitric acid and hydrochloric acid, and is one of the few reagents that can dissolve gold (a “royal”, or noble, metal). Aqua regia is usually composed of hydrochloric acid (HCl), nitric acid (HNO₃) and water in a 6:2:5 ratio. A 6:1 mixture of 32% hydrochloric acid and 65% nitric acid was used. Additionally, a small amount of Triton X-100 (C₁₄H₂₂O(C₂H₄O)_n, n = 9 – 10)), a non-ionic surfactant which assists the aqua regia in penetrating detailed structures, was added.

The etching procedure removed the gold between the electrodes, removing electrical shorts.

4.2.2.7 Assembly

The two wafers which form the trap are then assembled with a ceramic spacing wafer between, and fixed together using a UHV-compatible epoxy (Epotek, 353-ND). This epoxy requires heat curing, and becomes extremely fluid when heated. An alignment accuracy of better than 5 μm was achieved. The assembled trap is then ready for packaging (mounting on a carrier), and is depicted in Fig. 4.35.

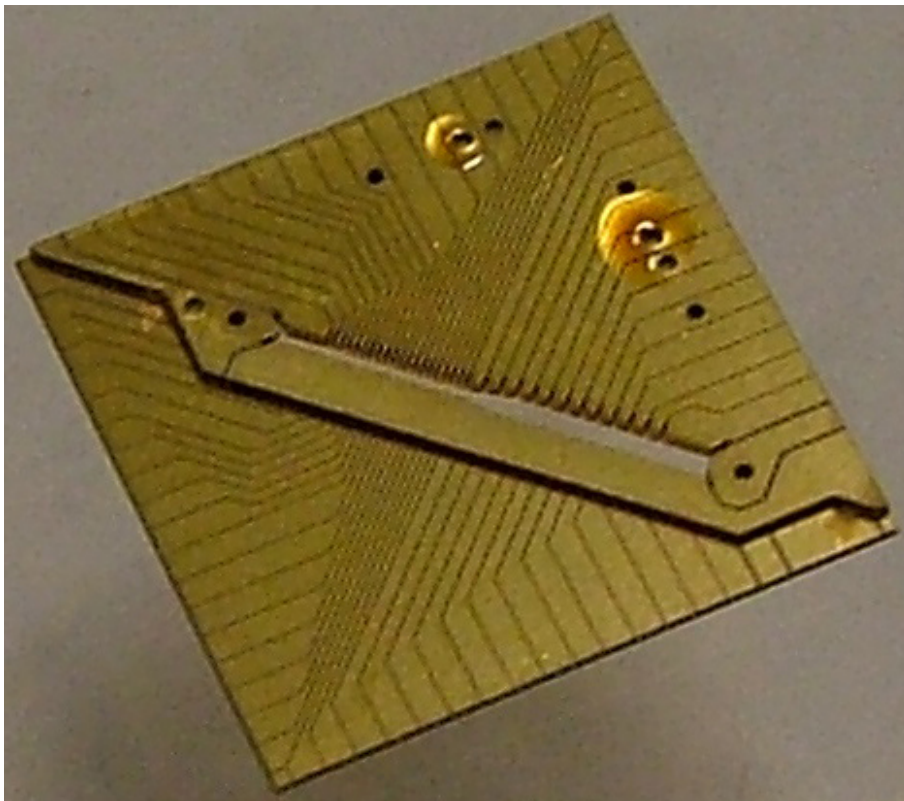


Figure 4.35: Photograph of the assembled linear two-layer trap.

Chapter 5

Experimental Setup

This chapter describes the hardware equipment necessary to operate the ion traps presented in the previous Chapter. This includes the vacuum system, the electrical mounting, the control system and all required lasers and optics.

5.1 Trap Mounting Hardware and Accessories

During this work, two trap setups have been used. They are mounted in two separate apparatus, reflecting the respective needs. Two different mounting schemes have been implemented. The first mounting scheme allows easy and rapid trap exchangeability, while the second mounting scheme tests integrated mounting and rf filtering circuitry fabricated using hybrid thick-film technology. The following subsection describes the mounting and electrical connections used in these two schemes.

Trap Mounting and Electrical Connections

Surface Trap *Bastille*

The ion trap used in experiments described in this thesis was the macroscopic trap *Bastille*, which is described in Chapter 4. *Bastille* is glued into the cavity of a 100-pin ceramic (alumina A440) pin grid array (CPGA) (e.g. *Kyocera*, KD-P85989-A) with an internal (die) cavity of $0.47'' \times 0.47''$ ($11.9 \text{ mm} \times 11.9 \text{ mm}$) and depth $0.04''$ ($\sim 1 \text{ mm}$) and package outer diameter of $1.32'' \times 1.32''$ ($33.5 \text{ mm} \times 33.5 \text{ mm}$). While many pin grid array packages are commercially available, most are used in conventional electronics applications and are composed of plastic, which is unsuitable for ultra-high vacuum (UHV) applications.

Bastilles electrodes are electrically connected to the CPGA by making wire bonds between *Bastille* and the bond pads on the CPGA. Each electrode is wire-bonded to several bond pads, so that multiple electrical connections exist to each electrode. This allows testing of applied voltages, and backup connections, in case any single wire bond becomes damaged. Fig. 5.1a shows *Bastille* mounted in the CPGA, after wire-bonding.

The CPGA holding *Bastille* is then plugged into an assembly consisting of pin receptacles (*Mill-Max*, 0672-3-15-15-30-27-10-0) whose bulkhead ring is sandwiched between holders fabricated (initially from alumina (ADS-995: nominal 99.5% Al_2O_3), but later) from the UHV compatible plastic (*Dupont*, Vespel SP-1). Alumina holders proved too fragile, so the more resilient Vespel was used. This assembly is depicted in Fig. 5.1b.

Each pin receptacle is soldered (using UHV-compatible solder (*Kester*, 275 [Sig06])) to the exposed end of a Kapton coated wire. These wires terminate at a single in-vacuum subminiature-

5.1. Trap Mounting Hardware and Accessories

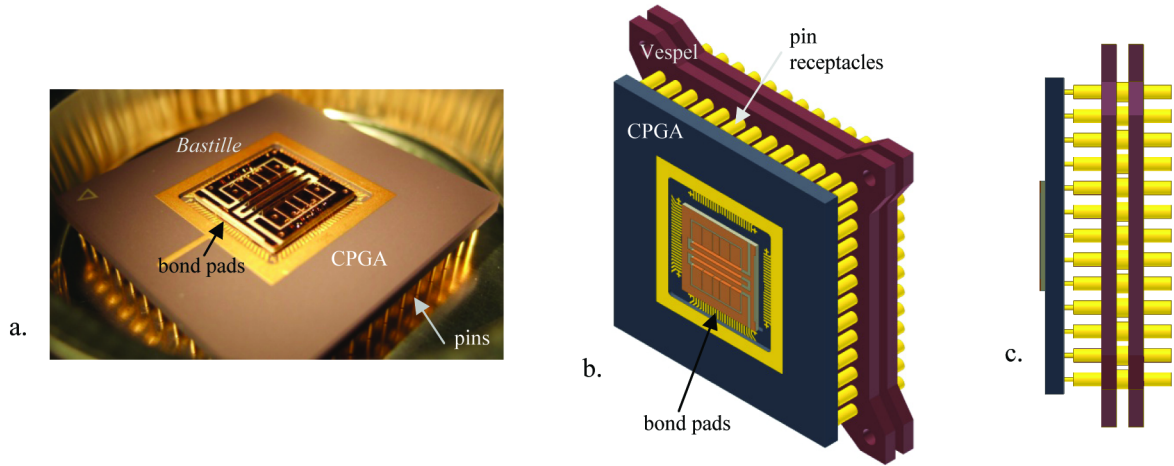


Figure 5.1: a). *Bastille* mounted in CPGA. b). Schematic of trap, CPGA, pin receptacles and Vespel pieces. c). side view of the mounting assembly, showing the bulkhead rings of the pin receptacles sandwiched between the Vespel pieces.

D socket, which plugs into the vacuum side of an electrical feedthrough fitted with a 25-pin subminiature-D connector.

Outside the vacuum chamber, the electrical connections immediately encounter a “filter box”, which provides low-pass filtering (through an RC circuit, with $R = 160 \text{ Ohm}$ and $C = 1 \mu\text{F}$, resulting in a threshold frequency of 1 kHz) of the voltages applied to the electrodes. Trap electrodes are susceptible to radiofrequency pick-up from the radiofrequency trap drive: a large radiofrequency pickup on segmented electrodes may cause undesirable trapping characteristics. Suppression of this pickup is achieved by placing low-pass filters as close as possible to the trap. The filter box is located directly at the electrical feedthrough and the electrical path length between electrodes and filters is $\sim 30 \text{ cm}$. Better shielding can only be achieved by placing low-pass filters inside the vacuum chamber, as is done in the second experimental setup.

Two-Layer Gold-on-Alumina Trap

The two-layer trap, whose design, fabrication and assembly has been described in Chapter 4, has a novel mounting. It is the nature of segmented ion traps to provide various electrodes at which the appropriate dc control voltages are applied to shape the trapping potential. The more complex segmented-electrode ion traps become, the more dc voltages need to be provided to the control electrodes. Each dc electrode requires individual low-pass filtering to avoid radiofrequency pickup, and most desirable are filters located very close to the electrodes.

Placing the low-pass filters as close as possible to rf sources could be achieved by connecting very small surface mount device (SMD) components onto the electrical connections near the trap carrier. However, as the number of dc electrodes increases and trap sizes decrease, this becomes tedious and undesirable.

For the mounting of the two-layer trap, a different method was developed which sought minimisation of manual assembly and suitability for scaling to large numbers of electrodes. A combined carrier/filter board, fabricated using UHV-compatible thick-film hybrid technology and sintered at high temperature (rendering it vacuum compatible) is used. In this approach, the resistors and capacitors of the low-pass filter are printed onto a ceramic carrier. The filter board/trap carrier is shown in Fig. 5.2. This mounting and filtering technology was designed as part of a collaborative effort within the EU STREP project MICROTRAP. Specifically, the carrier/filter boards were

Chapter 5. Experimental Setup

manufactured by the Hybrid Lab of the Detektorphysik und Elektronik group at the Universität Siegen.

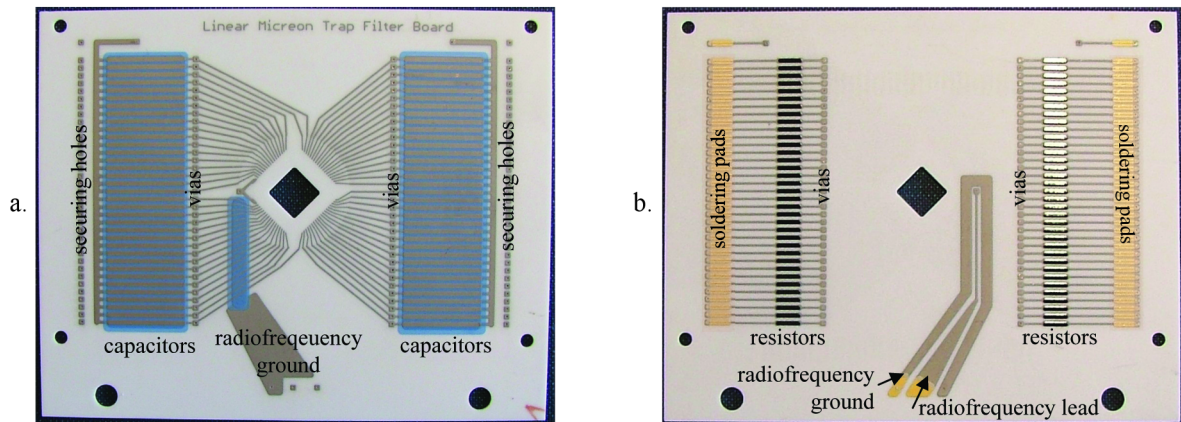


Figure 5.2: Trap carrier with on-board filters. a). Front view of the trap carrier. The trap is mounted above the cutout in the centre. Surrounding the trap are gold bond pads. Wire bonds connect the trap to the bond pads. Electrical wires travel radially to either side. The large rectangular expanses of material on both sides is formed of dielectric paste which is the central (insulating) region of the capacitors. To the left of the central cutout are wires for the radiofrequency. The rectangular block of material to the left of the cut-out isolates the radiofrequency leads from the dc leads. b). Backside view. The large radiofrequency lead is to the right of the cutout. The black regions are the resistors. The gold pads on the outer edges are the soldering pads for the electrical wires.

The carrier/filterboard has a $635\ \mu\text{m}$ thick ceramic substrate. The trap is mounted, and the capacitors (of the low-pass filters) printed, on the front side. The resistors (of the low-pass filters) are printed on the back side. The conducting wires are made of AgPd paste, with gold bond pads (for ease of wire-bonding). From the trap bond pads, conducting wires travel radially outwards to either side, where they encounter a via (electrical connection through layer(s) of a board). From here, the path diverges - on the front side, through a capacitor to electrical ground. The other branch, through a via to the back side, where it passes through a resistor, then along a wire to end at a gold-coated soldering pad to which wires are connected. There are also holes in the ceramic into which wires can be threaded for stress release. The wires then travel to the flange electrical feedthroughs

Capacitors are formed by layering a $20\ \mu\text{m}$ thick dielectric paste between electrodes of AgPd. The dielectric paste has a capacitance of $260\ \text{pF}$ per $30\ \text{mm}^2$: for the filter boards described here a capacitance of $55 (\pm 3)\ \text{pF}$ was chosen (obtained). Resistors are composed of a resistive paste. Resistors can be laser trimmed: once capacitance is measured, and the desired threshold frequency is chosen, the resistors are trimmed to an appropriate value. Trimming involves laser cutting small tracks through the resistive paste, in order to increase the effective length and width of the resistor, and therefore resistance. In this case, a threshold frequency of $1\ \text{MHz}$ required trimming of the resistors to $2.85\ \text{k}\Omega$, and detail of the laser trimmed resistor is shown in Fig. 5.3.

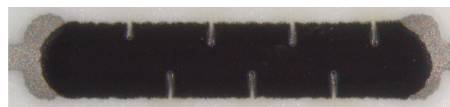


Figure 5.3: Laser trimming of the printed resistor allows precise choice of resistance. The silver regions to either side are the conductive AgPd wires, the black area in the centre is the resistive paste. The small notches cut into the top and bottom of the black resistive paste is the result of laser trimming.

5.1. Trap Mounting Hardware and Accessories

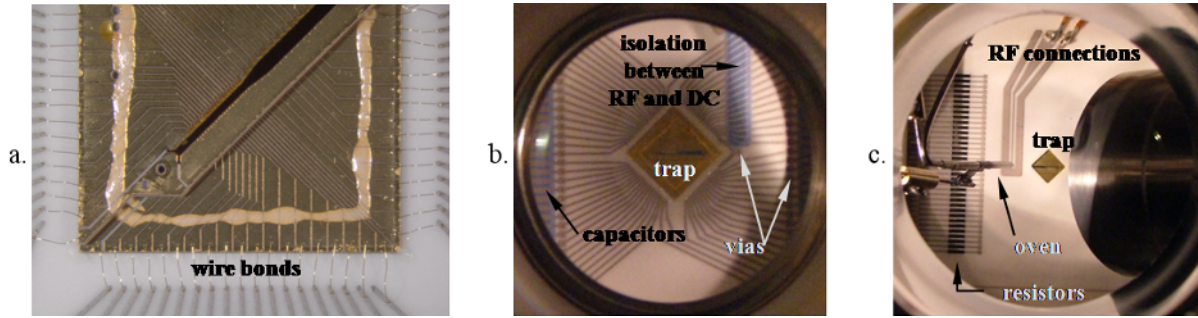


Figure 5.4: Carrier and trap mounted inside the vacuum chamber a). Detail view of the two-layer trap mounted on carrier/filter board. Wire bonds between trap electrodes and carrier bond pads can be seen. b). The carrier and trap mounted inside the vacuum chamber. c). Two-layer trap mounted on carrier/filterboard, inside vacuum chamber. Note the calcium oven, directed towards the trapping volume. Radiofrequency connections extend upwards. To the left side are dc connections, and the resistors of the low pass filters. The dc connections on the right side of the carrier are obscured by the inverted viewport.

The trap mounted on the carrier board can be seen in Fig. 5.4.

Trap Voltage Supplies

Radiofrequency Voltages

The radiofrequency voltage for the trap drive is produced by a signal generator (*Marconi Instruments*, 2022E) and amplified with a radiofrequency amplifier (Mini-Circuits, ZHL-5W-1). The signal generator used has a range of 10 kHz-1 GHz with 10 Hz frequency resolution, and can produce up to +6 dBm output power. The generated radiofrequency signal from the generator passes through an amplifier, via a directional coupler and through a helical resonator of resonant frequency 10.25 MHz. A quality factor of $Q \approx 150$ was measured from the absorption spectrum of the loaded helical resonator. The helical resonator transforms radiofrequency power into high voltage, with very little current [MS59]. Tuning of the frequency to the resonance is achieved by monitoring the back-reflected signal at a directional coupler (located between the amplifier and the helical resonator). Perfect input coupling causes the back-reflected signal to disappear. The output of the helical resonator is fed through dedicated high voltage few-pin electrical feedthroughs, to which Kapton coated UHV compatible high voltage wire is soldered. This wire connects to the CPGA (for *Bastille*) and passes through several wire bonds to connect to the radiofrequency electrode. The radiofrequency feedthroughs are distinct and spatially separated from the static voltage feedthroughs.

Static Voltages

Ion traps with segmented dc control electrodes afford a sophisticated manipulation of a tailored trapping potential. The trapping potential is a result of the voltages applied to the radiofrequency and segmented electrodes. Control of the trapping potential is achieved by applying time-dependent voltages to the segmented dc control electrodes.

Control voltages are provided by two analog output cards (*National Instruments*, PCI-6733) which each provide eight analog output channels with a nominal range of ± 10 V (absolute accuracy of 0.0177% over 24 hours, and an offset of ± 5.933 mV), an update rate of up to 10^6 samples per second (1 MS/s) and 16-bit resolution. A fast update rate is required for electrodes in critical shuttling regions, while electrodes whose voltage is less critical can be provided for with a slower card. An additional analog output card (*UEI*, PowerDAC) provides 32 channels with with a

Chapter 5. Experimental Setup

nominal range of ± 10 V, an update rate of 100 kS/s and a resolution of 16 bits. In total, the current experimental setup has 48 independent dc voltage control channels.

Where needed, amplification of these signals is achieved using a high speed amplifier (Apex, PA85A). This amplifier is chosen as it has an output voltage range of 450 Volts, a slew rate of $1 \text{ kV}/\mu\text{s}$ and a voltage noise of less than $3 \mu\text{V}/\sqrt{\text{Hz}}$. This would allow modification of the amplifier output by 10 volts in $1 \mu\text{s}$.

Calcium Oven

Calcium is delivered to the trap from a small oven loaded with fine grains of calcium in the form of an atomic vapour: at pressures around 10^{-11} mbar and temperatures over 500 K, atomic calcium sublimates at a sufficiently high rate for rapid trap loading. For the specific geometry of the oven in the experiment chamber, dissipating a continuous current of ~ 3.4 A provides the necessary heat for sublimation of atomic calcium in the form of fine grains.

The oven consists of three main components: a thin-walled (1.8 mm diameter) stainless steel tube, with a crimped lower end joined to a stainless steel electrode, a solid stainless steel electrode, and a thin tantalum foil which is spot-welded to each component, linking them. Granulated atomic calcium is filled into the tube to just below the level of the tantalum foil, and tightly packed. Each electrode is soldered to an electrical feedthrough (suitable for high currents). Outside the vacuum chamber, a current source is applied across the two electrical feedthroughs, resistively heating the calcium and ejecting vapourised atomic calcium in a directed beam. A cap with an aperture of diameter ~ 0.5 mm placed over the end of the oven tube achieves further collimation of the atomic vapour beam. The calcium vapour beam passes ballistically through the trapping region, where it can be ionised. More specific details about oven construction can be found in [Rot03, Rus08].

5.2 Vacuum Chamber and Vacuum Pumps

Our experiments seek lifetimes of the trapped ions on the order of a few hours to a few days. For this, an ultra-high vacuum environment (typically with pressures below 10^{-11} mbar) is sought, to ensure that the rate of collisions of the trapped ion(s) with background gas atoms is low. The entire vacuum vessel, consisting of a mounted ion trap, calcium oven, in-vacuum electrical connections, vacuum chamber, vacuum pumps, electrical feedthroughs and viewports is shown in Fig. 5.5. The individual components used for experiments with the *Bastille* trap are now described in detail.

Vacuum chamber

The chamber used to house the ion trap is a DN63CF six-way cross, the trap being located its vertex (cf. Fig. 5.5). Optical access to the trap is provided through three horizontal viewports. One is an inverted viewport whose face is close (~ 5 cm) and parallel to the trap surface. The other two viewports are located on ports whose axis is parallel to the trap axis. The vertical upper arm has an electrical feedthrough which connects the segmented electrodes to dc voltages. The vertical lower arm contains trap mounting hardware and holds the calcium oven. Only materials compatible with UHV environments can be used in trap construction, mounting and electrical connections. Inorganic metals and ceramics are typically UHV compatible, and organic compounds are not. Organic compounds which are UHV compatible include Teflon, Kapton, Vespel, specific glues/epoxies (e.g. *Epo-Tek*, 353ND) and specific solders.

5.2. Vacuum Chamber and Vacuum Pumps

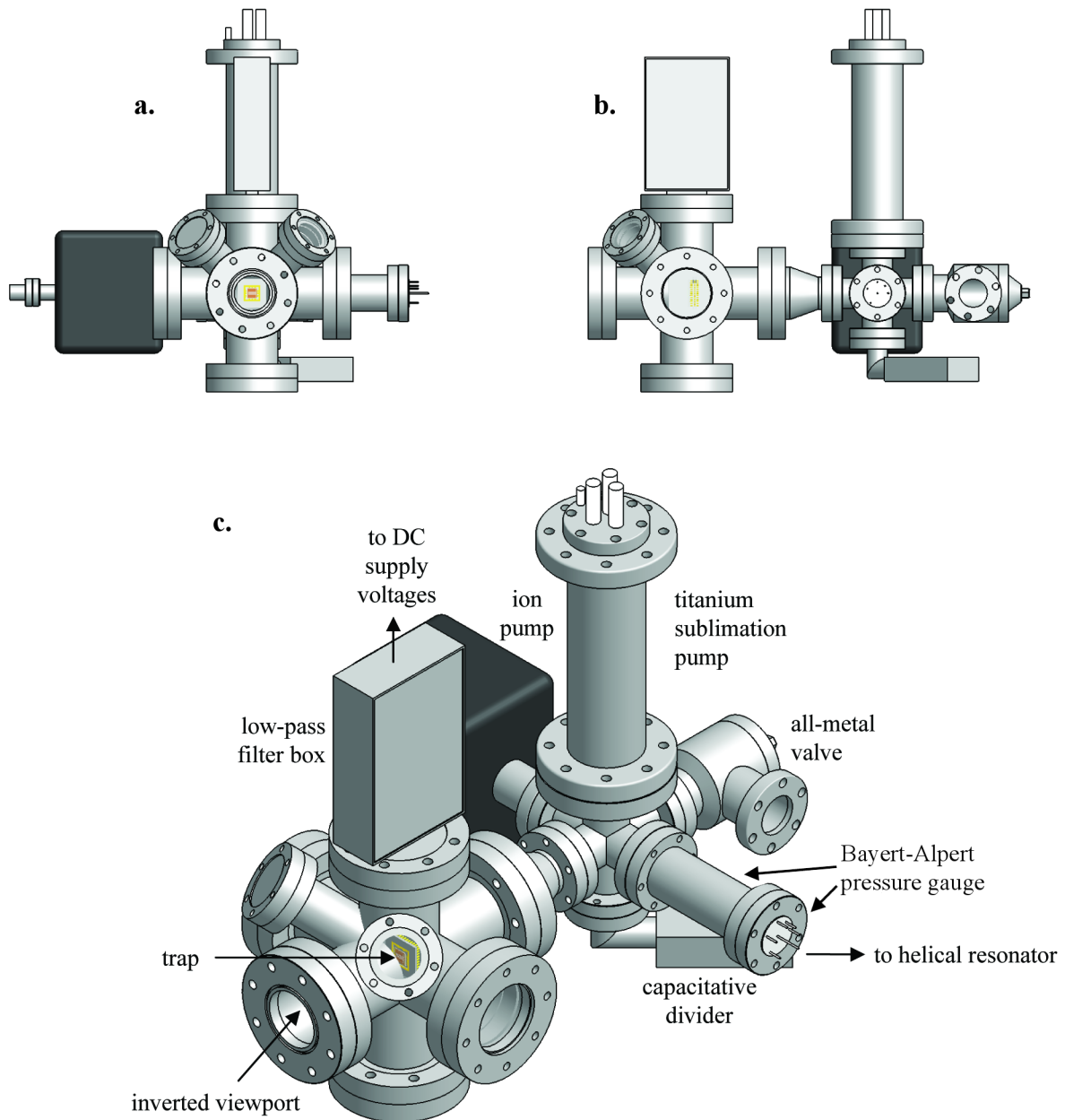


Figure 5.5: Vacuum apparatus for surface trap *Bastille*. a). view from the front, through the inverted viewport, to *Bastille*. b). view from the side. c). isometric view of the apparatus. Electrical connections to dc and radiofrequency electrodes are omitted for clarity.

Chapter 5. Experimental Setup

Vacuum Pumps

The final arm of the six-way cross described above connects via a conical reducer to a DN40CF six-way cross. This cross connects to vacuum pumping and measurement devices, and electrical feedthroughs for connection to rf voltages and the calcium ovens. An ion pump (*Varian*, StarCell 20L/s), and a titanium sublimation pump (*Varian*, 9160050) are attached to the small six-way cross. An all-metal angle valve allows connection to roughing and turbomolecular pumps, or to a residual gas analyser. Measurement of chamber vacuum pressure is achieved with a nude Bayard-Alpert ion gauge.

Achieving Ultra-High Vacuum After the vacuum components have been cleaned (usually with acetone in an ultrasonic bath) they are assembled. The chamber is then pumped down using roughing and turbomolecular pumps. At pressures below $\sim 10^{-6}$ mbar the ion pump may be operated. Finally, to reach the lowest pressures, the titanium sublimation pump is used. The titanium sublimation pumps operates by heating a titanium coated filament until titanium is sublimated and coats the surrounding vacuum chamber walls. The titanium then reacts chemically with the background gas in the vacuum chamber, removing it from the vacuum and bonding it to the walls. The titanium sublimation is activated intermittently, when chamber pressures have (for various reasons) risen above a desirable base operating pressure ($\sim 10^{-10}$ mbar).

The chamber is also baked to remove all water vapour from the stainless steel lattice. Viewports and electrical feedthroughs can generally withstand a maximum temperature of ~ 200 °C, while other components can withstand higher temperatures. First a blind bake (in which the apparatus with blank flanges in place of viewports and electrical feedthrough flanges) at 320 °C, is carried out for approximately one week, the apparatus is then fitted with viewports and electrical feedthroughs and baked at a lower temperature (< 200 °C). Temperatures were always ramped up or down slowly at ± 7 K/hr. Final pressures reached were in the low 10^{-11} mbar range.

Diagnostics The chamber can also be connected to a residual gas analyser (RGA) (*MKS*, e-Vision) via the all-metal valve port. This device allows monitoring of partial pressures in the chamber due to specific elements and compounds. In particular, it can be used for a sensitive leak test with helium gas: suspected leak points can be flooded with helium, and the RGA observed to see if this element is detected.

5.3 Laser Systems

The level scheme for $^{40}\text{Ca}^+$ was shown in Fig. 2.7, and contains the experimentally relevant transitions. Four laser sources are required; a laser at 397 nm to cool and monitor the ions, one at 729 nm to drive the qubit transition, and lasers at 866 and 854 nm to deplete the metastable D-levels. The four laser beams are divided to provide light for the three independent $^{40}\text{Ca}^+$ experiments. Two additional lasers at 422 nm and 375 nm are required for the photoionisation of atomic calcium. These lasers are shared between a number of different experiments in our group and the construction and maintenance of these lasers is an ongoing effort between all group members.

The lasers are located on three different optical tables. The first optical table contains the 397 nm and 729 nm lasers. The 397 nm laser is shared between three experiments: the segmented dc electrode ion trap, the $^{40}\text{Ca}^+$ quantum computation ion trap experiment, and the cavity quantum electrodynamics experiment. The 729 nm laser is currently used only by the linear ion trap and segmented ion trap experiment. The 397 nm and 729 nm lasers are coupled into fibers and sent to our experiment table. The 866 nm and 854 nm lasers are located on yet another laser table. These output of these two lasers is again divided between the three experiments. Beams reach the

trap table through a common optical fiber. The photoionisation lasers at 422 nm and 375 nm are located on a small optical bench. These lasers are shared between the three experiments (but not divided). Again, the two lasers are coupled into a common fiber and sent to the experiment table. The individual laser systems will now be described in more detail.

Laser system at 397 nm

The light at 397 nm laser acts on the $S_{1/2} \leftrightarrow P_{1/2}$ dipole transition and is used for Doppler cooling, state preparation and state detection. It is generated by frequency doubling the light from a Ti:Sapphire (Ti:Sa) laser at 794 nm (*Coherent*, CR-899-21), which is in turn pumped by a 532 nm solid-state laser (*Coherent*, Verdi V10). The Ti:Sapphire laser is frequency stabilised to a reference cavity using the Pound-Drever-Hall (PDH) method [DHK⁺83]. The reference cavity is isolated from temperature fluctuations of the environment by its location in a temperature stabilised vessel. One of the reference cavities mirrors is mounted on a piezoelectric transducer which is used to change therefore the resonant frequency of the cavity. The linewidth of this cavity has been estimated from excitation spectra to be ~ 200 kHz. The frequency-doubling stage is composed primarily of a commercial LBO doubler crystal (*Spectra Physics LAS*, 'Wavetrain'). A schematic representation of the laser setup is shown in Fig. 5.6.

The Ti:Sa is typically operated with ~ 7 W of pump power at 532 nm, which yields 500 mW at 794 nm. After frequency doubling, ~ 50 mW of ultraviolet light at 397 nm is available - this power is divided between three experiments in the laboratory.

Laser light at 397 nm is then passed through an acousto-optical modulator (AOM) which shifts the laser frequency by approximately +160 MHz. This AOM allows both near-resonant (zeroth order) and far-off resonant (first order) light to be coupled into a fiber and then transported to the experiment optical table. Here, the light traverses another AOM (in single-pass configuration) operated at +80 MHz which allows fast on-off switching of the light.

Laser systems at 866 nm and 854 nm

Laser light at 866 nm and 854 nm is used to repump the $D_{1/2}$ and $D_{3/2}$ levels, respectively, back to the $S_{1/2}$ ground state. Laser light at these wavelengths is provided by diode lasers (*Toptica*, DL-100) grating stabilised using the Littrow configuration.

The light from each laser is collimated, passed through an optical diode, and coupled to single mode fibers. Light exiting the fiber is directed to several locations. A schematic representation of these lasers setup is shown in Fig. 5.7.

A small fraction of light is redirected to a branch for frequency tuning and stabilisation. Frequency tuning is achieved by sending light to a photodiode which acts as input to a *Toptica* control box. Here, feed-forward from the scan control to the current control allows a mode-hop free frequency tuning up to 10 GHz at 850 nm. The free-running laser has a linewidth of ~ 1 MHz. For frequency stabilisation, light is directed to temperature stabilised cavities with finesse of $F \approx 10^3$. The light is then frequency stabilised using the Pound-Drever-Hall method, resulting in a laser linewidth of ~ 100 kHz.

The majority of the light is divided among the experiments, with a small amount being sent to a wavemeter for frequency monitoring. The light at 866 nm is sent through an AOM in double-pass configuration, driven at a centre frequency of ~ 200 MHz with a tuning range of ± 10 MHz. This AOM allows both frequency and amplitude tunability, as well as adequate switching (with an attenuation of ~ 40 dB). Stabilization and acousto-optic control of the laser at 854 nm is very similar. Light at 866 nm is then overlapped with light at 854 nm and coupled into a single-mode fiber which goes to the experiment table.

Chapter 5. Experimental Setup

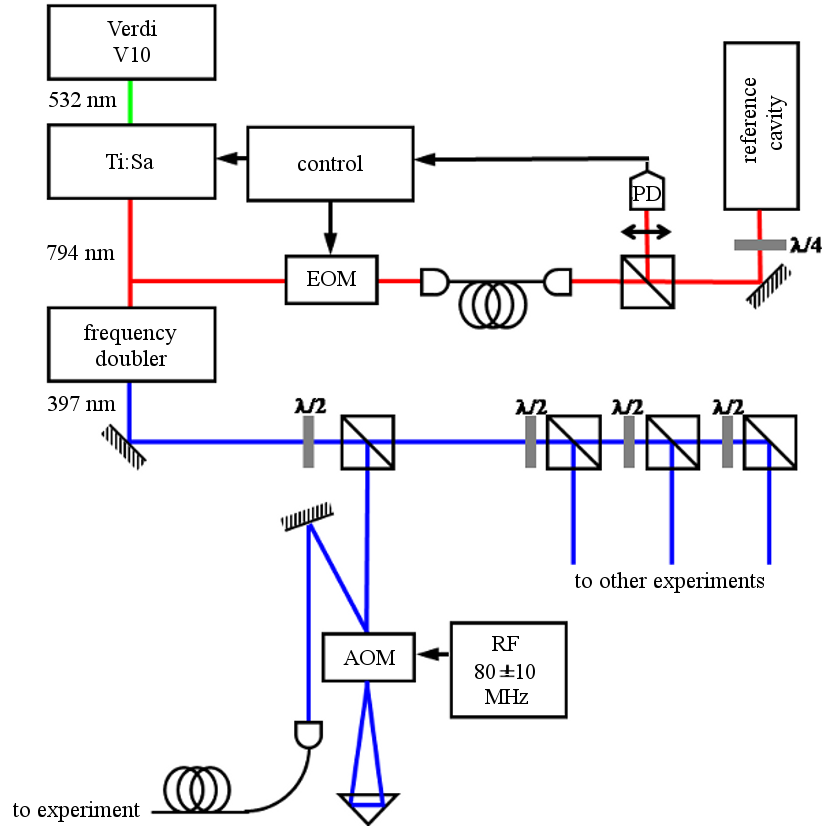


Figure 5.6: Schematic setup for the 397 nm laser. The laser light at 532 nm from a diode-pumped solid state laser (*Verdi*, V10) is used to pump a Ti:Sa ring laser (*Coherent*, CR-899-21). The light at 794 nm is then frequency doubled and divided into several branches. On one of the branches, the frequency of the light is shifted by +160 MHz, whereas in another branch the frequency of the light is shifted by -320 MHz. The light of this beam is coupled to separate single-mode fibers going to the experimental table.

Laser systems at 422 nm and 375 nm

Diode lasers (*Toptica*, DL100) at 422 nm and 375 nm enable photo-ionisation of atomic calcium in a two-step process [Rot03]. Light at 423 nm excites atomic calcium to the $4p^1P_1$ state, from here, light at 375 nm ionises the atom. These lasers are grating stabilised using the Littrow technique. While the frequency of the 375 nm laser is not critical, tuning of the 422 nm laser frequency is achieved by driving a piezoelectric transducer acting on the grating. The transition is collision broadened to about 1 GHz. The 422 nm laser is not stabilised but free-running.

Laser system at 729 nm

Light at 729 nm is used to drive the narrow $S_{1/2}$ to $D_{5/2}$ quadrupole transition. This light is produced by a very narrow band Ti:Sapphire laser (*Coherent*, CR-899-21) which is also pumped by a solid-state laser (*Coherent*, Verdi V10). The light at 729 nm is frequency stabilised using a PDH-locking scheme. The short-term (~ 1 s) linewidth is ~ 1 Hz, and this stability is achieved by locking to an evacuated and temperature stabilised (sub- μ K) high-finesse cavity ($F \approx 4 \times 10^5$) and by feeding back to both the laser cavity via a piezoelectric transducer, and additionally to an intra-cavity electro-optical modulator [Chw09].

Using a pump power of ~ 7 W at 532 nm, the Ti:Sa typically outputs 700 mW which, again, is shared between a number of experiments. Light is transferred to the experiment table via a single-mode fiber. The ion is illuminated with a power of $\sim 850 \mu$ W.

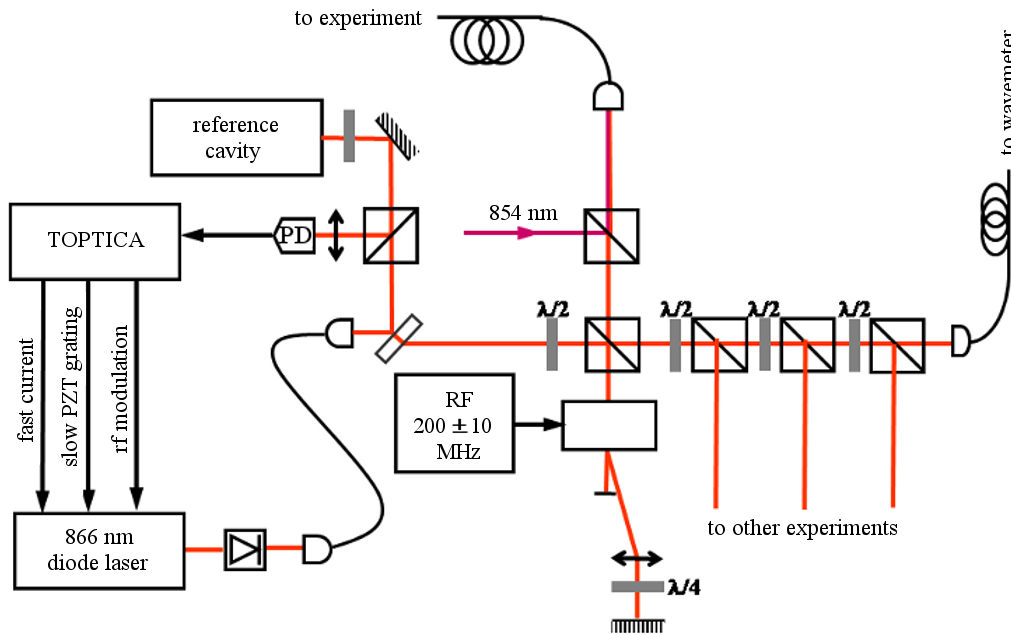


Figure 5.7: Schematic setup for the 866 nm laser. The setup for the 854 nm laser follows a similar scheme and for clarity those details are not reproduced here. The laser light from a diode laser running at 866 nm (*Toptica*, DL100) passes by an optical diode and is coupled to a single-mode fiber. The output of the fiber is divided amongst six branches. One branch is used for frequency stabilisation of the laser using the PDH scheme, while another is used for absolute frequency measurement in a wavemeter. The remaining four branches are allocated to the various experiments running in the laboratory. The experiments described in this thesis made use of one branch: a resonant 866 nm beam. The light of these beams is coupled to separate single-mode fibers going to the experimental table.

Frequency Calibration

Initially, wavelengths were measured using custom-built wavemeters with a relative precision of $\sim 10^{-7}$ [Bla00], using a temperature stabilised helium-neon laser as a reference. A commercial unit (*HighFinesse*, WS7), with relative accuracy of $\sim 10^{-7}$ (60 MHz absolute accuracy) has replaced these wavemeters. The wavemeter accuracy allows identification of the correct TEM₀₀ mode of the reference cavities.

5.4 Optical Access and Detection

Optical Access

The chamber, with viewport and laser beam directions, is shown in Fig. 5.8. The six-way cross with the trap at its vertex has four viewports which are used for optical access: three ports are used for laser beams and a final port for detection of atomic fluorescence. The trap defines the coordinate system, and is mounted in the vacuum apparatus such that the axes of the viewports coincide with the coordinate system. The x -axis of the trap is defined along the radiofrequency null. The y -axis is the direction perpendicular to this and parallel to the surface of the trap. The z -axis is the normal to the surface of the trap (and perpendicular to x - and y -axes). The axes of the vacuum ports coincide with the x -, y -, and z -axes of the trap. Looking directly at the surface trap through the inverted viewport (whose face is ~ 5 cm from the trap surface) is defined as the z -axis (cf. Fig. 5.8c). Most laser beams enter and exit through DN63CF ports on the x -axis: from the left, the 397 nm, 866 nm and 854 nm beams enter the chamber. Photoionisation (422 nm and 375 nm)

Chapter 5. Experimental Setup

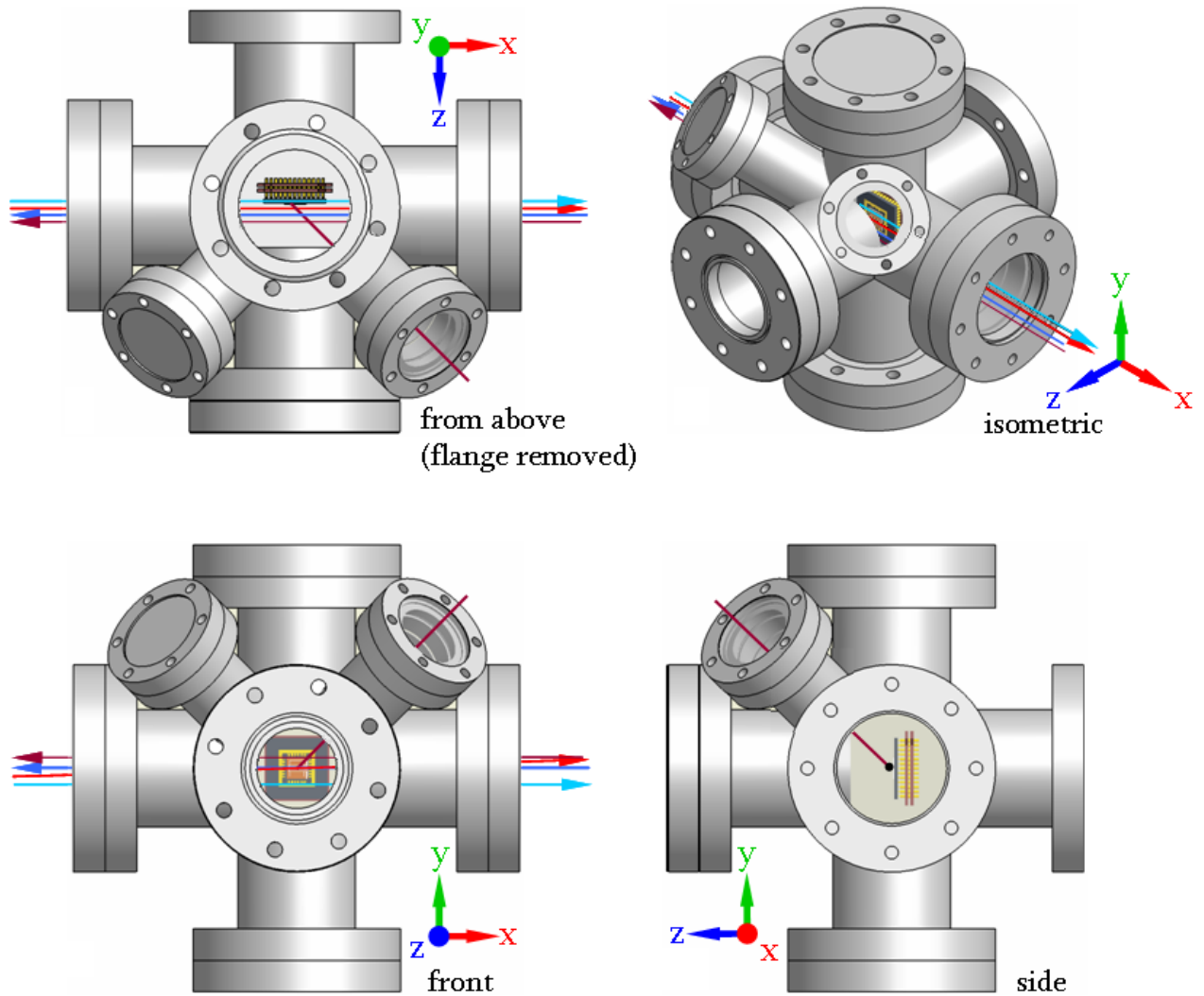


Figure 5.8: Vacuum chamber (without vacuum pumps), showing optical access. Laser beams at 397 nm and 866 nm pass from the left viewport across the surface of the trap (parallel to the trap axis) and exit at the right viewport. The 397 nm beam can be overlapped or separated from the 866 nm beam and pass at a slight oblique angle to the trap axis (in the xy -plane). Laser beams 729 nm, 375 nm and 422 nm also travel parallel to the trap axis, from the right port to the left. The port with face perpendicular to the axis defined by the equation $x = y = z$ can be used for optical access, and has been used for the beam at 729 nm. This beam does not leave the vacuum chamber: the beam is incident on the trap.

5.4. Optical Access and Detection

and 729 nm beams enter from the right. The Doppler cooling and detection beam at 397 nm has two possible directions: incident on the ion(s) at a slight angle to the x -axis, (in the xy -plane) or parallel to the x -axis. Finally, a DN40CF viewport parallel to the axis defined by the equation $x = y = z$ allows access along the (1,1,1)-direction: this port has sometimes been used for 729 nm light, however, beams incident through this port will be incident on the trap and will perturb the trapping potential by charging due to photoemission. All viewports are anti-reflection coated for 397 nm and 729 nm.

Detection

Imaging and state detection of ions is carried out either with an electron-multiplied charge-coupled device camera (EM-CCD) or with a photomultiplier tube (PMT). Fluorescence light at 397 nm is imaged using a custom-made lens with $f/\# = 1.7$, $NA = 0.28$ and focal length 67 mm onto a camera and photomultiplier tube (cf. Fig. 5.10).. Narrow linewidth spectral filters are used in front of the both the PMT and CCD in order to filter the photoionisation beams at 375 nm and 422 nm, the repumper beams at 854 nm and 866 nm, light at 729 nm and ambient light. Two or three filters (*Semrock*, Rochester, New York) are used in front of the camera and the PMT:

model number	centre wavelength (nm)	bandwidth (nm)	average transmission over bandwidth	transmission at 397 nm
FF01-377/50-25	377	50	> 85 %	93.23 %
FF01-386/23-25	836	23	> 90%	92.15 %
FF01-417/60-25	417	60	> 90%	95.26 %.

In front of the PMT the FF01-386/23-25 and FF01-417/60-25 filters are used in combination, which results in a bandwidth of 13 nm centered around 393 nm, with transmission at 397 nm of 87.78%. In front of the CCD camera three filters are used: two FF01-377/50-25 filters and one FF01-417/60-25 filter. This results in a bandwidth of 17 nm centered around 395 nm, with transmission at 397 nm of 82.96%. The use of three filters suppresses light with wavelengths between 300 and 345 nm, and between 405 and 1000 nm, to extremely low transmission levels, as depicted in Fig. 5.9.

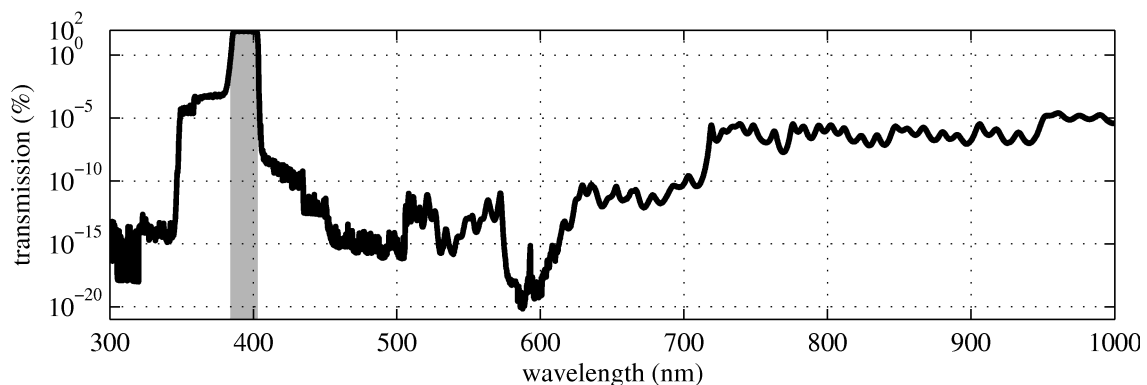


Figure 5.9: The combination of two FF01-377/50-25 filters and one FF01-417/60-25 filter (*Semrock*) result in a bandwidth of 17 nm centered around 395 nm, with transmission at 397 nm of 83%. Transmission is strongly suppressed at wavelengths from 300-345 nm, and from 405 to 1000 nm.

The camera used is an electron-multiplied charge-coupled device (EM-CCD) (*Andor*, iXon^{EM}+ DV885 JCS-VP) with 1004×1002 pixels of $8 \mu\text{m}$ pixel size (image area: $8 \text{ mm} \times 8 \text{ mm}$). At 400 nm, the quantum efficiency is $\sim 40\%$. The camera is typically operated at a temperature of -65°C .

The photomultiplier tube (*ET Enterprises*, 9111) consists of a bialkali photo cathode which is specified to have a quantum efficiency of 28% at 397 nm. The fluorescence from the ions is collected

Chapter 5. Experimental Setup

by a custom-built microscope objective (*SillOptics*, Germany) which images the trap centre to a focal plane 32 cm away from the objective. At this point, four adjustable blades (*Owis*, Spalt 40) serve as a diaphragm to reduce unwanted stray light.

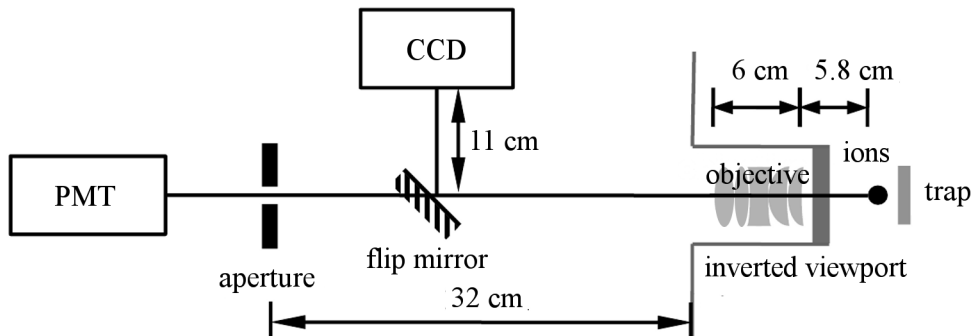


Figure 5.10: Detection schematic: atomic fluorescence at 397 nm passes through an objective (located 58 mm from the ions) and travels to either the CCD camera or photomultiplier tube. Slit apertures in the PMT path reduce stray light. Double filters in front of both CCD and PMT give a transmission of light at 397 nm of 88.8% with a bandwidth of 17 nm (centered around 395 nm).

5.5 Experimental Control

Hardware components are controlled by a computer using software self-written in LabView (platform and development environment for a visual programming language from *National Instruments*). Fig. 5.11 shows the different hardware components and their interconnection.

Control voltages to segmented dc electrodes or to acousto-optical modulators (used to control relative laser frequencies and intensities) are provided by analog output cards described in Subsect. 5.1. Voltages are then set via the LabView interface. Voltage ramps can also be programmed and launched on a trigger signal. For the sake of speed, these programs are written in C.

Manipulation of the qubit transition at 729 nm requires the provision of various phase-coherent and amplitude-shaped radiofrequency pulses. While this level of control was not required for experiments described in this thesis, it will be used in future experiments. To this end, a versatile frequency source (VFS) (detailed information about the development and operation of the VFS is documented in [Pha05, Sch08]) has been incorporated into the experimental hardware. The versatile frequency source provides two separate radiofrequency outputs which can provide up to sixteen different frequencies in each experimental cycle. A field programmable gate array (FPGA) controls a direct digital synthesis (DDS), which outputs frequency precise, phase coherent radiofrequency pulses. The FPGA also controls a digital to analog converter (DAC), which provides amplitude modulation. The DDS and DAC signals are combined in a variable gain attenuator (VGA), to provide a phase-coherent amplitude-shaped radiofrequency pulse. Typical rf pulse lengths required are 1 μ s to 100 ms, and the VFS provides this with a frequency resolution of about 0.1 Hz.

The variable frequency source also provides eight logic inputs (trigger signals) and sixteen logic (TTL) outputs. The timing resolution of 10 ns allows precisely timed digital signals.

Lasers used to manipulate the state of the ion are modulated in frequency and phase by AOMs which transfer frequency and phase information from the radiofrequency to the optical domain, with high bandwidth. In the experiments described in this thesis, relative laser frequencies (for the 397 nm and 866 nm lasers) and intensities (397 nm, 866 nm, 854 nm, 729 nm lasers) were controlled

5.5. Experimental Control

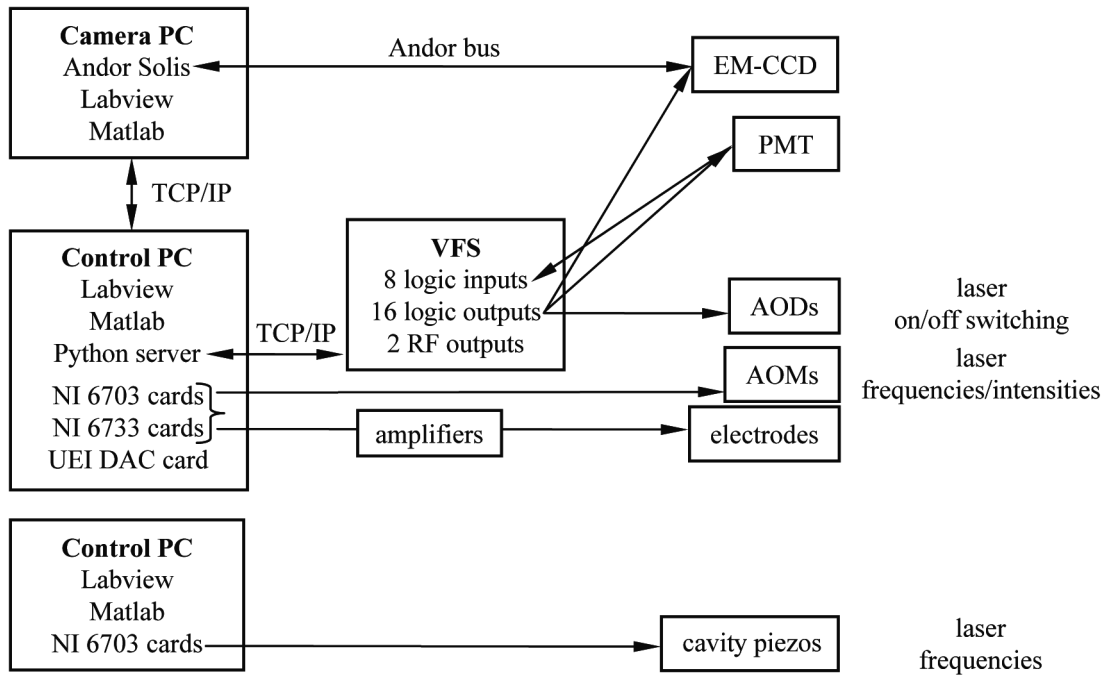


Figure 5.11: The experiment is controlled by software written in LabView running on three computers: one controls the majority of the experimental hardware and interfaces with the versatile frequency source (VFS), and another controls the absolute frequency of lasers via modification of cavity piezos. A third computer controls the CCD camera. This sketch depicts the individual hardware and software components and their interconnection.

by AOMs which were, in turn, controlled by analog output cards (*National Instruments, PCI-6703*). The absolute frequency of lasers (397 nm, 854 nm, 866 nm and 729 nm) is controlled by modification of the voltages applied to the piezoelectric transducers on each lasers reference cavity. This control is via an independent control computer.

The EM-CCD is controlled by an independent computer via an *Andor* bus, and *Andor Solis* is the camera control and analysis software platform. This computer communicates with the primary control computer via TCP/IP. Triggering of the EM-CCD is controlled by a trigger signal from the VFS. Readout of PMT data is performed with the counter present on one of the *NI-DAQ* boards (*PCI-6733*). Any additional digital outputs not requiring switching within a sequence are provided by digital outputs on the previously mentioned analog output cards.

Chapter 6

Experimental Results

This Chapter describes the experimental results obtained using surface trap *Bastille*. First, a method is described which uses long chains of ions to characterise the trap potential. This method is then applied to a long string of almost-equally spaced ions. Such a string may find application in a recent proposal of quantum computing. Next, the results of a series of experiments demonstrating the deterministic reordering of a string of ions in a linear surface trap are presented. Deterministic reordering is carried out in two ways, by moving the trap potential through either a two-dimensional path akin to a “three-point-turn”, or by rotating the weak trap axis around a stationary trap potential minimum, in a movement similar to a “pirouette”. The method by which this deterministic reordering of ions in a linear surface trap is achieved is then generalised to two-layer linear traps. This generalisation which may find application in a wide range of current traps.

6.1 A Long, Almost-Evenly Spaced String of Ions

While the Cirac-Zoller quantum computation proposal [CZ95] utilises a string of ions in a harmonic potential, this method becomes inefficient for large numbers of ions, as either the inter-ion spacing becomes too small for individual addressing of ions with a laser beam, or the axial trap frequency is too low for useful computation. One idea to circumvent these limitations is a quantum , or a segmented-electrode ion trap, which imagines a series of interconnected individual axial potentials created by segmented dc electrodes [KMW02] (cf. Subsect. 2.1.3).

A recent publication proposes a new approach to ion quantum computation [LZI⁺09]. One of the crucial components of this scheme is the use of an anharmonic axial trap potential provided by static electrode potentials which can stabilise a single linear crystal containing a large number of ions. The proposal considers an array of 120 nearly equidistant ions (inter-ion spacing distance of $\sim 10 \mu\text{m}$) with the central 100 qubit ions used for coherent quantum gate operations, and the ten ions at each edge continuously laser cooled.

The segmented electrode geometry of *Bastille* can be used to realise an anharmonic axial trap potential. To obtain an equally spaced string of ions, the axial trap potential required is quartic with a small quadratic component. Fig. 6.1a shows a CCD image of a long ion string, with the number of ions here being $N = 43$.

The electric field from a particle with charge Q at a distance r is given by:

$$\vec{E}(r) = -\frac{Q}{4\pi\epsilon_0} \frac{1}{r^2} \vec{r}, \quad (6.1)$$

where ϵ_0 is the electrical permittivity of free space. The ions act as a measurement probe, and their inter-ion spacing can be used to reconstruct the axial dc electric potential along the ion string. This process is carried out in the following steps.

6.2. Long Ion Strings as Electrical Field Probes

First, from a CCD image (cf. Fig. 6.1a) of the ions is taken. A several pixel high region of this image selected, and an axial brightness profile is calculated by summing the the brightness over the pixel columns (vertically). To this, a polynomial curve is fit, and the positions of the ions (Fig. 6.1b) are determined to be at the peaks of the polynomial fit. From this, the inter-ion spacing is calculated (Fig. 6.1c), and is then used to calculate the electric field arising from the trap potential E_{ext} .

Each ion i in the crystal experiences a force F_{tot} with two components, the external electric field $E_{\text{ext}} = -\nabla V_{\text{ext}}$ arising from the trap potential, and the Coulomb repulsion from other ions in the string $E_{\text{ions}, i \neq j}$:

$$\begin{aligned} F_{\text{tot},i} &= (E_{\text{ext}} + E_{\text{ions}, i \neq j}) \cdot Q \\ &= (-\nabla V_{\text{ext}} + E_{\text{ions}, i \neq j}) \cdot Q. \end{aligned} \quad (6.2)$$

Along the axis defined by the linear string of ions, the electric field arising from the ions' mutual Coulomb repulsion is given by:

$$E_{\text{ions}, i \neq j} = \sum_{i \neq j} \frac{Q}{4\pi\epsilon_0} \frac{1}{(x_i - x_j) |x_i - x_j|}.$$

The ions are stationary in the crystal, so the total force is zero. The external potential V_{ext} is therefore given by:

$$\begin{aligned} V_{\text{ext}} &= \int E_{\text{ions}, i \neq j} dx \\ &\approx \sum E_{\text{ions}} \cdot \Delta x_i \end{aligned}$$

where Δx_i is the inter-ion spacing.

Fig. 6.1d depicts the electric potential along the ion string, as calculated from the electric field derived from the inter-ion spacing depicted in Fig. 6.1c.

In the next section, this method of field measurement from the inter-ion spacing of an ion crystal is used as a probe of the effects of individual electrodes or sets of electrodes. Ion chains such as the long, almost-evenly spaced ion string experimentally realised and depicted here may find application in the aforementioned proposal.

6.2 Long Ion Strings as Electrical Field Probes

Characterisation of a new microtrap involves measuring the trap parameters, for example, the trap frequencies, and comparing the experimentally determined values with those of numerical simulations. While in traditional traps only the trap frequencies at one position are of interest, segmented traps allow placement of the ion along an extended axial region, and hence the potential over this range needs to be understood. This can be achieved by observing a single ion in different trap regions. However, when the axial potential can be made comparatively flat so that long strings of ions can be held in the trap, the spatial potential can also be inferred from the ion positions in the string. In this section, results are presented which use long strings of ions to characterise the electric field of the segmented linear ion trap *Bastille* over an extended region.

As presented in the previous Section, the inter-ion spacing of a string of ions can be used to reconstruct the trap potential along the axis of the ion crystal. Using long strings of ions and

Chapter 6. Experimental Results

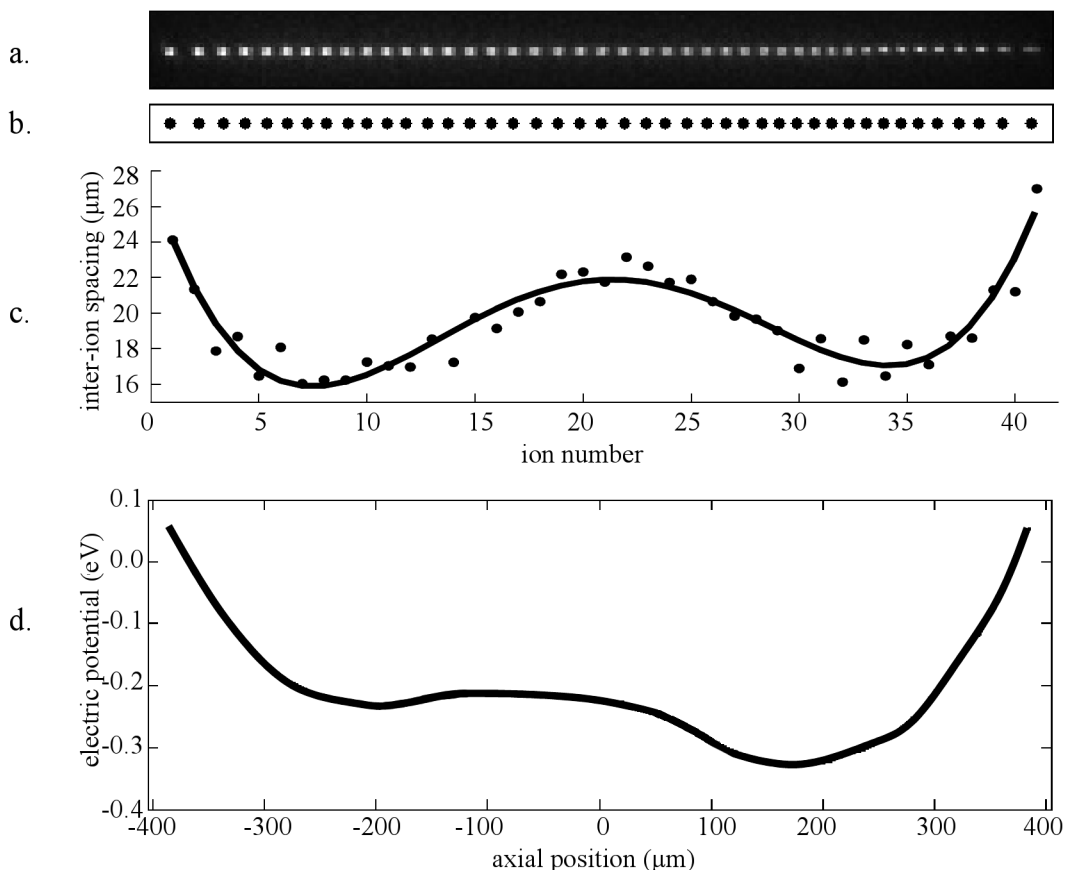


Figure 6.1: a). A CCD image of a 42-ion chain, b). the positions of the ions determined from this image, c). the inter-ion spacing and d). the deduced potential along the ion string.

covering large axial extents of the trap, the potential along the ion string axis can be investigated as a function of the individual electrode contributions. In this way, a long string of ions can be used as a probe of a trap's electric potential. Subsect. 4.1.1.2 described the basis potentials of the individual electrodes of surface trap *Bastille*. Using the method described above of reconstructing the trap's axial potential from the inter-ion spacing, long ion strings were used as a sensitive probe of the contributions to the trap potential from individual electrodes or sets of electrodes. Varying the voltage on one trap electrode (or group of electrodes) allows a mapping of the trap potential over a region of space.

The experimental procedure is as follows. The potential arising from one electrode set (the “electrode of interest”; EOI) is desired to be determined. Electrode voltages are set such that a long chain of ions are trapped. A voltage $U_{\text{EOI}}^{(i)}$ is then applied to the electrode of interest. A CCD image is taken, and from this, the electric field $E^{(i)}(x)$ is derived (using the method described above). Then, the voltage on the electrode of interest $U_{\text{EOI}}^{(i)}$ is varied, and the procedure is repeated for a range of voltages on the electrode of interest.

Each electric field $E^{(i)}$ can be thought of as comprising two components: the normalised field (field per volt) $\hat{E}_{\text{EOI}}^{(i)}$ arising from the electrode set of interest supplied with voltage $U_{\text{EOI}}^{(i)}$, and the background field E_{BG} :

$$E^{(i)} = E_{\text{BG}} + U_{\text{EOI}}^{(i)} \cdot \hat{E}_{\text{EOI}}^{(i)}.$$

The background field E_{BG} remains constant for every $E^{(i)}$, and the difference between two fields

6.2. Long Ion Strings as Electrical Field Probes

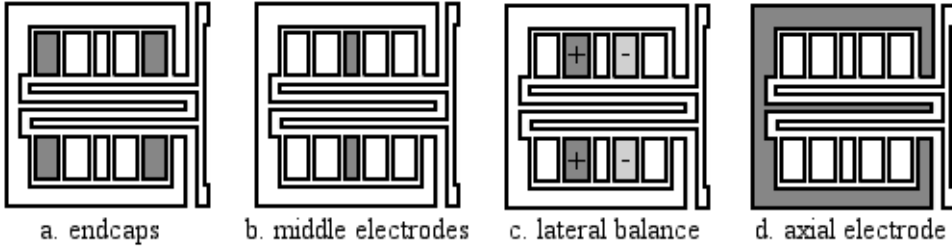


Figure 6.2: *Bastille* “electrodes of interest”. Measurements of the trap field using long ion strings as probe vary the voltage applied to these sets, while keeping voltages applied to all other electrodes constant.

j and k ($j, k \in i$) with different $U_{\text{EOI}}^{(i)}$ is given by:

$$E^{(k)} - E^{(j)} = U_{\text{EOI}}^{(k)} \cdot \hat{E}_{\text{EOI}} - U_{\text{EOI}}^{(j)} \cdot \hat{E}_{\text{EOI}}.$$

The normalised field arising from the electrode of interest is therefore given by:

$$\hat{E}_{\text{EOI}} = \frac{E^{(k)} - E^{(j)}}{U_{\text{EOI}}^{(k)} - U_{\text{EOI}}^{(j)}}. \quad (6.3)$$

The experimental data is the axial positions of the ions in a chain. As $U_{\text{EOI}}^{(i)}$ is varied, the ions can explore a region many times the length of a single chain, and thereby be used to find E_{EOI} over an extended region (here, several hundred micron). The point-wise averaged field \hat{E}_{EOI} is then integrated to yield the normalised electric potential $\hat{\phi}_{\text{EOI}}$ over the extended region.

The normalised potentials $\hat{\phi}_{\text{EOI}}$ are determined for several sets of “electrodes of interest”. As described previously (cf. Subsect. 4.1.1.2), *Bastille* is typically operated with electrodes grouped into sets, where a common voltage is applied to a set of electrodes. The electrodes of interest for which the normalised fields are measured are the endcaps (EC), the middle electrodes (ME), the lateral balance (LB) and the axial electrode (AE). As a reminder, these electrode sets are depicted in Fig. 6.2. Note that the lateral balance is the difference of voltages applied to steering electrodes located at different axial positions.

For the electrode (set) of interest, the number of different voltages $U_{\text{EOI}}^{(i)}$ applied varied between 5 and 47. Each string contained ~ 20 ions, and was 180–450 μm long. Over the set of voltages $U_{\text{EOI}}^{(i)}$ applied to the electrodes, the ion chain covered an axial extent of 500–850 μm .

The experimentally derived electric potentials can now be compared to simulated electric potentials. Simulated normalised electric potentials are calculated from two simulated electric potentials. In these simulations, the electrodes are supplied with U_{BG} (for the electrodes held at constant voltage), and with $[\min(U_{\text{EOI}}^{(i)}), \max(U_{\text{EOI}}^{(i)})]$, ie. the minimum and maximum $U_{\text{EOI}}^{(i)}$ for the entire set of $U_{\text{EOI}}^{(i)}$ for that electrode. For these two simulated potentials, the potential along the weak trap axis is taken. This may not be the radiofrequency null, depending on the values of U_{BG} and $U_{\text{EOI}}^{(i)}$, but is the trap axis along which the ion string is aligned. The simulated normalised electric potential is obtained from the difference of the simulated potentials divided by the difference in the minimum and maximum applied voltages.

Fig. 6.3 shows the calculated normalised electric potentials compared with the simulated normalised electric potential, which demonstrate a good qualitative agreement.

A quantitative analysis of the agreement between experimentally derived and simulated potentials would require a detailed error analysis. This is not carried out here. The error in the ion

Chapter 6. Experimental Results

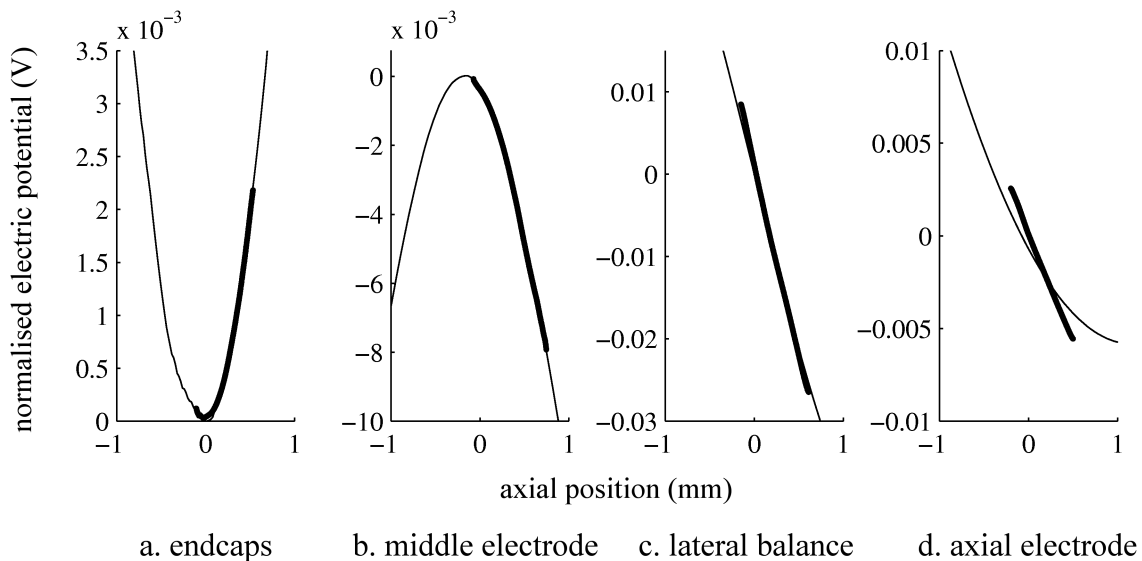


Figure 6.3: Comparison between experimental and simulated electric potential basis functions along the trap axis. a). endcaps, b). middle electrodes, c). lateral balance, d). axial electrode.

position is expected to be the main source of uncertainty in the field and potential calculations, and here an estimation of the error in ion position is derived from the electric field noise.

The electric field far from the electrodes is smooth, and can be fit with a polynomial. From the residuals (the difference between the data and the fit), the electric field noise can be estimated. The total electric field for one data set is investigated. In Fig. 6.1c, the average inter-ion spacing is $19.4 \mu\text{m}$. The electric field that one ion creates at the position of its nearest neighbours for this inter-ion spacing is 3.8 V/m . Here, the field from all other ions in the chain is neglected. The residuals are calculated to be $\delta E = 0.2 \text{ V/m}$. Therefore, the noise in the electric field is 5%. Using the electric field noise, the ion position uncertainty δx can be estimated via the relation

$$\frac{\delta E}{E} = 2 \frac{\delta x}{\Delta x},$$

which results in a position uncertainty of $0.49 \mu\text{m}$ (at the magnification used, equivalent to 0.3 pixels). The inter-ion spacing depicted in Fig. 6.1c could also be used to estimate the position uncertainty, by fitting the positions with a quartic potential, and determining the residuals from this fit.

There are also a number of less significant error sources. For the experimental data, these include voltage noise on the electrodes, the voltage resolution of the analog output cards, both of which are amplified, and voltage noise introduced by the amplifier. Regarding the simulation data, the electric potentials are exported over a grid with a $20 (10) \mu\text{m}$ spacing in the $x (y, z)$ directions. This resolution will limit the accuracy of the simulated potentials. A more detailed error analysis may result in better agreement between experimentally derived and simulated electric potentials.

A significant limitation of the field measurement method is that the axial position (x) of the ion string is difficult to control independently of the height of the string (z), as the electric fields produced by the electrode of interest are not purely axial. Variation of the voltage of the electrode of interest moves the ion string vertically as well as axially, by an amount dependent on the background potential. This effect has been taken into account for the computation of the theoretical curves, while the background potential has been assumed constant for the small voltage steps required in the computation of Eq. 6.3.

6.3. Deterministic Reordering of Ions

This Section described an accurate method for characterising the electric potential of a trap and mapping the deviations from the ideal case, using a string of ions as an electric field probe. For *Bastille*, the measured trap electric potential shows a qualitative agreement with the simulated electric potentials. A qualitative comparison would require a detailed error analysis, which is not presented here. The uncertainty in ion position is the expected main contribution to the potential error, and a method of estimating this from the electric field noise is presented.

6.3 Deterministic Reordering of Ions

Three important ion movement primitives for a multiplexed ion trap quantum computer are shuttling, turning corners and splitting and joining ion strings [KMW02]. These basic operations can be combined to implement high-level shuttling protocols. Shuttling of ions has been theoretically [RLB⁺06] and experimentally [RBD⁺02, HDS⁺07] investigated, and ion strings have been split and joined [RBD⁺02]. One of the aspects of the requirement of “turning corners” is as a method of reordering ions in a linear ion trap. Previously, this operation was thought to require junctions, that is, electrode structures which allow a radiofrequency null at an angle to the primary radiofrequency null. The original proposal of segmented traps pictorially represented a quantum CCD of different regions with radiofrequency nulls at right angles [KMW02], and a recent theoretical publication outlined ideal junction geometries [Wes08b] for radiofrequency trap networks. Junction geometries or intersections between network paths are a key ingredient in two-dimensional radiofrequency trap networks [OLA⁺08, LKOW07]. Experimental realisations of junction structures have included a second linear axis intersecting the first in either “T” [HOS⁺06, HYH⁺08]-, “Y” [Sinb, Sina, WAB⁺07, Sch09]- or “X” [BOV⁺09, ABLW08]- junction shapes. In the T-trap, ions were transported around a corner with a round-trip success probability in excess of 98%, with a corner-turning duration of 20 ms, and a predicted (simulated) energy gain of about 1.0 eV [HOS⁺06]. Only very recently, a transport through the junction of the X-trap has been achieved, with a success probability of greater than 0.999995, and an energy gain of less than 10^{-7} eV [BOV⁺09].

The following subsections describe two sets of experiments demonstrating the deterministic reordering of ions in a linear segmented ion trap. The first method involves utilising the lateral and transverse balance controls and moving the ion string around the endcap wall described in Subsect. 4.1.1.2. In this way, the ion traverses a triangular shape, executing a three-point turn which reverses the order of a two-ion string. The second method involves minimising the deviation of the centre of the string from the radiofrequency null and achieves a reordering of ions by a rotation of the weak principal axis through π . Finally, these methods of reordering in a linear trap are generalised and considered in the context of two-layer traps.

6.3.1 The Three-Point Turn

By moving the ions in two dimensions across the trap surface, the ions explore a region of potential where the weakest trap axis is not necessarily aligned with the radiofrequency null axis. This allows rotation of the weak trap axis and movement of the potential minimum axially and transversely. The “three-point-turn” path traversed by the ion string is depicted in Fig. 6.4. At starting position A the ions have a weak axis aligned along \vec{e}_x . Ramping the voltage by modifying the lateral balance voltage control (cf. Fig. 4.7), laterally displaces the ions to the right, while rotating the weak principal axis more towards the vertical. At position B, modification of the transverse balance control then moves the ion string transversely, with the weak principal axis rotating from (at the top of the transverse arm) $\vec{e}_{x,y}$ through \vec{e}_y (halfway through the transverse arm of the path, as pictured in C) to $\vec{e}_{-x,y}$ (at the bottom of the path). The lateral balance is decreased, which shifts the ion string to the left, returning the principal axis to be approximately aligned with \vec{e}_x (the

Chapter 6. Experimental Results

middle of this path is D). Here, the transverse balance is increased, returning the ions to their initial location, with the ions positions reversed.

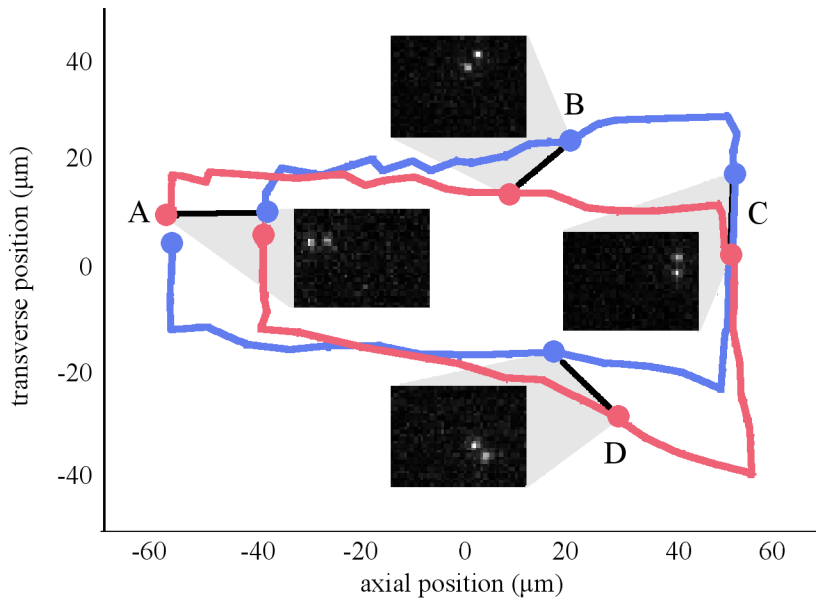


Figure 6.4: This graph shows the position of the two-ion crystal during the three-point-turn. As illustrated by the four insets that show CCD images of the ions at specific locations, the orientation of the ions varies as a function of the position, reflecting the shape of the local potential. The relative positions of the ions indicate the direction of the weak trap axis (along a line joining the two ions) - the angle of this axis with respect to the radiofrequency null varies from 0 to $\sim \pi/4$ through $\pi/2$ to $\sim 3\pi/4$ and finally to π . After completion of one full turn the ions have exchanged position.

Realisation of the three-point-turn path is achieved by varying the lateral and transverse balance controls, which affect the steering electrode voltages. Fig. 6.5 demonstrates a typical three-point-turn voltage ramp. During this sequence, all other voltages are kept constant, with $V_{EC} = 47.35$ V, $V_{ME} = 29.77$ V, $V_{offset} = 7.4$ V, $V_{AE} = 9.76$ V, with $V_{TB} = [0.50, 0.19]$ V and $V_{LB} = [4.99, 7.29]$ V.

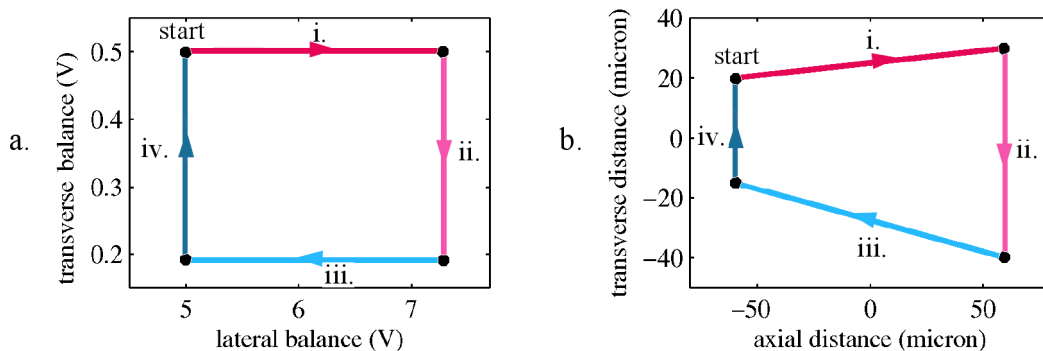


Figure 6.5: Correspondence between the modification of the lateral and transverse balance, and the paths traversed by the ions. The black points indicate a). the extrema of the lateral and transverse voltages, and b). the corresponding corner points of the “three-point turn”, likewise the paths in a). indicate the linear ramping of voltage and b). the paths traversed by the ions in real space.

The average of these electrode voltages give rise to a homogeneous electric potential as depicted in Fig. 6.6, with the lateral and transverse balance variations giving rise to slight potential modification, allowing the ions to explore the potential space.

6.3. Deterministic Reordering of Ions

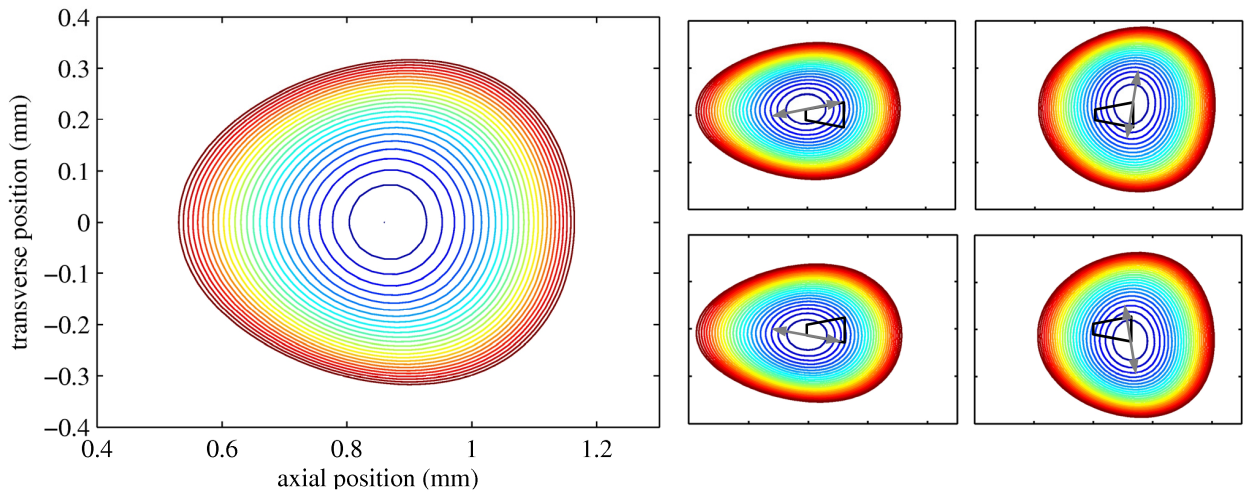


Figure 6.6: Contour plots of the net potential in the xy -plane, at the height (z) of the trap minimum. (Left) Contour plot of the background trap potential experienced by the ions during the three-point-turn ramp sequence. (Right) As the lateral and transverse balance controls are varied, the trap minimum is shifted and the orientation of the trap axes varies as a function of position.

Fig. 6.4 depicts the path of two ions during a single ramp sequence. To obtain this path, the ion positions were determined from successive individual CCD image frames. While such a “movie” seems to indicate that the two ions have reversed position, this data does not provide sufficient information to determine the reliability of reversal of ion position. Firstly, during this ramp path, the ions are continually Doppler cooled. Secondly, the ions could stochastically swap their positions in the crystal on a time-scale undetectable within the camera exposure time (of 100 ms). Instead, “labelling” the ions allows an accurate determination of the success of the reordering process. Labelling of an ion is achieved using the electron-shelving method - a 729 nm laser beam is shone on the ions and places an ion in the $D_{5/2}$ state, rendering it dark. If one and only one ion is dark, the three-point turn path can be traversed before the dark ion returns to the ground (fluorescing) state. At the end of the path, the state of the two ions is again determined by a fluorescence count: if bright and dark ions have changed positions, the reordering process has been successful. The efficiency of the reordering process is extracted from camera data by selecting those events in which before and after the voltage ramp exactly one ion is dark. In other cases, no conclusions about success of the position reversal operation can be made. The process is repeated many times to determine the statistics of the reordering operation.

The laser pulse sequence used to realise the experiment is shown in Fig. 6.7. In the first section, the ions are Doppler cooled, ie. the Doppler cooling laser at 397 nm is applied, in addition to the 866 nm and 854 nm lasers. Then, these lasers are switched off, and an unfocused 729 nm beam, incident upon all ions, is shone in. The pulse length of this laser is 0.2 seconds, and this hides one (and only one) ion with a probability of ~ 20 -50%. Immediately following this, with cooling and repumping beams on, the camera is triggered and takes a signal for 0.1 s. Areas of pixels around the ions images on the CCD camera can be defined - the *regions of interest (ROI)*. In these regions, of $\sim 3 \times 4$ pixels, the fluorescence counts from each ion can distinguish the ions state with virtually 100% precision (for further details, see [Rei05]). In the dark (with all lasers off), the voltages on the electrodes are ramped and the ions traverse the three-point-turn path. The cooling and repumping beams are switched on, and a camera image again records the fluorescence of the ions.

Using a voltage ramp time of 10 ms, a success rate of 93% was obtained (186 successful ion position reversals out of 199). The failure rate of 7% may be caused by a number of processes. First of all, the ions may collide with background gas particles and gain enough energy to swap positions

Chapter 6. Experimental Results

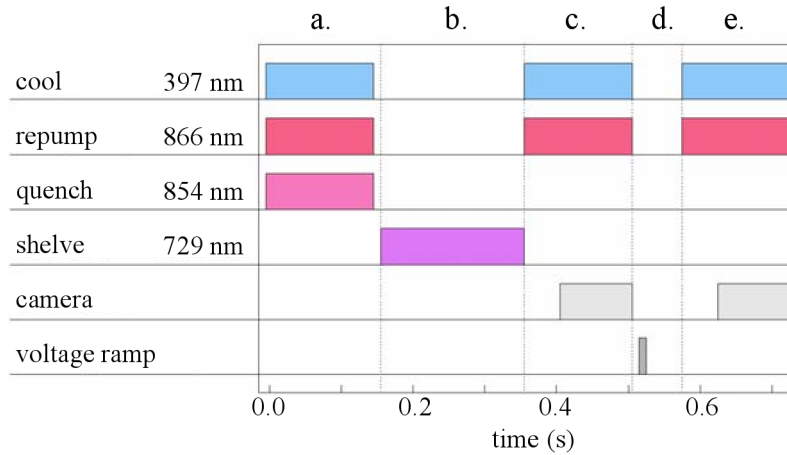


Figure 6.7: Pulse sequence for the verification of ion exchange: a). initialise ions to S state and Doppler cool, b). ion shelving, c). position detection, d). trap rotation without laser illumination, e). position detection.

in the two-ion crystal. Secondly, ions in the trap have some temperature, and for principal trap frequencies that are close to each other, ions are able to move around in the confining potential and reverse places in a chain. Using the same pulse sequence as in Fig. 6.7, but without ramping voltages to transport the ions (ie. the ions should remain in the same position), a swap rate of 9 or 7% was observed (spontaneous position reversal statistics for the upper left and upper right corners of the path are 59 reversals out of 65 events and 84/90 respectively). That means that the ions spontaneously change position with probability of 7 or 9% in these positions. The position reversal probability was also investigated when transporting the ions back and forth along each of the the four individual “arms” of the three-point-turn (ie. back and forth along i: the “upper arm”, back and forth along ii: the “right arm”, etc.). This transport should not induce a position reversal. For each of these paths, spontaneous position reversal probabilities of 21, 26, 6 and 3.5% were measured (with the following statistics: lower arm, 17 position reversals out of 82 events, right arm; 7/27, upper arm; 4/62, left arm; 2/58, respectively). While some individual “arms” have much higher individual intrinsic swap probabilities than the measured overall spontaneous position reversal probability for the entire path (equivalent to the 7% failure rate of the three-point-turn to reverse positions of the ions), the success probabilities of three-point-turn paths are time-dependent in that small voltage drifts on the electrodes cause paths to become non-optimal over time. So, while the three-point-turn statistics were taken when the path had been optimised for a high position reversal success probability, the measurement of the intrinsic reversal probability in the arms was carried out slightly later (~ 30 minutes – 1 hour), when this path was no longer optimal. As the path and its constituent arms were no longer optimal, they had a higher spontaneous position reversal probability. The failure rate of 7% is therefore corroborated by the spontaneous position reversal probabilities at the corners or in the individual arms of the three-point-turn path. It is suspected that at some point during the path, the principal trap frequencies are sufficiently close that, for the ions temperature, the ions can move about in the confining potential and spontaneously reverse position. The spontaneous position reversal is likely to be lowered by increasing the anisotropy between axial (weak) and radial trap frequencies.

6.3.2 The *Pirouette*

During the “three-point-turn” described in the previous section the spatial variation of the potential was used in order to rotate the weak trap axis and deterministically reorder a two-ion crystal with a high probability. However, the path described significantly displaces the ions from the

6.3. Deterministic Reordering of Ions

radiofrequency null, and is thus expected to contribute to ion heating. In order to overcome this undesired effect, the trap potential may instead be varied such that the trap axis is rotated while the trap minimum remains in its initial location, minimising the ion displacement from the radiofrequency null.

The rotation of the weak trap axis, maintaining the trap minimum in a fixed location on the radiofrequency null, may be likened to a “pirouette” movement. In this scheme, the rotation is not initiated by the trap displacement in a homogeneous field (via the lateral and transverse balance controls) but instead by an additional field with strong curvature that compresses and relaxes the trap along two principal axes that are tilted with respect to the original trap axes (cf. Subsect. 6.3.3). To create this field contribution, the diagonal control of the steering electrodes is used (cf. Subsect. 4.1.1.2).

Fig. 6.8a shows a two-ion crystal whose weak axis was rotated by π . Fig. 6.8b. shows the deduced path (from analysis of the CCD camera images) of the two ions through several π rotations.

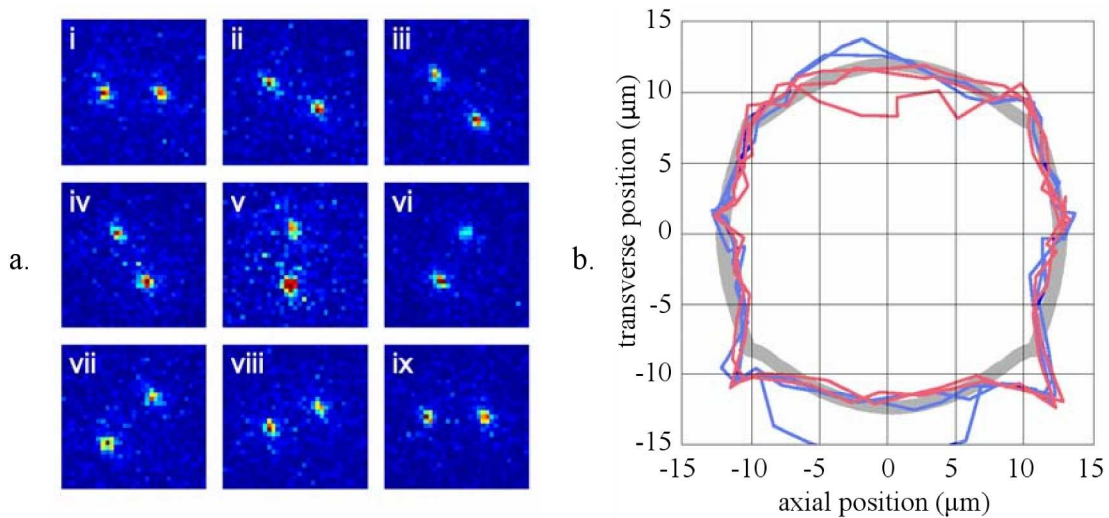


Figure 6.8: Ions positions during the “pirouette”. a). images of a two ion crystal with weak principal axis aligned along x (i) and rotated through various angles to $\pi/2$ (v) and finally to π (ix) as the voltage ramp is performed. The ions positions have been reversed. b). The path traced by two ions in a crystal through several such cycles, determined from camera images such as shown in a. The ion separation is $19.4 \pm 2.5 \mu\text{m}$.

A typical set of electrode voltages (and steering electrode control voltages) used to realise a π rotation of the weak axis is shown in Fig. 6.9. As will be detailed in a theoretical analysis of the potential (Subsect. 6.3.3), the two main contributions stem from the diagonal configuration of the steering electrodes and the combination of endcap and middle electrode variation.

To determine the success of the deterministic reordering of an ion crystal when its weak axis was rotated through π , one ion was labelled and the states of the ions before and after the voltage ramp were determined. The pulse sequence used was the same as described in Fig. 6.7.

For a rotation of the weak principal axis through π , a voltage ramp time of 10 ms was used, which achieved a success probability of 97 % (421/433 events). Within the counting statistics, no significant dependence on the speed of the voltage ramp or the direction of the rotation was observed (clockwise rotations: 189/193, anticlockwise rotations: 232/240). A voltage ramp time of 1.5 ms achieved a success rate of 97 % (32/33 events), while for a ramp time of 1 ms, the low-pass filter threshold frequency of 1 kHz deformed the voltage ramp significantly enough to lower the success rate to 72 % (although for completeness it is mentioned that this data was measured for a slightly different ramp on a different day). If the ions were held for the duration of the

Chapter 6. Experimental Results

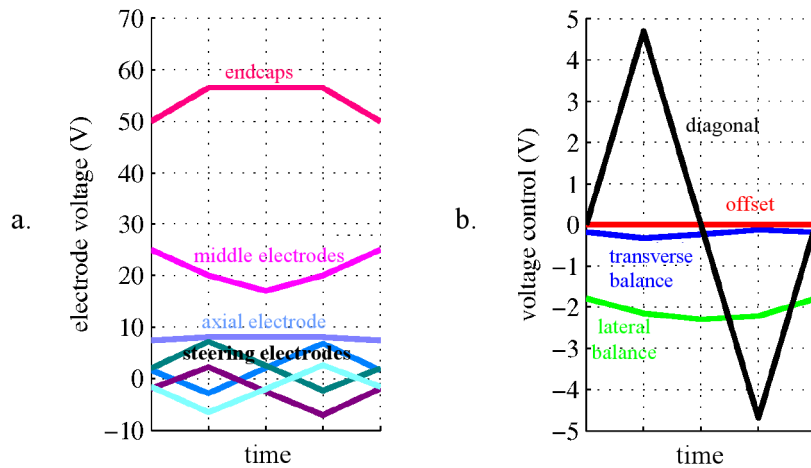


Figure 6.9: a). Voltages used to realise rotation of two or three ion crystal through π . b). illustrates control of the steering electrodes in the more intuitive bases (lateral balance, transverse balance, offset, diagonal) as introduced in Subsect. 4.1.1.2.

swap routine, without applying the swap voltage-ramps, the probability that they maintained their original ordering was measured at 97% (5/132 events). The swap probability of 97% is therefore limited only by the spontaneous position reversal probability of 3%. Notice that the pirouette success rate is higher than the three-point-turn success rate of 93%. One of the suspected reasons for the ions to spontaneously reverse position in the chain at some point is that they have a high enough temperature, for the trap principal frequencies, that they can move about within the confining potential and spontaneously reverse positions. The ions are less likely to spontaneously reverse position if the trap principal axes are highly anisotropic: if the weak trap frequency is much lower than the other principal frequencies, the ions will remain in a string and not spontaneously reverse positions. For the pirouette, exactly this principal trap frequency configuration was made. This is the likely mechanism by which the success probability of the pirouette is larger than that of the three-point turn. The cause of the inherent spontaneous position reversal probability of 3% in the pirouette is not known, however, it might be attributable to the high background pressure of the vacuum chamber (high 10^{-10} –low 10^{-9} mbar).

The “pirouette” was carried out also with larger (three- and four-) ion crystals.

An important characterisation of a trapped ion transport process is the energy gained by the ions (the heating rate). In this case, no direct measurement of the heating could be performed. Instead, an upper limit on the induced heating rate could be inferred from a sequence of 200 consecutive exchanges performed immediately following Doppler cooling. The sequence could be repeated 149 times before the ion was lost from the trap. While the ion loss does not need to be attributed to heating (the ion loss could have been occurred due to a collision with background gas), the observed survival statistics can be used to give an upper bound of the heating rate of 0.72 meV per half-turn. The derivation of this rate is now detailed.

To estimate the heating rate, the following assumptions are made:

- the probability for an ion to have energy E after n experiments is given by a thermal distribution characterized by a temperature T ,
- the ion is lost from the trap if it has energy E greater than the trap depth E_0 ,
- the heating mechanism is linear.

6.3. Deterministic Reordering of Ions

The ion has a loss probability in a single experiment of $p_{\text{loss},1}$, and the probability that the ion remains in the trap (the ‘‘survival’’ probability) for a single experiment is:

$$p_{\text{survival},1} = 1 - p_{\text{loss},1} .$$

The loss probability in each single experiment is independent, and so the survival probability for n consecutive experiments is given by

$$p_{\text{survival},n} = (1 - p_{\text{loss},1})^n .$$

We carry out a series of 149 experiments, and no ion is lost. Only on the 150th experiment has an ion loss occurred. A loss probability of $p_{\text{loss},1}$ in 149 consecutive experiments would therefore lead to the survival probability

$$p_{\text{survival},149} = (1 - p_{\text{loss},1})^{149} . \quad (6.4)$$

The energy of the ion in the trap can be described in the following way. For a given temperature T , the probability $p(E) dE$ of finding the ion with energy E within a range dE is proportional to $e^{-E/k_B T}$ (where k_B is Boltzmann’s constant) and to the density of states $D(E)$:

$$p(E) dE = p_0 D(E) e^{-E/k_B T} dE ,$$

with the density of states for a three-dimensional harmonic oscillator proportional to E^2

$$D(E) \propto E^2 .$$

The normalisation constant p_0 computes to

$$p_0 = \left(\int_0^\infty D(E) e^{-E/k_B T} dE \right)^{-1} = \frac{1}{2 (k_B T)^3} .$$

If the ion has energy E greater than the trap depth E_0 , it will leave the trap. So, the probability of ion loss is the integral of the probability $E > E_0$:

$$p_{\text{loss},1} = p_0 \int_{E_0}^\infty D(E) e^{-E/k_B T} dE .$$

and computes to

$$p_{\text{loss},1} = \frac{E_0^2 + 2E_0 k_B T + 2 (k_B T)^2}{2 (k_B T)^2} e^{-E_0/k_B T} . \quad (6.5)$$

Armed with relations between the ion loss in a series of experiments to the ion loss in a single experiment (Eq. 6.4), and the ion loss of an ion at temperature T in a trap of depth E_0 (Eq. 6.5), a loss probability for a single experiment $p_{\text{loss},1}$, with a confidence level of $F = 1 - \delta p$ that the real heating rate is not greater than the estimated rate, is now derived. That is, for the derived heating rate, there is only a δp probability that the real heating rate is higher than the derived heating rate. This means that the probability of obtaining the observed 149 consecutive survivals, if in fact the loss probability in one experiment is $p_{\text{loss},1}$ or larger, is at most δp :

$$p_{\text{survival},149} \leq \delta p \quad (6.6)$$

Chapter 6. Experimental Results

With this, and Eq. 6.4, $p_{\text{loss},1}$ is bounded by

$$p_{\text{loss},1} \leq 1 - \delta p^{1/149} \quad (6.7)$$

with a confidence level of $1 - \delta p$.

Inserting Eq. 6.5 we obtain:

$$1 - \delta p^{1/149} \geq \frac{E_0^2 + 2E_0 k_B T + 2(k_B T)^2}{2(k_B T)^2} e^{-E_0/k_B T} \quad (6.8)$$

The numerical solution can then only be found for a given value of δp : for $\delta p = 1\%$, which corresponds to a confidence level of 99%, the resultant temperature is $k_B T = 150 \text{ meV}$. This temperature characterises the energy distribution of an ion after a single experiment. For 200 half-rotations carried out in each experiment, and assuming a linear heating mechanism, this results in a maximum heating rate of $k_B \Delta T_{\text{max}} = 0.8 \text{ meV/half-rotation}$.

This heating rate compares favourably with the heating rate of $\sim 1 \text{ eV}$ per exchange reported when reordering ions through a T-junction [HOS⁺06]. The significant difference in heating rates is due to the ‘‘rf barrier’’ present in the complex junction geometry [HYH⁺08]. The estimated upper bound is still approximately three orders of magnitude higher than the heating rate measured when moving pairs of ions through an X-junction [BOV⁺09]. For proper comparison, more precise temperature measurements should be made in the present apparatus to characterise the heating rate for reordering ions in a linear trap.

6.3.3 Generalisation of Method to Two-Layer Trap Geometries

In the surface trap *Bastille* used in these experiments the ion movement is easily confined to two dimensions because the confinement along the z -axis (perpendicular to the trap surface) is by far the strongest, as described above. In many applications to date, the ions are trapped in the plane of the dc electrodes, e.g. in two-layer segmented traps [RBD⁺02, SHO⁺06, SPZS08]. It is therefore important to consider whether the strong asymmetry between the two ‘‘radial’’ axes in this experiment (and consequently the ability to perform the ion string rotation) arises from the fact that the ions are trapped outside the plane of the dc electrodes, or whether the results demonstrated here can be generalised to these other trap geometries. As a particular example, the segmented-electrode linear Paul trap dedicated to single-ion implantation into crystals [SLF⁺09] requires dopant ions to be sympathetically cooled by $^{40}\text{Ca}^+$ ions before being expelled towards the target. These experiments would find highly advantageous the implementation of a reordering strategy similar to the one presented here.

In the following, a brief summary of the general requirements for the rotation of an ion string will be considered, and appropriate geometries to generate the required fields in a two-layer segmented trap will be discussed. A full discussion can be found in [SHB⁺09]. A generic geometry as in Fig. 6.10a is assumed and a simple point charge model will be used to choose the optimal distance for the control electrodes. In this geometry the pseudopotential due to the radiofrequency voltage confines the ions along the y - and z -axis, and leaves them free along the x -axis.

6.3. Deterministic Reordering of Ions

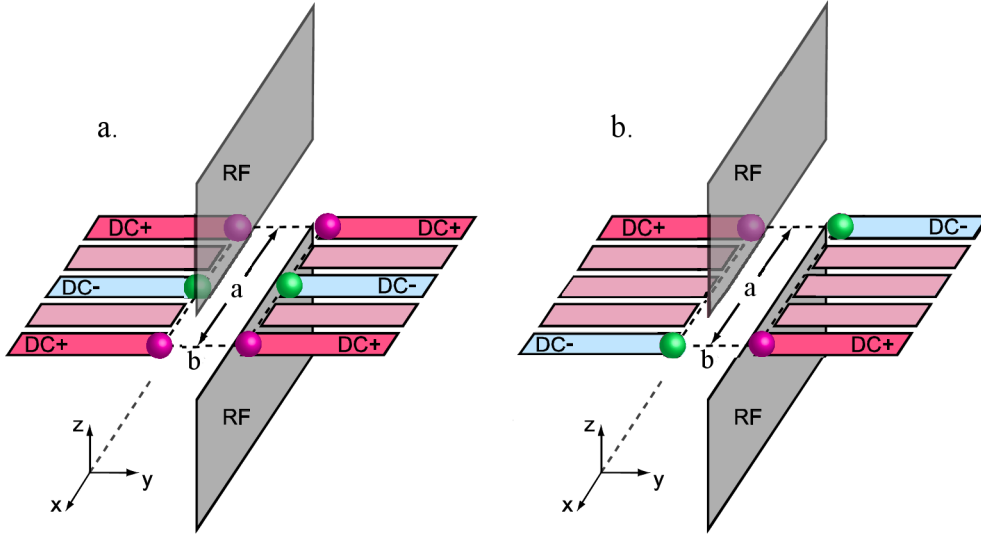


Figure 6.10: Model geometry for a three-dimensional segmented ion trap and the associated point charge model used to optimise the layout of control electrode. a). and b). respectively illustrate two different voltage configurations that are used to generate the transverse and diagonally oriented quadrupole fields: the resultant fields are sketched in Fig. 6.11.

The dc potentials can be used to continuously rotate the weak trap axis so that the ion string smoothly follows the orientation of the trapping potential. When the ion string is oriented transverse to the radiofrequency null, the dc confinement along the radiofrequency axis (here \vec{e}_x) has to be strongly increased, while it is weakened along one radial axis (here the y -axis). Moreover, the curvature of the potential along the principal trapping axes (i.e. the z -axis and the two time-dependent principal axes in the xy -plane) should be kept constant in order to avoid heating.

Such a rotation of the axes can be achieved by a time-dependent two-dimensional quadrupole field, $\Delta U(t)$, whose principal axes lie in the xy -plane. This field can be created from the superposition of two separate quadrupole fields, ΔU_{trans} and ΔU_{diag} , with the axes oriented along \vec{e}_x , \vec{e}_y for the first field, and diagonal to these for the second field (see also Fig. 6.11). The field to be added can be written as

$$\Delta U(t) = \hat{a}_{\text{trans}}(t) \Delta U_{\text{trans}} + \hat{a}_{\text{diag}}(t) \Delta U_{\text{diag}}$$

To establish this result, and the ideal time evolution of the relative quadrupole amplitudes \hat{a}_{trans} and \hat{a}_{diag} , a linear ion trap is considered, where an initial potential U_0 confines the ions aligned along the x -axis. The desired potential $U(t)$ is simply the potential U_0 , rotated by an angle $\theta(t)$ around the z -axis. The additional potential, $\Delta U(\theta)$ required to achieve smooth rotation of the trap weak principal axis by θ is given by

$$U(\theta) = U_{\text{trans}} \underbrace{\frac{1}{2}(1 - \cos(2\theta))}_{\hat{a}_{\text{trans}}} - U_{\text{diag}} \underbrace{\frac{1}{2}\sin(2\theta)}_{\hat{a}_{\text{diag}}}. \quad (6.9)$$

i.e. a time-dependent superposition of the two quadrupole fields ΔU_{trans} and ΔU_{diag} , with amplitudes \hat{a}_{trans} , and \hat{a}_{diag} oscillating sinusoidally at twice the rotation speed of the trap and with a relative phase shift of $\pi/2$. Fig. 6.11 illustrates the evolution of these amplitudes during a half rotation of the trap. \hat{a}_{trans} has a positive offset which acts to render the trap circular in the plane of rotation before adding a purely rotating two-dimensional quadrupole field.

Chapter 6. Experimental Results

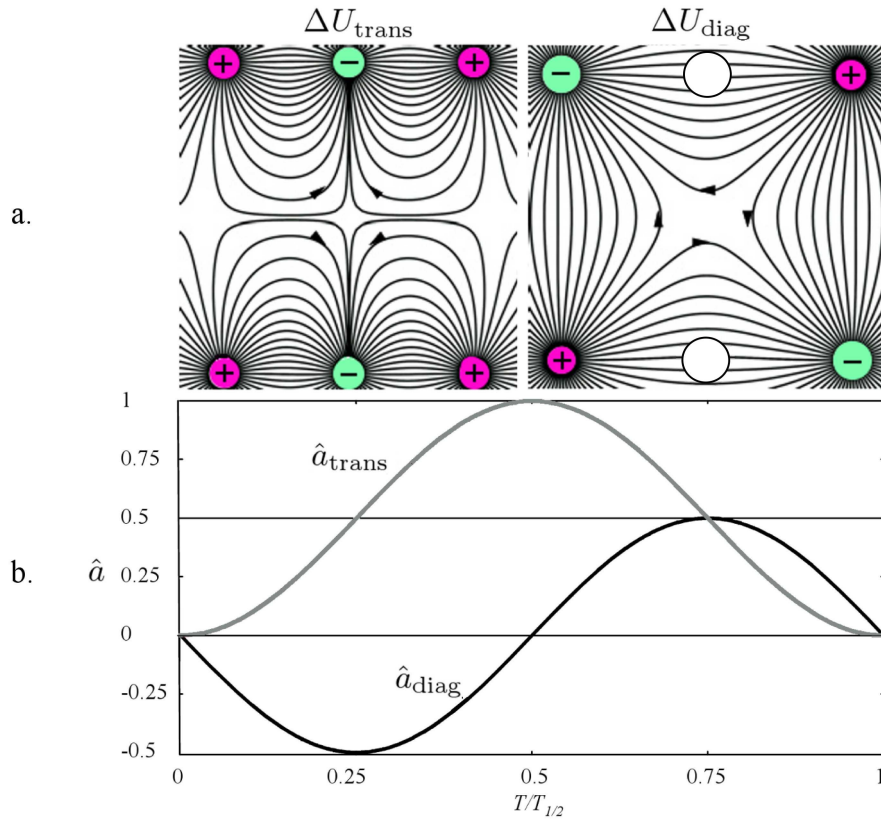


Figure 6.11: a). The field lines associated with the diagonal and transverse quadrupole potentials ΔU_{diag} and ΔU_{trans} , respectively, as created from single point charges located at the indicated positions (cf. Fig. 6.10). In the point charge configuration depicted on the right, no charges are assumed at the position of the middle electrodes. b). The sinusoidal curves represent the evolution of the respective fields strengths during a half rotation as computed in Eq. 6.9.

An optimum layout of electrodes to generate the two quadrupole fields required for the trap rotation can now be determined. For a segmented trap a set of six electrodes is considered, the tips of which line a rectangle, as shown in Fig. 6.10a. To estimate the resulting potential the electrodes are approximated by six point charges at the corners of a rectangle in the xy -plane. The effect of the leads and shielding by radiofrequency electrodes is neglected. For these simplifying assumptions the curvatures of the dc potential can be calculated analytically.

All six electrodes are required to create a transverse quadrupole field in the plane of the electrodes. The four outer electrodes are held at positive voltages, while the inner electrodes are held at negative voltages, as depicted in Fig. 6.10. A field approximating the required two-dimensional quadrupole field is obtained when the ratio of inner to outer electrode voltages is chosen as $(V_{\text{middle}}/V_{\text{corner}} = 2(1 + (a/b)^2)^{-\frac{3}{2}}$. The transverse quadrupole is strongest for $a/b \approx 1$ and, interestingly, for this ratio, the diagonal quadrupole has the same strength as the transverse quadrupole. This configuration thus represents an ideal choice for the geometry of the corner electrodes for the transverse quadrupole as well as for the electrodes for the diagonal quadrupole. Hence, if the width of each electrode segment is approximately half the slit width, three adjacent pairs of electrodes in a linear segmented trap can be used to efficiently rotate a string of trapped ions.

These generalised theoretical results can now be interpreted with respect to the electrode voltages used in the realisation of the “pirouette” (cf. Fig. 6.8). In the experiment, just five sampling

6.3. Deterministic Reordering of Ions

points were used, and while this is a coarse sampling of the expected sine and cosine functions, the general shape of these functions are reflected in the experimentally used waveforms (which used linear voltage ramps between the five voltage settings). The diagonal quadrupole is provided by the diagonal electrodes V_{diag} , and this is an approximate sine function, as shown in Fig. 6.9b. The experimental waveform is a positive sinusoidal due to the direction of rotation. The small sinusoidal amplitude of the transverse balance corrects for an offset between ion position and the true quadrupole centre. Fig. 6.9a shows an evolution on the endcaps and middle electrodes similar to the cosine function. The remaining (small) voltage excursions compensate for residual electric fields. The ions are not located in the electrode plane, and the motion perpendicular to the trap surface arising from variation of the endcaps and centre electrodes is counteracted by the axial electrode. In total, the electrode voltages for the one-point turn in the surface trap reflect strongly the expectations for a rotation with the ions in the electrode plane, thus corroborating the developed model.

Summary

The results presented in this Chapter demonstrate the experience gained using a macroscopic surface segmented ion trap. The electric potentials realisable in a segmented-electrode surface trap are considerably different from those in linear Paul trap geometries with more traditional geometries of a hyperbolic macroscopic electrodes, and the control of these potentials allowed the realisation of very long, almost-evenly spaced ion strings and the deterministic reordering of a string of ions. Furthermore, the understanding of these potentials, strengthened by the development of a method to measure the electric potential of an ion trap using long strings of ions, should prove valuable in further surface trap design and operation. The generalisation to two-layer trap designs of the trap potentials for realisation of deterministic reordering is hoped to find ready application.

Chapter 7

Summary and Outlook

Summary

Ion traps have proven to be a leading experimental implementation of a prototype quantum computer. The proposal of a quantum charged coupled device [KMW02], or, in common parlance, a “segmented(-electrode) ion trap” seeks extension of this considerable success into a truly scalable system. However, the route to a scalable ion trap quantum information processor remains technologically challenging. This thesis reports on efforts and results towards this goal.

The manufacturing of miniaturised ion traps has historically been hindered by high fabrication costs and failure to meet specifications and delivery dates, which has hampered advance of the field. While the ironing out of these wrinkles makes progress, the use of low-cost, quick fabrication turnaround time PCB traps allows understanding of scaling issues and control of segmented electrode potentials. Such a trap (cf. Section 4.1.1.1) was used for several experiments and the results reported in this thesis. Systematic variation of dc control voltages applied to segmented electrodes allowed for the characterisation and deep understanding of the trapping potentials of the trap. The simulation of trap potentials, and the understanding of *Bastilles* potential gained from these, was presented. While ion traps with simple harmonic axial potentials are limited in the number of ions they can usefully hold, the ability to create a tailored axial potential can be used to hold very long ion strings. This ion trap has realised ion strings of up to 43 ions, with spacings of $\sim 20 \mu\text{m}$ almost constant over the string. Such a string of ions was recently (theoretically) proposed for a novel scheme to implement quantum gates through radial oscillation modes. The exquisite control and understanding of the trapping potential gained in earlier experiments culminated in the achievement of deterministic reordering of ions in a string. While another scheme exists for the sorting of a four-ion crystal with two ion species in a string through successive tightening and relaxation of the axial trap potential [Win], this procedure is not (yet) deterministic, and necessarily induces heating. In this thesis, the deterministic reordering of an ion crystal in a linear ion trap, a manoeuvre previously believed possible only in “junction” traps was achieved. Using time-dependent dc control voltages, a two-ion crystal was moved along a “three-point turn” path, which ultimately results in a reversal in axial position of the two ions. This procedure was carried out as rapidly as 1.5 ms (limited only by existing low-pass filters), with a 93% success rate. The three-point turn path moves the ions away from the radiofrequency null and may therefore be expected to cause considerable motional heating. This can be avoided by modifying the three-point turn path to a “pirouette”, that is, rotation of the weak principal axis of the trapping potential while keeping the trap minimum in a fixed location. This allows an axial inversion of the position of ions in a string, while minimising the deviation of the position of the ions from the radiofrequency null. Such a pirouette was carried out for two-, three- and four-ion crystals, and the success achieved in swapping the ions positions was 97%, limited only by the background swap rate. These experiments

were carried out in a surface trap, while many miniaturised segmented ion traps are designed with two-layers. Therefore, the potential manipulation required to achieve this reordering was generalised theoretically in order to be applied to a wider range of trap geometries. This generalisation is assumed to find specific application and extension in other trap geometries.

While PCB traps such as *Bastille* allow rapid testing of different trap geometries and allow valuable understanding to be gained and interesting experiments to be carried out, common fabrication techniques do not allow realisation of dimensions amenable to the scale required for truly miniaturised ion traps useful for quantum computation. Instead, miniaturised ion traps need to be manufactured using microfabrication techniques and processes. In this direction, this thesis reports on contributions to a collaborative effort to produce a cutting-edge two-layer segmented ion trap. This trap has a number of desirable features lacking in previous trap designs. This thesis has reported on the numerous considerations required for the design and fabrication of such a trap.

Outlook

The two-layer trap described in this thesis has a large number of control electrodes and dimensions compatible with obtaining high secular frequencies. It should therefore provide a fertile test bed for future experiments in quantum information processing. However, the fabrication and assembly approach presented may require modification in order to be suitable for long-term advance in miniaturised segmented ion traps. Specifically, the definition of electrodes, both in substrate definition and cutting through electrode material, is a process requiring linear time resources in terms of machining. The finite resolution of the laser cuts might not be able to be reduced further for smaller traps. Additionally, the manual alignment of the two electrode and one spacer layers achieves only an accuracy of $\sim 5\ \mu\text{m}$: while suitable for the electrode dimensions of this trap, as electrode dimensions further decrease, if manual alignment cannot be improved then the realised final geometry will deviate significantly from the ideal geometry, perhaps significantly impeding the trap's performance. A truly scalable miniaturised segmented ion trap would be fabricated in a monolithic manner, that is, cast as a single piece. There have been efforts in this direction, however, these suffered from either low trap depths and high heating rates [Sti07], or difficulty in realising fabrication of the proposed structures [Bro07]. This remains an open problem, however trap fabrication research in our group, amongst others, and at trap foundries at Lucent and Sandia (initiated by IARPA), continue to tackle this challenging fabrication issue.

To realise arrays with very large numbers of ions, the number of control electrodes necessarily increases. In fact, some proposals for a “useful” ion trap quantum computer even indicate that control electrodes could number in the hundreds of thousands. While this might not necessarily happen tomorrow, segmented ion traps will probably come to contain hundreds of electrodes, all requiring physical wiring. Clever packaging solutions to connect these electrodes are therefore valuable. With packaging solutions one may also consider the incorporation of on-board electronics to control the electrodes.

In a similar vein, microchip traps could benefit from scaling of laser delivery and measurement infrastructure. As with photonics components, hybrid devices may be envisioned, which integrate optical components such as optical fibres, on-chip waveguides and MEMS optical devices onto the trap chip [Slu06a]. A scalable architecture for quantum computation involving fibre optic arrays for laser delivery and ion state measurement using MEMS mirrors, lensed fibres, and micro-cavities was proposed [KK07]. First experiments in this direction seek to integrate optical fibres onto the microtrap. A method for aligning fibres on a flat surface using lithography and SU-8 epoxy was developed for use with neutral atom traps (with excellent results) [LBW⁺05], and has been applied to the fluorescence detection of trapped ions in a microtrap [Geo08]. While not reported here,

Chapter 7. Summary and Outlook

work in this direction was also carried out as a part of this thesis [Zae07]. A modified *Bastille*, with two copper-coated optical fibres attached perpendicular to the geometrical trap centre, with centres at the height of the trap axis, was tested. In these experiments, experience was gained in the integration of optical fibres with microtraps. This research direction will be pursued both for the detection of fluorescence of ions in a miniaturised ion trap (a similar setup with an atom chip is described in [TSD⁺06]), and also to the integration of miniaturised traps and cavities formed from the spherical laser-ablated faces of fibres (similar to [CSD⁺07]).

One of the most considerable factors influencing segmented ion traps is the high electric field noise obtained as the ion-electrode distance decreases. Cryogenic cooling of trap surfaces can reduce the electric field noise, that causes decoherence of the motional state, by up to seven orders of magnitude [La08]. Future experiments with miniaturised ion traps can thus greatly benefit from being operated in a cryogenic environment, and research efforts in this direction are being made by our research group.

Bibliography

- [Aar05] S. Aaronson, *NP-complete Problems and Physical Reality*, ArXiv Quantum Physics e-prints **arXiv:quant-ph/0502072** (2005). Cited in page(s): 2.
- [ABLW08] J. M. Amini, J. Britton, D. Leibfried, and D. J. Wineland, *Microfabricated Chip Traps for Ions*, ArXiv e-prints **arXiv:0812.3907** (2008). Cited in page(s): 94.
- [AHM⁺95] R. Alheit, C. Hennig, R. Morgenstern, F. Vedel, and G. Werth, *Observation of instabilities in a Paul trap with higher-order anharmonicities*, Applied Physics B: Lasers and Optics **61** (1995), 277–283. Cited in page(s): 9.
- [All08] David Allcock, private communication, 2008. Cited in page(s): 34.
- [ASW⁺07] J. Amini, S. Seidelin, J. Wesenberg, J. Britton, B. Blakestad, K. Brown, R. Epstein, J. Home, J. Jost, C. Langer, D. Leibfried, R. Ozeri, and D. Wineland, *Multilayer Interconnects for Microfabricated Surface Electrode Ion Traps*, APS Meeting Abstracts, June 2007, p. K1017. Cited in page(s): 5.
- [ATLM06] D. Aveline, R. Thompson, N. Lundblad, and L. Maleki, *Loading and Manipulating Atoms on a Chip.*, APS Meeting Abstracts, May 2006, p. 1021. Cited in page(s): 29.
- [BAB⁺08] B. Blakestad, J. M. Amini, J. W. Britton, K. R. Brown, R. J. Epstein, J. P. Home, J. D. Jost, E. Knill, C. Langer, D. Leibfried, C. Ospelkaus, R. Ozeri, S. Seidelin, A. Vandevender, J. H. Wesenberg, and D. J. Wineland, *Ion transport through an X-intersection trap array*, APS Meeting Abstracts, May 2008, p. L2091. Cited in page(s): 5.
- [BCD02] R. Blume-Kohout, C. M. Caves, and I. H. Deutsch, *Climbing Mount Scalable: Physical-Resource Requirements for a Scalable Quantum Computer*, ArXiv Quantum Physics e-prints **arXiv:quant-ph/0204157** (2002). Cited in page(s): 3.
- [BCJ⁺00] H.-J. Briegel, T. Calarco, D. Jaksch, J. I. Cirac, and P. Zoller, *Quantum computing with neutral atoms*, Journal of Modern Optics **47** (2000), 415–451. Cited in page(s): 2.
- [BCL⁺07] K. R. Brown, R. J. Clark, J. Łabaziewicz, P. Richerme, D. R. Leibbrandt, and I. L. Chuang, *Loading and characterization of a printed-circuit-board atomic ion trap*, Phys. Rev. A **75** (2007), no. 1, 015401. Cited in page(s): 5 and 29.
- [BCS⁺04] M. D. Barrett, J. Chiaverini, T. Schätz, J. Britton, W. M. Itano, J. D. Jost, E. Knill, C. Langer, D. Leibfried, R. Ozeri, and D. J. Wineland, *Deterministic quantum teleportation of atomic qubits*, Nature **429** (2004), 737–739. Cited in page(s): 3, 5, and 26.
- [BDK92] R. G. Brewer, R. G. DeVoe, and R. Kallenbach, *Planar ion microtraps*, Phys. Rev. A **46** (1992), 6781. Cited in page(s): 11.

- [Ben80] P. Benioff, *The computer as a physical system: A microscopic quantum mechanical Hamiltonian model of computers as represented by Turing machines*, Journal of Statistical Physics **22** (1980), 563–591. Cited in page(s): 1.
- [Ben82] ———, *Quantum Mechanical Models of Turing Machines That Dissipate No Energy*, Physical Review Letters **48** (1982), 1581–1585. Cited in page(s): 1.
- [BHAW04] A. M. Blackburn, D. G. Hasko, H. Ahmed, and D. A. Williams, *Tungsten pedestal structure for nanotriode devices*, J. Vac. Sci. Technol. B **22** (2004), 1298–1302. Cited in page(s): 31.
- [BHI⁺89] J. J. Bollinger, D. J. Heinzen, W. M. Itano, S. L. Gilbert, and D. J. Wineland, *Test of the linearity of quantum mechanics by rf spectroscopy of the $^9\text{Be}^+$ ground state*, Physical Review Letters **63** (1989), 1031–1034. Cited in page(s): 1.
- [BHI⁺91] J. J. Bollinger, D. J. Heinzen, W. M. Itano, S. L. Gilbert, and D. J. Wineland, *A 303 MHz frequency standard based on trapped Be^+ ions*, IEEE Trans. Instr. Meas. **126** (1991), no. 40. Cited in page(s): 3.
- [BHIW86] J. C. Bergquist, R. G. Hulet, W. M. Itano, and D. J. Wineland, *Observation of quantum jumps in a single atom*, Physical Review Letters **57** (1986), 1699–1702. Cited in page(s): 3 and 15.
- [BKRB08] J. Benhelm, G. Kirchmair, C. F. Roos, and R. Blatt, *Towards fault-tolerant quantum computing with trapped ions*, Nature Physics **27** (2008), no. 4. Cited in page(s): 3.
- [Bla00] G. Blasbichler, *Ein Lambdameter mit 10^{-7} Messunsicherheit*, Master’s thesis, Universität Innsbruck, 2000. Cited in page(s): 84.
- [BLB⁺06] J. Britton, D. Leibfried, J. Beall, R. B. Blakestad, J. J. Bollinger, J. Chiaverini, R. J. Epstein, J. D. Jost, D. Kielpinski, C. Langer, R. Ozeri, R. Reichle, S. Seidelin, N. Shiga, J. H. Wesenberg, and D. J. Wineland, *A microfabricated surface-electrode ion trap in silicon*, ArXiv Quantum Physics e-prints **arXiv:quant-ph/0605170** (2006). Cited in page(s): 5.
- [BLP⁺88] R. Blatt, G. Lafyatis, W. D. Phillips, S. Stenholm, and D. J. Wineland, *Cooling in traps*, Physica Scripta Volume T **22** (1988), 216. Cited in page(s): 16 and 17.
- [BOV⁺09] R. B. Blakestad, C. Ospelkaus, A. P. VanDevender, J. M. Amini, J. Britton, D. Leibfried, and D. J. Wineland, *High fidelity transport of trapped-ion qubits through an X-junction trap array*, ArXiv e-prints **arXiv:0901.0533** (2009). Cited in page(s): 5, 94, and 101.
- [BPIW85] J. J. Bollinger, J. D. Prestage, W. M. Itano, and D. J. Wineland, *Laser-cooled-atomic frequency standard*, Physical Review Letters **54** (1985), 1000–1003. Cited in page(s): 1.
- [BRC⁺04] M. G. Blain, L. S. Riter, D. Cruz, D. Austin, G. Wu, W. R. Plass, and R. G. Cooks, *Towards the Hand-Held Mass Spectrometer: Design Considerations, Simulation, and Fabrication of Micrometer-Scaled Cylindrical Ion Traps*, Int. J. Mass Spectrom. **236** (2004), 91–104. Cited in page(s): 5.
- [Bro07] M. Brownnutt, *$^{88}\text{Sr}^+$ ion trapping techniques and technologies for quantum information processing*, Ph.D. thesis, Imperial College, 2007. Cited in page(s): 29 and 106.
- [BSW82] R. Blatt, H. Schnatz, and G. Werth, *Ultrahigh-Resolution Microwave Spectroscopy on Trapped $^{171}\text{Yb}^+$ Ions*, Physical Review Letters **48** (1982), 1601–1603. Cited in page(s): 1.

Bibliography

- [BWG⁺06] M. Brownnutt, G. Wilpers, P. Gill, R. C. Thompson, and A. G. Sinclair, *Monolithic microfabricated ion trap chip design for scaleable quantum processors*, New Journal of Physics **8** (2006), 232. Cited in page(s): 4 and 5.
- [BWHG03] P. J. Blythe, S. A. Webster, K. Hosaka, and P. Gill, *Systematic frequency shifts of the 467 nm electric octupole transition in $^{171}\text{Yb}^+$* , Journal of Physics B Atomic Molecular Physics **36** (2003), 981–989. Cited in page(s): 10.
- [CBB⁺05a] J. Chiaverini, R. B. Blakestad, J. Britton, J. D. Jost, C. Langer, D. Leibfried, R. Ozeri, and D. Wineland, *Surface-electrode architecture for ion-trap quantum information processing*, Quant. Inf. Comp. **5** (2005), no. 419. Cited in page(s): 4.
- [CBB⁺05b] J. Chiaverini, R. B. Blakestad, J. Britton, J. D. Jost, C. Langer, D. Leibfried, R. Ozeri, and D. J. Wineland, *Surface-Electrode Architecture for Ion-Trap Quantum Information Processing*, ArXiv Quantum Physics e-prints **arXiv:quant-ph/0501147** (2005). Cited in page(s): 4 and 20.
- [CBL⁺05] J. Chiaverini, J. Britton, D. Leibfried, E. Knill, M. D. Barrett, R. B. Blakestad, W. M. Itano, J. D. Jost, C. Langer, R. Ozeri, T. Schätz, and D. J. Wineland, *Implementation of the Semiclassical Quantum Fourier Transform in a Scalable System*, Science **308** (2005), 997–1000. Cited in page(s): 29.
- [CCF⁺00] D. Cassetari, A. Chenet, R. Folman, A. Haase, B. Hessmo, P. Krüger, T. Maier, S. Schneider, T. Calarco, and J. Schmiedmayer, *Micromanipulation of neutral atoms with nanofabricated structures*, Applied Physics B: Lasers and Optics **70** (2000), 721–730. Cited in page(s): 29.
- [CHH⁺00] D. Cassetari, B. Hessmo, A. Haase, P. Kruger, R. Folman, and J. Schmiedmayer, *Atom Chips - Microtraps and guides for atoms.*, APS Meeting Abstracts, June 2000, p. 305. Cited in page(s): 29.
- [Chw09] Michael Chwalla, *Precision spectroscopy with $^{40}\text{Ca}^+$ in a Paul trap*, Ph.D. thesis, Universität Innsbruck, 2009. Cited in page(s): 83.
- [CLRZ99] D. Cubric, B. Lencova, F. H. Read, and J. Zlamal, *References Comparison of FDM, FEM and BEM for electrostatic charged particle optics*, Nuclear Instruments & Methods in Physics Research A (1999), no. 427, 357–362. Cited in page(s): 39.
- [CLS⁺04] J. Chiaverini, D. Leibfried, T. Schätz, M. D. Barrett, R. B. Blakestad, J. Britton, W. M. Itano, J. D. Jost, E. Knill, C. Langer, R. Ozeri, and D. J. Wineland, *Realization of quantum error correction*, Nature **432** (2004), 602–605. Cited in page(s): 3.
- [CRSP98] L. Candido, J.-P. Rino, Nelson Studart, and F.M. Peeters, *The structure and spectrum of the anisotropically confined two-dimensional Yukawa system*, J. Phys.: Condensed Matter **10** (1998), 11627–11644. Cited in page(s): 13.
- [CSD⁺07] Y. Colombe, T. Steinmetz, G. Dubois, F. Linke, D. Hunger, and J. Reichel, *Strong atom-field coupling for Bose-Einstein condensates in an optical cavity on a chip*, Nature **450** (2007), no. 272. Cited in page(s): 107.
- [CZ95] J. I. Cirac and P. Zoller, *Quantum Computations with Cold Trapped Ions*, Physical Review Letters **74** (1995), 4091–4094. Cited in page(s): 2, 3, and 89.

- [DBIW89] F. Diedrich, J. C. Bergquist, W. M. Itano, and D. J. Wineland, *Laser cooling to the zero-point energy of motion*, Physical Review Letters **62** (1989), 403–406. Cited in page(s): 29.
- [DBJ00] I. H. Deutsch, G. K. Brennen, and P. S. Jessen, *Quantum Computing with Neutral Atoms in an Optical Lattice*, Fortschritte der Physik **48** (2000), 925–943. Cited in page(s): 2.
- [DBL⁺02] B. Demarco, A. Ben-Kish, D. Leibfried, V. Meyer, M. Rowe, B. M. Jelenković, W. M. Itano, J. Britton, C. Langer, T. Rosenband, and D. J. Wineland, *Experimental Demonstration of a Controlled-NOT Wave-Packet Gate*, Physical Review Letters **89** (2002), no. 26, 267901. Cited in page(s): 3.
- [Deh67] H. G. Dehmelt, *Radiofrequency spectroscopy of stored ions I - Storage*, Ad. At. Mol. Phys. **3** (1967), no. 53. Cited in page(s): 1 and 10.
- [Deh75] H. Dehmelt, *Proposed $10^{14} Dv < v$ Laser Fluorescence Spectroscopy on Tl^+ Mono-Ion Oscillator II (spontaneous quantum jumps)*, Bull. Am. Phys. Soc. **20** (1975), no. 60. Cited in page(s): 15.
- [DHB89] R. G. DeVoe, J. Hoffnagle, and R. G. Brewer, *Role of laser damping in trapped ion crystals*, Phys. Rev. A **39** (1989), 4362–4365. Cited in page(s): 16.
- [DHK⁺83] R. W. P. Drever, J. L. Hall, F. V. Kowalski, J. Hough, G. M. Ford, A. J. Munley, and H. Ward, *Laser phase and frequency stabilization using an optical resonator*, Applied Physics B: Lasers and Optics **31** (1983), 97–105. Cited in page(s): 82.
- [DHL⁺04] L. Deslauriers, P. C. Haljan, P. J. Lee, K.-A. Brickman, B. B. Blinov, M. J. Madsen, and C. Monroe, *Zero-point cooling and low heating of trapped $^{111}Cd^+$ ions*, Phys. Rev. A **70** (2004), no. 4, 043408. Cited in page(s): 3 and 29.
- [Dic53] R. H. Dicke, *The effect of collisions upon the Doppler width of spectral lines*, Physical Review **89** (1953), 472–473. Cited in page(s): 20 and 23.
- [Div00] D. P. Divincenzo, *The Physical Implementation of Quantum Computation*, Fortschritte der Physik **48** (2000), 771–783. Cited in page(s): 2.
- [DK02] R. G. DeVoe and C. Kurtsiefer, *Experimental study of anomalous heating and trap instabilities in a microscopic ^{137}Ba ion trap*, Phys. Rev. A **65** (2002), no. 6, 063407. Cited in page(s): 29.
- [DNBP94] F. Dfilippo, V. Natarajan, K. R. Boyce, and D. E. Pritchard, *Accurate atomic masses for fundamental metrology*, Physical Review Letters **73** (1994), 1481–1484. Cited in page(s): 1.
- [DOS⁺06] L. Deslauriers, S. Olmschenk, D. Stick, W. K. Hensinger, J. Sterk, and C. Monroe, *Scaling and Suppression of Anomalous Heating in Ion Traps*, Physical Review Letters **97** (2006), no. 10, 103007. Cited in page(s): 11, 20, and 29.
- [DPC⁺87] F. Diedrich, E. Peik, J. M. Chen, W. Quint, and H. Walther, *Observation of a phase transition of stored laser-cooled ions*, Physical Review Letters **59** (1987), 2931–2934. Cited in page(s): 3.
- [DRBH95] P. Domokos, J. M. Raimond, M. Brune, and S. Haroche, *Simple cavity-QED two-bit universal quantum logic gate: The principle and expected performances*, Phys. Rev. A **52** (1995), 3554–3559. Cited in page(s): 2.

Bibliography

- [DS00] J. Dongarra and F. Sullivan, *Guest Editors Introduction to the Top 10 Algorithms*, Computing in Science & Engineering **2** (2000), 22–23. Cited in page(s): 40.
- [Ebl06] Johannes Eble, *Stabilisierung von Lasern zum Erzeugen und Kühlen von Ionen in einer Paul-Falle*, Master’s thesis, Universität Ulm, 2006. Cited in page(s): 14.
- [EMSB03] J. Eschner, G. Morigi, F. Schmidt-Kaler, and R. Blatt, *Laser cooling of trapped ions*, Journal of the Optical Society of America B Optical Physics **20** (2003), 1003–1015. Cited in page(s): 24.
- [FAS04] L. Feenstra, L. M. Andersson, and J. Schmiedmayer, *Microtraps and Atom Chips: Toolboxes for Cold Atom Physics*, General Relativity and Gravitation **36** (2004), 2317–2329. Cited in page(s): 40.
- [Fey82] R. P. Feynman, *Simulating Physics with Computers*, International Journal of Theoretical Physics **21** (1982), 467–488. Cited in page(s): 1.
- [Fey85] ———, *Quantum mechanical computers*, Optics News **11** (1985), 11–20. Cited in page(s): 1.
- [Geo08] Elizabeth Marie George, *Fiber optic integration in planar ion traps*, Master’s thesis, Massachusetts Institute of Technology, Dept. of Physics., 2008. Cited in page(s): 106.
- [Gho95] Pradip K. Ghosh, *Ion Traps*, Clarendon Press, 1995. Cited in page(s): 9.
- [GKB⁺89] A. Gerhard, M. Kurz, J. Brutscher, H. Klein, and A. Schempp, *RF sparking experiments at 108.5 and 216 MHz*, IEEE Trans. Electr. Insul. **24** (1989), 1033–1036. Cited in page(s): 31.
- [GKW⁺04] S. Groth, P. Krüger, S. Wildermuth, R. Folman, T. Fernholz, J. Schmiedmayer, D. Mahalu, and I. Bar-Joseph, *Atom chips: Fabrication and thermal properties*, Applied Physics Letters **85** (2004), 2980. Cited in page(s): 29.
- [GKZ⁺08] R. Gerritsma, G. Kirchmair, F. Zähringer, J. Benhelm, R. Blatt, and C. F. Roos, *Precision measurement of the branching fractions of the $4p\ ^2P_{3/2}$ decay of Ca II*, European Physical Journal D **50** (2008), 13–19. Cited in page(s): 15.
- [GPQ⁺95] G. Gabrielse, D. Phillips, W. Quint, H. Kalinowsky, G. Rouleau, and W. Jhe, *Special Relativity and the Single Antiproton: Fortyfold Improved Comparison of p^- and p Charge-to-Mass Ratios*, Physical Review Letters **74** (1995), 3544–3547. Cited in page(s): 1.
- [GR87] L. Greengard and V. Rokhlin, *A Fast Algorithm for Particle Simulations*, Journal of Computational Physics **73** (1987), 325–348. Cited in page(s): 40.
- [Gre94] L. Greengard, *Fast Algorithms for Classical Physics*, Science **265** (1994), 909–914. Cited in page(s): 40.
- [GRL⁺03] S. Gulde, M. Riebe, G. P. T. Lancaster, C. Becher, J. Eschner, H. Häffner, F. Schmidt-Kaler, I. L. Chuang, and R. Blatt, *Implementation of the Deutsch-Jozsa algorithm on an ion-trap quantum computer*, Nature **421** (2003), 48–50. Cited in page(s): 3.
- [Hae00] Wolfgang Haensel, *Magnetische Mikrofallen für Rubidiumatome*, Ph.D. thesis, Ludwig-Maximilians-Universität München, 2000. Cited in page(s): 40.

Bibliography

- [HBD⁺05] P. C. Haljan, K.-A. Brickman, L. Deslauriers, P. J. Lee, and C. Monroe, *Spin-Dependent Forces on Trapped Ions for Phase-Stable Quantum Gates and Entangled States of Spin and Motion*, Physical Review Letters **94** (2005), no. 15, 153602. Cited in page(s): 3.
- [HDS⁺07] G. Huber, T. Deuschle, W. Schnitzler, R. Reichle, K. Singer, and F. Schmidt-Kaler, *Transport of ions in a segmented linear Paul trap in printed-circuit-board technology*, ArXiv e-prints **arXiv:0711.2947** (2007). Cited in page(s): 5, 25, and 94.
- [HHR⁺05] H. Häffner, W. Hänsel, C. F. Roos, J. Benhelm, D. Chek-Al-Kar, M. Chwalla, T. Körber, U. D. Rapol, M. Riebe, P. O. Schmidt, C. Becher, O. Gühne, W. Dür, and R. Blatt, *Scalable multiparticle entanglement of trapped ions*, Nature **438** (2005), 643–646. Cited in page(s): 3.
- [HHS⁺05] P. Hommelhoff, W. Hänsel, T. Steinmetz, T. W. Hänsch, and J. Reichel, *Transporting, splitting and merging of atomic ensembles in a chip trap*, New Journal of Physics **7** (2005), 3–18. Cited in page(s): 40.
- [HKP⁺07] R. Hanson, L. P. Kouwenhoven, J. R. Petta, S. Tarucha, and L. M. K. Vandersypen, *Spins in few-electron quantum dots*, Reviews of Modern Physics **79** (2007), 1217–1265. Cited in page(s): 2.
- [HML⁺06] J. P. Home, M. J. McDonnell, D. M. Lucas, G. Imreh, B. C. Keitch, D. J. Szwer, N. R. Thomas, S. C. Webster, D. N. Stacey, and A. M. Steane, *Deterministic entanglement and tomography of ion spin qubits*, New Journal of Physics **8** (2006), 188. Cited in page(s): 3.
- [HOS⁺06] W. K. Hensinger, S. Olmschenk, D. Stick, D. Hucul, M. Yeo, M. Acton, L. Deslauriers, C. Monroe, and J. Rabchuk, *T-junction ion trap array for two-dimensional ion shuttling, storage, and manipulation*, Applied Physics Letters **88** (2006), no. 3, 034101. Cited in page(s): 4, 5, 94, and 101.
- [HS75] T. W. Hänsch and A. L. Schawlow, *Cooling of gases by laser radiation*, Optics Communications **13** (1975), 68. Cited in page(s): 16.
- [HS06] J.P. Home and A.M. Steane, *Electrode Configurations for Fast Separation of Trapped Ions*, Quant. Inf. Comp. **6** (2006), no. 4-5, 289–325. Cited in page(s): 4, 26, and 28.
- [htt04] *Army Research Office: ARDA quantum computation roadmap*, 2004. Cited in page(s): 3.
- [htt06] *National Institute of Standards and Technology (NIST) Atomic Spectra Database (ASD)*, 2006. Cited in page(s): 15.
- [HYH⁺08] D. Hucul, M. Yeo, W. K. Hensinger, J. Rabchuk, S. Olmschenk, and C. Monroe, *On the transport of atomic ions in linear and multidimensional ion trap arrays*, Quant. Inf. Comp. **8** (2008), no. 501. Cited in page(s): 94 and 101.
- [IW82] W. M. Itano and D. J. Wineland, *Laser cooling of ions stored in harmonic and Penning traps*, Phys. Rev. A **25** (1982), 35–54. Cited in page(s): 16 and 32.
- [Jam98] D. James, *Quantum dynamics of cold trapped ions with application to quantum computation*, Appl. Phys. B **66** (1998), no. 181, 181–190. Cited in page(s): 12 and 15.
- [JC93] J. Jin and D. A. Church, *Precision lifetimes for the Ca^+ $4p^2P$ levels: Experiment challenges theory at the 1% level*, Physical Review Letters **70** (1993), 3213–3216. Cited in page(s): 15.

Bibliography

- [JMBW95] S. R. Jefferts, C. Monroe, E. W. Bell, and D. J. Wineland, *Coaxial-resonator-driven rf (Paul) trap for strong confinement*, Phys. Rev. A **51** (1995), 3112–3116. Cited in page(s): 11.
- [Jon00] J. A. Jones, *NMR Quantum Computation: A Critical Evaluation*, Fortschritte der Physik **48** (2000), 909–924. Cited in page(s): 2.
- [JPK00] D. Jonathan, M. B. Plenio, and P. L. Knight, *Fast quantum gates for cold trapped ions*, Phys. Rev. A **62** (2000), no. 4, 042307. Cited in page(s): 3.
- [Kan98] B. E. Kane, *A silicon-based nuclear spin quantum computer*, Nature **393** (1998), 133–137. Cited in page(s): 2.
- [KBL⁺05] A. Kreuter, C. Becher, G. Lancaster, A. Mundt, C. Russo, H. Häffner, C. Roos, W. Hänsel, F. Schmidt-Kaler, and R. Blatt, *Experimental and theoretical study of the 3d2D-level lifetimes of $^{40}\text{Ca}^+$* , Phys. Rev. A **71** (2005), no. 032504(12). Cited in page(s): 15.
- [KHT⁺00] N. Kjaergaard, L. Hornekaer, A.M. Thommesen, Z. Videsen, and M. Drewsen, *Isotope selective loading of an ion trap using resonance-enhanced two-photon ionization*, Appl. Phys. B **71** (2000), no. 207, 207–210. Cited in page(s): 35.
- [Kin23] K. H. Kingdon, *A Method for the Neutralization of Electron Space Charge by Positive Ionization at Very Low Gas Pressures*, Physical Review **21** (1923), 408–418. Cited in page(s): 1.
- [KK07] J. Kim and C. Kim, *Integrated Optical Approach to Trapped Ion Quantum Computation*, ArXiv e-prints [arXiv:0711.3866](https://arxiv.org/abs/0711.3866) (2007). Cited in page(s): 106.
- [KLM01] E. Knill, R. Laflamme, and G. J. Milburn, *A scheme for efficient quantum computation with linear optics*, Nature **409** (2001), 46–52. Cited in page(s): 2.
- [KMR⁺01] D. Kielpinski, V. Meyer, M. A. Rowe, C. A. Sackett, W. M. Itano, C. Monroe, and D. J. Wineland, *A Decoherence-Free Quantum Memory Using Trapped Ions*, Science **291** (2001), 1013–1015. Cited in page(s): 3.
- [KMW02] D. Kielpinski, C. Monroe, and D. J. Wineland, *Architecture for a large-scale ion-trap quantum computer*, Nature **417** (2002), 709–711. Cited in page(s): 4, 11, 24, 89, 94, and 105.
- [KPM⁺05] J. Kim, S. Pau, Z. Ma, H. R. McLellan, J. V. Gates, A. Kornblit, R. E. Slusher, R. M. Jopson, I. Kang, and M. Dinu, *System design for large-scale ion trap quantum information processor*, Quant. Inf. Comp. **5** (2005), no. 515. Cited in page(s): 5.
- [Ła08] Jarosław Łabaziewicz, *High Fidelity Quantum Gates with Ions in Cryogenic Microfabricated Ion Traps*, Ph.D. thesis, Massachusetts Institute of Technology, 2008. Cited in page(s): 29 and 107.
- [LBD⁺05] P. J. Lee, K.-A. Brickman, L. Deslauriers, P. C. Haljan, L.-M. Duan, and C. Monroe, *Phase control of trapped ion quantum gates*, Journal of Optics B: Quantum and Semiclassical Optics **7** (2005), 371. Cited in page(s): 3.
- [LBW⁺05] X. Liu, K.-H. Brenner, M. Wilzbach, M. Schwarz, T. Fernholz, and J. Schmiedmayer, *Fabrication of alignment structures for a fiber resonator by use of deep-ultraviolet lithography*, Applied Optics **44** (2005), 6857–6860. Cited in page(s): 106.

- [LCL⁺07] D. R. Leibbrandt, R. J. Clark, J. Łabaziewicz, P. Antohi, W. Bakr, K. R. Brown, and I. L. Chuang, *Laser ablation loading of a surface-electrode ion trap*, Phys. Rev. A **76** (2007), no. 5, 055403–055406. Cited in page(s): 48.
- [LD98] D. Loss and D. P. Divincenzo, *Quantum computation with quantum dots*, Phys. Rev. A **57** (1998), 120–126. Cited in page(s): 2.
- [LDM⁺02] D. Leibfried, B. Demarco, V. Meyer, M. Rowe, A. Ben-Kish, J. Britton, W. M. Itano, B. Jelenković, C. Langer, T. Rosenband, and D. J. Wineland, *Trapped-Ion Quantum Simulator: Experimental Application to Nonlinear Interferometers*, Physical Review Letters **89** (2002), no. 24, 247901. Cited in page(s): 3.
- [LDM⁺03] D. Leibfried, B. DeMarco, V. Meyer, D. Lucas, M. Barrett, J. Britton, W. M. Itano, B. Jelenković, C. Langer, T. Rosenband, and D. J. Wineland, *Experimental demonstration of a robust, high-fidelity geometric two ion-qubit phase gate*, Nature **422** (2003), 412–415. Cited in page(s): 3.
- [ŁGA⁺08] J. Łabaziewicz, Y. Ge, P. Antohi, D. Leibbrandt, K. R. Brown, and I. L. Chuang, *Suppression of Heating Rates in Cryogenic Surface-Electrode Ion Traps*, Physical Review Letters **100** (2008), no. 1, 013001. Cited in page(s): 5 and 29.
- [ŁGL⁺08] J. Łabaziewicz, Y. Ge, D. Leibbrandt, S. X. Wang, R. Shewmon, and I. L. Chuang, *Temperature Dependence of Electric Field Noise Above Gold Surfaces*, ArXiv e-prints **arXiv:0804.2665** (2008). Cited in page(s): 5.
- [LKOW07] D. Leibfried, E. Knill, C. Ospelkaus, and D. J. Wineland, *Transport quantum logic gates for trapped ions*, Phys. Rev. A **76** (2007), no. 3, 032324. Cited in page(s): 94.
- [LKS⁺05] D. Leibfried, E. Knill, S. Seidelin, J. Britton, R. B. Blakestad, J. Chiaverini, D. B. Hume, W. M. Itano, J. D. Jost, C. Langer, R. Ozeri, R. Reichle, and D. J. Wineland, *Creation of a six-atom ‘Schrödinger cat’ state*, Nature **438** (2005), 639–642. Cited in page(s): 3.
- [LŁC⁺09] D. R. Leibbrandt, J. Łabaziewicz, R. J. Clark, I. L. Chuang, R. Epstein, C. Ospelkaus, J. Wesenberg, J. Bollinger, D. Leibfried, D. Wineland, D. Stick, J. Sterk, C. Monroe, C. Pai, Y. Low, R. Frahm, and R. E. Slusher, *Demonstration of a scalable, multiplexed ion trap for quantum information processing*, ArXiv e-prints **arXiv:0904.2599** (2009). Cited in page(s): 29.
- [LWB⁺07] V. Letchumanan, G. Wilpers, M. Brownnutt, P. Gill, and A. G. Sinclair, *Zero-point cooling and heating-rate measurements of a single ⁸⁸Sr⁺ ion*, Phys. Rev. A **75** (2007), no. 6, 063425. Cited in page(s): 29.
- [LZI⁺09] G. Lin, S. Zhu, R. Islam, K. Kim, M. Chang, S. Korenblit, C. Monroe, and L. Duan, *Large Scale Quantum Computation in an Anharmonic Linear Ion Trap*, ArXiv e-prints **arXiv:0901.0579** (2009). Cited in page(s): 13 and 89.
- [MBG⁺06] D. L. Moehring, B. B. Blinov, D. W. Gidley, R. N. Kohn, M. J. Madsen, T. D. Sanderson, R. S. Vallery, and C. Monroe, *Precision lifetime measurements of a single trapped ion with ultrafast laser pulses*, Phys. Rev. A **73** (2006), no. 2, 023413. Cited in page(s): 1.
- [MECZ99] G. Morigi, J. Eschner, J. I. Cirac, and P. Zoller, *Laser cooling of two trapped ions: Sideband cooling beyond the Lamb-Dicke limit*, Phys. Rev. A **59** (1999), 3797–3808. Cited in page(s): 20 and 23.

Bibliography

- [MHS⁺04] M. J. Madsen, W. K. Hensinger, D. Stick, J. A. Rabchuk, and C. Monroe, *Planar ion trap geometry for microfabrication*, Applied Physics B: Lasers and Optics **78** (2004), 639–651. Cited in page(s): 20 and 22.
- [Mil89] H. C. Miller, *Surface flashover of insulators*, IEEE Trans. Electr. Insul. **24** (1989). Cited in page(s): 31.
- [MKH⁺09] T. Monz, K. Kim, W. Hänsel, M. Riebe, A. S. Villar, P. Schindler, M. Chwalla, M. Hennrich, and R. Blatt, *Realization of the Quantum Toffoli Gate with Trapped Ions*, Physical Review Letters **102** (2009), no. 4, 040501–040504. Cited in page(s): 3.
- [MMO⁺07] D. L. Moehring, P. Maunz, S. Olmschenk, K. C. Younge, D. N. Matsukevich, L.-M. Duan, and C. Monroe, *Entanglement of single-atom quantum bits at a distance*, Nature **449** (2007), 68–71. Cited in page(s): 3.
- [MOL⁺99] J. E. Mooij, T. P. Orlando, L. Levitov, Lin Tian, Caspar H. van der Wal, and Seth Lloyd, *Josephson Persistent-Current Qubit*, Science **285** (1999), 1036–1039. Cited in page(s): 2.
- [MS59] W. W. Macalpine and R. O. Schildknecht, *Coaxial resonators with helical inner conductor*, Proceedings of the IRE **47** (1959), no. 2099. Cited in page(s): 78.
- [MSS01] Y. Makhlin, G. Schoen, and A. Shnirman, *Quantum-state engineering with Josephson-junction devices*, Reviews of Modern Physics **73** (2001), 357–400. Cited in page(s): 2.
- [MSSM08] A. Marian, S. Schlunk, W. SchKörberllkopf, and G. Meijer, *AC electric trapping of neutral atoms*, APS Meeting Abstracts, May 2008, p. 4003. Cited in page(s): 29.
- [MT95] R. March and J. Todd, *Practical aspects of ion trap mass spectrometry*, vol. Volume 1, CRC Press, 1995. Cited in page(s): 9.
- [NHTD78] W. Neuhauser, M. Hohenstatt, P. Toschek, and H. Dehmelt, *Optical-Sideband Cooling of Visible Atom Cloud Confined in Parabolic Well*, Physical Review Letters **41** (1978), 233–236. Cited in page(s): 1.
- [NHTD80] W. Neuhauser, M. Hohenstatt, P. E. Toschek, and H. Dehmelt, *Localized visible Ba⁺ mono-ion oscillator*, Phys. Rev. A **22** (1980), 1137–1140. Cited in page(s): 1.
- [NSD86] W. Nagourney, J. Sandberg, and H. Dehmelt, *Shelved optical electron amplifier - Observation of quantum jumps*, Physical Review Letters **56** (1986), 2797–2799. Cited in page(s): 3 and 15.
- [OHDG06] B. Odom, D. Hanneke, B. D’Urso, and G. Gabrielse, *New Measurement of the Electron Magnetic Moment Using a One-Electron Quantum Cyclotron*, Physical Review Letters **97** (2006), no. 3, 030801. Cited in page(s): 1.
- [OLA⁺08] C. Ospelkaus, C. E. Langer, J. M. Amini, K. R. Brown, D. Leibfried, and D. J. Wineland, *Trapped-Ion Quantum Logic Gates Based on Oscillating Magnetic Fields*, Physical Review Letters **101** (2008), no. 9, 090502. Cited in page(s): 94.
- [OM01] M. H. Oliveira and J. A. Miranda, *Biot-Savart-like law in electrostatics*, European Journal of Physics **22** (2001), 31–38. Cited in page(s): 40 and 41.
- [Pau90] W. Paul, *Electromagnetic traps for charged and neutral particles*, Reviews of Modern Physics **62** (1990), 531–540. Cited in page(s): 7 and 9.

- [Pen36] F. M. Penning, *Glow discharge between coaxial cylinders at low pressures in an axial magnetic field*, *Physica* **3** (1936), no. 873. Cited in page(s): 1.
- [PGCZ95] T. Pellizzari, S. A. Gardiner, J. I. Cirac, and P. Zoller, *Decoherence, continuous observation, and quantum computing: A cavity QED model*, *Physical Review Letters* **75** (1995), 3788–3791. Cited in page(s): 2.
- [Pha05] P. T. T. Pham, *A general-purpose pulse sequencer for quantum computing*, Master’s thesis, Massachusetts Institute of Technology, 2005. Cited in page(s): 87.
- [PLB⁺06] C. E. Pearson, D. R. Leibbrandt, W. S. Bakr, W. J. Mallard, K. R. Brown, and I. L. Chuang, *Experimental investigation of planar ion traps*, *Phys. Rev. A* **73** (2006), no. 3, 032307. Cited in page(s): 4, 53, and 54.
- [POF58] W. Paul, O. Osberghaus, and E. Fischer, *Ein Ionenkäfig*, *Forschungsberichte des Wirtschafts- und Verkehrsministerium Nordrhein-Westfalen* **415** (1958). Cited in page(s): 1.
- [PPL⁺06] S. Pau, C. S. Pai, Y. L. Low, J. Moxom, P. T. A. Reilly, W. B. Whitten, and J. M. Ramsey, *Microfabricated Quadrupole Ion Trap for Mass Spectrometer Applications*, *Physical Review Letters* **96** (2006), no. 12, 120801. Cited in page(s): 5.
- [PS53] W. Paul and H. Steinwedel, *Ein neues Massenspektrometer ohne Magnetfeld*, *Zeitschrift für Naturforschung A* **8** (1953), no. 7, 448–450. Cited in page(s): 1 and 9.
- [RBD⁺02] M. A. Rowe, A. Ben-Kish, B. DeMarco, D. Leibfried, V. Meyer, J. Beall, J. Britton, J. Hughes, W. M. Itano, B. Jelenkovic, C. Langer, T. Rosenband, and D. J. Wineland, *Transport of quantum states and separation of ions in a dual rf ion trap*, *Quant. Inf. Comp.* **2** (2002), no. 257. Cited in page(s): 4, 5, 9, 26, 94, and 101.
- [RBG⁺92] M.C. Raizen, J.C Bergquist, J.M. Gilligan, W.M. Itano, and D.J. Wineland, *Linear trap for high-accuracy spectroscopy of stored ions*, *J. of Mod. Opt.* **233** (1992), no. 39. Cited in page(s): 3.
- [Rei05] Mark Reibe, *Preparation of Entangled States and Quantum Teleportation with Atomic Qubits*, Ph.D. thesis, Universität Innsbruck, May 2005. Cited in page(s): 96.
- [RGB⁺92] M. G. Raizen, J. M. Gilligan, J. C. Bergquist, W. M. Itano, and D. J. Wineland, *Ionic crystals in a linear Paul trap*, *Phys. Rev. A* **45** (1992), 6493–6501. Cited in page(s): 3.
- [RHR⁺04] M. Riebe, H. Häffner, C. F. Roos, W. Hänsel, J. Benhelm, G. P. T. Lancaster, T. W. Körber, C. Becher, F. Schmidt-Kaler, D. F. V. James, and R. Blatt, *Deterministic quantum teleportation with atoms*, *Nature* **429** (2004), 734–737. Cited in page(s): 3.
- [RHS⁺08] T. Rosenband, D. B. Hume, P. O. Schmidt, C. W. Chou, A. Bruschi, L. Lorini, W. H. Oskay, R. E. Drullinger, T. M. Fortier, J. E. Stalnaker, S. A. Diddams, W. C. Swann, N. R. Newbury, W. M. Itano, D. J. Wineland, and J. C. Bergquist, *Frequency Ratio of Al^+ and Hg^+ Single-Ion Optical Clocks; Metrology at the 17th Decimal Place*, *Science* **319** (2008), 1808. Cited in page(s): 1.
- [RKS⁺06] M. Riebe, K. Kim, P. Schindler, T. Monz, P. O. Schmidt, T. K. Körber, W. Hänsel, H. Häffner, C. F. Roos, and R. Blatt, *Process Tomography of Ion Trap Quantum Gates*, *Physical Review Letters* **97** (2006), no. 22, 220407. Cited in page(s): 3.

Bibliography

- [RLB⁺06] R. Reichle, D. Leibfried, R. B. Blakestad, J. Britton, J. D. Jost, E. Knill, C. Langer, R. Ozeri, S. Seidelin, and D. J. Wineland, *Transport dynamics of single ions in segmented microstructured Paul trap arrays*, *Fortschritte der Physik* **54** (2006), 666–685. Cited in page(s): 94.
- [RLK⁺06] R. Reichle, D. Leibfried, E. Knill, J. Britton, R. B. Blakestad, J. D. Jost, C. Langer, R. Ozeri, S. Seidelin, and D. J. Wineland, *Experimental purification of two-atom entanglement*, *Nature* **443** (2006), 838–841. Cited in page(s): 3.
- [RLR⁺04] C. F. Roos, G. P. Lancaster, M. Riebe, H. Häffner, W. Hänsel, S. Gulde, C. Becher, J. Eschner, F. Schmidt-Kaler, and R. Blatt, *Bell States of Atoms with Ultralong Lifetimes and Their Tomographic State Analysis*, *Physical Review Letters* **92** (2004), no. 22, 220402. Cited in page(s): 3.
- [RMK⁺08] M. Riebe, T. Monz, K. Kim, A. S. Villar, P. Schindler, M. Chwalla, M. Hennrich, and R. Blatt, *Deterministic entanglement swapping with an ion trap quantum computer*, *Nature Physics* **4** (2008), 839–842. Cited in page(s): 3.
- [Rot03] D. Rotter, *Photoionisation von Kalzium*, Master’s thesis, Universität Innsbruck, January 2003. Cited in page(s): 79 and 83.
- [RRH⁺04] C. F. Roos, M. Riebe, H. Häffner, W. Hänsel, J. Benhelm, G. P. T. Lancaster, C. Becher, F. Schmidt-Kaler, and R. Blatt, *Control and Measurement of Three-Qubit Entangled States*, *Science* **304** (2004), 1478–1481. Cited in page(s): 3.
- [Rus08] Carlos Manuel da Silva Baptista Russo, *Photon Statistics of a single ion coupled to a high-finesse cavity*, Ph.D. thesis, Universität Innsbruck, 2008. Cited in page(s): 79.
- [RYB⁺00] R. J. Rafac, B. C. Young, J. A. Beall, W. M. Itano, D. J. Wineland, and J. C. Bergquist, *Sub-dekahertz Ultraviolet Spectroscopy of $^{199}\text{Hg}^+$* , *Physical Review Letters* **85** (2000), 2462–2465. Cited in page(s): 1.
- [RZR⁺99] C. Roos, T. Zeiger, H. Rohde, H. C. Nägerl, J. Eschner, D. Leibfried, F. Schmidt-Kaler, and R. Blatt, *Quantum State Engineering on an Optical Transition and Decoherence in a Paul Trap*, *Physical Review Letters* **83** (1999), 4713–4716. Cited in page(s): 29.
- [Sch52] E. Schrödinger, *Are There Quantum Jumps?: Part II**, *Brit. J. Philos. Sci.* **III** (1952), 109–123. Cited in page(s): 7.
- [Sch08] Philipp Schindler, *Frequency synthesis and pulse shaping for quantum information processing with trapped ions*, Master’s thesis, Universität Innsbruck, 2008. Cited in page(s): 87.
- [Sch09] Stephan Schulz, *Scalable Microchip Ion Traps for Quantum Computation*, Ph.D. thesis, Universität Ulm, 2009. Cited in page(s): 94.
- [SCK⁺05] P. D. Schwindt, E. A. Cornell, T. Kishimoto, Y.-J. Wang, and D. Z. Anderson, *Efficient loading of a magnetic waveguide on an atom chip*, *Phys. Rev. A* **72** (2005), no. 2, 023612. Cited in page(s): 29.
- [SCR⁺06] S. Seidelin, J. Chiaverini, R. Reichle, J. J. Bollinger, D. Leibfried, J. Britton, J. H. Wesenberg, R. B. Blakestad, R. J. Epstein, D. B. Hume, W. M. Itano, J. D. Jost, C. Langer, R. Ozeri, N. Shiga, and D. J. Wineland, *Microfabricated Surface-Electrode Ion Trap for Scalable Quantum Information Processing*, *Physical Review Letters* **96** (2006), no. 25, 253003. Cited in page(s): 5.

- [SHB⁺09] F. Splatt, M. Harlander, M. Brownnutt, F. Zähringer, R. Blatt, and W Hänsel, *Deterministic reordering of $^{40}\text{Ca}^+$ ions in a linear segmented Paul trap.*, New Journal of Physics (2009), submitted. Cited in page(s): 101.
- [SHG⁺03] F. Schmidt-Kaler, H. Häffner, S. Gulde, M. Riebe, G. P. T. Lancaster, T. Deuschle, C. Becher, W. Hänsel, J. Eschner, C. F. Roos, and R. Blatt, *How to realize a universal quantum gate with trapped ions*, Applied Physics B: Lasers and Optics **77** (2003), 789–796. Cited in page(s): 3.
- [Sho94] P. W. Shor, *Algorithms for quantum computation: discrete logarithms and factoring*, Proceedings of the 35th Annual Symposium on Foundations of Computer Science, Santa Fe, NM, Nov. 20-22, IEEE Computer Society Press, 1994, pp. 124–134. Cited in page(s): 2.
- [Sho95] ———, *Scheme for reducing decoherence in quantum computer memory*, Phys. Rev. A **52** (1995), 2493. Cited in page(s): 2.
- [Sho96] ———, *Fault-tolerant quantum computation*, ArXiv Quantum Physics e-prints **arXiv:quant-ph/9605011** (1996). Cited in page(s): 2.
- [SHO⁺06] D. Stick, W. K. Hensinger, S. Olmschenk, M. J. Madsen, K. Schwab, and C. Monroe, *Ion trap in a semiconductor chip*, Nature Physics **2** (2006), 36–39. Cited in page(s): 4, 5, 9, 20, and 101.
- [SHR⁺03] F. Schmidt-Kaler, H. Häffner, M. Riebe, S. Gulde, G. P. T. Lancaster, T. Deuschle, C. Becher, C. F. Roos, J. Eschner, and R. Blatt, *Realization of the Cirac-Zoller controlled-NOT quantum gate*, Nature **422** (2003), 408–411. Cited in page(s): 3.
- [Sig06] Daniel Sigg, *Printed Circuit Boards for Ultra High Vacuum*, Tech. report, Laser Interferometer Gravitational Wave Observatory (LIGO), 2006. Cited in page(s): 75.
- [Sina] Kilian Singer, *Deterministic ultracold ion source targeting the heisenberg limit - towards scalable quantum computation and simulation*, QIon09, Workshop on Quantum Information and Quantum Dynamics in Ion Traps, Tel-Aviv, May 3, 2009. Cited in page(s): 94.
- [Sinb] ———, *Field calculation for ion traps*, oral presentation, Schrödinger Saal, IQOQI, Innsbruck, September 24, 2008. Cited in page(s): 94.
- [SKK⁺00] C. A. Sackett, D. Kielpinski, B. E. King, C. Langer, V. Meyer, C. J. Myatt, M. Rowe, Q. A. Turchette, W. M. Itano, D. J. Wineland, and C. Monroe, *Experimental entanglement of four particles*, Nature **404** (2000), 256–259. Cited in page(s): 3.
- [SLF⁺09] W. Schnitzler, N. M. Linke, R. Fickler, J. Meijer, F. Schmidt-Kaler, and K. Singer, *Deterministic Ultracold Ion Source Targeting the Heisenberg Limit*, Physical Review Letters **102** (2009), no. 7, 070501–070504. Cited in page(s): 101.
- [Slu06a] R. Slusher, *Scaling Up Ion and Atom Traps with Silicon Based VLSI and MEMS Technologies*, May 2006. Cited in page(s): 106.
- [Slu06b] Richart Slusher, *Scalable planar trapology*, Scalable planar trapology Workshop on Trapped Ion Quantum Computing, 2006. Cited in page(s): 29.
- [SM99] A. Sørensen and K. Mølmer, *Quantum Computation with Ions in Thermal Motion*, Physical Review Letters **82** (1999), 1971–1974. Cited in page(s): 3.
- [SNBT86] T. Sauter, W. Neuhauser, R. Blatt, and P. E. Toschek, *Observation of quantum jumps*, Physical Review Letters **57** (1986), 1696–1698. Cited in page(s): 1, 3, and 15.

Bibliography

- [SPSS06] S. Schulz, U. Poschinger, K. Singer, and F. Schmidt-Kaler, *Optimization of segmented linear Paul traps and transport of stored particles*, Fortschritte der Physik **54** (2006), 648–665. Cited in page(s): 21, 24, and 25.
- [SPSW93] C. A. Schrama, E. Peik, W. W. Smith, and H. Walther, *Novel miniature ion traps*, Optics Communications **101** (1993), 32–36. Cited in page(s): 11.
- [SPZS08] S. A. Schulz, U. Poschinger, F. Ziesel, and F. Schmidt-Kaler, *Sideband cooling and coherent dynamics in a microchip multi-segmented ion trap*, New Journal of Physics **10** (2008), no. 4, 045007. Cited in page(s): 4 and 101.
- [SRS⁺00] A. Steane, C. F. Roos, D. Stevens, A. Mundt, D. Leibfried, F. Schmidt-Kaler, and R. Blatt, *Speed of ion-trap quantum-information processors*, Phys. Rev. A **62** (2000), no. 4, 042305. Cited in page(s): 24.
- [Ste96] A. M. Steane, *Error Correcting Codes in Quantum Theory*, Physical Review Letters **77** (1996), 793–797. Cited in page(s): 2.
- [Ste97] A. Steane, *The ion trap quantum information processor*, Applied Physics B: Lasers and Optics **64** (1997), 623–643. Cited in page(s): 2 and 24.
- [Sti07] Daniel Lynn Stick, *Fabrication and Characterization of Semiconductor Ion Traps for Quantum Information Processing*, Ph.D. thesis, The University of Michigan, 2007. Cited in page(s): 45 and 106.
- [SWG01] A. G. Sinclair, M. A. Wilson, and P. Gill, *Improved three-dimensional control of a single strontium ion in an endcap trap*, Optics Communications **190** (2001), 193–203. Cited in page(s): 9.
- [TKK⁺00] Q. A. Turchette, D. Kielpinski, B. E. King, D. Leibfried, D. M. Meekhof, C. J. Myatt, M. A. Rowe, C. A. Sackett, C. S. Wood, W. M. Itano, C. Monroe, and D. J. Wineland, *Heating of trapped ions from the quantum ground state*, Phys. Rev. A **61** (2000), no. 6, 063418. Cited in page(s): 29.
- [TSC⁺06] P. Treutlein, T. Steinmetz, Y. Colombe, B. Lev, P. Hommelhoff, J. Reichel, M. Greiner, O. Mandel, A. Widera, T. Rom, I. Bloch, and T. Hänsch, *Quantum information processing in optical lattices and magnetic microtraps*, Fortschritte der Physik **54** (2006), 702–718. Cited in page(s): 29.
- [TSD⁺06] A. Takamizawa, T. Steinmetz, R. Delhuille, T. W. Hänsch, and J. Reichel, *Miniature fluorescence detector for single atom observation on a microchip*, Optics Express **14** (2006), 10976–10983. Cited in page(s): 107.
- [TWK⁺98] Q. A. Turchette, C. S. Wood, B. E. King, C. J. Myatt, D. Leibfried, W. M. Itano, C. Monroe, and D. J. Wineland, *Deterministic Entanglement of Two Trapped Ions*, Physical Review Letters **81** (1998), 3631–3634. Cited in page(s): 3.
- [VC05] L. M. Vandersypen and I. L. Chuang, *NMR techniques for quantum control and computation*, Reviews of Modern Physics **76** (2005), 1037–1069. Cited in page(s): 2 and 3.
- [WAB⁺07] J. H. Wesenberg, J. M. Amini, R. B. Blakestad, J. Britton, K. R. Brown, R. J. Epstein, J. P. Home, W. M. Itano, J. D. Jost, C. Langer, D. Leibfried, R. Ozeri, S. Seidelin, and D. J. Wineland, *Analytical methods for design of surface-electrode ion traps*, June 2007, Poster K1012. Cited in page(s): 94.

- [WBI⁺87] D. J. Wineland, J. C. Bergquist, W. M. Itano, J. J. Bollinger, and C. H. Manney, *Atomic ion Coulomb clusters in an ion trap*, Physical Review Letters **59** (1987), 2935–2938. Cited in page(s): 3.
- [WBID80] D. J. Wineland, J. C. Bergquist, W. M. Itano, and R. E. Drullinger, *Double-resonance and optical-pumping experiments on electromagnetically confined, laser-cooled ions*, Optics Letters **5** (1980), 245–247. Cited in page(s): 3.
- [WD75] D. J. Wineland and H. G. Dehmelt, *Proposed $10^{14} D\nu < \nu$ Laser Fluorescence Spectroscopy on Tl^+ Mono-Ion Oscillator III (side band cooling)*, Bull. Am. Phys. Soc. **20** (1975), no. 637. Cited in page(s): 16.
- [WDW78] D. J. Wineland, R. E. Drullinger, and F. L. Walls, *Radiation-Pressure Cooling of Bound Resonant Absorbers*, Physical Review Letters **40** (1978), 1639–1642. Cited in page(s): 1 and 16.
- [Wes08a] J. H. Wesenberg, *Electrostatics of surface-electrode ion traps*, Phys. Rev. A **78** (2008), no. 6, 063410. Cited in page(s): 40.
- [Wes08b] ———, *Ideal intersections for radio-frequency trap networks*, ArXiv e-prints **arXiv:0802.3162** (2008). Cited in page(s): 94.
- [WGFS09] S. Whitlock, R. Gerritsma, T. Fernholz, and R. J. C. Spreeuw, *Two-dimensional array of microtraps with atomic shift register on a chip*, New Journal of Physics **11** (2009), no. 2, 023021. Cited in page(s): 29.
- [WI79] D. J. Wineland and W. M. Itano, *Laser cooling of atoms*, Phys. Rev. A **20** (1979), 1521–1540. Cited in page(s): 16.
- [WI81] ———, *Spectroscopy of a single Mg^+ ion*, Physics Letters A **82** (1981), 75–78. Cited in page(s): 1.
- [WIBH87] D. J. Wineland, W. M. Itano, J. C. Bergquist, and R. G. Hulet, *Laser-cooling limits and single-ion spectroscopy*, Phys. Rev. A **36** (1987), 2220–2232. Cited in page(s): 1.
- [Win] D. Wineland, oral presentation, Schrödinger Saal, IQOQI, Innsbruck, June 6, 2008. Cited in page(s): 5, 35, and 105.
- [WLB⁺05] D. J. Wineland, D. Leibfried, M. D. Barrett, A. Ben-Kish, J. C. Bergquist, R. B. Blakestad, J. J. Bollinger, J. Britton, J. Chiaverini, B. Demarco, D. Hume, W. M. Itano, M. Jensen, J. D. Jost, E. Knill, J. Koelemeij, C. Langer, W. Oskay, R. Ozeri, R. Reichle, T. Rosenband, T. Schätz, P. O. Schmidt, and S. Seidelin, *Quantum control, quantum information processing, and quantum-limited metrology with trapped ions*, ArXiv Quantum Physics e-prints **arXiv:quant-ph/0508025** (2005). Cited in page(s): 4 and 29.
- [WMI⁺97] D. J. Wineland, C. Monroe, W. M. Itano, D. Leibfried, B. E. King, and D. M. Meekhof, *Experimental issues in coherent quantum-state manipulation of trapped atomic ions*, ArXiv Quantum Physics e-prints **arXiv:quant-ph/9710025** (1997). Cited in page(s): 10.
- [WMI⁺98] D. J. Wineland, C. Monroe, W. M. Itano, B. E. King, D. Leibfried, D. M. Meekhof, C. Myatt, and C. Wood, *Experimental Primer on the Trapped Ion Quantum Computer*, Fortschritte der Physik **46** (1998), 363–390. Cited in page(s): 10.
- [YND91] N. Yu, W. Nagourney, and H. Dehmelt, *Demonstration of new Paul-Straubel trap for trapping single ions*, Journal of Applied Physics **69** (1991), 3779–3781. Cited in page(s): 11.

Bibliography

- [YTN02] J. Q. You, J. S. Tsai, and F. Nori, *Scalable Quantum Computing with Josephson Charge Qubits*, Physical Review Letters **89** (2002), no. 19, 197902. Cited in page(s): 2.
- [Zae07] F. A. Zaehring, *Faseroptische Detektion gespeicherter Calciumionen in einer Mikrofalle*, Master's thesis, Universität Innsbruck, 2007. Cited in page(s): 107.